FREEFORM OPTICAL SURFACE FORM METROLOGY WITH SERIAL DATA ACQUISITION

by

Todd Noste

A dissertation submitted to the faculty of
The University of North Carolina at Charlotte
in partial fulfillment of the requirements
for the degree of Doctor of Philosophy in
Mechanical Engineering

Charlotte

2020

Approved by:

_____
Dr. Christopher Evans

_____
Dr. Jimmie Miller

_____
Dr. Edward Morse

_____
Dr. Wesley Williams

ABSTRACT

TODD NOSTE. Freeform Optical Surface Form Metrology with Serial Data Acquisition. (Under the direction of DR. CHRISTOPHER EVANS)

Freeform optics, or optics with no axis of rotational invariance, provide optical designers more degrees of freedom, flexibility, and opportunity for innovation increasing optical performance and system integration while decreasing the form factor. Advancements in optical fabrication have enabled freeform surface manufacture with greater precision. Metrology instruments and techniques are needed to verify the performance of freeform optical surfaces and systems to keep up with design and manufacture. Freeform optics often have high slopes, no axis of symmetry, and a large departure from spherical, making traditional metrology techniques inadequate. This research was conducted to enable form measurements of freeform mirrors in the 250 mm class for a next generation three mirror anastigmatic (TMA) telescope complete with a statement of the measurement uncertainty to fill the gap in metrology of freeform optics. A flexible metrology instrument that could measure relatively large optics with customizable probe paths and sampling strategies was needed while maintaining the required uncertainty.

Measurements were made using a Moore Nanotech 100UMM 4-axis coordinate measurement machine (CMM) with a probe path that allows for estimation of the thermal error and the possibility of compensation. A mathematical model was developed for the 100UMM using transformation matrices populated with the part and probe position vectors, probe displacement, machine carriage positions, geometric machine errors and probing errors. The model is used in geometric error compensation and a Monte Carlo simulation used for evaluating the task specific uncertainty. The geometric machine errors were measured for error compensation and the uncertainty in those measurements was used in the Monte Carlo simulation for task specific un-

certainty evaluation of parts measured on the 100UMM. The mathematical model is also used to solve for the machine carriage positions to automate writing the machine language (g-code) for programming the probe path.

A chromatic confocal optical probe was used to measure the reflective freeform optics. The Precitec chromatic confocal probe used is non-contact, has a large angle of acceptance, a 4.5 mm working distance and a 300 μm range. Initially, a point by point measurement strategy was used. To reduce overall measurement time for point to point measurements, the probe path was chosen using the traveling salesman approach. The traveling salesman problem (TSP) uses an algorithm to reduce the total distance traveled during the measurement in 3D space.

Thermal characteristics of the 100UMM were evaluated using drift tests and temperature measurements. Drift tests are used to evaluate the amount of correlation between temperature and probe displacement. An environmentally controlled enclosure was installed around the 100UMM to stabilize the temperature of the ambient air, the high-pressure air going to the air bearings and the hydraulic oil for the hydrostatic bearings. The enclosure is designed to hold the metrology loop at 20 °C +/- 0.1 °C.

Despite housing the 100UMM in an environmentally controlled enclosure, thermal error estimation and correction was necessary. Through probe path optimization and planning, thermal drift was estimated and corrected while the measurement time was reduced further decreasing the thermal drift. Limiting carriage movement while recording measurement data reduces the amount of thermal drift due to moving heat sources from the hydrostatic bearings and the drive motors on the carriages.

The measurement time was reduced by a considerable amount by changing from a point by point measurement mode to a scanning measurement mode. By reducing measurement time, time varying errors including thermal error contributions are also reduced. The scanning mode, where the probe is moved over the surface of the

part while recording the probe displacement, requires reading the machine scales directly and syncing the data acquisition of the probe displacement and machine carriage positions. The inability to sync the machine carriage positions and probe displacement at precisely the same time results in data age uncertainty. The data age uncertainty is reduced by limiting the carriage velocity, and number of carriages moving simultaneously.

According to the guide to the expression of uncertainty in measurement (GUM) a measurement is not complete without a statement of uncertainty. A Monte Carlo simulation is used to evaluate the task specific uncertainty of parts measured on the CMM. The Monte Carlo simulation utilizes the mathematical machine model populated with the uncertainty in the machine and probe error measurements used for error compensation to evaluate the uncertainty in the best estimate of the surface being measured and specified measurands.

To validate the metrology instrument and process, two half scale mirrors of third (tertiary) mirror in the AFRL TMA telescope was measured many times and in multiple setups for repeatability and reproducibility. The measurement result and statement of uncertainty were compared with the prescription and tolerances for acceptance. A spherical mirror made of glass was measured on a Fizeau interferometer and the 100UMM for a comparison of the measurement results after error compensation.

ACKNOWLEDGEMENTS

I would like to thank my advisor/mentor Dr. Chris Evans for always being available for guidance, consultation and discussion and for initiating the projects which provided funding for myself and for this research. Dr. Jimmie Miller provided invaluable wisdom and I would like to thank him for being patient in passing on his knowledge and being available for discussion whenever needed. For her contributions to this dissertation and research I would especially like to acknowledge/thank my research partner and colleague Laura Hopper. An additional thank you to my dissertation committee members Dr. Edward Morse and Dr. Wesley Williams for reviewing my work and their helpful comments and insight.

In addition I would like to thank John Brien, Greg Caskey, Kumar Arumugam, Prithiviraj Shanmugam, Dr. Stuart Smith, Dr. Steve Patterson, Dr. Harish Cherukuri, Nick Horvath, Dr. Matt Davies, Geoffrey Heacock, Brian Dutterer, Dr. Jannick Rolland, Dr. Aaron Bauer, Dr. Eric Schiesser, Dr. Hossein Shahinian, Dr. John Taylor, Jennifer Chastain, Dr. John Zeigert, Dr. Tony Schmitz, Dr. Scott Smith and all of the professors I had the privilege of learning from throughout my education.

For funding, equipment contributions and support I would like to thank the following organizations: the Graduate Assistant Support Program (GASP) at the University of North Carolina at Charlotte, National Science Foundation, Optipro Systems, Air Force Research Laboratory, Center for Freeform Optics, Center for Precision Metrology, Lawrence Livermore National Laboratory, Lion Precision, Zygo Corporation, and the American Society of Precision Engineers.

This research was supported by the National Science Foundation I/UCRC Center for Freeform Optics (IIP-1338877, IIP-1338898, IIP-1822049 and IIP-1822026).

TABLE OF CONTENTS

LIST OF TABLES

LIST OF FIGURES

LIST OF ABBREVIATIONS

AFRL Air Force Research Laboratory

ASME American Society of Mechanical Engineers

CA Clear Aperture

CeFO Center for Freeform Optics - an industry/university cooperative research center

CMM Coordinate Measurement Machine - instrument for dimensional measurements using a probe

CNC Computer Numerical Control

CPM Center for Precision Metrology - an interdisciplinary association of UNC Charlotte faculty and student researchers, allied with industrial partners in the research, development and integration of precision metrology as applied to manufacturing.

DAQ Data Acquisition - hardware used to measure the signal from a sensor or module and relay that information to the computer and software for capturing or manipulating data

DTM Diamond Turning Machine - used for machining with single crystal diamond tools with the part or diamond tool being rotated on a spindle

GUM Guide to the expression of uncertainty in measurement - "establishes general rules for evaluating and expressing uncertainty in measurement that are intended to be applicable to a broad spectrum of measurements" [12]

HTM Homogeneous Transformation Matrices - used to rotate, translate, and scale vectors and positions in three dimensional spaces

ISO International Organization for Standardization

NA Numerical Aperture

NBS National Bureau of Standards - former name of the NIST

NIST National Institute of Standards and Technology - a physical sciences laboratory and a non-regulatory agency of the United States Department of Commerce and the U.S. national metrology institute (NMI)

NPL National Physical Laboratory - the national measurement standards laboratory for the United Kingdom

OD Outer Diameter

PTB Physikalisch-Technische Bundesanstalt - NMI of the Federal Republic of Germany

RHR Right Hand Rule - the use of the right hand to determine the positive direction or rotation of a Cartesian coordinate system among other relationships

SEA Spindle Error Analyzer - system from Lion Precision which includes seven thermistors, five capacitance gages, software, steel ball artifacts, and a capacitance gage nest

TSP Traveling Salesman Problem - a set of algorithms for finding the shortest total path for a series of points or destinations

VIM International Vocabulary of Metrology - basic and general concepts and associated terms in metrology

GLOSSARY

air bearing use pressurized air which is evenly forced into a small gap which allows the bearing to rotate or translate on a small cushion of air with no metal-to-metal contact and little friction. iv

calibration set of operations that establish the relationship between values of quantities indicated and value realized by standards [13]. 11

carriage moving part of machine tool that allows for the manipulation of the part, tool, or measurement device. iii

combined standard uncertainty "standard uncertainty of the result of a measurement when that result is obtained from the values of a number of other quantities, equal to the positive square root of a sum of terms, the terms being the variances or covariances of these other quantities weighted according to how the measurement result varies with changes in these quantities" [12]. 160

error "result of a measurement minus a true value of the measurand" [13]. iii

fiducial origin also called the functional point, is the point of interest at which the coordinate systems overlap when the carriages are at specific positions. 39

freeform surfaces defined as surfaces with no axis of rotational invariance (within or beyond the part) [14]. 10

hydrostatic bearing supports the carriage by pumping hydraulic oil through a small orifice onto the ways creating a thin layer of oil eliminate metal-to-metal contact, to decrease friction and allow the carriage to move smoothly. iv

interferometry a broad range of techniques that uses the principle of superposition and wave interference to measure a quantity usually displacement or distance. 7

least squares fit minimizes the sum of the squares of the residuals. 53

linear motor electric induction motor that produces linear motion with the stator and rotor oriented parallel to each other. 23

measurand the quantity to be measured [12]. 229

self-calibration A measurement procedure by which an estimate of the errors in the part can be separated from an estimate of errors in the instrument [15],[16]. 7

standard uncertainty "uncertainty of the result of a measurement expressed as a standard deviation" [12]. 16

task specific uncertainty task specific uncertainty in coordinate measurement is the measurement uncertainty that results, computed according to the ISO Guide to the Expression of Uncertainty in Measurement, when a specific feature is measured using a specific inspection plan. [17]. iii

thermistor shortened from thermally sensitive resistor is a sensor for measuring temperature. 27

transformation matrices matrices used to manipulate vectors and positions in three dimensional spaces in both linear translations and rotation. iii

uncertainty of measurement "parameter associated with the result of a measurement, that characterizes the dispersion of the values that could reasonably be attributed to the measurand" [13]. 15

vector model modelling the machine with vectors connecting the origins of the coordinate systems. 47

CHAPTER 1: INTRODUCTION

The focus of this research is form measurements of freeform reflective optics for a next generation telescope in the 250 mm class. Freeform optical surfaces can be defined as surfaces with no axis of rotational invariance (within or beyond the part) [14]. Freeform optics introduce a specific set of challenges that must be addressed to achieve the uncertainty required for this research. A set of techniques were developed to address some of these challenges. Instruments and equipment were selected focusing on freeform optics metrology. Specifically, the choice of probes and probe path with special attention to thermal error will be discussed.

Though freeform optics offer optical designers many advantages they can have large slopes, rotationally varying form, large deviations from spherical, and other aspects that make traditional metrology techniques unsuitable or impractical [3]. The need for a flexible metrology instrument and techniques that can be used on a wide variety of optics with a range of slopes, radius of curvatures, clear apertures and materials while maintaining a level of uncertainty has been identified. A set of freeform mirrors from a three mirror anastigmat telescope project funded by the Air Force Research Laboratory (AFRL) through the Center for Freeform Optics (CeFO) are used as a case study for the ideas presented in this research. For testing, two of the tertiary (third) mirrors were manufactured at half scale with an aluminum substrate and a Nickel Phosphorus coating.

The Moore Nanotech 100UMM coordinate measurement machine (CMM) at the University of North Carolina at Charlotte (UNCC) was used to measure the optics. The 100UMM is based on a diamond turning machine. A chromatic confocal optical probe from Precitec was chosen. Serial data acquisition was used where the probe

displacement, the carriage positions of the CMM, and time are recorded for each measurement point. This data is used to generate the measured surface of the part (mirror). Other techniques are available for measuring freeform optics that have strengths and weaknesses when compared to the 100UMM; the goal of this research was to demonstrate a cost effective, adaptable solution for optics up to 260 mm in diameter with stated uncertainty.

A mathematical model was developed for the 100UMM allowing error compensation and task specific uncertainty evaluation. The critical machine errors were measured and put into the model for geometric machine error bias compensation. Following error compensation, the uncertainty in the measurement of the machine errors is used with the mathematical model in a Monte Carlo simulation for task specific uncertainty for the specified measurands. The result is a best estimate of the surface with a stated uncertainty and point by point evaluation of uncertainty for parametric descriptions of the surface being measured.

Probe path planning was used to reduce thermal effects by shortening the measurement time and to estimate and compensate for the thermal drift during the measurement. Optimized probe paths can also provide equal data spacing and reduce carriage motions, decreasing thermal gradients and drift.

It should be noted that a CMM based on a diamond turning machine is somewhat unique. There may be more research in common with on-machine metrology or in situ metrology than with traditional CMM research. The machine error measurements for the 100UMM are the same that would be conducted on a diamond turning machine. The part is mounted horizontally on the 100UMM as well which is uncommon for a CMM.

There is prior research in some aspects of this dissertation, but the uniqueness is in bringing it all together. The task specific uncertainty evaluation using the uncertainty in the geometric machine errors propagated through the mathematical model used in

Monte Carlo simulation does not occur in the research found in a literature review.

Freeform optics are relatively new when compared to traditional optical surfaces. Researchers are still looking for metrology solutions to meet the demands of the advancements of design and manufacture. Not many of the researchers mention uncertainty in discussing freeform optics metrology. There are researchers using a Monte Carlo simulation for uncertainty evaluation, but they do not use a mathematical model of the machine.

There is substantial research in thermal error compensation and evaluation, but no research was found in the literature review pertaining to probe path planning for thermal error estimation and compensation. The concentric circle probe path developed in this research provides such an opportunity and is not as complicated as much of the thermal error compensation in the literature.

1.1 Background and Literature

Like most research projects, there are many sources of information that aided in this research. There are also other research groups working on similar projects and approaches to the problem. Some of the prior research and important influences will be discussed. Also, other notable research in this area. The research areas that overlap with this dissertation include:

- Precision Engineering
  - Kinematics
  - Repeatability
- Thermal Issues
  - Drift tests
  - Environmental control
  - Error compensation
- Coordinate Measurement Machines
  - Virtual machines

  - Repeatability
  - Error modeling
  - Monte Carlo simulations
  - Optical CMMs
  - Thermal errors
- Freeform Optics Metrology
  - Fiducials and datums
- Diamond Turning Machines
- Uncertainty Evaluation
  - Monte Carlo simulation
  - Combined standard uncertainty
  - Task specific uncertainty
- Machine Tool Metrology
  - Reversal, closure, and error separation
  - Edlen's equation
  - Mathematical model of machine errors
  - Error compensation

1.2 Historical

Precision engineering principles laid the groundwork for this research. It is important to understand the literature and research that came before. By no means an exhaustive list, a few notable pieces of literature are summarized below that served as an invaluable source of philosophy, technique, and information. It is interesting how some of the issues in metrology and precision engineering evolve but are not new. Researchers have been working on thermal errors, coordinate metrology, and error compensation for many years.

The Power of Deterministic Thinking in Machine Tool Accuracy - James B. Bryan [18]

The philosophy put forth by Mr. Bryan is a great starting point for understanding precision engineering and the thought and attention to detail needed to be successful. An important take away from this paper which summarizes determinism in the abstract is as follows; the "belief in the idea that machine tools obey cause and effect relationships that are within our ability to understand and control and that there is nothing random or probabilistic about their behavior." The paper goes on to describe eight rules to follow when adopting the philosophy. As they could be used in many situations and pursuits, they are included below.

1. Don't depend on breakthroughs. Identify the weakest link in the system and concentrate on upgrading it.
2. Be patient, it takes time to sort out the variables, but it can be done and the rewards are worth it.
3. Keep design solutions as simple as possible.
4. Don't assume anything, measure with good equipment and carefully designed tests.
5. Don't use statistics indiscriminately, they are generally not necessary for the limited number of variables in a machine tool.
6. Suspect temperature, dirt, loose joints, and friction as the most likely sources of apparent non-repeatability.
7. Keep Loxham's law in mind. "An automatic machine is always operating perfectly. It may not be doing what is required, but that's because it isn't suitably arranged."
8. Remember that "random results are the consequence of random procedures."

International Status of Thermal Error Research - James B. Bryan [19]

Published in 1967, this report was the work of a "new CIRP Subgroup formed to deal with the overall problem of thermal effects errors in machine tools and metrology." CIRP is the International Academy for Production Engineering. This Subgroup

was formed with inspiration from the paper by E. R. McClure "The Significance of Thermal Effects in Manufacturing and Metrology." They started by looking at the international status of the problem and what needs to be done about it. Through the survey they found that "the errors caused by thermal deformations have the same or higher order of magnitude as those errors due to the kinematic accuracy and the static and dynamic compliance." It could be argued that the same holds true today, the thermal effects are the limiting factor of precision measurement. One of experts surveyed stated "The near future will see a concentration of effort to control room temperature. This will be paralleled by efforts to isolate or eliminate heat sources in existing equipment. Better thermal design of new equipment will follow." These efforts are still being undertaken at many laboratories, institutions and manufacturers.

In classifying the thermal problems, they broke the "overall thermal problems" into two categories, the first being "the effects of uniform temperatures other than 68 °F," and "the effects of non-uniform temperatures." This paper was revisited and updated in a 1991 CIRP keynote [20].

Thermal Effects in Dimensional Metrology - Wm. Brewer, James B. Bryan, Eldon R. McClure, J. W. Pearson [21]

This paper discusses the effect that thermal variation has on dimensional metrology. They found that "in the field of close tolerance work, thermal effect is the largest single source of error, large enough to make corrective action necessary." The authors performed drift tests over long time periods to correlate the temperature variation and measurement variation much like was done in this research.

An interesting conclusion reached in the paper was that "the usual efforts to correct for thermal error by applying expansion "correction," or by air conditioning the working area do not always solve the problem and are based on an incomplete understanding of the problem." The same conclusion could be drawn from the research in this dissertation.

Self-Calibration: Reversal, Redundancy, Error Separation, and 'Absolute Testing' - Chris J. Evans, Robert J. Hocken, W. Tyler Estler [15]

Self-calibration or more specifically reversal is an important concept in metrology and in this research. Reversal was used in the machine tool metrology of the 100UMM and allowed for the error separation from the machine and the artifact. The section on Estler's face motion reversal and straightedge reversal were used as a guide in measuring the error motions of the X and C carriages (Section 5.10). There are several other useful examples of self-calibration including closure, redundancies, averaging and reversal techniques. The topics cover a broad range of applications from a disc sander to interferometry, levels, and coordinate measuring machines.

1.3 Dissertations

An important source of information that is often neglected, dissertations are often very specific and in depth. A few of the dissertation resources used in this research are added below.

Manufacturing Accuracy through Control of Thermal Effects - Eldon Ray McClure [22]

This work is the PhD dissertation of Eldon Ray McClure at the University of California, Berkeley in 1955. In the dissertation suggests two methods of "reducing or eliminating thermal effects." The first being an automatic error compensation using a lumped-parameter model with identified parameters for error prediction. The second is the regulation of structural temperatures by means of fluid coolants. In this research a version of both methods will be discussed in terms of metrology.

McClure sets out to prove "that thermal effects, contrary to common belief, are not random, but highly deterministic," that the two ways of reducing or eliminating thermal effects "can decrease thermal effects to the level of other systematic error sources" and "the control of thermal effects is economically significant in terms of both the cost of achieving it and the returns gained from it."

Although McClure is talking about manufacturing, many of the concepts discussed are relevant to metrology, especially since the machine used in this research is based off a manufacturing machine.

A Process to Evaluate Commercial Software Packages that Estimate Measurement Uncertainty Through Simulation - Jonathan Beaman [23]

Commercial software simulation packages provide a task specific uncertainty and often use a Monte Carlo simulation for evaluating the uncertainty. The author compares two such packages with a calibrated artifact to determine the uncertainty evaluation performance. It is pointed out that improved results from the software packages require a skilled technician or operator. The dissertation also includes general information on coordinate measurement machines and uncertainty.

Principles and Techniques for Designing Precision Machines - Layton Hale [24]

The author sums up the purpose of this thesis with the following statement "this thesis is written to advance the reader's knowledge of precision engineering principles and their application to designing machines that achieve both sufficient precision and minimum cost." The thesis starts by introducing four case studies from Lawrence Livermore National Laboratory. The main body of the thesis is a collection of precision engineering principles and techniques as the title might suggest. Many of the items discussed are backed by examples including equations, diagrams, and code in Mathcad. The figures and tables are excellent with solid models, tables, and plots. The appendices contain more Mathcad and MATLAB code with more general topics like least-squares fitting, transformations matrices and determinism.

Minimizing Task-Specific Uncertainty in CMM-Based Freeform Optics Metrology - Michael Uwakwe [25]

An application of in-situ self-calibration and error separation. A shift-rotation technique is used on coordinate measurement machines to measure freeform optics. The task-specific uncertainty is reduced by "separating machine error contributions from

test surface measurements." The technique was used in Monte Carlo simulations for a proof of concept and then on a Zeiss F-25 micro CMM and a MarSurf LD260 profilometer fitted with an additional linear and rotary stage. The optics were also measured on a Fizeau interferometer and a stitching coherence scanning interferometer. The results from the error separation are compared to the interferometer measurements and decomposed into rotationally variant (RV) and rotationally invariant (RI) components of the corrected freeform surface and the machine/instrument errors. The N-rotation technique is used in the shift-rotation to "obtain the RV components of the test surface and reference." The shift in the shift-rotation technique is done to calculate a "difference between the initial and sheared measurement data" leading "to the RI components of the test surface and reference errors." The shift is a known displacement, where uncertainty in the amplitude and direction influence the uncertainty in estimation of the RI errors.

The shift rotation technique is also used in separating out mid spatial frequencies showing "the complete or partial error separations of mid-spatial frequencies, and how mid-spatial frequency errors affect the separation of mid-spatial frequencies." The appendices include an estimate of sensitivity to error motions in the probing direction.

1.4 Freeform Optics

To lay the groundwork for studying freeform optics metrology, an understanding of freeform optics and how they differ from 'traditional' optics is important. A few of the resources used to better understand freeform optics and how they are defined are provided below.

Freeform Optical Surfaces: A Revolution in Imaging Optical Design - Rolland J. Thompson K [26]

The authors make a case for freeform optical surfaces revolutionizing imaging optical design. A brief history of the freeform optical surface is also included for context

and a definition of freeform optics. The first examples of a "true freeform surface in imaging optics" provided include those for Polaroid's SX-70 camera and the Alvarez variable focus lens. The paper includes a definition of freeform surfaces by "stating the technology that enables this revolution." The definition provided is "Freeform Optical Surface, Modern Definition (post-2000) An optical surface that leverages a third independent axis (C-axis in a diamond turning terminology) during the creation process to create an optical surface with as-designed non-symmetric features."

While it does not provide a good definition for the purposes of this research, it does have a unique approach to defining the freeform optical surface. There is also a discussion of several ways to define freeform surfaces and some of the mathematical functions and software. The different types of freeform optical surfaces are broken into five types and each is discussed with a short history and applications. The paper is concluded with a statement that "at the same time, each and every community along the supply chain must learn new concepts and develop new tools to leverage these revolutionary shapes." While it is not clear where in the supply chain this research would fall, it is the purpose to develop new tools for the metrology of such shapes.

Manufacturing and Measurement of Freeform Optics - F.Z. Fang, X.D. Zhang, A. Weckenmann, G.X. Zhang, C. Evans [14]

This paper discusses the diverse applications of freeform optics along with, as the title might suggest, the manufacture and measurement of them. For this research, the definition of freeform surfaces comes from the first sentence of this paper. The authors define freeform surfaces "as surfaces with no axis of rotational invariance (within or beyond the part)." The advantages of freeform optics are listed with several ways that freeform surfaces can be defined. There is also a section on measuring freeform optics with both contact and non-contact measurements and on-machine and offline measurements. The advantages and disadvantages of each are discussed.

1.5 Coordinate Measurement Machines

Coordinate metrology research was reviewed during this project and was vital to understanding the process and how error compensation and uncertainty evaluation are performed. A few of the resources used to increase understanding are discussed below.

Coordinate Measuring Machines and Systems - Robert J. Hocken, Paulo H. Pereira [1]

The section of this book that was integral to this research is titled "Error Compensation of Coordinate Measurement Machines" by Guoxiong Zhang. The author discusses the mathematical model used in this research for error compensation and the Monte Carlo simulation. The book also covers such topics in coordinate measuring machines as reversal techniques for calibration, measurement uncertainty, environmental and temperature considerations, probing systems, algorithms and filters, and performance evaluation.

Hydrostatic, Aerostatic, and Hybrid Bearing Design - W. Brian Rowe [27]

When working with air bearings or hydrostatic bearings this book is a must read. The author has vast experience and has reduced the subject into easy to understand analysis and theory. This book was used in this research to investigate thermal issues in the hydrostatic bearings.

Task specific uncertainty in coordinate measurement - R. Wilhelm, R. Hocken, H. Schwenke [17]

The authors describe an approach to task specific uncertainty using a virtual coordinate measuring machine (VCMM) that "estimates an uncertainty statement for a particular measurement task on a particular CMM according to Monte Carlo simulation results." This is the same approach taken in this research with a different name and slightly different implementation. Sources of uncertainty in CMMs are discussed including a flow chart with "error components that lead to uncertainty." An interest-

ing concept is introduced called simulation by constraints which the authors describe as "a generalization of the virtual CMM." There is also mention of a project called the Expert CMM where the problem is divided into "two conceptual steps, computing the uncertainty of individual point coordinates and propagating this uncertainty through the part program to obtain the final uncertainty in the measurand."

1.6 Environmentally Controlled Enclosures

A collection of papers that use environmentally controlled enclosures to increase the repeatability of machine tools and metrology instruments were referenced. A couple are included here that provide historical context to the enclosure used in this research. A common theme in these papers is the need to control temperature and thermal drift to achieve precision metrology or manufacturing.

Techniques for Precision Air Temperature Control - Hans Hansen [28]

This paper provides a look at several enclosures for controlling air temperature around machines and what to consider when designing precision air temperature control. The enclosures discussed are installed at Lawrence Livermore National Laboratory (LLNL). The author stresses the importance of analyzing the heat sources of the machine, the dynamics of the temperature control system and the "mode of control implemented." The author states that "the work has also demonstrated that large improvements in the performance of temperature control systems do not necessarily have to be complicated or expensive." This research echoes that sentiment with the enclosure around the Nanotech 100UMM. Rather than retrofitting or building a new laboratory, precision air temperature control can be achieved by installing an enclosure around the machine with readily available materials and a reasonable budget.

There is guidance for heat load and control system considerations for air temperature control. A review of the enclosure built around the Baby Optics Diamond Turning Machine (BODTM) states that a "major factor contributing to the capability of the machine is its high repeatability which is made possible by minimizing thermal

distortions." Thermal distortions are controlled by closed flow cooling to the spindle drive motor and controlling the ambient air temperature. An interesting aspect of the enclosure was the reheat that consisted of an array of 100 W light bulbs (tungsten filament) with a variable power source from the temperature controller. Light bulbs were selected for availability and a fast response time.

The air temperature control of a shop at the Materials Fabrication Division at LLNL was evaluated and found to be insufficient for their requirements. The shop was retrofitted from an on/off controller with a 0.3 °F dead band to a digital PID control with an improvement from +/- 2.0 °F to +/- 0.5 °F for around $1000. The paper is from 1983 but digital controllers are probably much cheaper now. For further efficiency two temperature feedback probes were added to reduce a 60 second delay between the initial temperature feedback sensor and the heat exchanger for the air conditioner.

Precision temperature control for optics manufacturing - Jeffrey Roblee [29]
Another paper about precision temperature control from LLNL. This paper is focused on the principles and design considerations of precision temperature control with an emphasis on "the use of heat exchangers with large flowrates of coolant." LLNL has/had diamond turning machines that use an external oil shower, air showers and a combination of air shower and internal water cooling in "areas of concentrated heating" such as spindle drive motors. Machine coolant is the focus of the paper with a small section on air conditioning with an example of the system around the Large Optics Diamond Turning Machine (LODTM). The differences between the two systems is discussed.

An equation is provided for sizing heat exchangers with a list of considerations in selecting an appropriate heat exchanger as follows in order of importance, "low sensitivity to flowrate errors, good mixing and uniform heat transfer, fast transient response, ease of fabrication, and low pressure drop." The control method suggested

is a flowrate-controlled heat exchanger.

The author points out that although many of the principles of liquid temperature control systems apply to air conditioning systems, air is more difficult to control due to its lower heat capacity and larger volume. The flow distribution over the machine should be uniform, high velocity, and time invariant. For the enclosure around the 100UMM a reheat is used after the temperature of the air is cooled below the desired temperature, so the flowrate of the coolant is steady. The paper concludes with a list of important considerations in precision temperature control in liquids and air. Many of them are important features of the 100UMM enclosure. The list is provided below.

1. Minimizing heat load variations and decreasing their rate of change
2. Increasing the thermal response time of critical machine components
3. Using large flowrates of coolant
4. Selecting the proper variable-flowrate heat exchanger for the application
5. Using a method of flow control that is appropriate to the application
6. Encouraging mixing to improve bulk temperature measurements of the machine coolant
7. Using a proportional plus integral action controller for improving temperature control precision
8. Employing cascaded control loops for improving disturbance rejection

1.7 International Standards

International standards provide a very precise description of machine errors and machine testing for machine tools and coordinate metrology instruments. Uncertainty evaluation and the language used in describing measurement uncertainty has also been standardized.

ISO-230 Test code for machine tools [4], [30]

The Nanotech 100UMM is based on a diamond turning machine so it has some of the characteristics of a machine tool. The ISO-230 standards offer a concise definition

of the machine errors, instructions for testing, and the evaluation of measurement uncertainty in the machine error measurements. Part 1 of the standard covers the geometric accuracy of machines operating under no-load or quasi-static conditions. It is assumed that this is the condition of the 100UMM during measurements. Part 3 covers the determination of thermal effects. Part 9 is a technical report for the estimation of measurement uncertainty for machine tool tests according to ISO 230 with basic equations.

Evaluation of measurement data - Guide to the expression of uncertainty in measurement [12]

The internationally accepted guide for evaluating uncertainty. Known as the GUM, this document provides a detailed set of rules and guidance for evaluating and expressing uncertainty in measurements. The guide is meant to be general enough so that it can be applied to all measurements. In this research we are mostly concerned with displacement and temperature measurements but many times those measurements are realized through voltage, current or resistance measurements. From the GUM, uncertainty of measurement is defined as "doubt about the validity of the result of a measurement." For the purposes of this research the definition will be used to describe a "quantitative measure of this concept [12]." Perhaps more specific and applicable definition for this research would be a "parameter, associated with the result of a measurement, that characterizes the dispersion of the values that could reasonably be attributed to the measurand."

An important distinction made in the GUM for this research is between the two types of uncertainty evaluation defined as Type A and Type B evaluations of uncertainty. Type A is the "method of evaluation of uncertainty by the statistical analysis of a series of observations" and Type B is the "method of evaluation of uncertainty by means other than the statistical analysis of series of observations." As this research is based on metrology, there are important concepts in the GUM that provide a back-

ground and understanding that is essential in interpreting results of a measurement. The first is a proper definition of the measurand. Next, that a measurement is not complete without a statement of the uncertainty. The appendix has specific examples of evaluating uncertainty and elaborates on terms used. This research provides a path to evaluate the uncertainty in measurements made on the 100UMM and is focused on measuring freeform reflective optics in the 250 mm class. The rules and guidance from the GUM will be followed for this research and many of the concepts will be discussed further as they pertain with the topics below.

Evaluation of measurement data - Supplement 1 to the "Guide to the expression of uncertainty in measurement" - Propagation of distributions using a Monte Carlo method [31]

A great resource for the Monte Carlo method including the general simulation design to ways to sample probability distribution functions and case studies. There is a section describing a comparison between the GUM uncertainty framework or law of propagation of uncertainty and the Monte Carlo method as described in the supplement.

Advantages or features of the Monte Carlo method are listed with the most applicable to this research being the "reduction in the analysis effort required for complicated or non-linear models, especially since the partial derivatives of first or higher order used in providing sensitivity coefficients for the law of propagation of uncertainty are not needed," and "generally improved estimates of" the output quantity, Y, for non-linear models. There is generally an "improved standard uncertainty associated with the estimate of Y for non-linear models."

1.8 Recent Advancements in Freeform Metrology

The state of the art in freeform optics was investigated for context into where this research fit into the current literature. Particularly with task specific uncertainty and probe path planning. A few of these references are summarized below.

Advanced Metrology - Freeform Surfaces - X. Jane Jiang, Paul J. Scott [11]

Although this book is not directly aimed at optical freeform surfaces, there is a lot of useful information. Some of the useful topics in the book are different methods to represent freeform surfaces with advantages and disadvantages, sampling strategies for freeform surfaces to encapsulate the design intent, geometrical fitting, and surface reconstruction of freeform surfaces. The chapter on geometrical fitting was particularly enlightening with guidance on the correct method to use and the differences between algebraic and geometrical fitting. Zernike polynomials are also discussed as they relate to freeform surfaces, design, and manufacturing. For this research algebraic fitting was used.

Metrology for the manufacturing of freeform optics - Todd Blalock, Brian Myer, Ian Ferralli, Matt Brunelle, Tim Lynch [32]

The authors work for a company, Optimax that manufactures freeform optics. The paper discusses three instruments used in freeform optics metrology. The first is a Leitz PMM 866 contact CMM with a scanning probe that has an "accuracy" of +/- 0.5 μm. To increase the accuracy and reduce damage to the optical surface the machine was used in a point by point mode. They also discuss the fiducials used to establish datums on one of the parts that was measured with the CMM.

The next instrument was a Panasonic UA3P high accuracy profilometer. The paper gets a little confusing when the profilometer is described but it appears that the instrument is used for form measurements. A comparison with the Leitz CMM shows that for the same amount of measurement time, the UA3P "was able to capture more data than the CMM as well as quantify more detail in the mid-spatial frequency error measurement." They quote an accuracy of 50 nm when surface angles are less than 30 degrees. The machine is equipped with an atomic force measurement probe with a displacement interferometer for position measurement. It appears that the UA3P is faster and has a higher resolution than the CMM although it was unable to

probe the fiducials on the side of the part.

The authors were developing a fringe reflection (deflectometry) measurement instrument for fast, non-contact freeform measurements. They were able to capture the mid spatial frequency error signatures that the Leitz CMM and UA3P data showed in a much faster time. The stated downside was the inability to measure relative to the fiducials, but they are looking into other types of fiducials.

Freeform Surface Characterization and Instrument Alignment for Freeform Space Applications - Manal Khreishi, et al [33]

This paper comes from a group of researchers that are mostly from NASA. The paper describes the instrument and techniques used to align and characterize two freeform mirrors for a compact telescope. The instrument is a Leitz PMM-C 700 CMM with a non-contact Precitec LR optical probe. They quote a sub-micron accuracy for the CMM and a resolution of roughly 3 nm in Z. A Precitec probe is also used for this research with the same operating principle but different specifications. The authors measured and aligned two freeform mirrors for a compact telescope called the XY Penta and another set for a three mirror anastigmat called the L'Ralph. The mirrors used in this research for the AFRL project are also for a three mirror anastigmat. The only quantitative data from the mirror measurements was a stated "average percentage difference between the design and the as-built polynomial coefficients of M1" of less than 2%.

To align the optics, the 3D surface data was fit to the sag formula. The best fit optical surface was determined relative to reference optics or fiducials. Tooling balls were used in the paper with the L'Ralph optics. The tooling balls were aligned to "CMM-calibrated positions" using a laser radar metrology instrument for what was referred to as "system-level metrology." The wavefront was measured using a double pass test with an interferometer. The final alignment was "guided by the optical model with feedback from interferometry."

Importance of fiducials on freeform optics - Matt Brunelle, Joe Yuan, Kate Medicus, Jessica DeGroote Nelson [34]

Another paper from the employees at Optimax. The authors propose a method for adding reference surfaces to freeform optics to aid in the manufacture and metrology of optics. The fiducials locate and orient the optical surface to characterize the figure error and are used in optical system alignment. The fiducials create a coordinate system and help measure wedge and center thickness on optics that do not have symmetry like freeform optics. To constrain the six degrees of freedom for contact measurements, a plane, line, and point were used as fiducial examples. Another example uses three sphere center points as fiducials.

For optical measurements like on a Fizeau interferometer, the authors provide an example using a computer-generated hologram (CGH) with alignment features on the CGH and optic. Although this process is interesting, it is not applicable to this research.

A set of guidelines are described for designing fiducials including, "easy access across all machine platforms involved in the manufacture," do not interfere with the optical surface, if multiple step manufacturing is used, do not change the fiducials between steps, and establish the fiducials during the first step in generating the optical surface. Mounting features should be used as fiducials if possible. Figure correction and metrology should use the same fiducials and be referenced in the same way.

To study the effect of changing the order that the fiducials are referenced, a test part was used and measured on a contact CMM. Three flats were used, labeled X, Y and Z, with the reference plane, line and point changing between the flats each time. It was found that planes were likely not orthogonal and that varying the order changed the figure error and tilt in the part.

An important point made is to make fiducials large enough to "repeatably create and locate a reference coordinate system, effectively locking in all degrees of freedom

of the optical surface." In this research the fiducials are used to center the part, a flat is used for 'clocking', and a flat annulus around the clear aperture establishes tilt. Since there is tilt in the prescription this is important in separating tilt in the measurement from that of the prescription.

New advancements in freeform optical metrology - Scott DeFisher, Greg Matthews, James Ross [35]

This paper is about the UltraSurf and some of the probes they use. This research began with a study of the UltraSurf 5x at Optipro Systems in Ontario, NY. The UltraSurf is an air bearing CMM with five axes, three linear and two rotary. It uses non-contact single point probes with sub micrometer resolution. The machine offers a degree of flexibility like the 100UMM with interchangeable probes. The authors discuss ways of making the feedback to the manufacturing machine easier and more streamlined. The sensors in the paper are a chromatic confocal sensor much like the one used in this research, a low-coherence interferometer, and a LADAR probe for high resolution thickness measurements.

Strategy for a flexible and noncontact measuring process for freeforms - Andreas Beutler [36]

The author works for Mahr who sells a cylindrical measuring machine called the MarForm MFU200 that is designed to measure optical freeform surfaces. The machine can be used with optical and tactile probing systems. The paper also discusses fiducials for freeform optical surfaces. The measurement strategy discussed is like the one in this research with concentric circles and diametral measurements. The system can measure parts up to 250 mm in diameter, but it is stated that a typical part would be limited to 100 mm diameter since the fiducials are typically outside the clear aperture and require a certain amount of travel range in the x direction of the machine. A measurement uncertainty of the form error (PV) of 100 nm is quoted depending on the slope and size of the part.

CHAPTER 2: MOORE NANOTECH 100UMM COORDINATE MEASUREMENT MACHINE

The need for an instrument to measure freeform optics was met by the Moore Nanotech 100UMM. The 100UMM is a CMM with interchangeable probes and allows for flexibility in part mounting and probe path generation. The machine is controlled by the computer numerical control (CNC) programming language M- and G-code. The versatility, access to the machine components and the ability to write part measurement programs in MATLAB allowed for the generation of custom probe paths and measurement techniques. Parts up to 400 mm clear aperture (CA) are measurable with some restrictions such as weight, balance and fixturing. The 100UMM (shown in Figure 2.1) is located at the University of North Carolina at Charlotte (UNCC) in the Center for Precision Metrology (CPM).

Figure 2.1: Moore Nanotech 100UMM before the environmentally controlled enclosure was installed.

The 100UMM has four positioning carriages, including two linear carriages and two rotary carriages. The linear carriages use hydrostatic bearings while the rotary carriages use air bearings. The part is mounted on the C carriage while the probe is mounted on the B carriage. The C carriage has a vacuum port through the center of the carriage used to mount parts. The B and C carriages have a scraped surface used to provide a flat mounting surface. A diagram showing the carriage configuration, travel directions, and coordinate systems for the 100UMM can be found in Figure 2.2.

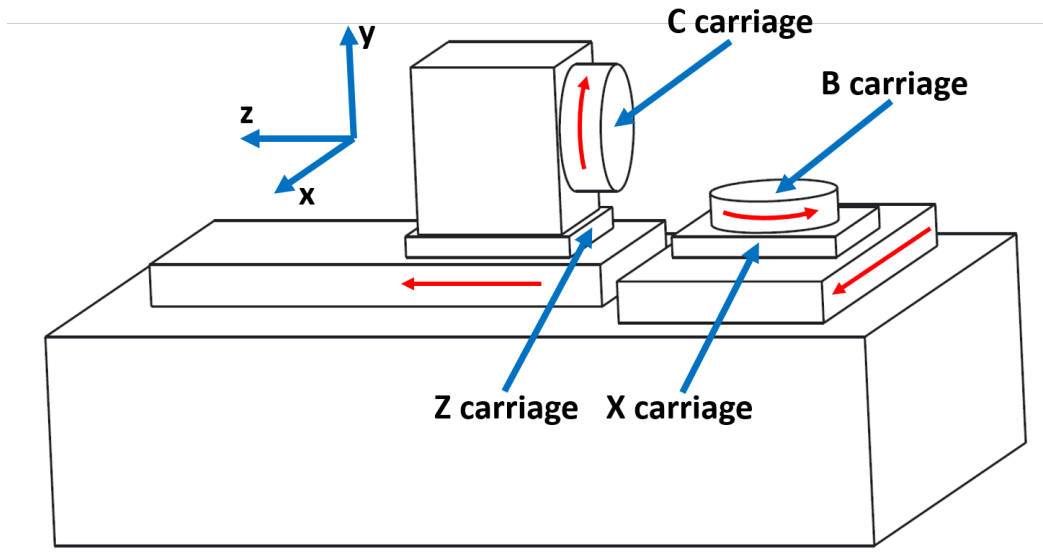

Figure 2.2: Moore Nanotech 100UMM coordinate measurement machine carriage orientation and coordinate system [3].

The 100UMM is based on a diamond turning machine with axes designations shown in Figure 2.2. The linear axes have nanometer positioning resolution and the rotary axes have 0.036 arc second positioning resolution.

2.1 Machine Characteristics

The linear machine carriages are supported by a granite slab. The granite slab is supported by four passive pneumatic vibration isolators attached to a steel frame. The B carriage is supported by the X carriage that is attached granite base. Also attached to the granite base is the Z carriage which supports the C carriage. Between the C carriage and Z carriage is a granite "tombstone" used to support the C carriage and allow it to be oriented horizontally. The B carriage has 180° of rotation while the C carriage is free to rotate 360 ° The X carriage hydrostatic bearing, supporting ways, and linear motor used to control the carriage position can be seen in Figure 2.3.

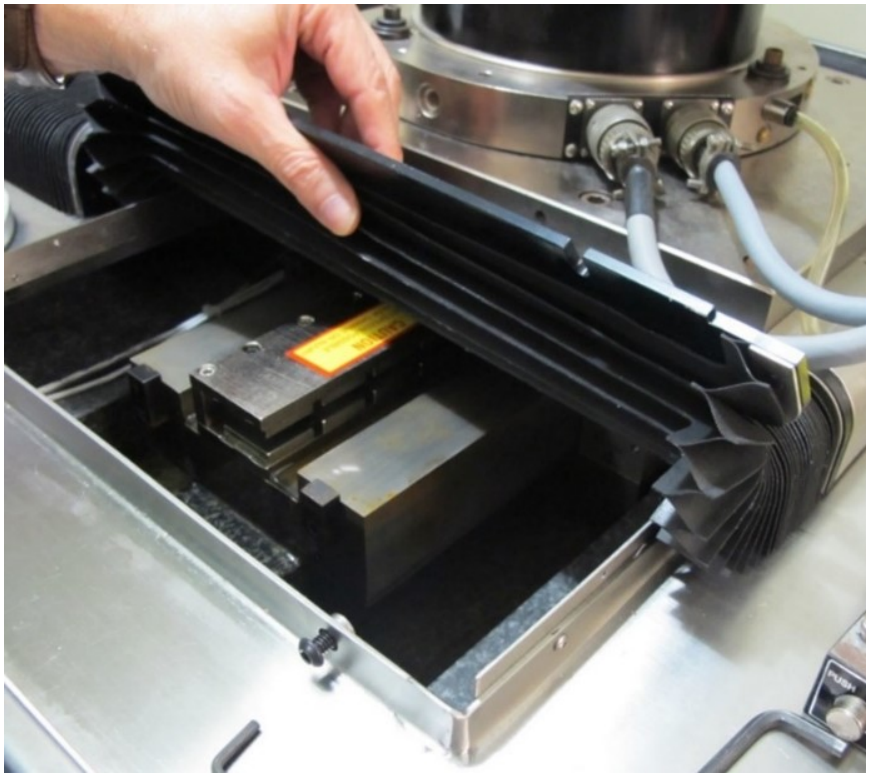

Figure 2.3: X carriage ways with the linear motor in the center and showing the stainless-steel tray.

A stainless-steel tray supported by the steel frame covers the machine to keep contaminates out of the hydrostatic bearings. The tray can be seen in Figure 2.3. The glass machine scales (linear encoder) which read the position of the two linear axes are made by Sony. The scales provide position feedback to the controller to reach the desired carriage position. The rotary carriages use two encoders per carriage to reduce eccentricity errors.

The part being measured is typically supported by the C carriage by either vacuum, waxed to a mounting plate, or bolted to an adapter that can be fastened to the C face plate with screws. The probe is supported on the B carriage with the probe and collet system on a 3 degree of freedom stage with differential micrometers. The probe holder allows for flexibility in the types and orientation of the probes. The probe holder can be seen in Figure 2.4.

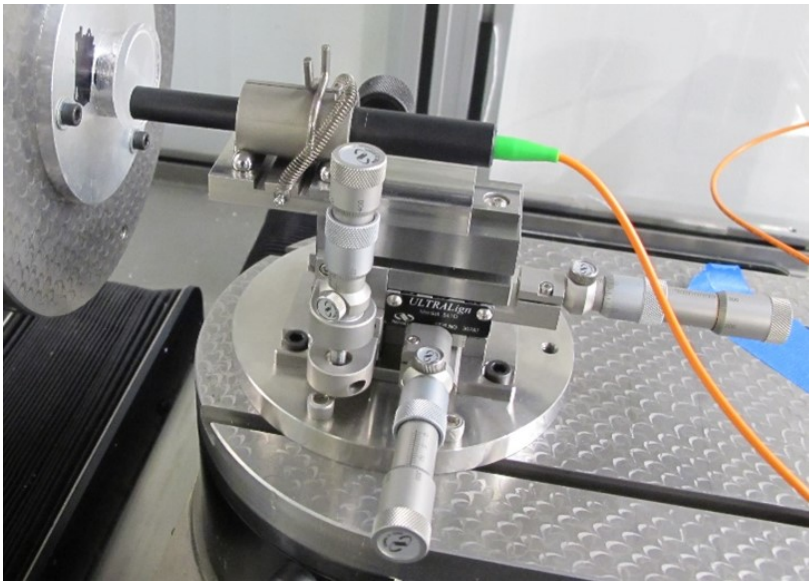

Figure 2.4: Three degree of freedom probe holder designed for the Nanotech 100UMM with a removable collet system for interchangeability of probes. The probe shown is a STIL chromatic confocal probe.

Parts are measured on the 100UMM using a scanning mode where the probe is moved across the surface of the part while recording the probe displacement and carriage positions at nominally the same time. This allows for parts to be measured more rapidly than a point by point measurement where the machine would be moved to a measurement point and after a settle out period, the probe displacement and carriage positions would be recorded.

2.2 Environmentally Controlled Enclosure

The 100UMM is surrounded by an environmentally controlled enclosure designed to hold the metrology loop to +/- 0.1 °C. In practice this is approximated by controlling the ambient air, hydrostatic bearing oil outlet, and the high-pressure air temperatures at 20 °C +/- 0.1 °C. The enclosure was a multidisciplinary senior design project at UNCC funded by the CPM. Thermal drift in the part and machine are reduced by maintaining a controlled ambient temperature. The freeform mirrors being measured were manufactured and have specifications at 20 °C as standardized by ISO 1 [37]. The uncertainty contribution from converting the dimensions with the coefficient of

thermal expansion (CTE) is avoided by measuring the mirrors at 20 °C. This is especially important due to the mirrors being made from two different metals making any correction more difficult. The final full-size mirrors will be made from a material with a low CTE. By defaulting to ISO 1 it falls on the designer to determine the appropriate dimensions and tolerances for the desired shape of the part at operating temperature. Figure 2.5 shows the environmentally controlled enclosure around the 100UMM during machine tool metrology with the electronic levels.

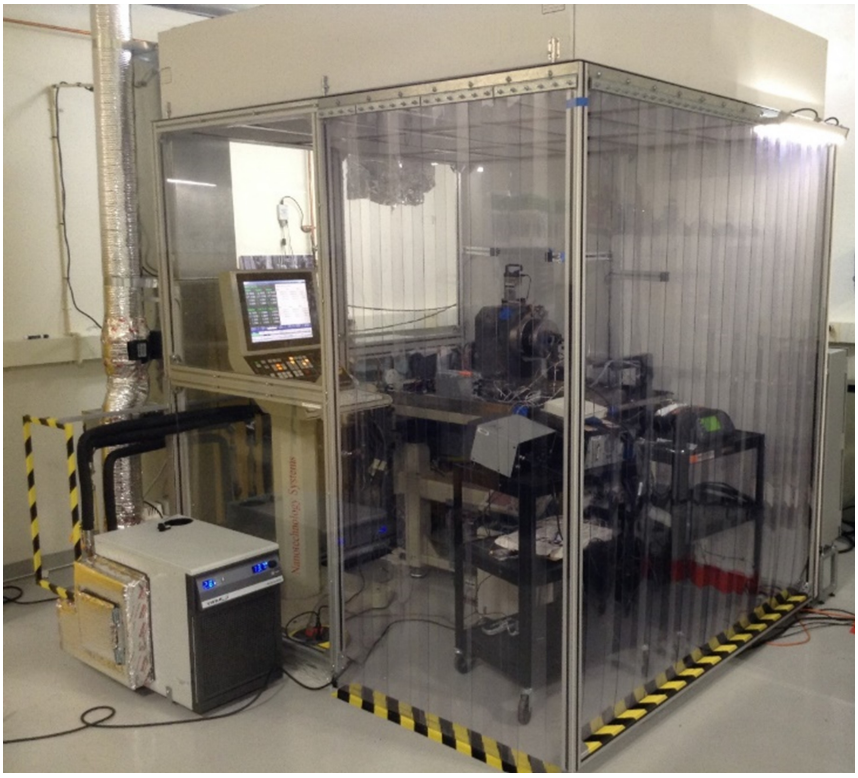

Figure 2.5: Moore Nanotech 100UMM surrounded by the environmentally controlled enclosure showing the chiller, curtains and plenum.

The ambient air is cooled to around 17 °C and re-heated to 20 °C before entering the enclosure. It is faster to heat the air with a resistive heater than to cool with the chiller allowing for a quicker response and more control. There is also a chance to remove some of the humidity out of the air. The conditioned air comes down from the overhead plenum and returns under the machine into the return ducting. The

enclosure has a positive pressure to reduce contaminants and pulls nominally 10% makeup air from outside the enclosure. The high-pressure air for the air bearings is ran through a copper tube inside the ambient air return duct to act as a heat exchanger to bring the high-pressure air temperature to 20 °C. There is also an air tank under the machine to act as a buffer or damper and emergency air supply where the air has a chance to come to equilibrium at 20 °C.

A LabVIEW program controls the enclosure. There are several thermistors used as feedback to the control system. These values are saved every minute for reference if there is an error or an anomaly in a measurement. The enclosure also has an independent temperature monitoring system for investigative purposes should the control system malfunction or the LabVIEW program stop.

2.3 Hydrostatic Bearings

The hydrostatic bearings on the X and Z carriages ride on two steel ways as shown in Figure 2.3. As the hydraulic oil exits the bearing and goes from 250 psi gage pressure to atmospheric pressure it heats up. The hydrostatic oil is cooled by a liquid to liquid heat exchanger using the chiller water and heated with a resistive reheat and feedback sensor in the oil flow to control the temperature. The hydraulic pump also heats the oil, but the heat exchanger is between the pump and the hydrostatic bearing. The oil temperature is being controlled such that the oil exiting the bearing is 20 °C. This means that the oil temperature exiting the heat exchanger and in the bearing before reducing pressure will be below 20 °C. The linear motor produces heat during operation and moves with the carriage heating the ways. The larger the distance traveled and depending on velocity, the more heat is generated. The probe path research and alterations to the enclosure were to reduce error due to thermal drift.

The hydraulic oil for the hydrostatic bearings goes from the hydraulic pump to a damper then to the heat exchanger. The hydraulic oil tank, pump and damper are

situated below the machine on the end away from the carriages. As air moves under the machine and to the return duct in the enclosure it passes over the hydraulic system. The hydraulic system including the tank, pump, filter, damper, and gages can be seen in Figure 2.6.

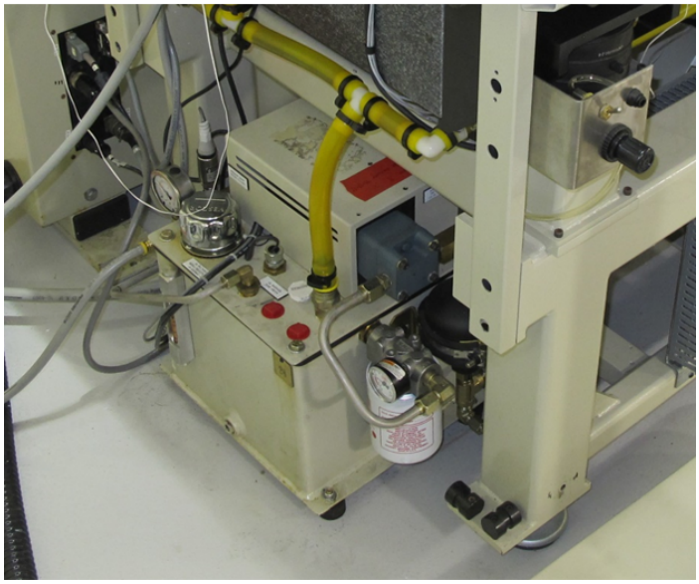

Figure 2.6: Hydraulic power unit for the Moore Nanotech 100UMM coordinate measurement machine before the environmentally controlled enclosure was installed.

The liquid to liquid heat exchanger is shown in Figure 7 with a 3D printed outer shell and brazed plate heat exchanger inside. A turbulator was necessary to get ample mixing of the oil for reheating.

Figure 2.7: Heat exchanger for the hydraulic oil using the chiller water and resistive heater to control the oil temperature.

The coolant connections are on the left side and the oil connections on the right. It was determined by measuring the oil temperature that the hydraulic oil temperature before going into the bearing was lower than at the exit. This led into an investigation into the heat produced by a pressure drop in the hydraulic oil. The equation was covered in Dr. Patterson's Precision Machine Design course at UNCC and was found in Reference [27]. It is assumed that there is no friction power (the power to move the bearing) since it is a low speed bearing and friction in negligible. The pumping power is defined as the "power to pump fluid through a bearing [27]." The pumping power can be described by equation 2.1.

$$H_p = P_s q \tag{2.1}$$

Where H_p is the pumping power, P_s is the gage pressure, and q is the flow. To find the change in temperature the power is related to the heat within the liquid, or oil in this case. Generally described by equation 2.2.

$$heat = mass\ flow\ x\ specific\ heat\ x\ temperature\ rise \tag{2.2}$$

The equation could also be written as equation 2.3.

$$H_p = \rho q c \Delta T \tag{2.3}$$

Where ρ is the density, c is the specific heat capacity and ΔT is the change in temperature. Using equations 2.1 and 2.3 the change in temperature becomes [27]:

$$\Delta T = \frac{P_s}{\rho c} \tag{2.4}$$

Using values for the oil and pressure drop in the 100UMM system the increase in temperature is approximated by equation 2.5.

$$\Delta T = \frac{P_s}{\rho c} = \frac{1723.69\ kPa}{862\ \frac{kg}{m^3}\ 1.887\ \frac{kJ}{kgK}} = 1.06\ K \tag{2.5}$$

Where ΔT is the change in temperature, C_p is the specific heat at constant pressure, ρ is the density, and P_0 is the initial pressure. It was found that as the oil leaves the hydrostatic bearing, it heats by 1 K. A temperature increase of 0.7 K was found experimentally by measuring the hydraulic oil as it left the bearing and at a fitting before going into the bearing. The temperature couldn't be taken at the exact location the oil leaves the bearing which could explain the difference between the calculated and experimentally determined temperatures.

2.4 Alterations to Enclosure

As the thermal drift issues were investigated, alterations to the enclosure were tested and implemented. Not all the changes worked as planned and some were abandoned. The changes were made to improve the effectiveness of the enclosure and to reduce thermal drift in the measurement result. The goal is to provide a thermally stable machine and environment during part measurements.

To mitigate the machine, part, and probes from radiative coupling with the exterior of the enclosure, mylar blankets were used to cover the opaque and clear parts of the machine enclosure. Mylar blankets are sometimes called "space blankets". They were

also placed on top of the plenum. With the mylar blankets covering the enclosure, drift tests were conducted again to investigate any change in the influence of the temperature outside the enclosure. No change in the drift could be identified with the blankets so they were removed. Figure 2.8 shows the machine covered with the mylar blankets.

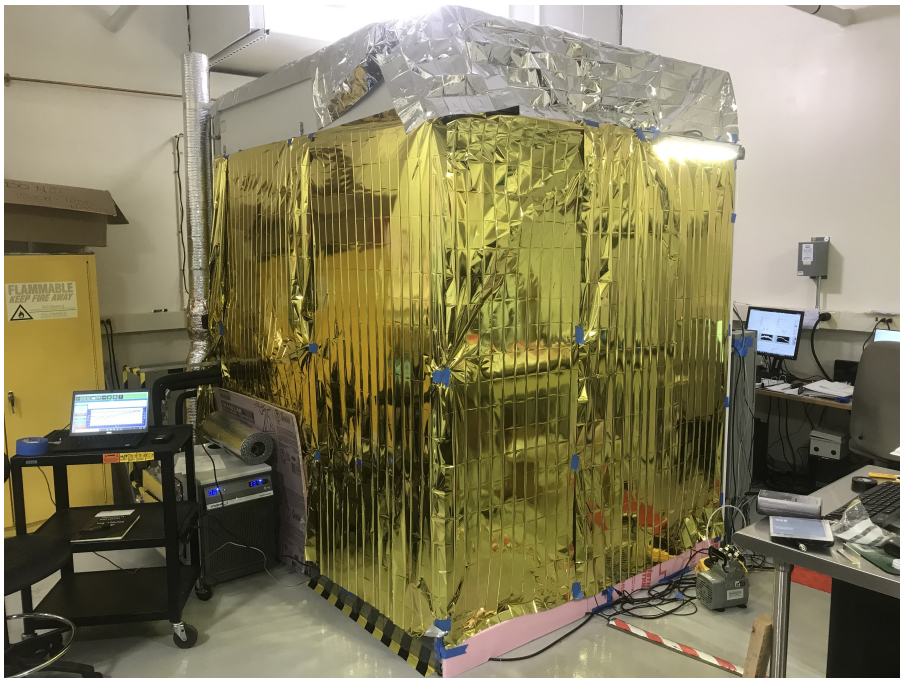

Figure 2.8: Mylar blankets covering the enclosure to investigate the effect of radiative coupling on the Nanotech 100UMM, measurement probe, and part.

The mylar blankets are very thin. When close to the blankets it is possible to see through them. It is possible that with a thicker blanket or multiple layers there would be more of an effect. Foam was used in the gaps under the curtains to seal up some of the air gaps and next to the chiller to insulate from heat expelled by the chiller.

A fan and ducting were added to remove the heat generated by the chiller and force it toward the ceiling into the return air for the laboratory. Bubble wrap with mylar on either side insulates the fan and ducting ensuring that most of the heat makes it to the outlet. The ducting and fan can be seen on the corner of the enclosure in Figure 2.8.

To isolate the granite base of the machine from the return air, the high pressure air tank, solenoids and electronics on the front of the machine and the hydraulic system under the rear of the machine, foam covered in mylar and aluminum tape was used. Several smaller sheets were used to fit between the frame and the rubber mounts that support the granite base when the pneumatic isolators are not pressurized. Figure 2.9 shows the foam board used from the front of the machine.

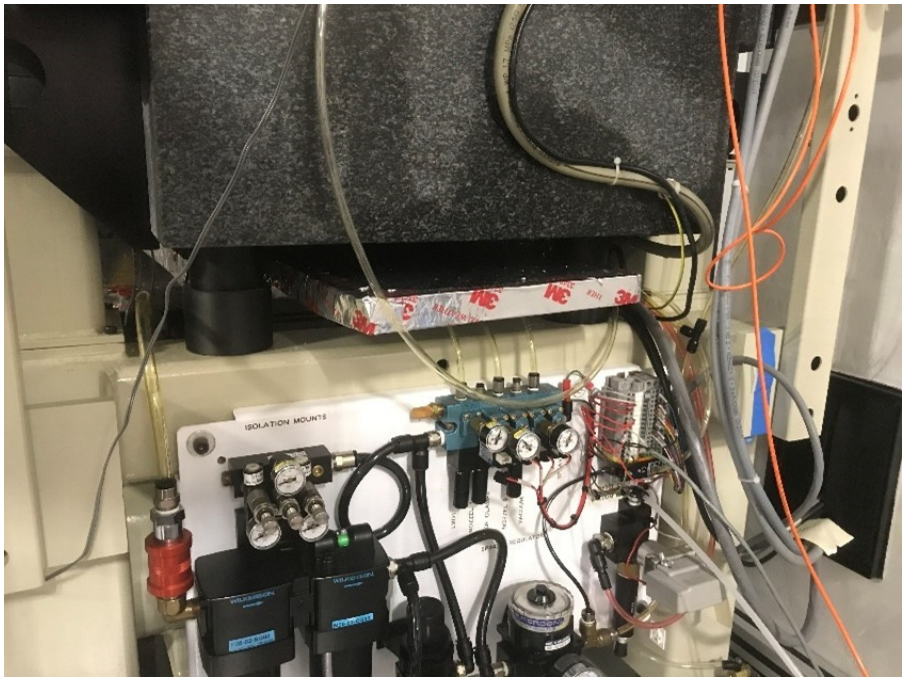

Figure 2.9: Foam covered in mylar and aluminum tape was used to isolate the granite base of the machine from the return air, electronics on the front of the machine and the hydraulic system in the rear of the machine.

The high-pressure air that supplies the air bearings comes from the laboratory supply. Before entering the enclosure, the air is filtered several times for particulate, water, and oil aerosols and goes through a desiccant tower to dry the air. A heat exchanger was added in the return ducting for the enclosure between the air tank on the machine and the desiccant tower to reduce the temperature of the air from the laboratory before entering the air tank on the machine. The air tank on the machine acts as an emergency supply in case something disrupts the air supply to the machine

allowing enough time for the machine to come to a stop and avoid damaging the air bearings. The heat exchanger consisting of a copper tube in the return ducting is shown in Figure 2.10.

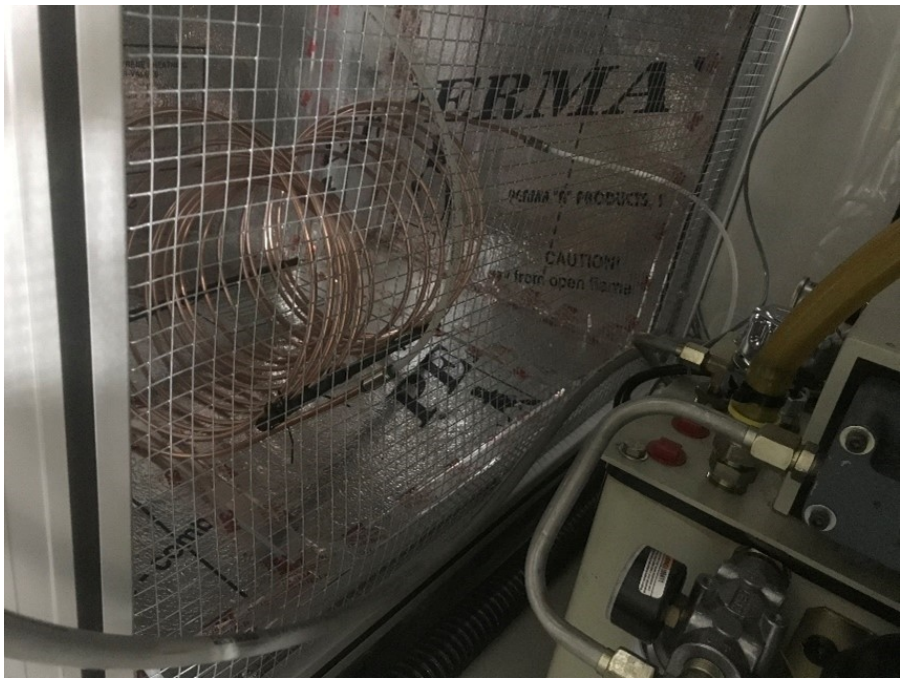

Figure 2.10: High pressure air heat exchanger made from copper tubing in the air return ducting for the environmentally controlled enclosure.

The same foam board that was placed below the machine was used to direct the air from the plenum over the machine and away from the air return. The foam board can be seen in Figure 2.11 over the return at the back of the machine.

Figure 2.11: Directing the downdraft from the plenum over the machine rather than into the return ducting.

Other alterations were made to increase the mixing in the plenum and the hydraulic oil for more efficient cooling and heating, respectively. The filters between the plenum and enclosure were adjusted by adding more layers to even out the flow over the enclosure from overhead.

The vacuum pump was changed from a venturi inside the enclosure to a diaphragm pump outside the enclosure to reduce the thermal load and acoustic noise inside the enclosure. The electronics cabinet for the 100UMM was also placed outside the enclosure, removing a large heat load next to the machine. While it could not be moved an appreciable distance from the machine due to the wiring harness, an insulated wall was placed between the electronics cabinet and the machine.

In Reference [1], ways to mitigate environmental effects and the importance of environmental control are discussed. There are several great resources discussed above in the introduction that discuss in more detail environmental and temperature control. The enclosure around the 100UMM is similar to the one discussed in Reference [28], except light bulbs were used for the re-heat. Hansen discusses the improvements in machine tool accuracy by reducing non-repeatable errors of which thermal error is a

large contributor due to thermal deformation of the machine structure.

2.5 Measurement Triggering

To automate the measurement process on the 100UMM, a triggering mechanism was implemented. Triggering starts and stops data recording on a LabVIEW program (separate from the enclosure). Automation was critical to reducing human error by removing an operator from the measurement process. The amount of time to take a measurement is drastically reduced and measurements could be repeated and run during off hours without disrupting the life of an operator. Thermal drift is minimized by allowing for a delay in starting a measurement to when thermal loads are reduced, the laboratory air handler is mid cycle, and the part and machine can 'soak out' after switching parts or equipment.

The spray mist solenoid, from the 100UMM being an adapted diamond turning machine, is used to trigger a measurement on/off. The controller has spray mist commands in the M-codes. This allows a command to be entered in the machine code among the positioning or preparatory commands. A point by point measurement uses this command to trigger a measurement once the machine carriages are in position and enough dwell time has elapsed to reduce dynamics from the carriage positioning.

To convert the solenoid activation to a digital signal, an opto-isolator was used. The digital signal is read into LabVIEW by a DAQ. The opto-isolator allows for the high voltage and high amperage going to the spray mist solenoid to be read by the DAQ as a digital signal. When the spray mist command is active and electricity is sent to the spray mist solenoid, a LED is turned on and a photodetector senses the light triggering the measurement.

2.6 Reading the Machine Scales

To achieve a scanning mode on the 100UMM the scales need to be accessed with as little delay in the position data as possible. The easiest way, and with the least

amount of lag, to achieve this was accessing the signal from the machine scales before the machine controller. A major concern in reading the machine scales was affecting the performance of the machine by influencing the position data going to the machine controller. Fortunately, the 100UMM was fitted with a Heidenhain IBV 606 interface box. In this application the IBV 606 tunes the encoder signals coming from the machine scales. It is used to match the gain of sine/cosine signals, balance their DC offsets, and to adjust the quadrature phase to 90 degrees. In addition, the box splits the signal without effecting the machine operation. The encoder signal is sent to a Heidenhain EIB 741 external interface box that divides one period of the signal down to 4096 pieces, often called interpolating. This meant reading the A quad B signal directly from the scales and independently interpolating that signal and turning it into counts. Each count (equal to a distance traveled) is recorded in the LabVIEW program.

The machine carriage positions are read into LabVIEW at nominally the same time as the probe displacement. The time difference between the scale position and probe displacement introduces an error into the measurement or a data age uncertainty [10].

2.7 Measurement Process

To use the process laid out in this research a set of procedures must be followed so that the required information and measurements are available to be entered into the data processing programs. To use the mathematical model, certain offsets and positions need to be recorded. Care must be taken to keep the part and mounting surfaces clean. When the probe is in the probe holder it is easy to bump while setting up the part. When dealing with the part held by vacuum before the safety is put into place, the probe should be moved far enough away that if the vacuum fails and the part falls it will not damage the probe. Also, a piece of foam can be used to catch the part. Generally, the following steps should be done in order. This list is mainly for the AFRL optics with associated fiducials.

1. Turn on vacuum pump
2. Machine should be in MPG mode to use the hand wheel, changing the incremental distance as necessary to jog the machine during setup
3. Decide orientation of the B carriage (for larger parts, the B carriage must be parallel to X carriage)
4. Place probe holder with base on the B carriage, securing with T-nuts and screws
5. Gently place probe in collet depressing the spring with a pair of pliers ensuring the collet is not too close to the optics
6. Place collet and probe assembly onto kinematic mount, fully seated into balls and against pin, ensuring the spring is in the groove without touching the sides
7. Place probe setting ball on face of the C carriage and initiate vacuum with switch on top of C carriage
8. Attach vacuum safety around probe setting ball
9. Center probe setting ball on rotational axis of the C carriage using electronic indicator and rubber handled screwdriver
10. Center probe on ball using crowning technique (Probe Setting and Alignment: Section 4.8)
11. Move Z carriage back (positive direction)
12. Remove vacuum safety
13. Remove steel ball probe setting artifact
14. Attach glass flat probe setting artifact with vacuum ensuring mating surfaces are clean
15. Attach vacuum safety around probe setting flat
16. Follow procedure for aligning probe perpendicular to the carriage travel (Probe Setting and Alignment: Section 4.8)
17. Remove vacuum safety
18. Remove glass flat probe setting artifact

19. Clean part mounting surfaces and clear aperture (carefully)
20. Mount part on C carriage
21. Center part using the electronic indicator and a rubber handles screwdriver following the directions in Section 7.2
22. Establish clocking datum using the flat fiducial on the top or bottom of the part, setting the electronic indicator stand on the X carriage to tram the fiducial
23. If vacuum is used, attach safety making sure the safety does not disturb the part but is close enough to restrict the part movement as to not damage the probe if vacuum failure occurs
24. Bring probe into range of the optic placing the probe displacement in desired position
25. Set and record G-54 offsets for B, C, X, and Z carriages in the machine controller by typing in the the values shown for the machine carriage positions at the centered, null, and clocked position into the G-54 offset window
26. Measure distance between probe tip and rotational axis of B carriage in the Z direction using the method described in Section 4.8
27. Tape down any wires or cables (do not use duct tape; painters or electrical tape is preferred)
28. Switch machine to auto and make sure the single block and dry run buttons are not illuminated
29. Load measurement program
30. Take pictures of the setup including the part, probe, and machine coordinates (offsets) at zero
31. Start the LabVIEW program on the data acquisition computer (note the settings)
32. Hit "cycle start" (the green button)
33. When finished back part away from the probe

34. Save the measurement data with a very descriptive name
35. It helps to save the g-code with the measurement data

The distance, in the x direction, between the probe centered on the part and the fiducial origin should approximate the distance the probe is from the rotational axis of B in the x direction. This distance is needed in the mathematical model as one of the inputs is the probe coordinates in the B carriage system.

CHAPTER 3: MATHEMATICAL MODEL

A mathematical model for the 100UMM was developed to enable machine error compensation and task specific uncertainty evaluation. The model uses transformation matrices and position vectors to establish "the mathematical relationship between final volumetric errors of a machine and its individual components [1]." The model is a frame-based model where the frame and each of the carriages are assigned a coordinate system [3]. The origin of these coordinate systems is selected to make the machine tool metrology and modeling easier. Part coordinates in the supporting carriage coordinate system, machine error measurements, machine carriage positions, probe position in its supporting carriage coordinate system, probe displacement and probing errors populate the transformation matrices and position vectors. The machine carriage positions are read directly from the scales as described above. The model can be solved for the measurement point in part coordinates. Repeating for the entire data set of measurement points, the measured surface is generated. The measurement points represent a surface that is compensated with the machine errors in the model.

With the mathematical model and measurements of the error motions of the machine carriages, error compensation is possible. Error compensation removes the bias in the measurement from the carriage error motions leaving the uncertainty in the error motion measurements. With a Monte Carlo simulation the task specific uncertainty can be evaluated. The Monte Carlo simulation uses the mathematical model populated with the uncertainty in the machine error measurements and probe displacement along with other uncertainty contributions. By running the simulation many times, statistical methods can be used to evaluate the uncertainty in the best

estimate of the surface and parameters calculated from the best estimate of the surface.

The use of homogeneous transformation matrices (HTMs) and how to populate them will also be discussed. Two position vectors will be solved for, the probe position vector and the part position vector using transformation matrices. The term fiducial origin will be used to define the point of interest used in the model and for machine tool metrology. The fiducial origin represents a starting point for the model. It is assumed that the machine components and part being measured are all rigid bodies meaning that they will not deform under a load or while moving.

3.1 Building a Coordinate System

The machine could be described as a BXFZC or CZFXB, using machine nomenclature in References [1], [2] depending where the part and probe are located. This indicates the order that the machine carriages are oriented and how the model will be constructed. Each carriage and the frame are assigned a coordinates system. The coordinate systems are based on the cartesian coordinates system with three orthogonal axes x, y, and z. A frame-based model will be used meaning that the frame is fixed, and the other coordinates systems move with respect to the frame coordinates system. The origin of the coordinate systems is chosen to make the machine error measurements more convenient.

3.2 Forward Kinematics vs. Reverse or Inverse Kinematics

Forward kinematics will be used in solving for the measurement solution where the positions of the carriages and probe displacement are known, and the position of the probing point in a defined coordinate system is solved for. Inverse kinematics would be if the part coordinates were known and the carriage positions were solved for. Inverse kinematics is used for probe path generation to command the carriage positions for part measurement.

3.3 Coordinate Frames

The model consists of 5 coordinate systems, one for each carriage and one for the frame. The following symbols will be used when referring to the coordinates systems, axes of coordinate systems and origins of the coordinate systems.

F - Frame (Base) of machine

${}_{CS}$F - The frame coordinate system

${}_{O}$F - The origin of the frame coordinate system

${}_{X}$F - The x axis of the F coordinate system

${}_{Y}$F - The y axis of the F coordinate system

${}_{Z}$F - The z axis of the F coordinate system

The same symbols and subscripts will follow for the coordinate systems listed below.

X - X carriage (linear), ${}_{CS}$X, ${}_{O}$X, ${}_{X}$X, ${}_{Y}$X, and ${}_{Z}$X

Z - Z carriage (linear), ${}_{CS}$Z, ${}_{O}$Z, ${}_{X}$Z, ${}_{Y}$Z, and ${}_{Z}$Z

C - C carriage (rotary), ${}_{CS}$C, ${}_{O}$C, ${}_{X}$C, ${}_{Y}$C, and ${}_{Z}$C

B - B carriage (rotary), ${}_{CS}$B, ${}_{O}$B, ${}_{X}$B, ${}_{Y}$B, and ${}_{Z}$B

The rotary carriages have an axis of rotation or the axis about which they rotate. For the C carriage it is the z axis and for the B carriage it is nominally the y axis.

${}_{A}$C - Rotation axis of C

${}_{A}$B - Rotation axis of B

3.4 Defining the Coordinate System

The five coordinates systems overlap at the position described below when Z_O is equal to Y_O. This is the point where the coordinate systems will be defined and will serve as a starting position where the model is concerned, not to be confused with the home position of the machine. The height in the y direction of ${}_{A}C$ is nominally fixed as there is no Y carriage. The origin of the frame coordinate system will be

called the fiducial origin. The fiducial origin will be the point where, at this starting position, the origin of all the coordinate systems and the axes overlap.

For the purposes of this model the ${}_{A}C$ is used as the z axis of the frame coordinate system, ${}_{CS}F$. To determine the x axis a plane is made using ${}_{A}C$ and ${}_{A}B$ where ${}_{A}B$ is aligned to intersect ${}_{A}C$ by moving the X carriage. The point where these two axes meet is the fiducial origin. The x axis of the ${}_{CS}F$ is perpendicular to this plane. The y axis of ${}_{CS}F$ is simply orthogonal to both the x axis and z axis of ${}_{CS}F$. The fiducial origin is shown in Figure 3.1.

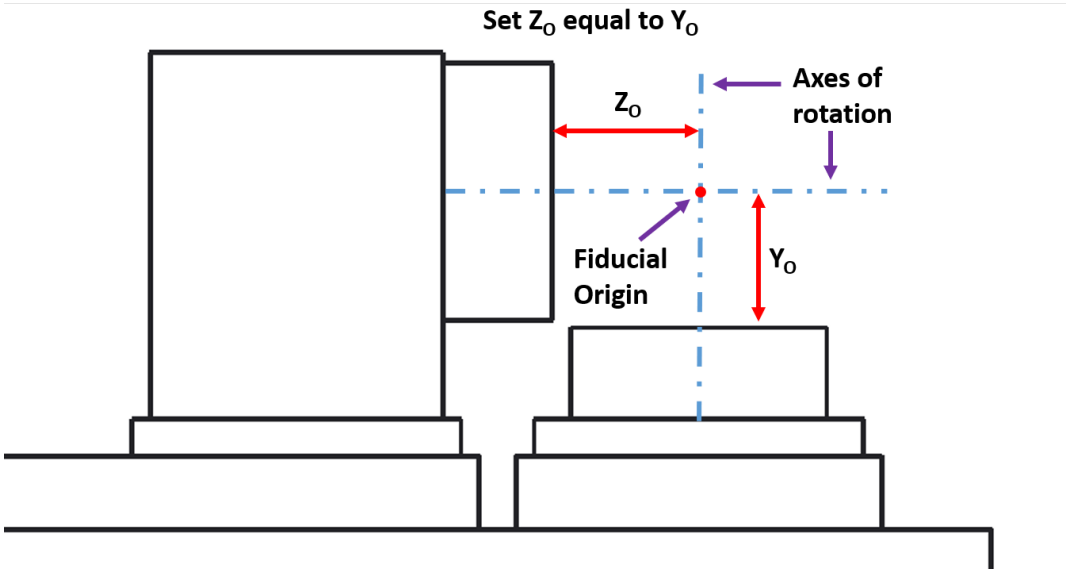

Figure 3.1: Setting the carriage positions for the fiducial origin of the mathematical model of the Nanotech 100UMM.

For ease of measurement and since the location of the origins of the five coordinates systems are arbitrary, it was easier to locate them all at the fiducial origin, a location that could be measured and defined. Figure 3.2 shows the location of the five coordinate systems at the fiducial origin when Z_O is equal to Y_O. The coordinate systems move with the respective carriages, apart from the frame coordinate system which does not move.

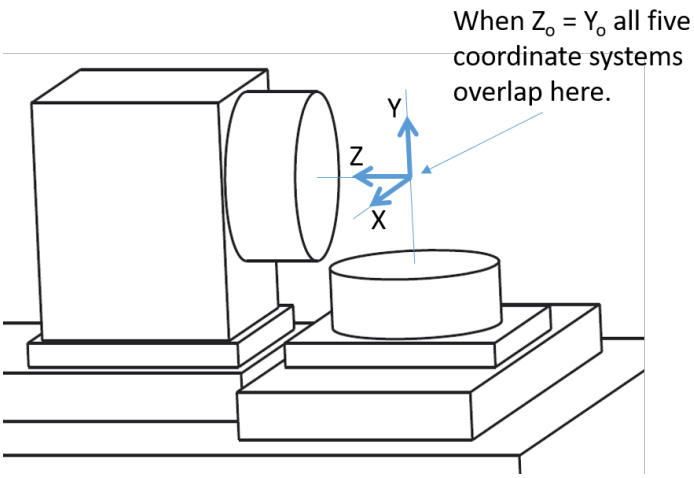

Figure 3.2: Location of coordinate systems when X_m, Z_m, β, and θ are at the carriage positions for the fiducial origin. All five coordinate systems of the mathematical model overlap at the fiducial origin.

3.5 Machine Carriage Positions

The machine carriage position is the position read off the position display (scale reading) and is close to the position commanded by the controller. The difference is referred to as following error. The machine position is used in the model to relate machine errors to a physical position of the carriage. The carriages have the subscript M to indicate the machine position. The Greek letter β is used for the carriage position of the B carriage and θ for the carriage position of the C carriage.

X_M - Machine position of the X carriage

Z_M - Machine position of the Y carriage

B_M - Machine position of the B carriage

C_M - Machine position of the C carriage

The machine positions at the fiducial origin are the position of the carriages when ${}_AC$ and ${}_AB$ intersect, or the machine carriage positions where the carriage coordinate systems overlap.

X_{MO} - Origin machine position of the X carriage

Z_{MO} - Origin machine position of the Z carriage

B_{MO} - Origin machine position of the B carriage

C_{MO} - Origin machine position of the C carriage

The home position of the machine is when X_M, Z_M, B_M, and C_M are all equal to zero. This is done by selecting the home button on the control panel shown in Figure 3.3, then pressing the button corresponding to which carriage that is to be homed and pressing either the "+" or "-" button.

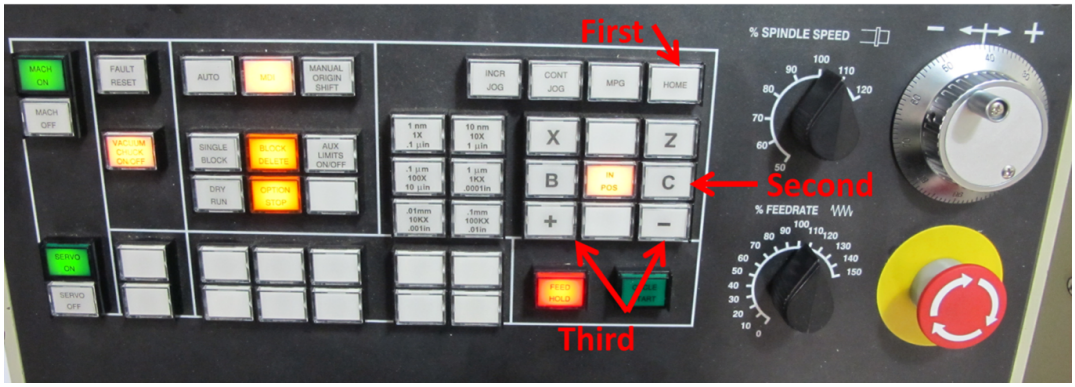

Figure 3.3: Homing the machine carriages using the control panel for the Nanotech 100UMM.

The repeatability of the homing system can be added to the uncertainty budget and Monte Carlo simulation as an uncertainty contributor.

3.6 Units and the Metric System

Dimensions, measurements, and machine values use the metric system. For the small angle approximation, the angle in radians is used. The 100UMM uses millimeters and degrees as units.

3.7 Defining the Vector Model

Let ${}_OF$ be the fiducial origin at the ${}_AC$ and ${}_AB$ intersection, also assigned as the origin of the frame coordinate system. The position of the X carriage, $X_M = X_{MO}$ is chosen so that ${}_AC$ intersects with ${}_AB$, the point defining the fiducial origin. Y_O is the distance of ${}_OF$ above the face of B table at this position. Let Z_{MO} equal Z_M when ${}_OF$ is located at a distance $Z_O = Y_O$ from the face plate of the C carriage to

${}_{A}B$. The coordinate systems are overlapping at the fiducial origin when,

$$Z_M = Z_{MO} \tag{3.1}$$

$$X_M = X_{MO} \tag{3.2}$$

$$C_M = C_{MO} = 0°. \tag{3.3}$$

$$B_M = B_{MO} = 3.6°. \tag{3.4}$$

The coordinate systems ${}_{CS}F$, ${}_{CS}X$, ${}_{CS}Z$, ${}_{CS}C$ and ${}_{CS}B$ are all aligned at this point with: ${}_{O}F = {}_{O}X = {}_{O}Z = {}_{O}B = {}_{O}C$. When the machine carriages move we are left with a distance between the origins of each coordinate system depicted in Figure 3.4.

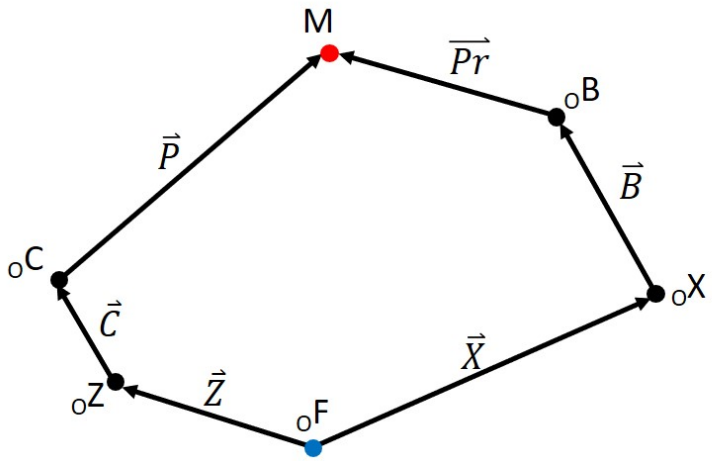

Figure 3.4: Vector model showing the relationship between the origins of each coordinates system and the vectors connecting the origins of each coordinate system [3].

These vectors between the coordinate systems include the nominal carriage motion, machine error motions, and position vectors of the part and probe. From machine error measurements we have the vectors and the measured errors as a function of the position of the carriage being measured.

$$\left[\overrightarrow{P}\right]_C = [M]_C \tag{3.5}$$

$$\left[\overrightarrow{C}\right]_Z = \left[{}_{O}C\right]_Z \tag{3.6}$$

$$\left[\overrightarrow{Z}\right]_F = \left[{}_OZ\right]_F \tag{3.7}$$

$$\left[\overrightarrow{X}\right]_F = \left[{}_OX\right]_F \tag{3.8}$$

$$\left[\overrightarrow{B}\right]_X = \left[{}_OB\right]_X \tag{3.9}$$

$$\left[\overrightarrow{Pr}\right]_B = \left[M\right]_B \tag{3.10}$$

The vector $\overrightarrow{C}$ is from ${}_OZ$ to ${}_OC$ as a function of θ, the nominal carriage position of the C carriage. This is shown in Figure 15. The vector sum following each path meets at M, the measurement point. This is where the probing point meets the part, closing the loop. Note the point M is a single measurement point. To reconstruct a surface, many measurement points will be needed. The vector model will change for each measurement point and will need to be solved each time. For part measurements we want the measurement point, M, in the ${}_{CS}C$. We can do this by solving for the part vector in the ${}_{CS}C$. To differentiate between the two paths to M, we will use the $\overrightarrow{P}$ and $\overrightarrow{Pr}$ vectors in the solution.

3.8 Vector Model

When solving for the probe vector in ${}_{CS}$B we are looking for M in the ${}_{CS}$B. When solving for the part vector in ${}_{CS}$C we are looking for M in the ${}_{CS}$C to compare with the nominal part vector or measurement point at that point to find the error.

$\overrightarrow{P}$ is the vector from the origin of the C coordinate system to the part surface at the measurement point.

$$\overrightarrow{P} = \overrightarrow{{}_OCM} \tag{3.11}$$

$\overrightarrow{Pr}$ is the vector from the origin of the B coordinate system to the probing point at the measurement point.

$$\overrightarrow{Pr} = \overrightarrow{{}_OBM} \tag{3.12}$$

$\overrightarrow{C}$ is the vector from the origin of the Z coordinate system to the origin of the C

coordinate system.

$$\overrightarrow{C} = \overrightarrow{{}_{O}Z_{O}C} \tag{3.13}$$

$\overrightarrow{Z}$ is the vector from the origin of the Z coordinate system to the origin of the C coordinate system.

$$\overrightarrow{Z} = \overrightarrow{{}_{O}F_{O}Z} \tag{3.14}$$

$\overrightarrow{X}$ is the vector from the origin of the Frame coordinate system to the origin of the X coordinate system.

$$\overrightarrow{X} = \overrightarrow{{}_{O}F_{O}X} \tag{3.15}$$

$\overrightarrow{B}$ is the vector from the origin of the X coordinate system to the origin of the B coordinate system.

$$\overrightarrow{B} = \overrightarrow{{}_{O}X_{O}B} \tag{3.16}$$

From Figure 3.4 we can see that:

$$\overrightarrow{P} + \overrightarrow{C} + \overrightarrow{Z} = \overrightarrow{X} + \overrightarrow{B} + \overrightarrow{Pr} \tag{3.17}$$

To add the representations, we must have them all in the same reference frame. All vectors are measured with respect to their supporting carriages of structure, so they need to be transformed to a common coordinate system. In this case we use the frame coordinate system.

$$\left[\overrightarrow{P}\right]_{F} + \left[\overrightarrow{C}\right]_{F} + \left[\overrightarrow{Z}\right]_{F} = \left[\overrightarrow{X}\right]_{F} + \left[\overrightarrow{B}\right]_{F} + \left[\overrightarrow{Pr}\right]_{F} \tag{3.18}$$

Rotation matrices are used to transform to a common reference frame:

$$\left[\overrightarrow{P}\right]_{F} = R_{\overrightarrow{CF}}\left[\overrightarrow{P}\right]_{C} = R_{\overrightarrow{ZF}}R_{\overrightarrow{CZ}}\left[\overrightarrow{P}\right]_{C} \tag{3.19}$$

$$\left[\overrightarrow{C}\right]_{F} = R_{\overrightarrow{ZF}}\left[{}_{O}C\right]_{Z} \tag{3.20}$$

$$\left[\overrightarrow{Z}\right]_{F} = \left[{}_{O}Z\right]_{F} \; as\; measured \tag{3.21}$$

$$\left[\overrightarrow{X}\right]_F = \left[{}_OX\right]_F \text{ as measured} \tag{3.22}$$

$$\left[\overrightarrow{B}\right]_F = R_{\overrightarrow{XF}}\left[{}_OB\right]_X \tag{3.23}$$

$$\left[\overrightarrow{Pr}\right]_F = R_{\overrightarrow{BF}}\left[\overrightarrow{Pr}\right]_B = R_{\overrightarrow{XF}}R_{\overrightarrow{BX}}\left[\overrightarrow{Pr}\right]_B \tag{3.24}$$

Note that the order of multiplication is important as with all matrix multiplication. Substituting equation 3.19 to 3.24 into equation 3.18 including the rotation matrices, the model is now:

$$R_{\overrightarrow{ZF}}R_{\overrightarrow{CZ}}\left[\overrightarrow{P}\right]_C + R_{\overrightarrow{ZF}}\left[{}_OC\right]_Z + \left[{}_OZ\right]_F = \left[{}_OX\right]_F + R_{\overrightarrow{XF}}\left[{}_OB\right]_X + R_{\overrightarrow{XF}}R_{\overrightarrow{BX}}\left[\overrightarrow{Pr}\right]_B \tag{3.25}$$

The probe or part position vectors can be solved for. In this research we are primarily concerned with the part position vector. The equation above can be re-arranged such that:

$$R_{\overrightarrow{ZF}}\left[R_{\overrightarrow{CZ}}\left[\overrightarrow{P}\right]_C + \left[{}_OC\right]_Z\right] + \left[{}_OZ\right]_F = \left[{}_OX\right]_F + R_{\overrightarrow{XF}}\left[\left[{}_OB\right]_X + R_{\overrightarrow{BX}}\left[\overrightarrow{Pr}\right]_B\right] \tag{3.26}$$

$$R_{\overrightarrow{ZF}}\left[R_{\overrightarrow{CZ}}\left[\overrightarrow{P}\right]_C + \left[{}_OC\right]_Z\right] = -\left[{}_OZ\right]_F + \left[{}_OX\right]_F + R_{\overrightarrow{XF}}\left[\left[{}_OB\right]_X + R_{\overrightarrow{BX}}\left[\overrightarrow{Pr}\right]_B\right] \tag{3.27}$$

$$R_{\overrightarrow{CZ}}\left[\overrightarrow{P}\right]_C + \left[{}_OC\right]_Z = R^{-1}_{\overrightarrow{ZF}}\left[-\left[{}_OZ\right]_F + \left[{}_OX\right]_F + R_{\overrightarrow{XF}}\left[\left[{}_OB\right]_X + R_{\overrightarrow{BX}}\left[\overrightarrow{Pr}\right]_B\right]\right] \tag{3.28}$$

$$R_{\overrightarrow{CZ}}\left[\overrightarrow{P}\right]_C = -\left[{}_OC\right]_Z + R^{-1}_{\overrightarrow{ZF}}\left[-\left[{}_OZ\right]_F + \left[{}_OX\right]_F + R_{\overrightarrow{XF}}\left[\left[{}_OB\right]_X + R_{\overrightarrow{BX}}\left[\overrightarrow{Pr}\right]_B\right]\right] \tag{3.29}$$

Solving for the part vector in the C coordinate frame.

$$\left[\overrightarrow{P}\right]_C = R^{-1}_{\overrightarrow{CZ}}\left[-\left[{}_OC\right]_Z + R^{-1}_{\overrightarrow{ZF}}\left[-\left[{}_OZ\right]_F + \left[{}_OX\right]_F + R_{\overrightarrow{XF}}\left[\left[{}_OB\right]_X + R_{\overrightarrow{BX}}\left[\overrightarrow{Pr}\right]_B\right]\right]\right] \tag{3.30}$$

Solving for the probe vector in the B coordinate frame we get.

$$\left[\overrightarrow{Pr}\right]_B = R^{-1}_{\overrightarrow{BX}}\left[-\left[{}_OB\right]_X + \left[R^{-1}_{\overrightarrow{XF}}\left[-\left[{}_OX\right]_F + R_{\overrightarrow{ZF}}\left[R_{\overrightarrow{CZ}}\left[\overrightarrow{P}\right]_C + \left[{}_OC\right]_Z\right] + \left[{}_OZ\right]_F\right]\right]\right] \tag{3.31}$$

3.9 Error Term Naming Convention

To better understand the equations, a description of the error terms will be discussed. The full list of error terms and symbols can be found in Appendix A. Figure 3.5 and Figure 3.6 show the error motions and coordinate systems for linear and rotary carriages, respectively. The error motions are a function of the carriage position and will be measured as such. The linear carriage position will be a displacement and the rotary carriage position will be an angle. Each carriage has six degrees of freedom.

Linear carriages have a nominal motion in the X and Z directions for the 100UMM. Shown in Figure 3.5 is the X carriage showing the six degrees of freedom.

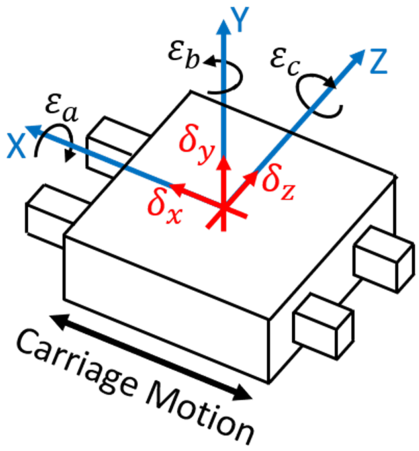

Figure 3.5: Linear carriage error motions and nominal carriage motion showing the six degrees of freedom based on the ISO 230 standard [4].

For the linear carriage there is one linear displacement or positioning error and two straightness errors, shown in red and denoted by delta. There are also three angular errors shown in black denoted by epsilon. Rotary carriages on the 100UMM have a nominal motion around the Y and Z axes. Figure 3.6 shows the configuration of the B carriage on the 100UMM with a nominal rotation about the Y axis and the six degrees of freedom of the carriage.

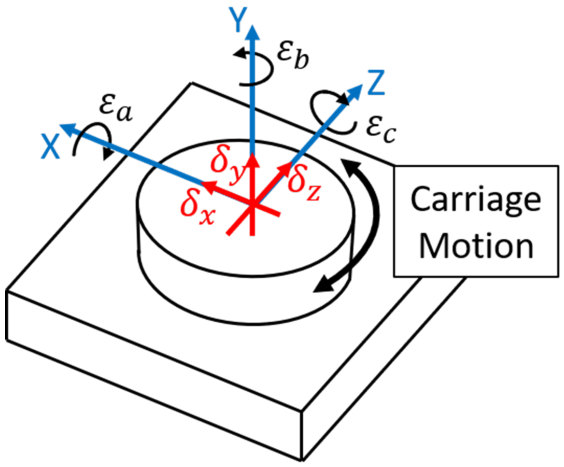

Figure 3.6: Rotary carriage error motions and nominal carriage motion showing the six degrees of freedom based on the ISO 230 standard [4].

The rotary carriage has three straightness or linear error terms denoted by delta and shown in red and three angular error terms denoted by epsilon and shown in black. One of the angular terms will be the positioning error. Error motions in the rotary carriages are a function of the carriage position. The errors are labeled $\delta_x(\theta)$, $\delta_y(\theta)$, and $\delta_z(\theta)$ for the linear errors and $\varepsilon_x(\theta)$, $\varepsilon_y(\theta)$, and $\varepsilon_z(\theta)$ for the angular errors with θ being the rotation angle or position of the rotary carriage. The linear errors are the deviation of the origin of the carriage coordinate system while the angular errors are the rotation of the carriage coordinate system or axis of rotation about three mutually perpendicular axes [1].

The 100UMM has four carriages with six degrees of freedom each, making 24 total error motions, considering the carriages independently. When put into a machine, the carriages must be considered in relation to each other. This introduces the squareness error terms making a total of 32 error motions. Of the 32 error motions only 29 are considered in the model. Three of the squareness terms are not used due to how the model coordinate systems are defined.

The squareness or non-perpendicularity of the carriages are determined in relation to the frame coordinate system. Squareness is a non-perpendicularity in the move-

ment of a carriage. For a linear carriage this is the direction of travel, for a rotary carriage this is the axis of rotation. ISO 230 refers to the rotary carriage axis of rotation as the 'axis average line' of a rotating component [4].

3.10 Angular Error Terms

The angular error terms are indicated using the Greek letter ε. The subscript indicates which axis of the coordinate system in which the error is rotating. The carriage is indicated by the symbol in the parenthesis. The angular errors rotate around the axis indicated of the supporting coordinates system (carriage or frame) with respect to the coordinate system indicated. The measurement of the rotation of the B carriage about the x-axis of the X coordinate system with respect to the X coordinate system ($_{CS}X$) would be written $\varepsilon_x(\beta)$. The positive direction of the angular error motions is defined using the right-hand rule (RHR) where the thumb on the right-hand points in the positive direction of the axis indicated and the fingers wrap around the axis in the positive direction.

3.11 Linear Displacement and Straightness Error Terms

As the carriage is rotated or translated, linear deviations of the origin of the carriage coordinates system are called the straightness or linear errors. For a rotary carriage there are three linear errors perpendicular to each other along the three axes of the coordinate system. For a linear carriage there is two straightness errors and a linear displacement or positioning error.

The linear displacement and straightness error terms are indicated using the Greek letter δ. Like the angular error terms, the subscript refers to the axis along which the error is displaced while the letter in the parenthesis indicates the carriage. Together the symbols indicate the translation of the origin of the coordinate system of the carriage in the parenthesis along the axis in the subscript of the supporting carriage coordinate system with respect to that coordinate system. The translation of the

origin of the C carriage coordinate system along the x-axis of the Z coordinate system with respect to the Z coordinate system would be $\delta_x(\theta)$. The linear displacement and straightness error terms may be referred to as linear errors.

The linear displacement or positioning error is the deviation of the origin of the carriage coordinate system from nominal or intended carriage motion. The straightness errors are deviations of the origin of the carriage coordinate system perpendicular to the direction of motion.

Straightness is calculated by taking the linear least squares fit from the data and subtracting that best fit line. The residual is the straightness error. This is shown graphically in Figure 3.7.

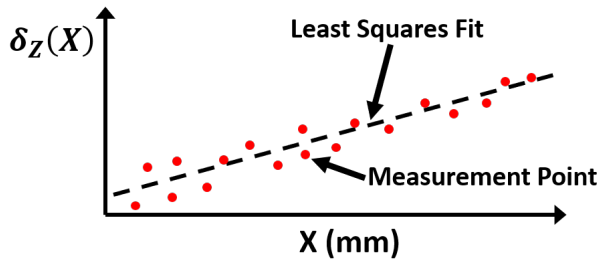

Figure 3.7: Taking out the best fit line from the straightness measurement data.

3.12 Squareness Error Terms

The squareness terms are indicated using the Greek letter α. The first subscript refers to the carriage coordinate system and the second refers to the axis in the frame coordinate system of the non-perpendicularity. In other words, the first subscript is the carriage coordinate system under investigation and the second subscript is in the direction of the error. The way to read $\alpha_{x.y}$ is the squareness error of the X carriage in the Y direction of the frame coordinate system. The measurement of the non-perpendicularity of the B axis of rotation with respect to the C axis of rotation in the Z direction would be $\alpha_{b.z}$. For the X carriage squareness with the C axis of rotation in the Z direction, $\alpha_{x.z}$ would be used. This error may be referred to as the

C-X carriage squareness informally. Figure 3.8 provides a graphical explanation of squareness.

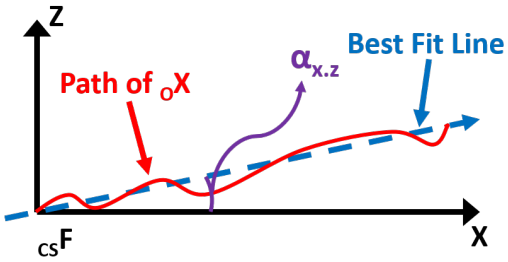

Figure 3.8: Squareness measurement for the X carriage in the Z direction of the frame coordinate system.

Three squareness error terms can be eliminated due to the rotational axis of the C carriage, ${}_{A}C$, being the reference axis and the rotational axis of the B carriage, ${}_{A}B$, being used in building the coordinate system. Meaning the C carriage does not have a squareness error and the B carriage only has a squareness term in the Z direction so the terms $\alpha_{b.x}$, $\alpha_{c.x}$, $\alpha_{c.y}$ are not considered in the mathematical model. From a Renishaw document describing the ISO 230 standard definition and realization of the squareness error [38]:

> "ISO 230-1 section 3.6.7 defines the squareness error between two axes of linear motion as "the difference between the inclination of the reference straight line of the trajectory of the functional point of a linear moving component with respect to its corresponding principal axis of linear motion and (in relation to) the inclination of the reference straight line of the trajectory of the functional point of another linear moving component with respect to its corresponding principal axis of linear motion."

ISO 230-1 states that the reference straight lines may be obtained by straight line fitting the measured trajectory of a functional point on each axis using either [30];

a) the mean minimum zone reference straight line, or

b) the least squares fit reference straight line, or

c) the end-point fit reference straight line

There is a relation between the straightness and squareness errors in the same direction of the coordinate system. The squareness is defined as the inclination of the reference straight line while the straightness is the deviation from the reference straight line.

3.13 Summary

The 29 errors that are considered in the mathematical model are summarized in Table 3.1. The table of the error motions uses the nomenclature described above.

Table 3.1: Machine error notation based on References [1], [2] and [3].

Description	Errors
linear displacement error in linear carriage	$\delta_x(X), \delta_z(Z)$
angular positioning error in rotary carriage	$\varepsilon_b(\beta), \varepsilon_c(\gamma)$
straightness	$\delta_y(X)$, $\delta_z(X)$, $\delta_x(Z)$, $\delta_y(Z)$, $\delta_x(\beta)$, $\delta_y(\beta)$, $\delta_z(\beta)$, $\delta_x(\gamma)$, $\delta_y(\gamma)$, $\delta_z(\gamma)$
angular error - roll	$\varepsilon_a(X), \varepsilon_c(Z)$
angular error - pitch	$\varepsilon_c(X), \varepsilon_a(Z)$
angular error - yaw	$\varepsilon_b(X), \varepsilon_b(Z)$
angular error - tilt	$\varepsilon_a(\beta), \varepsilon_a(\gamma)$, $\varepsilon_b(\beta), \varepsilon_b(\gamma)$
squareness (in parenthesis not considered)	$\alpha_{x.y}$, $\alpha_{x.z}$, $\alpha_{z.x}$, $\alpha_{z.y}$, $\alpha_{b.z}$ ($\alpha_{b.x}$, $\alpha_{c.x}$, $\alpha_{c.y}$)

3.14 Defining Matrices

Matrices are used to perform transformations in three dimensional spaces. Position vectors and rotational transformation matrices are used. The position vectors will be used for the linear errors such as straightness and linear displacement errors and a

change in machine carriage position.

3.15 Transformation Matrices

The rotational transformation matrices are between coordinates systems while the position vectors are between the origins of the coordinate systems.

$R_{\overrightarrow{ZF}}$ is the vector representation transformation from ${}_{CS}Z$ to ${}_{CS}F$

$R_{\overrightarrow{CZ}}$ is the vector representation transformation from ${}_{CS}C$ to ${}_{CS}Z$

$R_{\overrightarrow{BX}}$ is the vector representation transformation from ${}_{CS}B$ to ${}_{CS}X$

$R_{\overrightarrow{XF}}$ is the vector representation transformation from ${}_{CS}X$ to ${}_{CS}F$

3.16 Nominal Rotation Matrices

The nominal rotation matrix from B coordinate system to X coordinate system is:

$$R_{\overrightarrow{BX}} = \begin{bmatrix} \cos\beta & 0 & \sin\beta \\ 0 & 1 & 0 \\ -\sin\beta & 0 & \cos\beta \end{bmatrix} \tag{3.32}$$

The nominal rotation matrix from Z coordinate system to X coordinate system is:

$$R_{\overrightarrow{ZF}} = \begin{bmatrix} 1 & 0 & 0 \\ 0 & 1 & 0 \\ 0 & 0 & 1 \end{bmatrix} \tag{3.33}$$

The nominal rotation matrix from the C coordinate system to the Z coordinate system is:

$$R_{\overrightarrow{CZ}} = \begin{bmatrix} \cos\beta & -\sin\beta & 0 \\ \sin\beta & \cos\beta & 0 \\ 0 & 0 & 1 \end{bmatrix} \tag{3.34}$$

The nominal rotation matrix from the X coordinate system to the F coordinate system is:

$$R_{\overrightarrow{XF}} = \begin{bmatrix} 1 & 0 & 0 \\ 0 & 1 & 0 \\ 0 & 0 & 1 \end{bmatrix} \tag{3.35}$$

3.17 Nominal Position Vectors

The nominal linear matrix for the movement of the X carriage is:

$$\left[{}_{O}X\right]_{F} = \begin{bmatrix} X_M - X_{MO} \\ 0 \\ 0 \end{bmatrix} \tag{3.36}$$

The nominal linear matrix for the movement of the X carriage is:

$$\left[{}_{O}Z\right]_{F} = \begin{bmatrix} 0 \\ 0 \\ Z_M - Z_{MO} \end{bmatrix} \tag{3.37}$$

The rotary carriages B and C do not have a nominal linear transformation.

3.18 Introducing Errors into the Model

To complete the mathematical model the errors are added into the position vector and rotation transformation matrices. The errors are a function of the position of the carriage they are associated with.

3.19 Linear Error Matrices

The linear deviation in the origin of the coordinate system as the rotary carriage rotates are modeled by vectors. The linear error vector matrices populated with the

straightness errors are shown in equation 3.38 and 3.39.

$$\left[{}_{O}B\right]_{X} = \begin{bmatrix} \delta_X(\beta) \\ \delta_Y(\beta) \\ \delta_Z(\beta) \end{bmatrix} \tag{3.38}$$

$$\left[{}_{O}C\right]_{Z} = \begin{bmatrix} \delta_X(\theta) \\ \delta_Y(\theta) \\ \delta_Z(\theta) \end{bmatrix} \tag{3.39}$$

The nominal displacement of the linear carriages and the origin of the coordinate systems with respect to the supporting coordinate system are modeled by the vectors:

$$\left[{}_{O}X\right]_{F} = \begin{bmatrix} \delta_X(X) + X_M - X_{MO} \\ \delta_Y(X) \\ \delta_Z(X) \end{bmatrix} \tag{3.40}$$

$$\left[{}_{O}Z\right]_{F} = \begin{bmatrix} \delta_X(Z) \\ \delta_Y(Z) \\ \delta_Z(Z) + Z_M - Z_{MO} \end{bmatrix} \tag{3.41}$$

These vectors incorporate the straightness errors, linear carriage positioning errors, nominal carriage motion or the machine carriage position, and the carriage position of the fiducial origin. They can also include the squareness terms for the linear carriages.

3.20 Small Angle Approximation

The small angle approximation was used due to the errors being small angles. The approximation can be seen below. This simplifies the multiplication and inversion of the error rotation matrices. The rotations around the three Cartesian axes are multiplied to get the rotation error matrices for each of the carriages.

$$\epsilon = small\ angle \tag{3.42}$$

$$\sin\epsilon \approx \epsilon \tag{3.43}$$

$$\cos\epsilon = 1 - \frac{\epsilon^2}{2} \approx 1 \tag{3.44}$$

3.21 Rotational Error Matrices

The transformation matrices are shown below for the transformation from one carriage coordinate system to another. Each carriage is supported by another carriage or the frame. The errors are measured in respect to the carriage or frame that supports the carriage being measured. When measuring the errors, it is assumed that all carriages except the one under investigation are not moving. Using the small angle approximation three rotation matrices can be combined into one. Following [1]:

$$\begin{aligned} R(x) = &\begin{bmatrix} \cos(\varepsilon_z(X)) & -\sin(\varepsilon_z(X)) & 0 \\ \sin(\varepsilon_z(X)) & \cos(\varepsilon_z(X)) & 0 \\ 0 & 0 & 1 \end{bmatrix} \cdots \\ \cdots &\begin{bmatrix} \cos(\varepsilon_z(X)) & 0 & \sin(\varepsilon_z(X)) \\ 0 & 1 & 0 \\ -\sin(\varepsilon_z(X)) & 0 & \cos(\varepsilon_z(X)) \end{bmatrix} \begin{bmatrix} 1 & 0 & 0 \\ 0 & \cos(\varepsilon_z(X)) & -\sin(\varepsilon_z(X)) \\ 0 & \sin(\varepsilon_z(X)) & \cos(\varepsilon_z(X)) \end{bmatrix} \end{aligned} \tag{3.45}$$

Small angle approximation:

$$R(x) = \begin{bmatrix} 1 & -\varepsilon_z(X) & 0 \\ \varepsilon_z(X) & 1 & 0 \\ 0 & 0 & 1 \end{bmatrix} \begin{bmatrix} 1 & 0 & \varepsilon_y(X) \\ 0 & 1 & 0 \\ -\varepsilon_y(X) & 0 & 1 \end{bmatrix} \begin{bmatrix} 1 & 0 & 0 \\ 0 & 1 & -\varepsilon_x(X) \\ 0 & \varepsilon_x(X) & 1 \end{bmatrix} \tag{3.46}$$

Combined to equal:

$$R(x) = \begin{bmatrix} 1 & -\varepsilon_z(X) & \varepsilon_y(X) \\ \varepsilon_z(X) & 1 & -\varepsilon_x(X) \\ -\varepsilon_y(X) & \varepsilon_x(X) & 1 \end{bmatrix} \tag{3.47}$$

3.22 Error Rotation Matrices

The rotational error from ${}_{CS}B$ to ${}_{CS}X$ is shown below. If the errors are small:

$$R_{\overrightarrow{BX}} = \begin{bmatrix} 1 & -\varepsilon_z(\beta) & \varepsilon_y(\beta) \\ \varepsilon_z(\beta) & 1 & -(\varepsilon_x(\beta) \\ -\varepsilon_y(\beta) & \varepsilon_x(\beta) & 1 \end{bmatrix} \tag{3.48}$$

The rotational error from ${}_{CS}Z$ to ${}_{CS}F$ is shown below. If the errors are small:

$$R_{\overrightarrow{ZF}} = \begin{bmatrix} 1 & -\varepsilon_z(Z) & \varepsilon_y(Z) \\ \varepsilon_z(Z) & 1 & -\varepsilon_x(Z) \\ -\varepsilon_y(Z) & \varepsilon_x(Z) & 1 \end{bmatrix} \tag{3.49}$$

The rotational error from ${}_{CS}C$ to ${}_{CS}Z$ is shown below. If the errors are small:

$$R_{\overrightarrow{CZ}} = \begin{bmatrix} 1 & -\varepsilon_z(\theta) & \varepsilon_y(\theta) \\ \varepsilon_z(\theta) & 1 & -\varepsilon_x(\theta) \\ -\varepsilon_y(\theta) & \varepsilon_x(\theta) & 1 \end{bmatrix} \tag{3.50}$$

The rotational error from ${}_{CS}X$ to ${}_{CS}F$ is shown below. If the errors are small:

$$R_{\overrightarrow{XF}} = \begin{bmatrix} 1 & -\varepsilon_z(X) & \varepsilon_y(X) \\ \varepsilon_z(X) & 1 & -\varepsilon_x(X) \\ -\varepsilon_y(X) & \varepsilon_x(X) & 1 \end{bmatrix} \tag{3.51}$$

The inverse of an infinitesimal matrix is simply the transpose or a change in sign in the angles.

$$R^{-1}_{\overrightarrow{CZ}} = \begin{bmatrix} 1 & \varepsilon_z(\theta) & -\varepsilon_y(\theta) \\ -\varepsilon_z(\theta) & 1 & \varepsilon_x(\theta) \\ \varepsilon_y(\theta) & -\varepsilon_x(\theta) & 1 \end{bmatrix} \tag{3.52}$$

Adding in the nominal rotations $R_{\overrightarrow{CZ}}$ becomes:

$$R_{\overrightarrow{CZ}} = \begin{bmatrix} cos(\theta + \varepsilon_z(\theta)) & -sin(\theta + \varepsilon_z(\theta)) & \varepsilon_y(\theta) \\ sin(\theta + \varepsilon_z(\theta)) & cos(\theta + \varepsilon_z(\theta)) & -\varepsilon_x(\theta) \\ -\varepsilon_y(\theta) & \varepsilon_x(\theta) & 1 \end{bmatrix} \tag{3.53}$$

Inverting the matrices becomes more difficult with the nominal rotations added to the rotation matrix as it is no longer infinitesimal. Equation 3.11 shows the inverse for a rotation matrix with the nominal rotation [1].

$$R_{\overrightarrow{CZ}} = \begin{bmatrix} cos(\theta + \varepsilon_z(\theta)) & sin(\theta + (\varepsilon_z(\theta)) & -\varepsilon_y(\theta) \\ -sin(\theta + \varepsilon_z(\theta)) & cos(\theta + \varepsilon_z(\theta)) & \varepsilon_x(\theta) \\ \varepsilon_y(\theta)cos(\theta) + \varepsilon_x(\theta)sin(\theta) & -\varepsilon_x(\theta)cos(\theta) + \varepsilon_y(\theta)sin(\theta) & 1 \end{bmatrix} \tag{3.54}$$

3.23 Squareness

The C carriage was chosen to not have any squareness error terms. Stated another way the C carriage axis of rotation is the reference axis to which others are compared. Using this reference axis, we can define the other two axes. This reduces the number of squareness errors to five. It is important to remember the sign convention and how the errors were measured.

Using the small angle approximation, the squareness angle is multiplied by the carriage position in the mathematical model coordinate system for the linear carriages or simply added to the corresponding angular error for the rotary carriages. As the carriage moves away from the fiducial origin the magnitude of the squareness error gets larger.

$$R_{\overrightarrow{BX}} = \begin{bmatrix} 1 & -\varepsilon_z(\beta) & \varepsilon_y(\beta) \\ \varepsilon_z(\beta) & 1 & -(\varepsilon_x(\beta) + \alpha_{b.z}) \\ -\varepsilon_y(\beta) & \varepsilon_x(\beta) + \alpha_{b.z} & 1 \end{bmatrix} \tag{3.55}$$

$$\left[{}_{O}X\right]_{F} = \begin{bmatrix} \delta_X(X) + X_M - X_{MO} \\ \delta_Y(X) + (X_M - X_{MO})\alpha_{x.y} \\ \delta_Z(X) + (X_M - X_{MO})\alpha_{x.z} \end{bmatrix} \tag{3.56}$$

$$\left[{}_{O}Z\right]_{F} = \begin{bmatrix} \delta_X(Z) + (Z_M - Z_{MO})\alpha_{z.x} \\ \delta_Y(Z) + (Z_M - Z_{MO})\alpha_{z.y} \\ \delta_Z(Z) + Z_M - Z_{MO} \end{bmatrix} \tag{3.57}$$

3.24 Homogeneous Transformation Matrices

The position vector and rotation transformation matrices can also be written as homogeneous transformation matrices (HTMs). The part vector in the ${}_{CS}C$ can be found by using the following HTMs.

$$\left[\overrightarrow{P}\right]_{C} = \left(H_{\overrightarrow{CZ}}\right)^{-1}\left(H_{\overrightarrow{ZF}}\right)^{-1}\left(H_{\overrightarrow{XF}}\right)\left(H_{\overrightarrow{BX}}\right)\left[\overrightarrow{Pr}\right]_{B} \tag{3.58}$$

The HTMs above can be found by putting together the rotation and linear transformation matrices into the format shown below. They are used here to combine transformation matrices however they have other properties and uses such as computer graphics that will not be discussed here.

$$H_{\overrightarrow{BX}} = \begin{bmatrix} R_{\overrightarrow{BX}} & \left[{}_{O}B\right]_{X} \\ 0\,0\,0 & 1 \end{bmatrix} \tag{3.59}$$

$$H_{\overrightarrow{XF}} = \begin{bmatrix} R_{\overrightarrow{XF}} & \left[{}_{O}X\right]_{F} \\ 0\,0\,0 & 1 \end{bmatrix} \tag{3.60}$$

The transformation from the ${}_{CS}Z$ to ${}_{CS}F$ is shown however when solving for the part vector the inverse matrix is needed.

$$H_{\overrightarrow{ZF}} = \begin{bmatrix} R_{\overrightarrow{ZF}} & \left[{}_{O}Z\right]_{F} \\ 0\,0\,0 & 1 \end{bmatrix} \tag{3.61}$$

When taking the inverse, it is not enough to simply take the inverse of the rotation

transformation matrices but to also multiply the linear transformation by the negative inverse of the rotation transformation.

$$H_{\overrightarrow{ZF}}^{-1} = \begin{bmatrix} R_{\overrightarrow{ZF}}^{-1} & -R_{\overrightarrow{ZF}}^{-1}\left[{}_{O}Z\right]_{F} \\ 0\,0\,0 & 1 \end{bmatrix} \tag{3.62}$$

If close attention is paid to the following equation taken from above it is noticeable where this necessity comes from. Figure 3.9 shows the relationship between the position vectors and rotation matrices with the HTMs.

$$H_{\overrightarrow{CZ}}{}^{-1} = \begin{bmatrix} R_{\overrightarrow{CZ}}{}^{-1} & -R_{\overrightarrow{CZ}}{}^{-1}[{}_{O}C]_{Z} \\ 0\,0\,0 & 1 \end{bmatrix} \qquad H_{\overrightarrow{ZF}}{}^{-1} = \begin{bmatrix} R_{\overrightarrow{ZF}}{}^{-1} & -R_{\overrightarrow{ZF}}{}^{-1}[{}_{O}Z]_{F} \\ 0\,0\,0 & 1 \end{bmatrix}$$

$$[P]_{C} = R_{\overrightarrow{CZ}}{}^{-1}\left[-[{}_{O}C]_{Z} + R_{\overrightarrow{ZF}}{}^{-1}\left[-[{}_{O}Z]_{F} + [{}_{O}X]_{F} + R_{\overrightarrow{XF}}\left[[{}_{O}B]_{X} + R_{\overrightarrow{BX}}[Pr]_{B}\right]\right]\right]$$

Figure 3.9: Building the inverse transformation matrices.

The same is the case for the transformation from the ${}_{CS}C$ to ${}_{CS}Z$.

$$H_{\overrightarrow{CZ}} = \begin{bmatrix} R_{\overrightarrow{CZ}} & \left[{}_{O}C\right]_{Z} \\ 0\,0\,0 & 1 \end{bmatrix} \tag{3.63}$$

$$H_{\overrightarrow{CZ}}^{-1} = \begin{bmatrix} R_{\overrightarrow{CZ}}^{-1} & -R_{\overrightarrow{CZ}}^{-1}\left[{}_{O}C\right]_{Z} \\ 0\,0\,0 & 1 \end{bmatrix} \tag{3.64}$$

3.25 Checking the Model in MATLAB

To determine whether the signs are correct in the model some simple shapes were entered into the model along with a single error. The single error shows up in the final position of the part or probe. Each error was checked to ensure the sign convention is correct and the anticipated outcome occurs. Using large errors, it is easier to see them manifest through the transformations.

3.26 Error Compensation

The mathematical model is used for error compensation of parts measured on the 100UMM. The model enables the measured machine errors and probe errors to be used to remove the bias in a measurement. The Guide to Uncertainty in Measurement (GUM) is followed in generating and stating a complete measurement result which includes a statement of uncertainty [12]. The GUM states that,

> "It is assumed that the result of a measurement has been corrected for all recognized significant systematic effects and that every effort has been made to identify such effects."

Using this as a guide for the 100UMM, compensation of the systematic effects of the machine errors were completed after identifying them. The errors identified in the model were evaluated for sensitivity to the mirrors being measured and included in the compensation. The result of the error compensation is a best estimate of the surface which can be used to calculate a deviation from the prescription, fit polynomials or calculate parameters. Figure 3.10 shows a flow chart for the error compensation using the mathematical model to produce a best estimate of the surface and best estimate of other measurands such as parameters and polynomial fits.

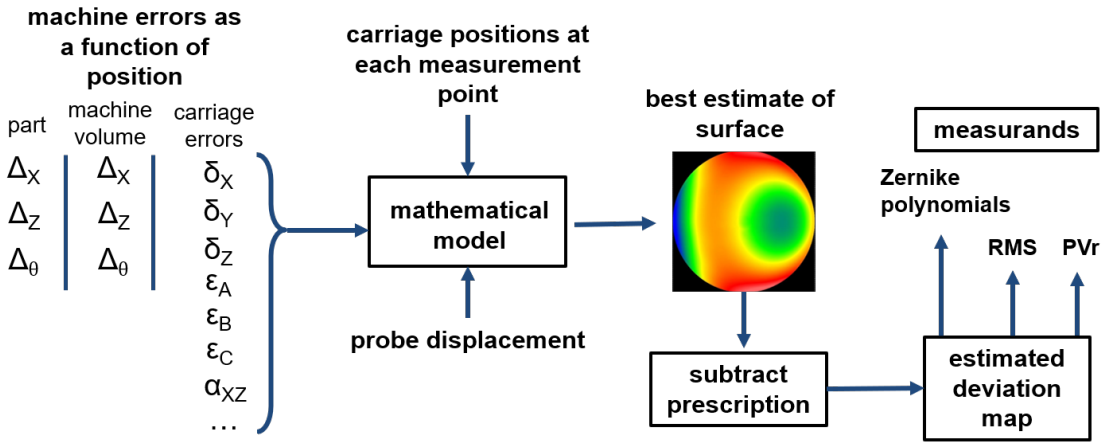

Figure 3.10: Flow chart showing error compensation using the mathematical model for the Moore Nanotech 100UMM using generic variables for the inputs into the mathematical model.

Error compensation starts with the mathematical model populated with the measured machine carriage error motions as a function of the machine carriage positions. The probe displacement and the position of the carriages for each of the measurement points are input into the model. The model is then solved for a best estimate of the surface from which the prescription can be subtracted producing the estimated deviation map. Note that the model is solved for each of the measurement points. Parameters and polynomials can be calculated from the best estimate of the surface or the deviation map depending on how they are specified. It may also be necessary to rotate the surface to take out tilt introduced in mounting the part on the machine. The mirrors have tilt in the prescription, so a fiducial is used to provide a datum to establish the tilt.

The probe errors such as the non-linearity and data age are compensated for before going into the mathematical model. These errors will be discussed in the probe sections (Sections 4.7 and 8.11). After compensating for the systematic errors, the task specific uncertainty is evaluated using the uncertainty in the machine error measurements and the mathematical model in a Monte Carlo simulation.

Since the part is measured in the G-54 offset coordinates system and the machine

errors are measured in the machine coordinate system it is necessary to subtract the offsets from the carriage positions in the measurement data for error compensation.

3.27 Compensation vs. Correction

A distinction is made between error correction and error compensation. Error correction is the act of physically correcting an error by changing the machine or instrument in some way. This could be by better aligning two carriages or placing the instrument in an environmentally controlled environment. Error compensation is the act of adjusting the controller, data processing or part program to compensate for the error. This would likely entail measuring the error and producing an error compensation table for the controller or in data processing, to use the measured error after the measurement.

In manufacturing the error must be corrected or compensated for before the part is made. In metrology, in most cases, the error can be corrected or compensated for after data acquisition. Errors that are repeatable are easier to compensate. Time varying or seemingly random errors are nearly impossible to compensate or correct for without a way to estimate or evaluate them is written into the part measurement program, as was done as part of this research. It may be possible to correct data that has been measured before the error measurements if nothing has changed with the machine or instrument. If the machine has been moved or a part has been replaced the repeatable errors may change.

3.28 Error Compensation Program

The error compensation program in MATLAB starts with loading in data from the machine error measurements (carriage positions, measured errors), zeroed at the fiducial origin and in machine coordinates. Errors considered in the error compensation are as follows.

Straightness and positioning errors:

- Dxx - X carriage positioning error
- Dzx - X carriage horizontal straightness
- Dzz - Z carriage positioning error
- Dzc - Axial error motion of C carriage

Angular errors:

- Exx - X carriage roll
- Exz - Z carriage pitch
- Exz - Z carriage pitch
- Eyx - X carriage yaw
- Eyz - Z carriage yaw
- Ezx - X carriage pitch
- Ezz - Z carriage roll
- Eyc - C carriage tilt around the y axis

The following is in a "for" loop, with each loop solving for the compensated coordinate of a measurement point in the C carriage coordinate system. In one loop:

1. Set unused errors to zero
2. Interpolate machine error measurement data for machine carriage positions of the measurement points
3. Convert error measurements from seconds to radians
4. Set machine carriage positions
5. Set fiducial origin position
6. Set probe position in B coordinate system
7. Build rotation matrices (error and nominal)
8. Invert rotation matrices (Rcz, Rfz, Rbx) and combine nominal and error rotation matrices
9. Build position vectors with straightness and positioning errors, carriage positions, and fiducial origin coordinates.

10. Combine and solve equation for part coordinates in the C coordinate system.

3.29 Monte Carlo Simulation

A Monte Carlo simulation is used to evaluate the task specific uncertainty of parts measured on the 100UMM. Following the GUM, the Monte Carlo method is used in "the propagation of probability distributions through a mathematical model of measurement as a basis for the evaluation of uncertainty of measurement [31]. "The Monte Carlo method is used in a broad range of applications extending well beyond metrology or even engineering. Loosely defined, the Monte Carlo method uses random sampling of probability distributions in an iterative fashion to solve complex problems through statistical means.

In this research the complex problem is the uncertainty evaluation of the freeform mirror measurements. The BIPM published a supplement to the GUM that deals specifically with the Monte Carlo method [31]. The supplement provides guidance on the Monte Carlo simulation as it pertains to uncertainty evaluation in measurement and implementation of the method. It is important to point out that the problem is deterministic however quantifying all the degrees of freedom and influences is extremely difficult. Determinism in this case is "the idea that machine tools obey cause and effect relationships that are within our ability to understand and control and that there is nothing random or probabilistic about their behavior [18]." For a system with many variables, some events or effects can appear to be random. For the effects we cannot measure, we will assume that they have a given distribution.

The Monte Carlo simulation starts with the mathematical model with the same inputs from the error compensation mathematical model. In addition to the error compensation inputs, the uncertainty in the machine error motion measurements as a function of carriage position and the uncertainty of the probe error measurements as a function of the probe displacement are input. Each of the measurement uncertainties are given a distribution. The Monte Carlo simulation is made up of many

iterations, each producing a possible outcome of the model based on the compensated measurement data and the uncertainty in the machine error measurements.

Each iteration of the Monte Carlo simulation solves the mathematical model for each of the measurement points. This can be computationally expensive for a large amount of iterations and a large amount of measurement points. The amount of data storage available must be managed as well. The probability distributions of the uncertainty in the machine error measurements are randomly sampled for each iteration of the simulation or for each measurement point depending on the error. For example, the uncertainty contribution due to probe noise would be sampled every measurement point and the uncertainty contributions from the machine error measurements would be sampled once per iteration. The sampled values are put into the mathematical model and added to the associated machine or probe error, then a possible surface is generated, for each iteration of the simulation. This is done for many iterations then the outputs are statistically analyzed.

One way to think of the simulation is as a virtual machine. There are software packages for CMMs that work on this idea. See Reference [17] for more. Each iteration of the Monte Carlo simulation would be a possible machine. The part is then measured on this possible machine in the simulation. Each of the possible machines produces a possible measurement result. The possible measurement results are then analyzed statistically to produce a task specific uncertainty.

Several distributions are used to describe the uncertainty in error measurements. These include triangle, normal, and uniform distributions. The type of distribution is chosen based on the measurement data and an educated assumption of the physical characteristics of what the distribution is modeling. For this research, the normal distribution was mostly used. To visualize the process a flow chart of the Monte Carlo simulation can be seen in Figure 3.11.

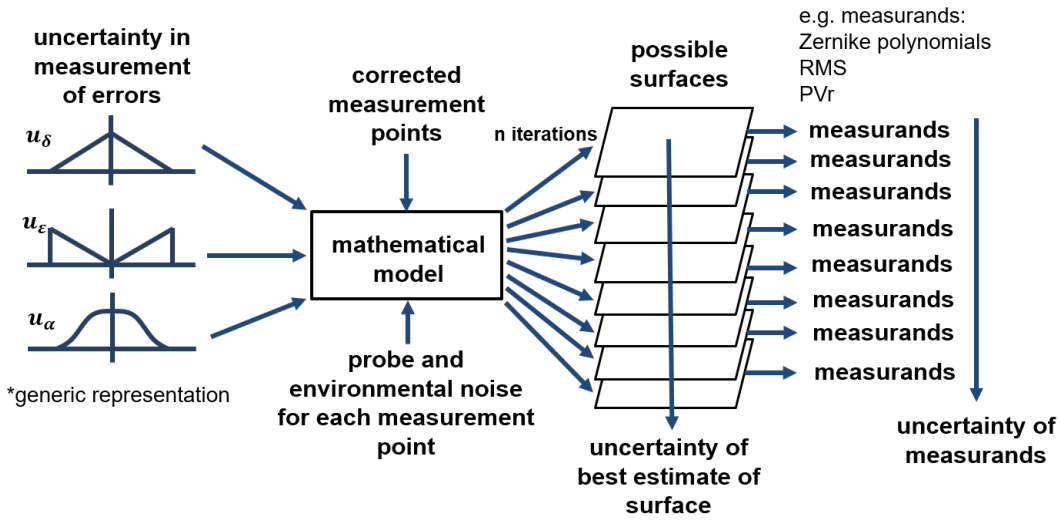

Figure 3.11: Flow chart showing the Monte Carlo simulation using the mathematical model for the Moore Nanotech 100UMM with each iteration generating a possible surface of the optic being measured.

The supplement to the GUM for the Monte Carlo method discusses the output for a Monte Carlo simulation [31]:

> "Also within the framework, the PDF taken to characterize the output quantity is used to provide a coverage interval, for a stipulated coverage probability, for that quantity."

To set up the Monte Carlo simulation, the machine scales data, machine error measurements, uncertainty in the machine error measurements, and the probe data must be in the machine coordinates. The model will transfer the coordinate systems to the fiducial origin.

The Monte Carlo simulation was programmed in MATLAB. The simulation was programmed as a sub-function so that it could be incorporated into the data processing of different measurements. To expedite the program and to take advantage of modern computing, the program was run on an 8-core processor using the parallel processing toolbox in MATLAB. There were a few issues using parallel processing in a sub function that were solved by putting the machine error measurements and

uncertainty for the machine error measurements into the input of the sub-function.

The Monte Carlo simulation ends up being a lot of data that needs to be stored and processed. The computer used has 64 GB of RAM however this was only enough memory for a simulation of 200 iterations. The program saves the data each iteration in case the program fails the data will not be lost. The computer could only process (average and standard deviation) a thousand iterations at a time for a full data set. The data sets are broken into individual circumferential measurements allowing them to be processes separately then saved to be combined in a separate program. This increases the number of iterations that can be processed.

The best estimate of the surface comes from the error compensated measurement data and the task specific uncertainty comes from the Monte Carlo simulation. The best estimate of the surface can be used to estimate parameters that describe the surface (for example statistical parameters such as rms, coefficients of fit parameters, or power spectral density) and the Monte Carlo simulation can be used to evaluate the uncertainty in those parameters. Notice that there is a difference between calculating a measurand from individual possible surfaces and from an average of the possible surfaces.

The result of an iteration in the Monte Carlo simulation is an (X, Y, Z) coordinate for each measurement point. The (X, Y, Z) coordinates differ from the error compensation data by the amount of deviation sampled from the machine error measurement uncertainty and ran through the model. This ends up being small deviations from the error compensation values compared to the overall magnitude of the measurement values. With each iteration having a slightly different set of (X, Y, Z) coordinates, the mean should tend toward the error compensation values and the standard deviation will be used in the uncertainty evaluation. Due to the way that the optics are specified in optical design software, the Z value parallel to the optical axis is of most interest. This will be shown in a histogram for a few select measurement points.

3.30 Task Specific Uncertainty Evaluation

For the purposes of this research the definition of task specific uncertainty "in coordinate measurement is the measurement uncertainty that results, computed according to the IS0 Guide to the Expression of Uncertainty in Measurement (GUM), when a specific feature is measured using a specific inspection plan [17]." The specific feature is the form of the surface on the mirror being measured and any specified measurands. The inspection plan is the probe path that was chosen, the measurement machine, the probing method, and the part fixturing. The probe path includes the data spacing, feed rate, sampling method, etc.

The results from the Monte Carlo simulation are used to evaluate the task specific uncertainty. The uncertainty in the best estimate of the surface is evaluated by taking the standard deviation of each measurement point through each iteration of the Monte Carlo simulation. The same approach is used for other measurands or parameters. The parameters are calculated for each possible surface then the standard deviation of those values is used to evaluate the uncertainty. This approach is shown in Figure 3.11. For this research, the uncertainty in the height value (Z) in the direction of the optical axis is of concern.

3.31 Monte Carlo Simulation Program

The program for the Monte Carlo simulation in MATLAB starts by loading in data from machine error measurements with the carriage positions and measured error at those positions. The measurements are in machine coordinates. The measurement uncertainty for the machine errors is also loaded into the program. A list of the error motions used in the Monte Carlo simulation is given below. Note that the B axis is not used and therefore the error motions are not considered. Error motions with a negligible contribution to the parts being measured are also omitted from the simulation.

Straightness and positioning errors:

- Dxx - X carriage positioning error
- Dzx - X carriage horizontal straightness
- Dzz - Z carriage positioning error
- Dzc - Axial error motion of C carriage

Angular errors:

- Exx - X carriage roll
- Exz - Z carriage pitch
- Exz - Z carriage pitch
- Eyx - X carriage yaw
- Eyz - Z carriage yaw
- Ezx - X carriage pitch
- Ezz - Z carriage roll
- Eyc - C carriage tilt around the y axis

The Monte Carlo simulation consists of two nested loops. The outer loop is an iteration of the Monte Carlo. Each iteration of the outer loop can be thought of as a possible machine, following the virtual machine analogy. The inner "for" loop solves for the compensated coordinate of a measurement point in the C carriage coordinate system with the sampled uncertainty distributions added to the carriage errors in the model. In one inner loop:

1. Set unused errors to zero
2. Interpolate error measurement data for machine carriage positions of the measurement point
3. Interpolate uncertainty in the error measurement data for machine carriage positions of the measurement point
4. Add error and uncertainty
5. Convert angles from seconds or degrees to radians

6. Set machine carriage positions
7. Set fiducial origin position
8. Set probe position in B coordinate system
9. Build rotation matrices in equation (error and nominal)
10. Invert rotation matrices (Rcz, Rfz, Rbx) and combine nominal and error rotation matrices
11. Build position vectors with straightness and positioning errors, carriage positions, and fiducial origin coordinates
12. Combine and solve equation for part coordinates in the C coordinate system

The inner loop goes through all the measurement points and the outer loop iterates through the number of iterations in the Monte Carlo simulation.

CHAPTER 4: DISPLACEMENT MEASUREMENT PROBES

The Nanotech 100UMM and the 3 degree of freedom probe holder with interchangeable collets permits several different probes to be used. For part measurements in this research the machine is primarily used with chromatic confocal probes due to their versatility in measuring freeform optics. The probe holder is designed to hold capacitance gages, an LVDT, a C-LVDT from Lion Precision, a fiber optic intensity probe from Philtec, and several chromatic confocal probes. Each probe type has unique characteristics and use different technologies. Depending on the application a specific probe may be best suited. The probes used in this research are discussed below. The probe holder allows for adjustment of the probe to align the probe with the machine carriages and parts being measured.

4.1 Contact vs. Non-contact

A non-contact probe was chosen over a contact probe due to the difficulties in determining the probe to part contact on a freeform surface and the possibility of scratching the surface of the part. Although probing forces can be low, some optics have features inimical to contact metrology such as coatings, plating, or the material on the optical surface. There is also the chance that a piece of dirt or debris can be dragged across the part if not cleaned properly.

Determining the contact point between a freeform part and the surface of a probe ball can be difficult. There are techniques to adjust for the probe radius, but they are 2 dimensional or require prior knowledge of the surface. Not only is the contact point in question, but any form error in the ball will also affect the measurement result. A

way to overcome the error is to use the probe normal to the surface but requires a well-known probing point in relation to the axis of rotation or the coordinate system of the supporting carriage. The prescription must also be well known, or an iterative process would need to be used where the surface is measured enough times to reduce the possible error below an acceptable level. The contact probes considered were the LVDT probe which has a 5/32-inch (0.1563 inch or about 4 mm) diameter tungsten carbide ball and the C-LVDT which has a 0.25-inch (6.35 mm) diameter ball.

The resulting error for a concave surface, like the AFRL TMA half scale tertiary, is greater near the edges where the slope is larger. The error of interest is in the direction perpendicular to the direction of travel. The error in the direction of travel can be determined using a morphological filter. As the stylus travels around the mirror the contact point on the mirror changes. Consider the two-dimensional case shown in Figure 4.1.

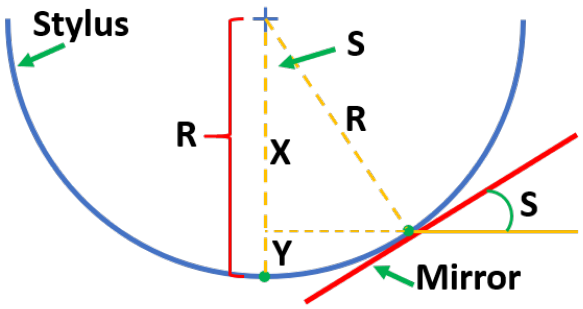

Figure 4.1: Error due to the radius of a contact probe and the changing contact point with the surface being measured.

$$cos(S) = \frac{X}{R} \tag{4.1}$$

$$X = R * cos(S) \tag{4.2}$$

$$Y = R - X = R - R * cos(S) \tag{4.3}$$

Where R is the stylus radius, S is the slope and Y is the error in the height (Z direction), or displacement recorded. This calculation for the worst case of the mirrors

in this paper where the maximum slope is roughly 10° is show below.

$$Y = 3.175\,mm - 3.175\,mm * cos(10^{\circ}) = 0.0482\,mm \approx 50\,\mu m \tag{4.4}$$

The worst case error would be roughly 50 μm, well above an acceptable level for freeform optics. The direction of the error changes depending on position. A smaller probe diameter would decrease the error but would decrease the contact area, increasing the likelyhood of damaging the optical surface.

The velocity of the probe over the surface with a contact probe must be low enough that there are no dynamic affects from the probe going over a change in slope, defects, or debris on the surface. More information regarding this issue as it pertains to the C-LVDT can be found in [39]. The probe also acts as a morphological filter or mechanical filter that removes high spatial frequency content and rounds off 'sharp' corners. Since we are measuring form, filtering out high spatial frequencies was not a concern.

Non-contact probes considered include the capacitance gages, fiber optic intensity probe, and chromatic confocal probes. The capacitance gages have a standoff and geometry or size that do not allow for the measurement of large slopes without operating probe normal. They can also drift over long periods of time and are sensitive to humidity. Capacitance gages do allow for a very precise measurement and are easy to use. The fiber optic intensity probe did not have the desired repeatability and needed a new calibration for each setup and material. The "spot" of the probe is rectangular, which left some question to how the probe was interacting with a part that has a local spherical shape of varying radius of curvature. The probe is robust, easy to set up, and has a relatively small size.

A disadvantage of optical probes is that interactions of the light used with a range of materials and manufacturing processes in freeform optics is not always well understood. Also, if these interactions between the optical probe and manufactured surface

change with position on the optic. The chromatic confocal was chosen for the reasons above however there were still some questions that needed to be investigated further or at least determined that the effect on the measurement result would be insignificant. Some of the questions investigated include: could the diamond turned surface be acting as a grating? If so, the direction of the grating is changing at different points on the surface. How does this effect a chromatic confocal probe? For a polished glass surface, the interaction seems straight forward but what about highly reflective metal surfaces. What is the effective spot size? Does it change with a change in slope? These questions are compared to a contact probe where the mechanical contact is well known unless the contact forces are small and/or the contact area is small. The chromatic confocal probe was discussed in Reference [10] as it pertains to freeform metrology.

Noise in the probes was determined by taking static measurements. The probes were set up measuring a target with a small structural loop between the probe and target. Displacement is read for a short period and the mean and standard deviation are calculated to quantify the noise in the probe and electronics.

After considering the optics measured in this research and the advantages and disadvantages listed above, a non-contact probe was chosen. The issues with the non-contact probes, specifically the chromatic confocal probe was investigated and corrected when possible.

4.2 Capacitance Gauges

The capacitance gages used are from the Lion Precision Spindle Error Analyzer (SEA). The system has five capacitance gages that were designed for use in a fixture for measuring spindle errors, as the name might suggest, and with the software included. The capacitance gages can also be used individually with the analog outputs from the capacitive driver.

Capacitance gages require the target material to be conductive material. Some ca-

pacitance gages also have small measurement ranges when compared to other probes. Due to the geometry of the probe and the standoff required the capacitance gages are not well suited for steep slopes. They can also be sensitive to changes in humidity. An in-situ calibration was also required for the uses in this research.

4.3 STIL OP300VM

The initial chromatic confocal probe used in this research was the STIL OP300VM. Like other chromatic confocal probes, the STIL is a non-contact point sensor. The operating principle is like the Precitec chromatic confocal discussed below. It was set up for triggering using the built-in function in the provided software and the spray mist command in the 100UMM controller.

The probe did not work well with highly reflective surfaces such as diamond turned mirrors. No matter how low the intensity was set, it would be saturated at the detector. A misalignment of the LED reduced the intensity so that the detector would not be saturated for highly reflective surfaces.

4.4 Philtec μDMS-RC25

The Philtec μDMS-RC25 is a USB powered fiber optic displacement sensor. The sensor is a reflective type transducer based on detecting the intensity of reflected light [5]. The maximum data sample rate is 16,000 samples per second. There is a pair of fiberoptic detectors in the sensor tip, light reflected off a target follows two separate paths to the electronics where a ratiometric calculation provides the distance measure which is independent of varying surface reflectance [5].

The fiber optic probe receives an analog input signal that is sent to a digital processor with calibration data that is stored on-board the sensor. The internal processor interpolates the calibration data table and converts the analog input into a linearized distance measure [5]. The sensor can be gapped for measurements anywhere within the sensor's total operation range.

It is recommended to use the probe within a certain range where the RC function is closest to linear. For this probe it is between 0.2 mm to 0.5 mm from the target surface. For maximum repeatability, the probe must be calibrated for every orientation or every time the fiber optic bundle is repositioned. The sensor can hold up to 25 calibration tables.

4.5 Precitec Chromatic Confocal Probe

To measure the freeform mirrors for this research, the Precitec chromatic confocal probe was selected. The probe was chosen considering the following attributes: non-contact, high angle of acceptance, range of materials that could be measured, repeatability, working distance and measurement range. The probe is connected to the sensor box by a multi-mode fiber optic cable. The sensor boxes used for this research were the Precitec CHRocodile SE and Precitec CHRocodile 2.

The chromatic confocal probe uses chromatic aberration in the lenses of the probe to focus the spectrum of light from the white light LED over the measuring range of the probe. For a given displacement a wavelength of the white light will be at focus, therefore it will return through the system where it is fed into a spectrometer contained in the sensor box. A pinhole acts as a filter so that the out of focus wavelengths are not returned to the spectrometer. The wavelength at focus will show a peak in the intensity. This is shown in Figure 4.2.

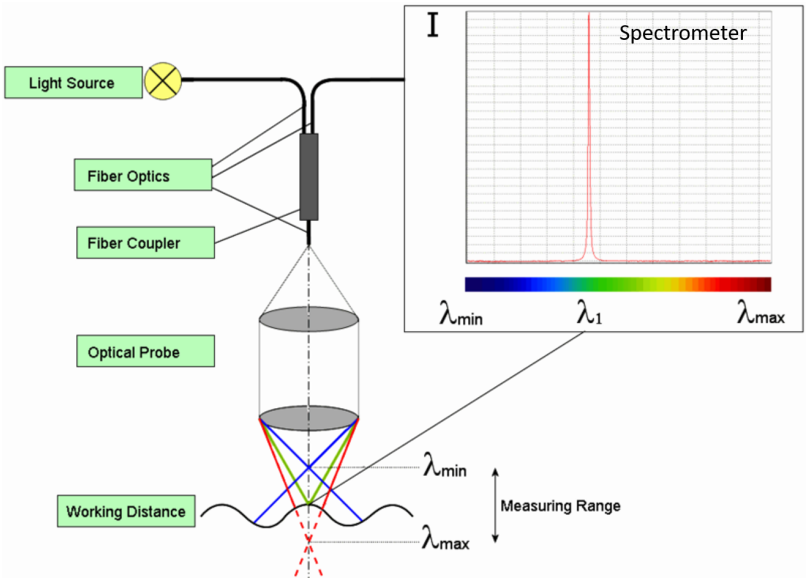

Figure 4.2: Chromatic confocal probe operating principles showing the output of the spectrometer and the components of the probe and sensor box [6].

The wavelength is then matched to a displacement determined by calibrating the probe. Chromatic confocal probes come in different sizes with a variety of specifications from several manufactures. Specifications of the Precitec chromatic confocal probe and sensor used for this research can be found in Table 4.1.

Table 4.1: Precitec chromatic confocal probe specifications.

Specification	Value
measuring range	300 μm
working distance	4.5 mm
axial resolution	3 nm
linearity	100 nm
lateral resolution	2.5 μm
numerical aperture	0.5 nm
angle of acceptance	+/- 30°
spot diameter	5 μm

A series of probe qualification tests were completed before using the probe. It was found that the amplification coefficient (i.e. linear fit to displacement calibration data at a fixed angle) varies. At low slopes ($<$ 10 degrees), the effect is relatively small (roughly 2 %). One approach is to use the probe in a nulling mode, using Z carriage motions to minimize the change in the probe position relative to the surface, but adding Z carriage errors. A slope correction can also be implemented by compensating the probe reading using a predetermined correction factor. For diamond turned surfaces an additional calibration and linearity correction was implemented when not using the probe in a nulling mode. After considering the application and different aspects of each probe it was decided to use a chromatic confocal probe from Precitec.

4.6 LabVIEW

The measurement data acquisition LabVIEW program was written using subVIs provided from Heidenhain and the NI-VISA driver. The Heidenhain interpolation box (EIB 741) is read into the computer over an ethernet cable. The Precitec sensor box is connected to the computer using a USB cable. The USB is read into LabVIEW using the VISA driver. The Heidenhain box is set to read the scale data using an internal trigger which was set to match the rate that the probe is sending data. The internal trigger is adjusted so that the buffer does not fill up on the EIB 741 since it operates on first in first out (FIFO). If the buffer has more than one set of position data, the data collected is going to be old. The rates are matched between the probe and scales however there is some variation in the rate for each of the sub systems that shows up in the data age uncertainty.

The sensor box has adjustments for the rate at which data is sent and how much averaging is done on the box. The rate is set to 4000 Hz with a varying amount of averaging depending on the measurements being taken. There are also settings for what is sent from the sensor box over the USB. The setting was set to only send displacement data. The parameters are sent to the sensor box during startup of the

LabVIEW program.

4.7 Data Age Uncertainty

Differing data age causes a temporal discrepancy between the probe displacement and scales position data. If there is a bias in the data age it can be corrected. If there is a variation in the data age (data age uncertainty) it must be accounted for in the measurement uncertainty budget. The data age uncertainty is a function of the feed rate, filtering, and computer timing. Several methods are being investigated to quantify and correct for the data age.

4.8 Probe Setting and Alignment

Probe setting artifacts that mount using a vacuum chuck are used on the 100UMM for aligning the probe to the machine carriage motion. Proper alignment reduces measurement uncertainty and allows for a broader range of parts to be measured. An example would be using the probe normal to the part surface, it is necessary to know how far the probing point is from the axis or rotation of the B carriage. Probe setting includes measuring and calculating this distance. The artifacts are made of different materials and sizes to allow a range of reflectances and slopes. The probe setting artifacts that attach by vacuum have a safety collar to make sure that if the vacuum fails the artifact does not fall into the probe and cause damage.

To center the chromatic confocal probe on the rotational axis of the C carriage, a 1-inch steel ball is used. Balls of varying material and size were also purchased for use on the 100UMM. First, the ball is centered on the rotational axis using a Mahr electronic indicator and adjustable stand. After mounting the ball, the indicator is moved into contact with the hemisphere of the ball. As the C carriage is rotated, when centered, the indicator will show a minimum change in displacement. Deviations in the displacement will be reduced to the carriage error and deviations from spherical in the ball over the path traced by the indicator. Figure 4.3 shows the ball centering

process with the electronic indicator and rubber handled screwdriver for tapping.

Figure 4.3: Centering the 1-inch steel ball using an electronic indicator and rubber handled screwdriver for centering the probe on the rotational axis of the C carriage.

To center the probe, the X carriage is moved back and forth moving the probe across the ball to 'crown' the ball in the x direction, looking for the carriage position that shows the smallest (minimum) probe displacement. Crowning the ball centers the probe on the center of the ball in the direction of the probing axis. Since the ball was centered on the axis of rotation of the C carriage, the probe is centered on axis of rotation of the C carriage. Due to the nature of a sphere, the change in displacement for a given amount of carriage motion decreases when close to the center of the ball as the slope of the ball is decreased. There is no adjustment on the machine for the Y direction, so the three degree of freedom probe mounting system is used to adjust for the Y direction height of the probe. The ball is crowned using the differential micrometer to center the probe on the ball in the Y direction, again, looking for

minimum probe displacement. This setup is shown in Figure 4.4.

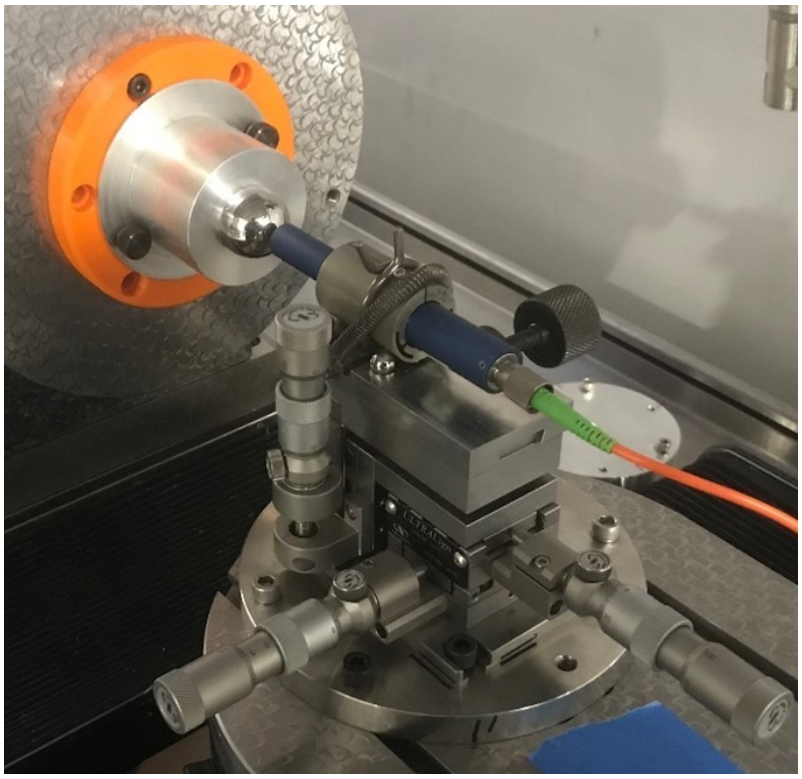

Figure 4.4: Probe setting to center the probe on the rotational axis of the C carriage using the 1-inch steel ball.

The probe is used perpendicular to the C carriage face or coaxial to the rotational axis of the C carriage. This is possible when measuring freeform optics due to the relatively large angle of acceptance of the chromatic confocal probe. A polished glass window that has a form of $\lambda/4$ is used to align the probe perpendicular to the face of the C carriage. The axis of rotation of the C carriage is nominally perpendicular to the motion of the X carriage. This relationship will be used to align the probe. The X carriage is moved back and forth, moving the probe over the window, and the window is rotated until the displacement of the probe is nominally steady. This happens when the tilt from mounting the window is vertical as shown on the right of Figure 27. Note that the window could be oriented 180° for the same effect. The B carriage is then rotated until a minimum probe displacement is found shown on the

left of Figure 4.5.

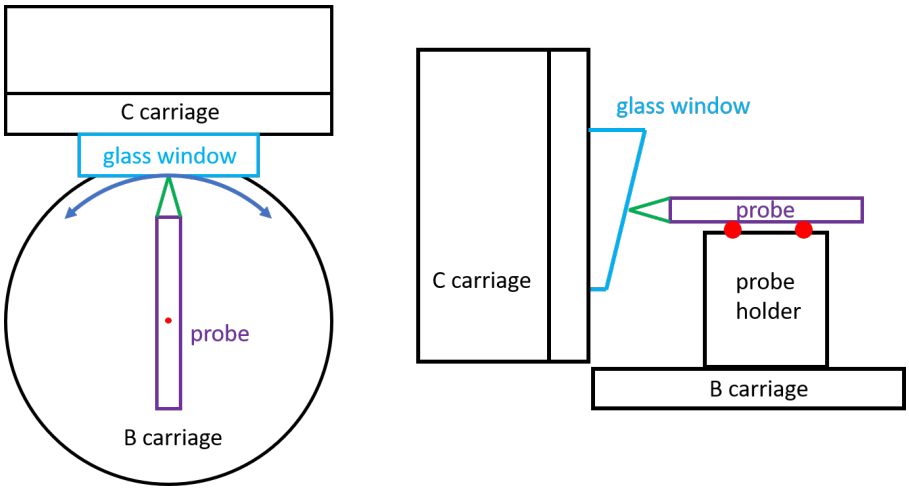

Figure 4.5: Aligning the probe perpendicular to the X carriage motion using a glass window by scanning in the X direction and rotating the B carriage. Left is a top view. Right is a side view.

The process described aligns the probe perpendicular to the X carriage motion and therefore with the face of the C carriage in the Z direction. Due the lack of motion about the X axis, the probe alignment in the Y direction is set by the probe holder and face of the B carriage. Figure 4.6 shows one of the glass windows used to align the probe to the X carriage motion.

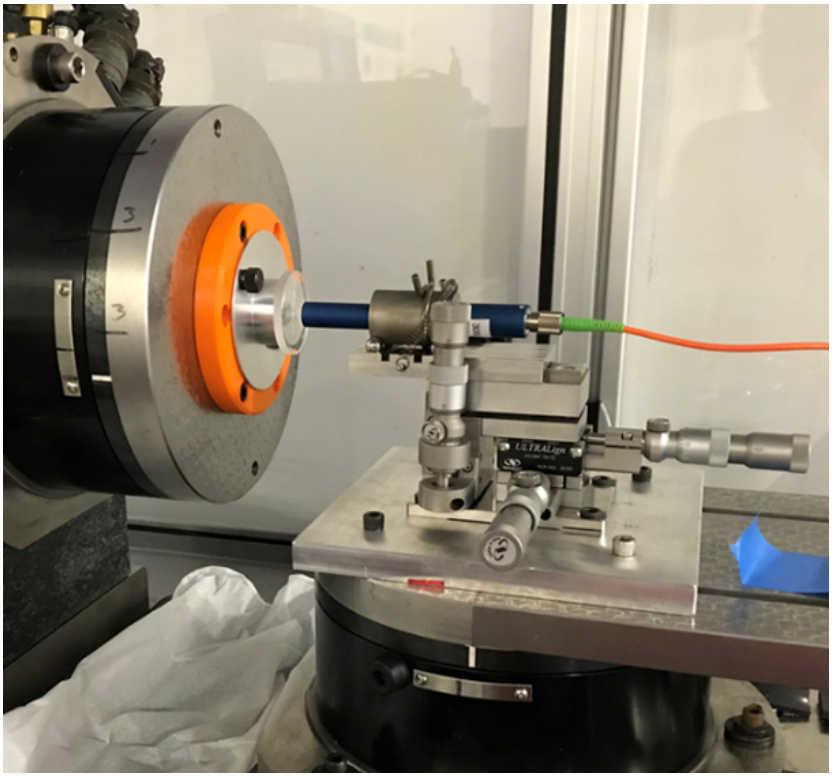

Figure 4.6: Probe setting using a glass window to align the probe perpendicular to the X carriage motion. (Photo credit: Laura Hopper)

Beyond the two alignments discussed it is necessary to know the distance from the functional point of the probe or probing point and the rotational axis of the B carriage. This will allow the machine to be used probe normal and is also entered into the mathematical model. To measure this distance a calibrated steel ball is used. The steel ball is centered on the rotational axis of the C carriage using the electronic indicator. Figure 4.7 shows the two positions to measure the distance.

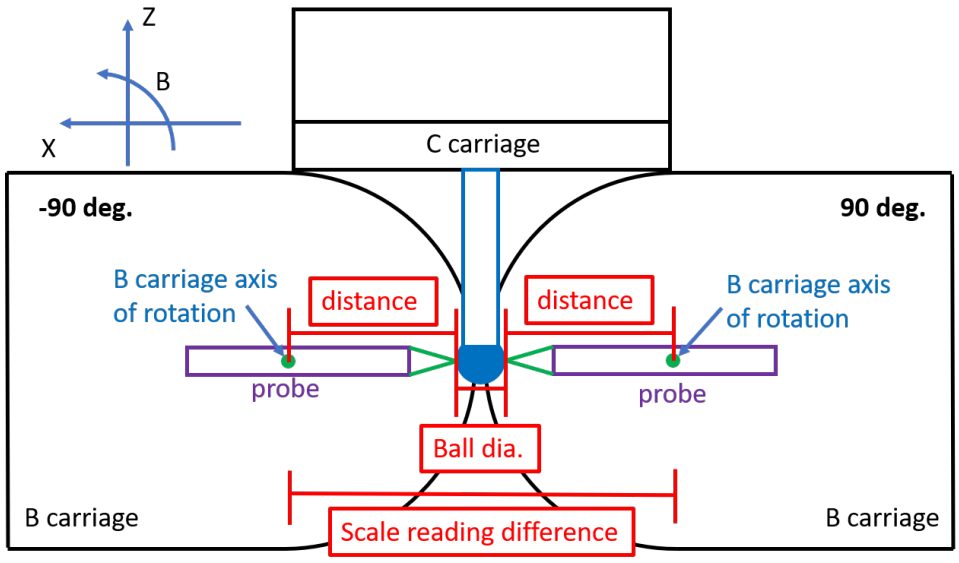

Figure 4.7: Measuring the distance between the rotational axis of the B carriage and the functional probing point using a ball.

The calculation is relatively simple once the scale readings are recorded. The calibrated diameter of the steel ball is subtracted from the difference in the scale readings at the two positions and divided by two. It may be clearer by looking at Figure 4.7.

$$distance = \frac{scale\ reading\ difference - ball\ dia.}{2} \tag{4.5}$$

If the center of the ball is located at the fiducial origin, or near enough, the X carriage position of the fiducial origin will between the 90° and -90° positions. This should align the rotational axis of the C carriage with the rotational axis of the B carriage in the X direction.

CHAPTER 5: MACHINE TOOL METROLOGY

The geometric machine errors were measured for error compensation and task specific uncertainty evaluation. The error motions most sensitive to the parts being measured on the machine were prioritized. Measuring the machine errors was done with the mathematical model in mind. To achieve the uncertainty necessary for this research, meticulous attention must be given to each detail in the measurement such as fixturing, probe setting, thermal stability, and alignments. Fixturing is important for thermal stability and repeatability as many techniques require a reversal which must be done without distorting the shape of the artifact or optics being used.

5.1 Coordinate systems

Error motions were measured based on the coordinate system in the mathematical model. For the linear error motion measurements to be valid for the model, the indicator or probe must be placed at the origin of the carriage being measured. This is not required for the angular error motions. The error motions represent the motion of the carriage coordinate system as the carriage is moved. While measuring the errors it was assumed that if a carriage was not being measured, it was rigidly attached to the supporting carriage or frame and had no effect on the measurement.

5.2 Fiducial Origin

The fiducial origin is defined by the mathematical model and represents the point at which the carriage and frame coordinate systems overlap. The definition of the fiducial origin is realized by finding the carriage positions that the rotational axis of the C and B carriages intersect as discussed above (Section 3.4). These carriage positions then become the positions at which the machine error measurements are

zeroed out, meaning that at the fiducial origin there is no machine error in the model. As the carriage positions move away from the fiducial origin the error motions become non-zero.

To align the rotational axes of the B and C carriages, precision ground shafts were placed in the holes in the center of the carriages. Machinist's squares were used to ensure that the shafts were perpendicular to the face of the carriages. This method was also used to align the capacitance gage in the horizontal straightness of the X carriage. The setup is shown in Figure 5.1.

Figure 5.1: Using precision ground shafts and machinist squares to align the rotational axes of the B and C carriages and to align the capacitance gage with the fiducial origin.

The X carriage was moved so that the shaft on the C carriage was just barely touching the square that was being located by the shaft in the B carriage. This aligns the B and C carriages in the X direction which is how the fiducial origin is defined in the mathematical model. A top view is shown in Figure 5.2.

Figure 5.2: Showing the top view of the alignment process for the rotational axes of the B and C carriages.

The distance in the Z direction from the face of the C carriage to the precision ground shaft in the B carriage gives an estimate of the fiducial origin position in the Z direction. This should be the same distance as the distance from the face of the B carriage to the precision ground shaft in the C carriage. See Figure 3.1 where the fiducial origin is defined.

It was assumed that these holes are aligned with the axis of rotation of the carriages. The precision ground shafts are a slip fit in the holes allowing little motion once inserted. The precision machinists' squares keep the precision ground shaft perpendicular to the face of the carriage. Error in the machinist's squares and the ability to align the shafts is an uncertainty contribution to the realization of the fiducial origin. There is an uncertainty contribution to the task specific uncertainty of part measured using the model and Monte Carlo simulation by how well the fiducial origin is located and how well the probes are aligned for the measurement of each of the machine errors. The other methods used to determine an estimate of the carriage positions that define the fiducial origin will be investigated and compared.

The machine carriage positions of the fiducial origin are shown in Table 5.1.

Table 5.1: Machine carriage positions of the fiducial origin for the mathematical model on the Nanotech 100UMM.

Carriage	Position
X	92.222 mm
Z	-185.158175 mm
C	0°
B	3.6°

5.3 Measuring and Identifying Critical Errors

The mathematical model of the 100UMM has 29 errors. It was not necessary to measure all the errors since the measurements being made were not sensitive to every error motion in the model. The errors critical to the freeform optic measurements were identified and measured. Given enough time and resources a full error map of the machine could be completed. Errors that had negligible effect due to the range of motion of the carriages or the shape of the optic were not measured. These errors were evaluated by using the prescription and mathematical model in MATLAB to find what a reasonable assumption of the error would be. Some errors like those of the B carriage were neglected due to that carriage not being used.

The AFRL optics are specified in the Z direction or along the optical axis. This meant that the probe did not need to be used normal to the surface, removing the need to use the B carriage. Some of the errors were "low hanging fruit" so they were measured while measuring critical errors like pitch in the Z carriage and roll in the X carriage. Several of the errors could be considered sine errors or 2nd order effects as they are a function of the slope of the surface. The maximum slope of the optics being measured is 10°. For example, a displacement error in the X carriage does not directly affect the measurement result in the Z direction. Positioning in the C carriage has even less affect since the part is mostly rotationally invariant with just

the freeform shape that is slowly varying over an azimuth.

5.4 Y Direction Sensitivity when Measuring on the Diameter

There are several errors that are either in the Y direction of the machine coordinate system or manifest in the measurement of the AFRL optics in the Y direction. The analysis of the Y direction sensitivity is assuming that the part is measured along the diameter or radius of the part with a probe on the Z axis of the B carriage coordinate system or the X-Z plane of the B carriage coordinate system. This includes the concentric circle probe path (Section 7.7) as the probe is on the diameter of the part as the C carriage is rotated. Remember, at the fiducial origin the rotational axis of the C carriage defines the Z axis, and the part and probe are centered on the rotational axis of the C carriage. The probe alignment in the Y direction falls into this analysis.

It was assumed that since the measurement is on the diameter the slopes in the Y direction are low. To be sure the prescription was used in MATLAB to determine the Y direction sensitivity. The largest slope is toward the outside diameter so the most error, as the actual measurement point deviates from the desired measurement point, will be toward the edge of the clear aperture. The prescription was used to calculate lines in the Y direction at several radial positions. Figure 5.3 shows the lines in red and the positions of the measurement point for a simulated error in the Y direction as green dots.

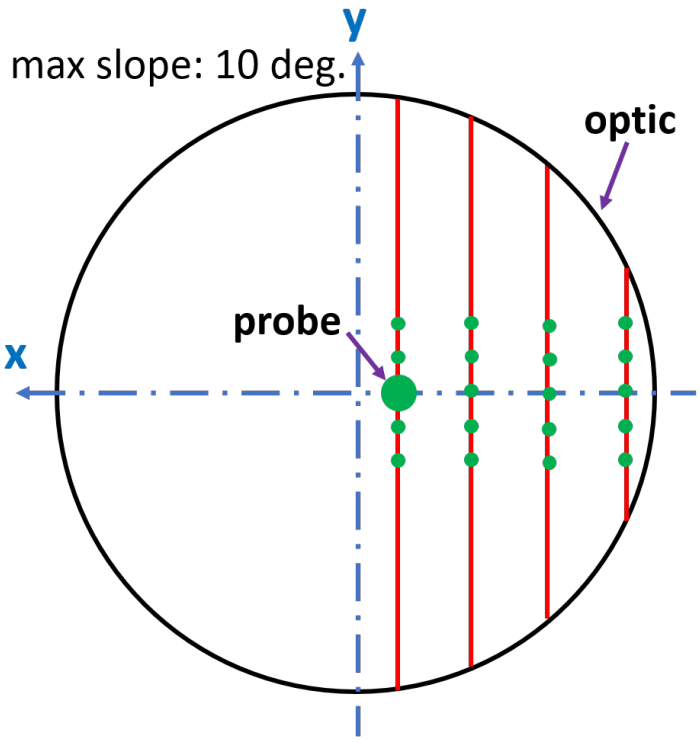

Figure 5.3: Y direction sensitivity simulation, for measuring the AFRL half scale tertiary optics, in MATLAB.

The spacing of points on the Y direction line (green dots) was 10 μm. The misalignment error in the Y direction was simulated by taking the difference of the Z height from the center line (x-axis) to a distance (error) in the Y direction. The line and the possible error are shown in Figure 5.4.

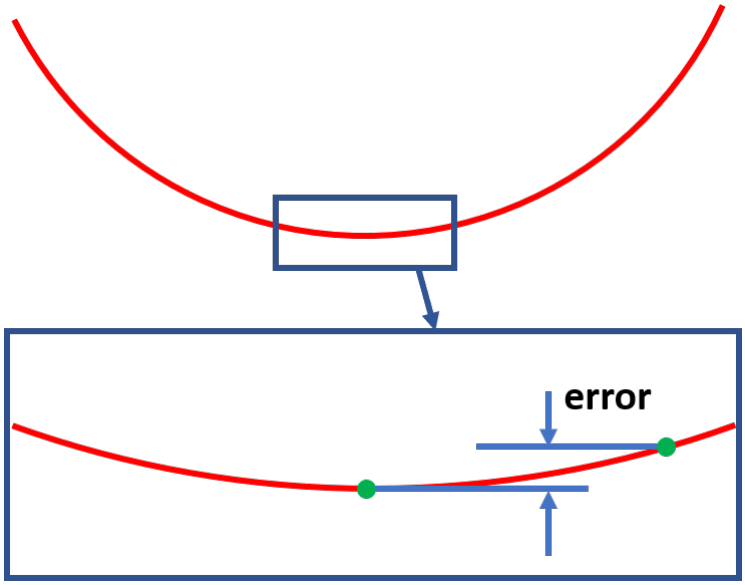

Figure 5.4: Z height error due to Y direction probe misalignment while measuring the AFRL half scale tertiary optics.

It was assumed that the worst case would be close to the OD of the part. The probe travels along the diameter of the part during measurements, so the probe position simulated is along the X axis shown in Figure 5.3. Although the error is expected to be largest at the OD, a point was chosen 1 mm inside the OD to allow enough distance in the Y direction for the simulated misalignment. Figure 5.5 shows the Z height error plotted against the simulated error in the Y direction for distances of 10 μm to 100 μm.

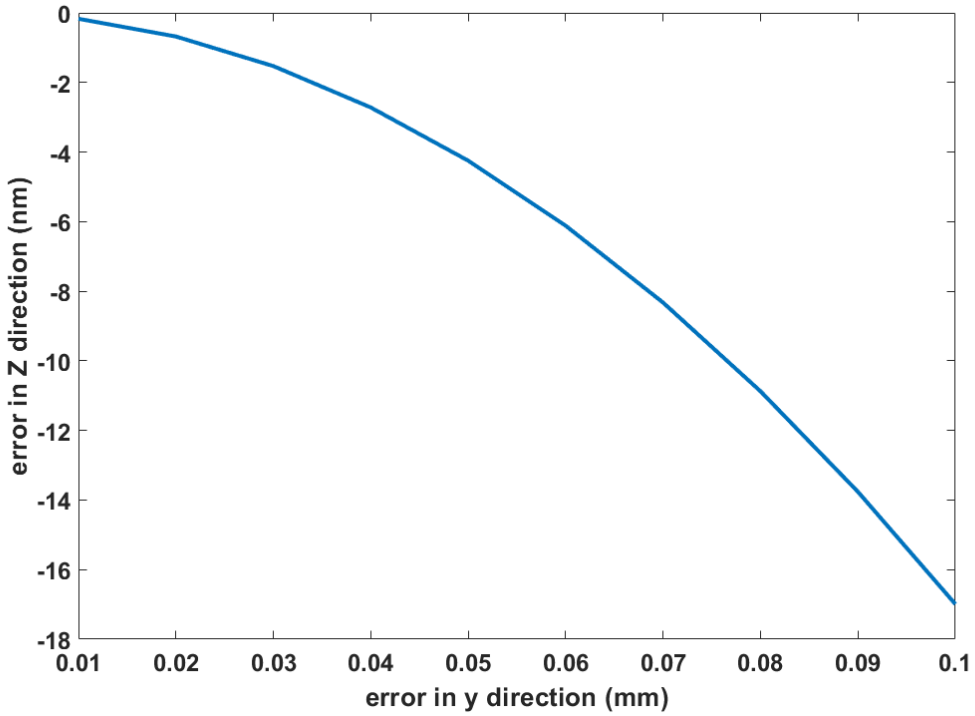

Figure 5.5: Simulated sensitivity of the Z height for an error that misaligns the probe in the Y direction while measuring the AFRL half scale tertiary optics.

As is expected, the slope of the error gets steeper the farther the probe is from the X axis. The error is under 2 nm for an error of 30 μm or less. The error contribution can be managed if the sum of all the error contributions to the misalignment of the probe in the Y direction is less than 30 μm. Roll error in the X carriage also has a small component in the Y direction.

5.5 Roll in the X Carriage

An estimation of how the roll in the X carriage influences the X carriage straightness and deviation in Y direction was calculated. It was hypothesized that the roll in the X carriage would make up a large part of the X carriage horizontal straightness and to a small extent the X carriage vertical straightness. The component of the roll that effects the Y direction or the X carriage vertical straightness is small due to the probe location in relation to the fiducial origin.

The roll in the X carriage is considered in the mathematical model as well but the distance of the probe from the fiducial origin in the Y direction makes the error contribution small. In the model the roll is considered from the fiducial origin not the point at which the roll is physically about.

The effect of roll in the X carriage on the X carriage straightness was estimated using the max roll in the machine error measurements and the estimated distance between the center of rotation for the carriage and the probe in the Y and Z directions. Figure 5.6 shows a diagram of the X and B carriage with the probe holder and the distances used in the estimation.

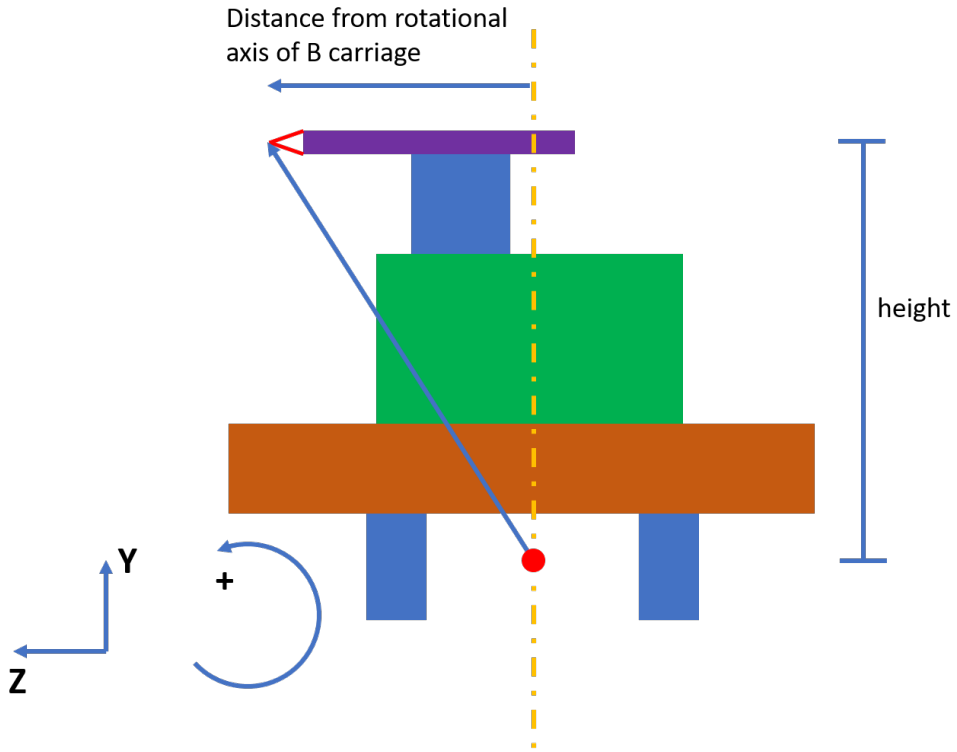

Figure 5.6: X carriage roll and how it effects the X carriage straightness and probe location in the Y direction.

The effect that the X carriage roll would have on the Z position and Y position of the probe displacement and the X carriage straightness error is estimated in Figure 5.7.

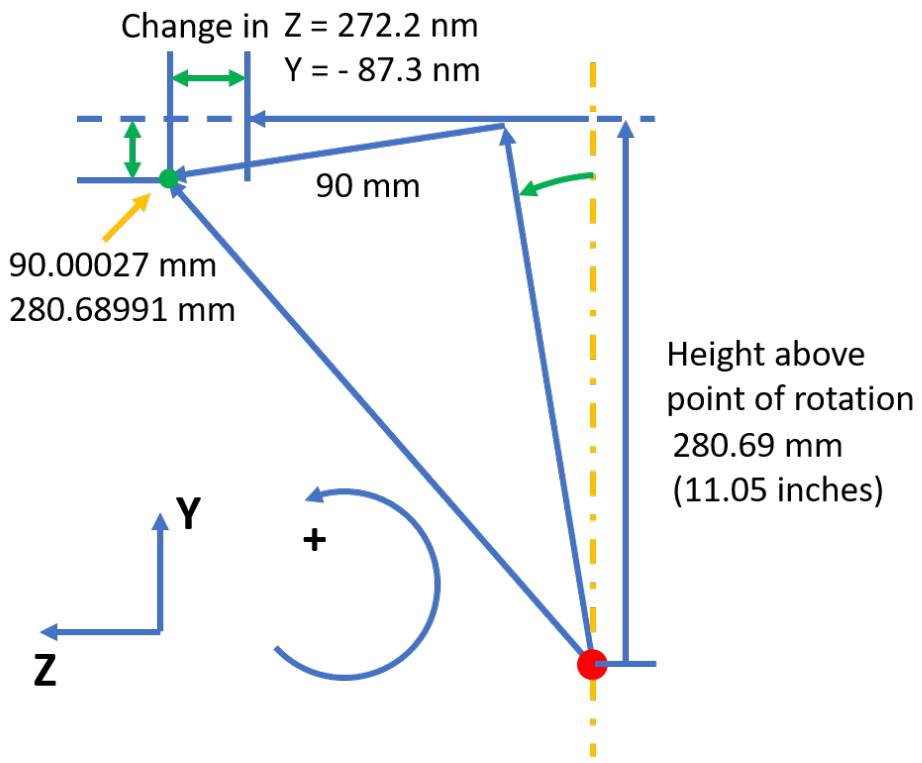

Figure 5.7: Estimating the effect of the X carriage roll on the probe displacement and the X carriage straightness error on the Nanotech 100UMM.

It is assumed that much of the X carriage horizontal straightness error is due to the X carriage roll. The change in the Z and Y direction are shown in equation 5.1.

$$\begin{bmatrix} Z' \\ Y' \end{bmatrix} = \begin{bmatrix} cos(0.2\ sec) & sin(0.2\ sec) \\ -sin(0.2\ sec) & cos(0.2\ sec) \end{bmatrix} \begin{bmatrix} 90\ mm \\ 280.69\ mm \end{bmatrix} = \begin{bmatrix} 90.00027\ mm \\ 280.68991\ mm \end{bmatrix} \quad (5.1)$$

The difference between the rotated position and original position was found to be:

$\Delta Y = -87.3nm$

$\Delta Z = 272.2nm$

The Y direction would be included in the X carriage vertical straightness and the Z direction would be included in the X carriage horizontal straightness. The amount of error estimated by the X carriage roll is less than the amount of X carriage horizontal straightness. Yaw in X and Z carriages also make up a small error contribution.

5.6 Summary

The primary carriages used in this research are the X and C carriages with relatively small movements in the Z carriage. The B carriage was not used so the six error motions for that carriage were not considered. The errors that were measured are listed in Table 5.2 with the same naming convention is used as above.

Table 5.2: Summary of the error motions that were measured and not measured on the Nanotech 100UMM. Error notation based on References [1], [2] and [3].

Description	Measured Errors	Not Measured Errors
linear displacement error in linear carriage	$\delta_x(X), \delta_z(Z)$	
angular positioning error in rotary carriage		$\varepsilon_b(\beta), \varepsilon_c(\theta)$
straightness	$\delta_z(X)$, $\delta_z(\theta)$	$\delta_y(X)$, $\delta_x(Z)$, $\delta_y(Z)$, $\delta_x(\beta)$, $\delta_y(\beta)$, $\delta_z(\beta)$, $\delta_x(\theta)$, $\delta_y(\theta)$
angular error - roll	$\varepsilon_x(X), \varepsilon_z(Z)$	
angular error - pitch	$\varepsilon_z(X), \varepsilon_x(Z)$	
angular error - yaw	$\varepsilon_y(X), \varepsilon_y(Z)$	
angular error - tilt	$\varepsilon_y(\theta)$	$\varepsilon_x(\beta), \varepsilon_x(\theta)$, $\varepsilon_y(\beta)$
squareness (in parenthesis not considered)	$\alpha_{x.z}$	$\alpha_{x.y}$, $\alpha_{z.x}$, $\alpha_{z.y}$, $\alpha_{y.z}$ ($\alpha_{y.x}$, $\alpha_{z.x}$, $\alpha_{z.y}$)

5.7 Compensating for Bias Measured in Machine Tool Metrology

According to the GUM, the bias in a measurement is removed before the uncertainty is evaluated. An excerpt from the GUM is provided to capture the language used in the document [12].

"Systematic error, like random error, cannot be eliminated but it too can

> often be reduced. If a systematic error arises from a recognized effect of an influence quantity on a measurement result, hereafter termed a systematic effect, the effect can be quantified and, if it is significant in size relative to the required accuracy of the measurement, a correction ... or correction factor ... can be applied to compensate for the effect. It is assumed that, after correction, the expectation or expected value of the error arising from a systematic effect is zero."

5.8 Angular Error Measurements

Electronic levels were used for the roll and pitch measurements and the angular interferometer for the yaw measurements. The levels cannot be used for yaw measurements because they rely on gravity to work so they must be placed vertically. Tilt around the Y axis of the C carriage was measured using Estler's face motion reversal.

5.9 Reversal

There is a collection of metrology techniques which use reversal to separate the error of an artifact from those of the machine or instrument being measured [15]. Reversal can be a powerful tool for self-calibration and error separation. In machine tool metrology it usually requires flipping the artifact and reversing the direction of the probe.

5.10 Estler's Face Motion Reversal

Estler's face motion reversal was used to measure the C carriage face motions of the 100UMM machine. The axial error motion of the carriage labeled $\delta_z(\theta)$ in the mathematical model, is measured directly. The tilt error in the carriage about the Y axis, $\varepsilon_y(\theta)$, and the shape of the artifact are also measured. The three positions of the optical flat artifact and probe used in the measurement are shown in Figure 5.8.

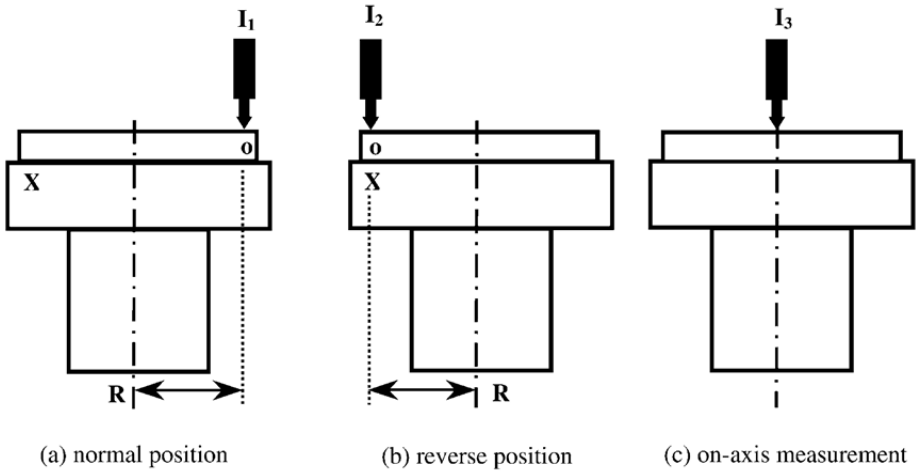

Figure 5.8: Estler's face motion reversal using a single indicator showing the three positions of the probe and optical flat [7].

A ball was used for measuring I_3 for ease of centering and crowning to get the center of rotation of the C carriage. The glass flat shown in Figure 5.9 was used as the artifact in the face motion reversal.

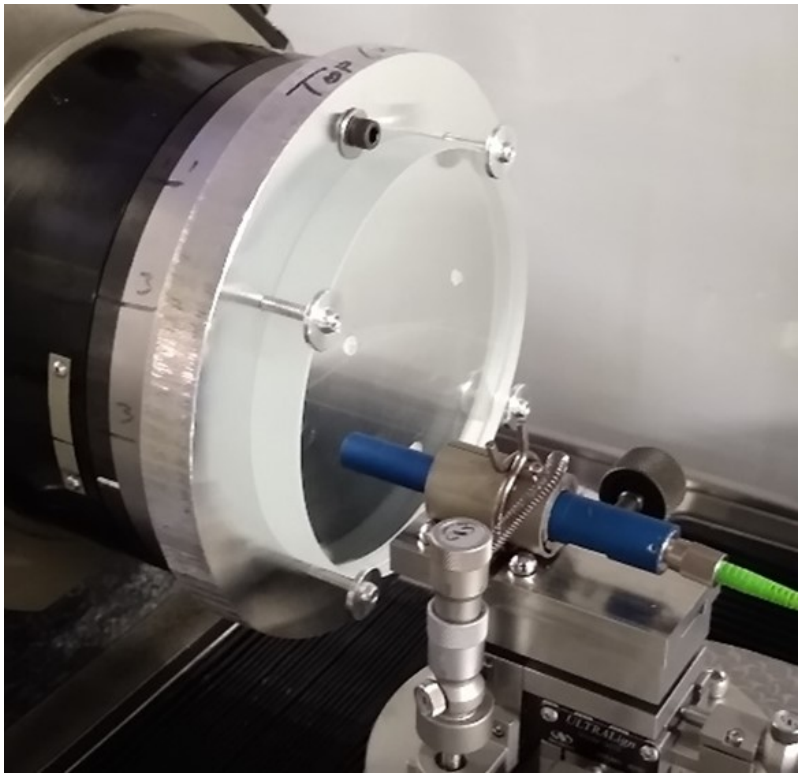

Figure 5.9: Estler face motion reversal using the Precitec chromatic confocal probe and 6-inch glass window.

The optical flat was attached to the aluminum fixture using 5-min epoxy with small washers as spacers to reduce the influence of any instability in the epoxy. An annealed borosilicate glass window was used as the artifact with a 6-inch diameter and thickness of 3/4 inch. Large diameter head screws were used as a safety against epoxy failure. If the epoxy fails, the safety will keep the glass window from damaging the probe. The first design used wax to hold the window with the same size and location as the epoxy. The wax ultimately failed during centering of the part after reversal.

To solve for the residual face motion the fundamental is removed from the measurements, removing the once-per-revolution mounting and fundamental error motion terms, denoted in the equations with a prime [15], [40]. The equations from [15] and [40] are shown in equation 5.2 and equation 5.3.

$$I_1^{'}(\theta) = P(R,\theta) - R * T(R,\theta) + A(\theta) \tag{5.2}$$

$$I_2^{'}(\theta) = P(R,\theta) + R * T(R,\theta) + A(\theta) \tag{5.3}$$

Where P is the part shape, T is the tilt error motion, A is axial error motion equal to I_3, θ is the carriage position and R is the radial distance of the measurement for I_1 and I_2. Solving for the part shape.

$$P(R,\theta) = \frac{1}{2}(I_1^{'}(\theta) + I_2^{'}(\theta)) - I_3^{'}(\theta) \tag{5.4}$$

To calculate the tilt error of the carriage the radius is used with the probe displacements [15].

$$T(R,\theta) = \frac{1}{R}\left(\frac{I_2^{'}(\theta) - I_1^{'}(\theta)}{2} - I_3^{'}(\theta)\right) \tag{5.5}$$

By looking at equation 5.5, the measurement result is the difference between the two measurements on either side of the carriage over the distance between the measurements subtracting the axial error motion of the carriage over the radial distance. The measurement gives the tilt in the C carriage about the Y axis. For this research

we are not interested in the shape of the artifact. The residual face motion will be used in the error compensation and the uncertainty in the face motion measurement will be used in the Monte Carlo simulation for the task specific uncertainty. The displacement error used to calculate the angular error is shown in Figure 5.10.

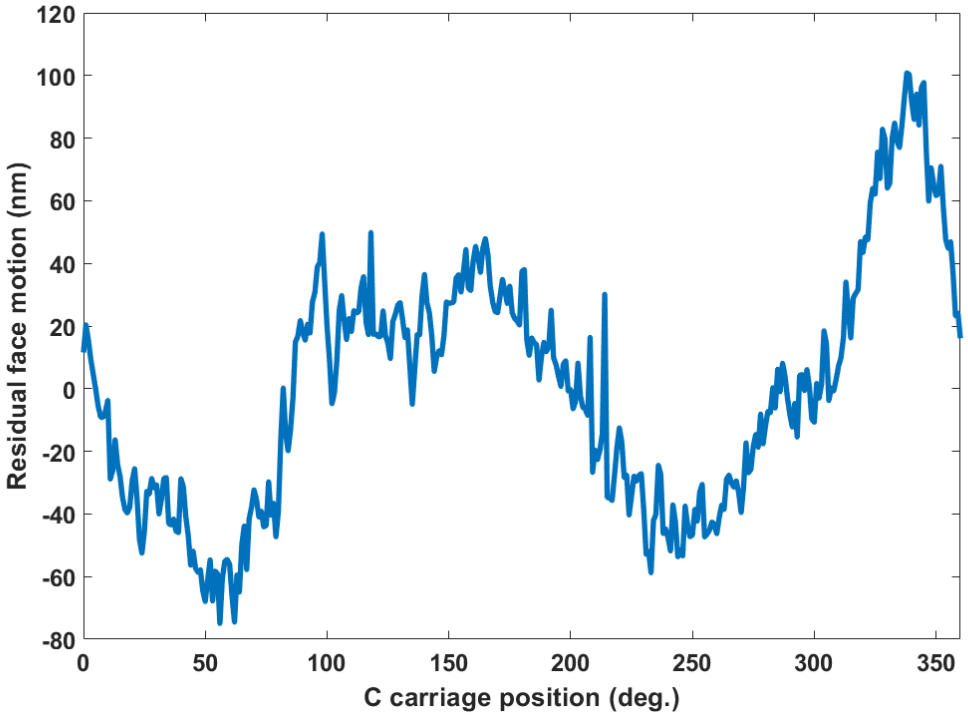

Figure 5.10: Residual face motion from Estler's face motion reversal on the C carriage of the Nanotech 100UMM.

The tilt error motion of the C carriage is shown in Figure 5.11 calculated from equation 5.5.

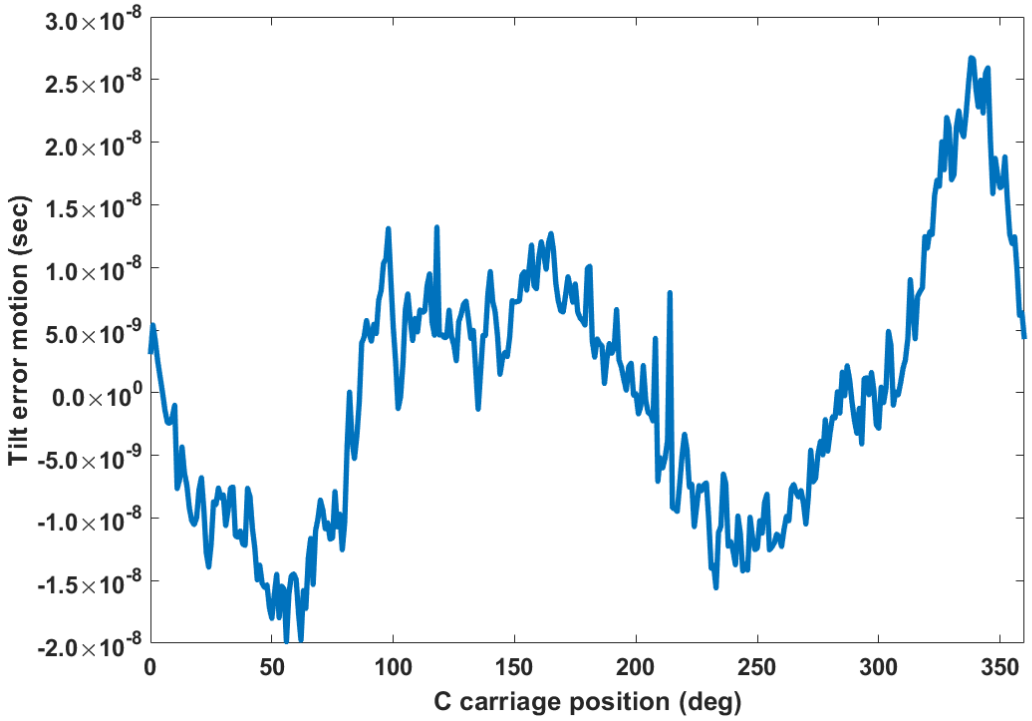

Figure 5.11: Estler's face motion reversal to determine the tilt error motion in the C carriage on the Nanotech 100UMM.

The measurement of the axial error motion of the C carriage was completed as part of the Estler's face motion reversal. The axial error motion directly affects the measurement result as it is in the direction of the probe displacement. The axial error motion is also subtracted in calculating the tilt error in the carriage. The results are shown in Figure 5.12.

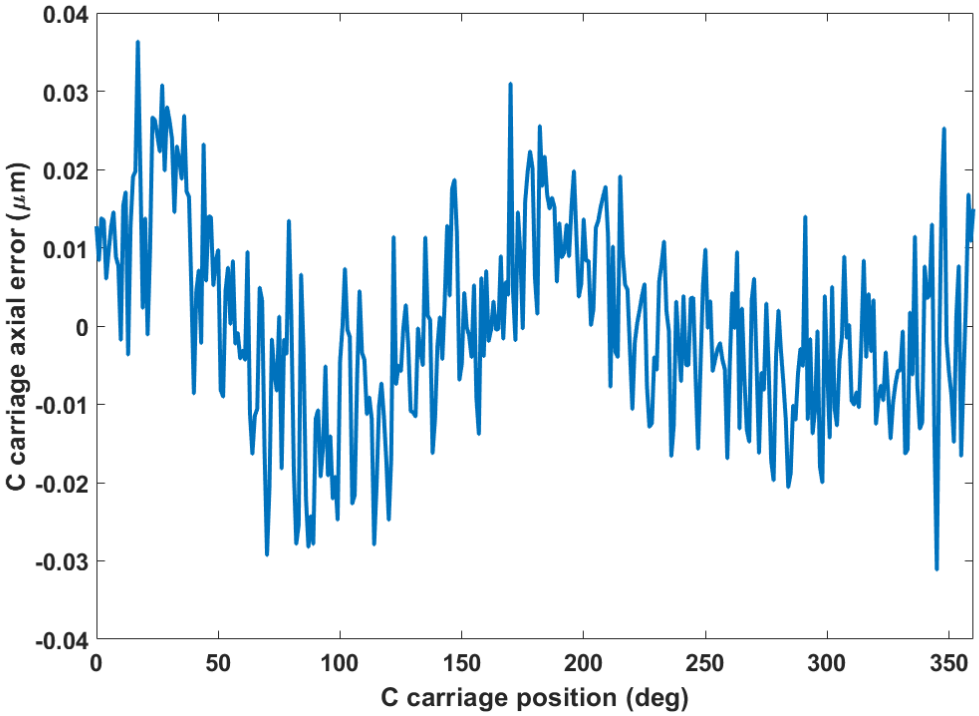

Figure 5.12: Estler's face motion reversal center measurement of the C carriage on the Nanotech 100UMM for axial error motion with fundamental removed.

Synchronous and asynchronous errors shown in Figure 5.10 and 5.12. For error compensation the synchronous errors are considered. Asynchronous is the data that does not repeat while the synchronous is the repeating data found by averaging over many revolutions for a given position of the rotary carriage.

5.11 Electronic Levels

The electronic levels use a pendulum on blade flexures to measure a change in angle. The manual explains the operation as "tilting the head causes a change in the position of the pendulum's shading loop in relation to the center leg of the core. This produces an electrical imbalance in the amount of flux passing through the two secondary coils, delivering a signal proportional to the displacement of the pendulum [8]." When using two levels the difference is used to determine a change in angle between the two levels. One of the levels is placed on a stationary part of the machine while the other is placed

on the carriage being measured. Since the machine is on vibration isolation air bags, a single level would not be suitable. As the machine carriages move, the tilt of the granite slab and the machine suspended by the pneumatic vibration isolators changes. A diagram of the functional parts of an electronic level is shown in Figure 5.13.

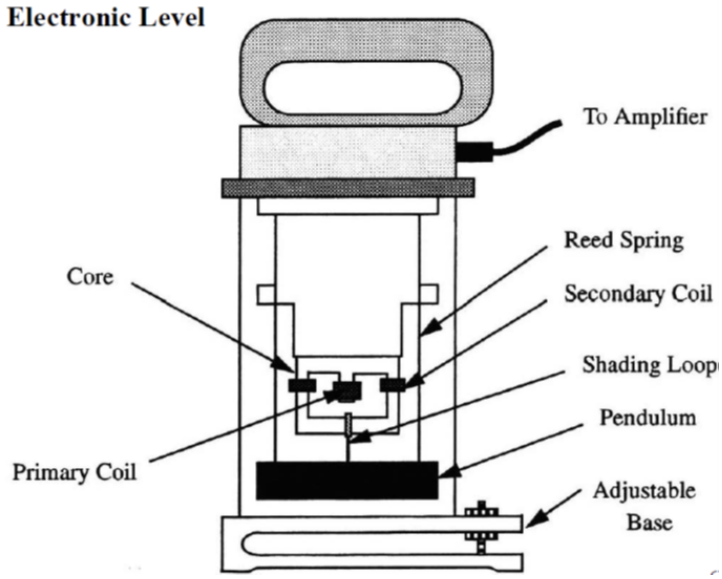

Figure 5.13: Electronic Level Diagram showing the components of the levels [8].

Due to the levels operating with gravity, only the roll and pitch of the linear carriages was measured with the levels. Measurements were made before and after the environmentally controlled enclosure was installed for comparison.

5.12 Measurement Setup

The electronic levels were used to measure the pitch and roll angular errors of the X and Z carriages. A NI myRIO was used for data acquisition using the analog out of the amplifier or signal analyzer for the electronic levels. The carriage being measured is moved while the other carriage is held still representing the frame which in this case is the reference. The scales are zeroed before each measurement and any bias is taken out of the data by subtracting the value at the beginning (or fiducial origin) of the measurement from each measurement. The data is averaged and subtracted from the interpolated value at the fiducial origin for use in the mathematical model.

The X carriage was moved between machine positions X_M equals 0 mm to 190 mm while the Z carriage was moved between machine positions Z_M equals 0 mm and -190 mm. The forward direction for the measurements of the X carriage is taken from machine position X_M equals 0 mm to 190 mm while the reverse measurements are taken from machine position X_M equals 190 mm to 0 mm. The forward direction for the measurements of the Z carriage is taken from machine position Z_M equals 0 mm to -190 mm while the reverse measurements are taken from machine position Z_M equals -190 mm to 0 mm. Measurements were taken every 5 mm over the 190 mm travel of each carriage. For each position, six measurements were taken in one second intervals after a settle out time since the levels use a pendulum. The measurements were averaged for each position and that value was taken as the measurement for that position in each set of measurements. Five sets of measurements for the forward and reverse direction were averaged to get the final values shown in the figures below.

The front of the signal analyzer can be seen in Figure 5.14. The range is adjustable using the knob shown. For the measurements, each scale was zeroed separately then the difference was zeroed. The range used was the smallest from -10 arc sec to 10 arc sec. The knob with A, B, and 'BOTH' selections is used to select between the levels or to subtract one from the other.

Figure 5.14: The front of the signal analyzer for the electronic levels.

The signal analyzer takes the signals from the levels and subtracts one from the other. The sign of the signal is changed using the switches on the back of the signal analyzer. It is highly recommended to check the levels are in the correct orientation and have the appropriate sign before each measurement to avoid any confusion. To test the direction put light pressure on the level and the dial should go positive or negative and match the coordinate system of the carriage being measured. The switches can be seen in Figure 5.15.

Figure 5.15: Switching the sign of the signal from the electronic levels using the switches on the back of the signal analyzer.

The output signal from the signal analyzer is +/- 10 Volt. This signal is wired to the analog input of the myRIO which runs a LabVIEW program recording the data. The LabVIEW program saves the data to a spreadsheet in the CSV format which can later be processed in Excel or MATLAB.

The levels were glued to the support underneath them using 5 min. epoxy for the measurements. The cables were also taped to ensure that they would not affect the measurement. The setup for a single level can be seen in Figure 5.16.

Figure 5.16: Attaching the electronic level using 5 min. epoxy and tape to secure the wire.

Notice that there is a fine adjust knob with a locking nut for zeroing the electronic level. The level sits on feet that cannot be seen in the figures as the five-minute epoxy is placed at the feet. The epoxy should not be between the feet and the support but on the side as shown.

5.13 Measuring Roll in the Z Carriage

The roll in the Z carriage is the error term $\varepsilon_z(Z)$ in the mathematical model. The roll in Z was measured by using the setup shown in Figure 5.17. For this measurement, the X carriage is not moved, and the Z carriage was moved between Z_M equals 0 to Z_M equals -190 depending on the direction.

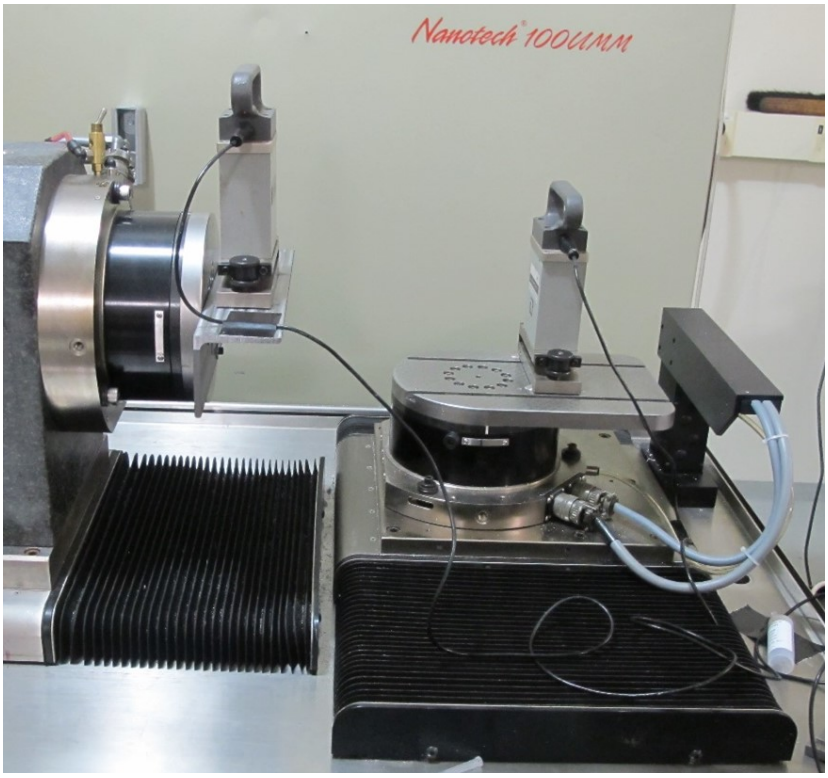

Figure 5.17: Electronic levels setup for measuring roll in the Z carriage and pitch in the X carriage before the environmentally controlled enclosure was installed.

The measured roll in the Z carriage is shown in Figure 5.18. This data was not used for the error compensation and Monte Carlo simulation but for a comparison between the error measurements before and after the enclosure was installed.

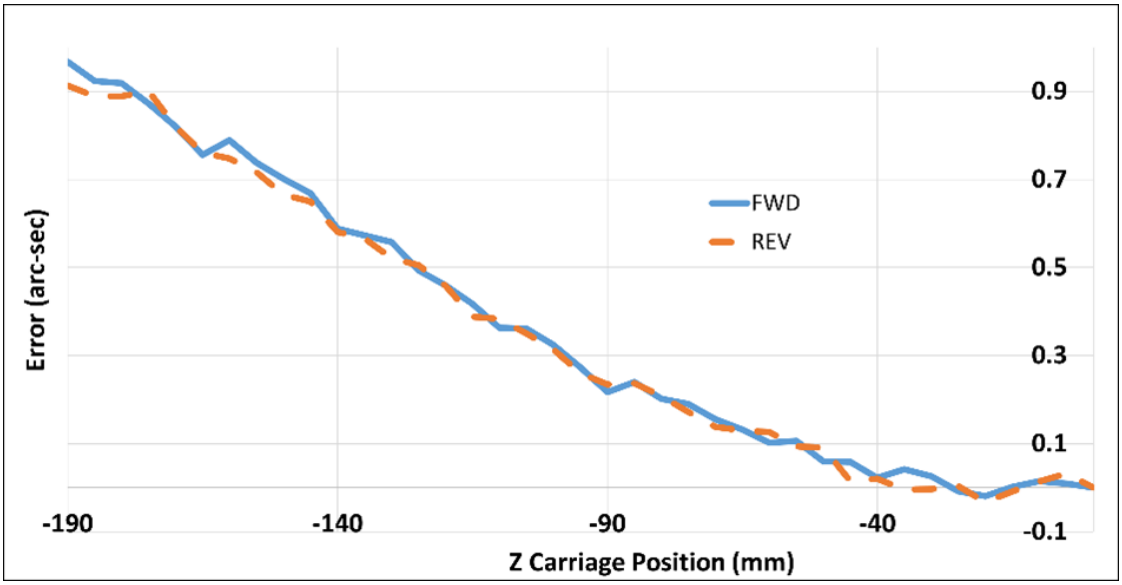

Figure 5.18: Z carriage roll in the forward direction (Z position of 0 to Z position of -190). Z carriage roll in the reverse direction (Z position of -190 to Z position of 0).

The maximum roll in the Z carriage was found to be 0.97 arc sec. This can be seen graphically in Figure 5.18. The maximum error in the Z carriage roll for the reverse direction was found to be 0.91 arc sec.

5.14 Measuring Pitch in the X Carriage

In the model, the pitch in the X carriage is represented by the error term $\varepsilon_z(X)$.The pitch in the X carriage was measured to be -3.96 arc sec. The X carriage pitch can be seen in Figure 5.19.

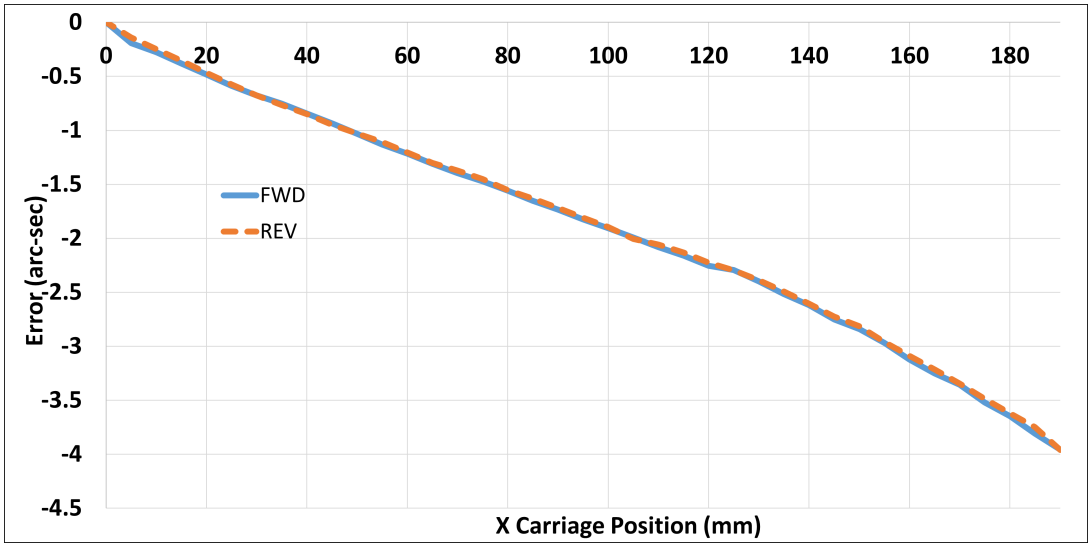

Figure 5.19: X carriage pitch in the forward direction (X position of 0 to X position of 190). X carriage pitch in the reverse direction (X position of 190 to X position of 0).

The maximum X carriage pitch for the reverse direction was measured to be -3.96 arc sec. The amount of X carriage pitch was considerably larger for the measurement before the enclosure was installed. The data from after the enclosure was installed looks a lot like the before data if a line is removed. The data before the enclosure was installed with a line removed is shown in Figure 5.20.

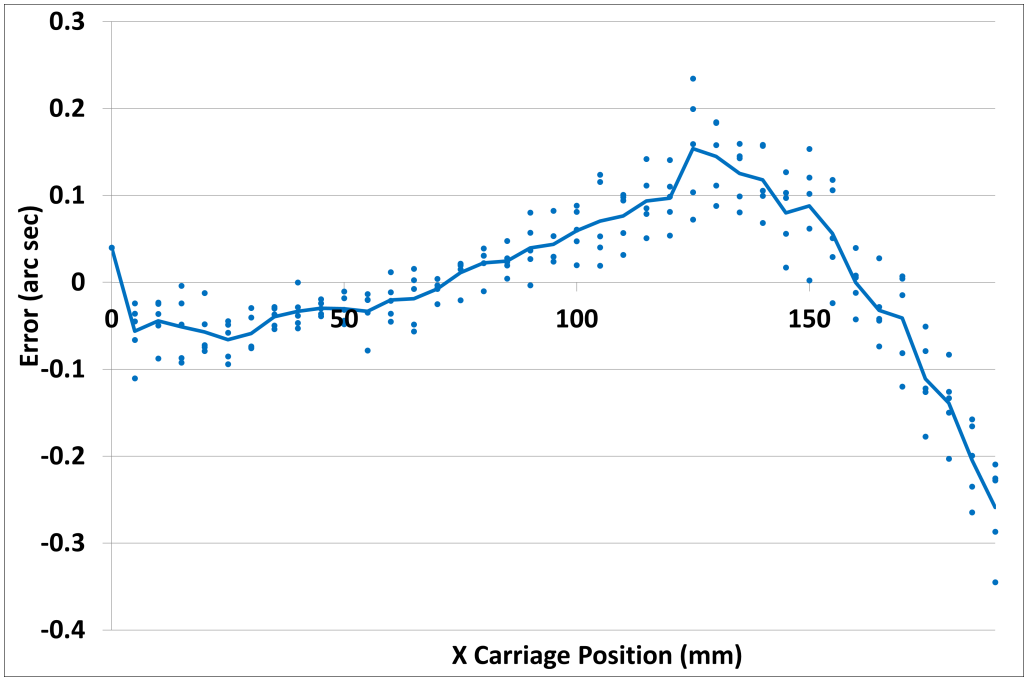

Figure 5.20: X carriage pitch with a line removed before the environmentally controlled enclosure was installed.

This discrepancy could be due to the heating of the ways as the carriage moves from one end to the other. The end that the ways that the carriage was positioned before the measurement starts will be near the temperature of the hydraulic oil exiting the bearing. Once the carriage starts moving to the other end the hydraulic oil exiting the bearing with start heating the ways.

5.15 Measuring Roll in the X Carriage

The roll in the X carriage is the error term $\varepsilon_x(X)$ as defined above. Roll in the X carriage was measured using the electronic levels. The setup can be seen in Figure 5.21.

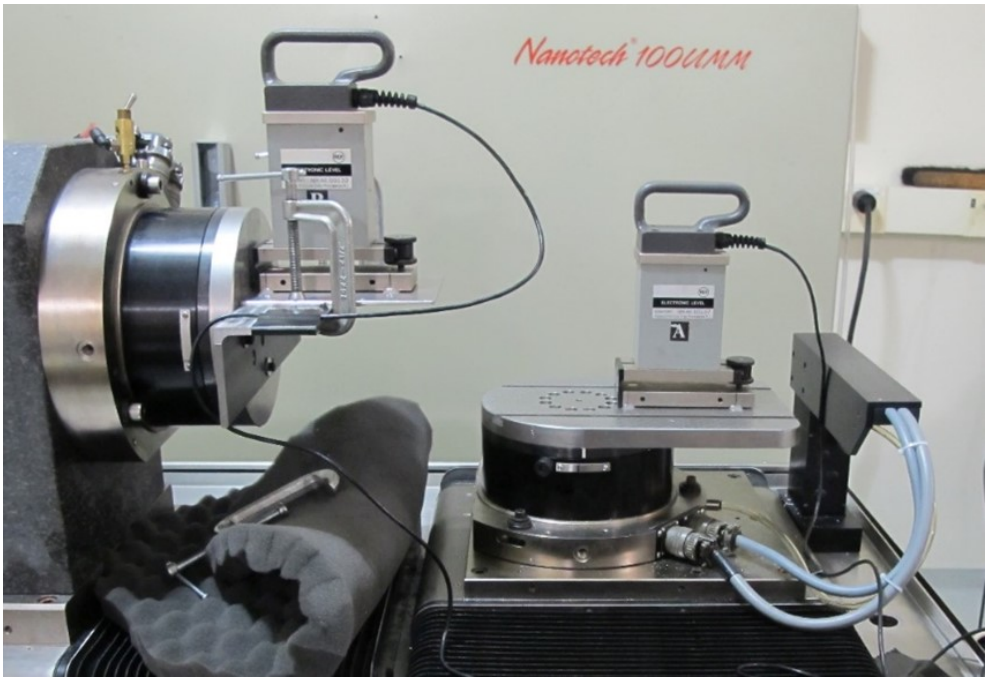

Figure 5.21: Electronic levels setup for measuring roll in the X carriage and pitch in the Z carriage before the environmentally controlled enclosure was installed.

The maximum roll in the X carriage is measured to be 0.41 arc sec. This can be seen graphically in Figure 5.22. The data was shifted to zero before being averaged so all the sets of data are normalized.

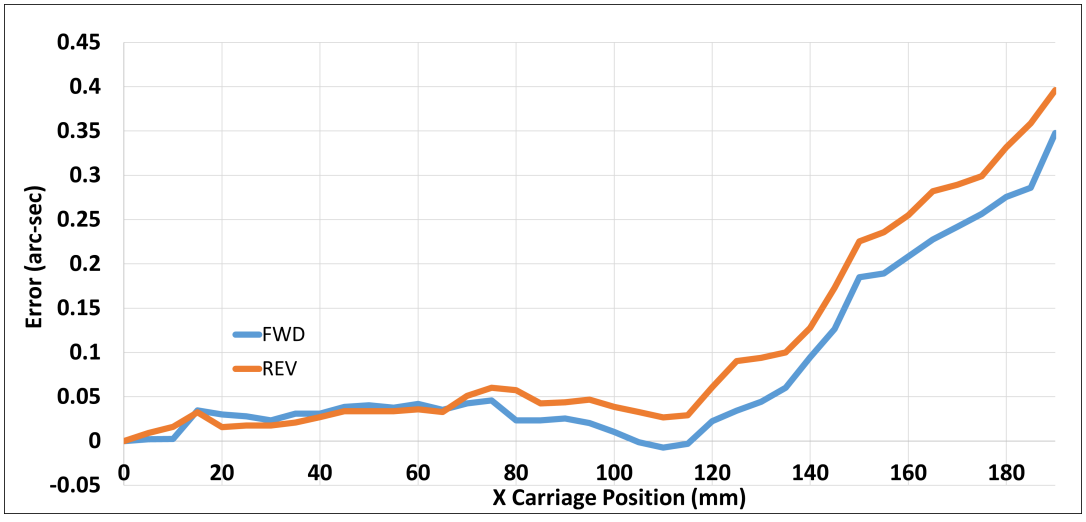

Figure 5.22: X carriage roll in the forward direction (X position of 0 to X position of 190). X carriage roll in the reverse direction (X position of 190 to X position of 0).

The maximum roll in the X carriage for the reverse direction was found to be 0.40

arc sec. When comparing the two lines for the forward and reverse roll in the X carriage roll, we can see that they follow the same trend with some variations.

5.16 Measuring Pitch in the Z Carriage

Pitch in the Z carriage is represented by the error term $\varepsilon_x(Z)$, in the model. The maximum pitch in the Z carriage was measured to be -5.70 arc sec. This can be seen graphically in Figure 5.23.

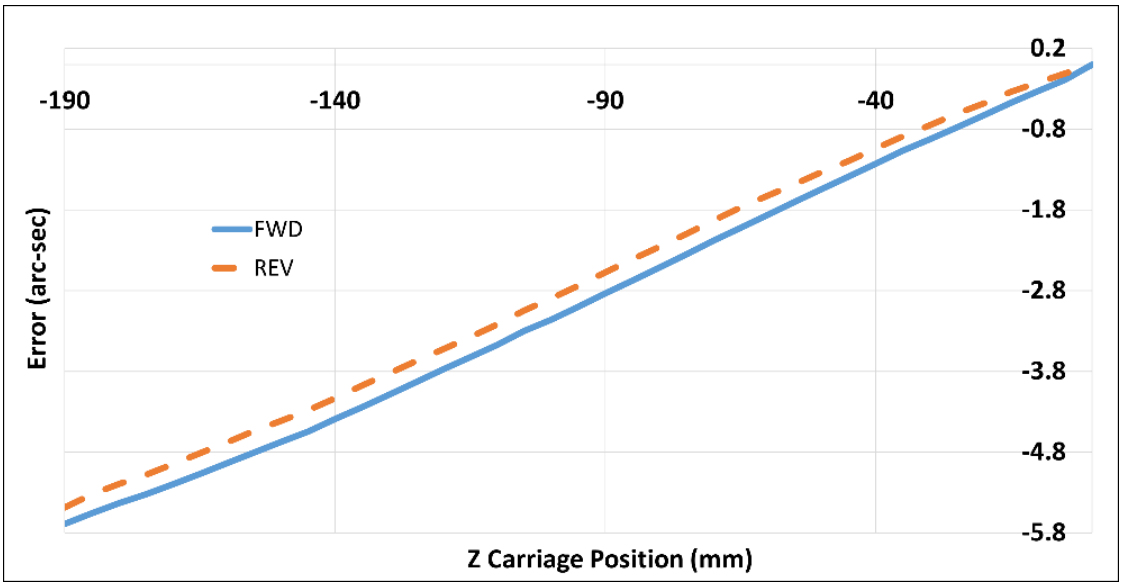

Figure 5.23: Z carriage pitch in the forward direction (Z position of 0 to Z position of -190). Z carriage pitch in the reverse direction (Z position of -190 to Z position of 0).

The Z carriage pitch was measured to be -5.49 arc sec in the reverse direction. As with the other differential levels measurements of the Z carriage the amplitude is considerably larger than the measurements after the enclosure was installed.

5.17 Electronic Levels Data after the Enclosure

Using the same Federal differential levels as above the measurements were retaken after the temperature-controlled enclosure was installed and optimized. Including the temperature control of the hydraulic oil for the hydrostatic bearings. The DAQ was changed and the machine was used to trigger the measurements. The DAQ used was the NI USB-6001 14-Bit 20 kS/s Multifunction I/O. The setup to measure roll in the

Z carriage and pitch in the X carriage is shown in Figure 5.24.

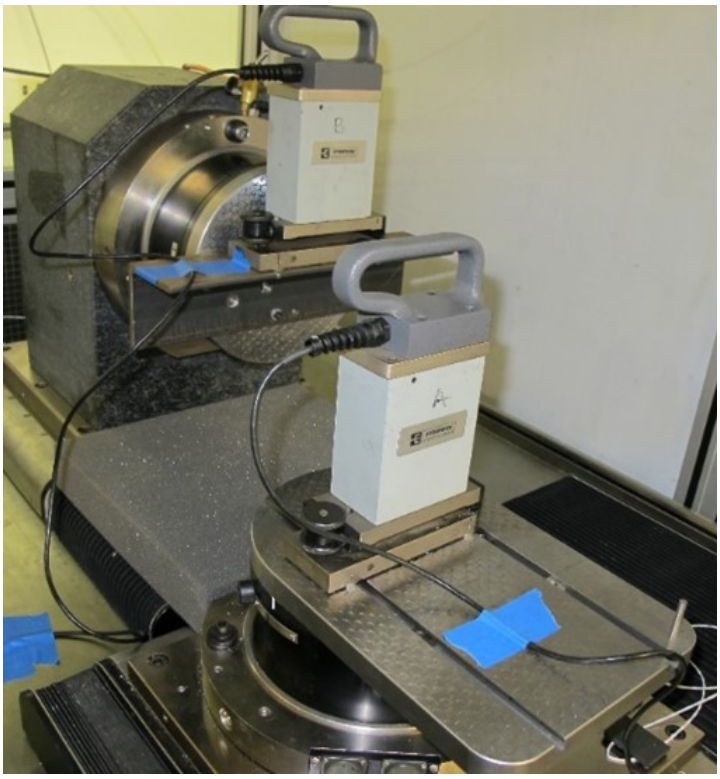

Figure 5.24: Electronic levels setup for measuring roll in the Z carriage and pitch in the X carriage after the environmentally controlled enclosure was installed.

The setup and epoxy locations are the same as the measurements taken before the enclosure was installed. The only difference is the location the location of the level on the Z carriage was changed when measuring roll in the X carriage and pitch in the Z carriage (Figure 5.25). The level was placed on the granite "tombstone" instead of on the C-carriage. This was safer in case the C carriage servo disengaged and should be more stable as the C carriage is no longer in the loop between the two levels. The pneumatic vibration isolators were deflated during the measurements.

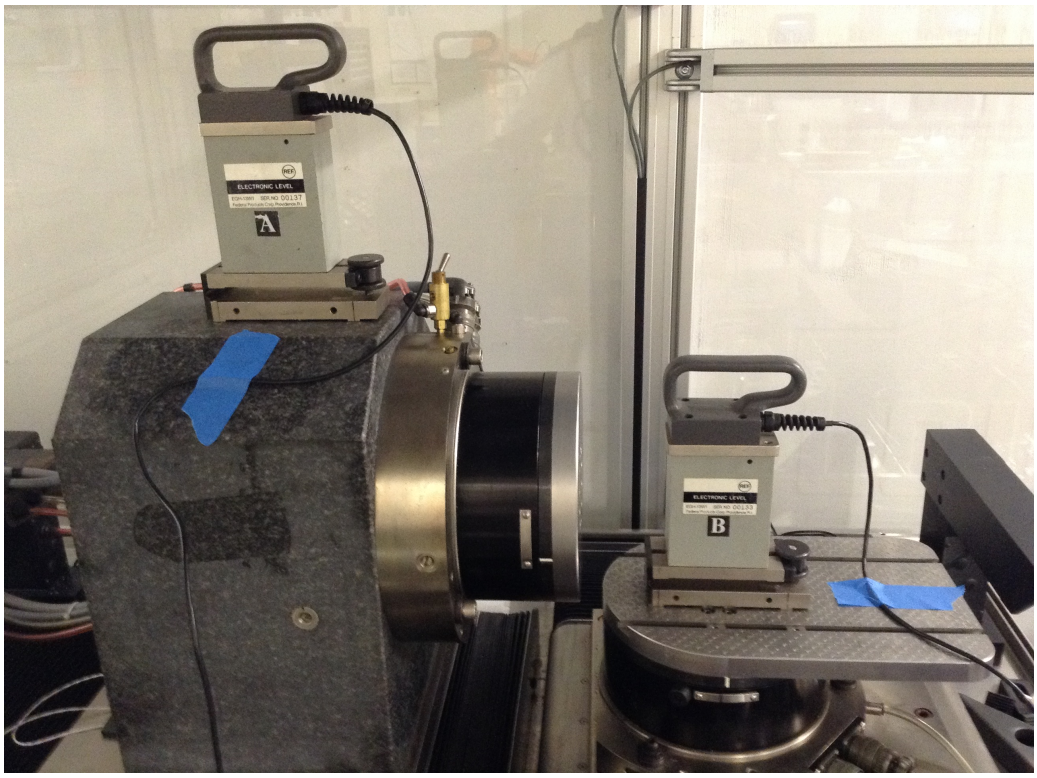

Figure 5.25: Measuring pitch in the Z carriage and roll in the X carriage with differential electronic levels.

These measurements are the ones used in the mathematical model for the error compensation and Monte Carlo simulation. For use in the mathematical model the measurement is adjusted so that the zero crossing is at the machine carriage position at the fiducial origin. The uncertainty in these measurements is used in the Monte Carlo simulation. The figures show error bars for one standard deviation below and above the mean. Like the previous measurements the levels must be stationary to provide an accurate reading. The measurements were taken every five mm throughout the full carriage range from 0 mm to 190 mm on the X carriage and 0 mm to -190 mm for the Z carriage.

5.18 Measuring Roll in the Z Carriage

Roll in the Z carriage has a peak to valley of about 0.9 sec before the enclosure and about 0.6 sec after the enclosure. The roll in the Z carriage is shown in Figure 5.26.

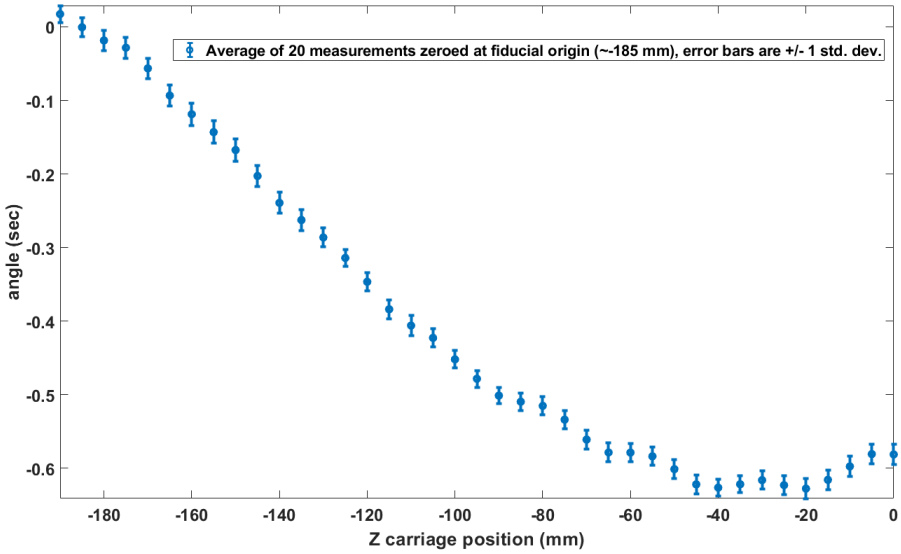

Figure 5.26: Roll in the Z carriage after the enclosure was installed measured with the electronic levels.

5.19 Measuring Pitch in the X Carriage

The pitch measurements before and after the enclosure was installed are quite different. This discrepancy could be due to the heating of the carriage ways by the hydrostatic bearing and hydraulic oil as the carriage moves. This effect was reduced with the enclosure and control of the hydrostatic oil temperature.

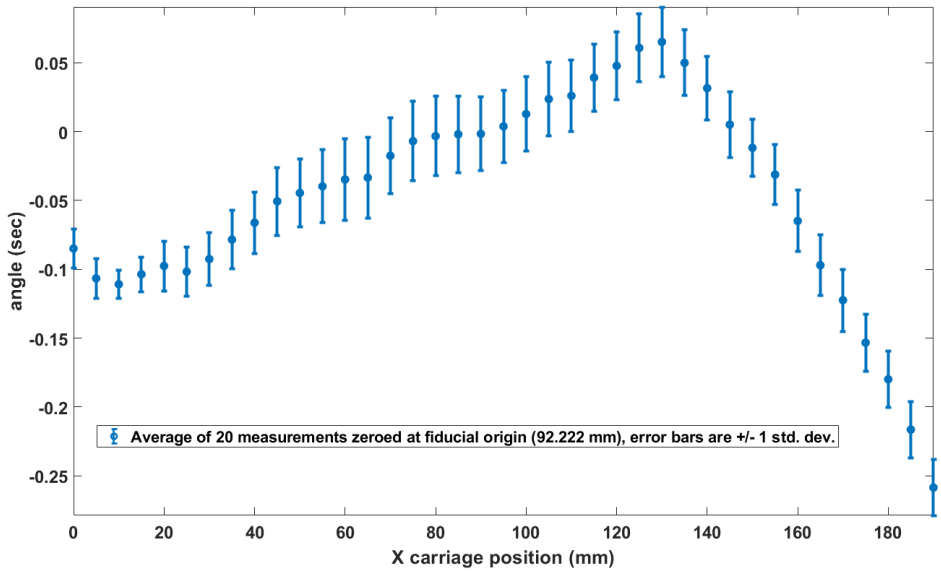

Figure 5.27: X carriage pitch after the enclosure was installed measured with the electronic levels.

5.20 Measuring Roll in the X Carriage

The roll in the X carriage is shown in Figure 5.28. Interestingly, there is some similarity between the X carriage roll and the X carriage pitch.

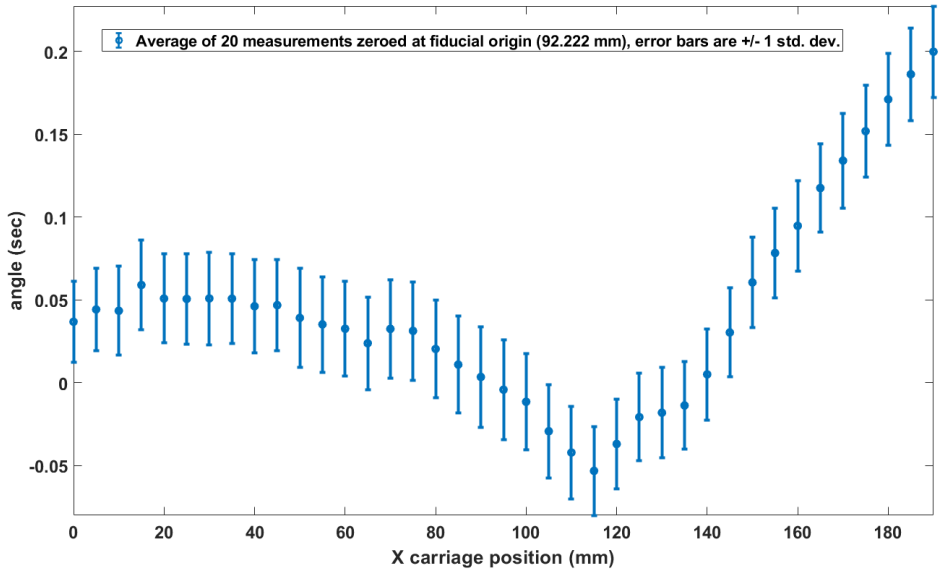

Figure 5.28: X carriage roll after the enclosure was installed measured with the electronic levels.

5.21 Measuring Pitch in the Z Carriage

Pitch in the Z carriage after the enclosure reduced to a peak to valley of 2.5 seconds from about 6 seconds before the enclosure was installed. Pitch in the Z carriage is shown in Figure 5.29.

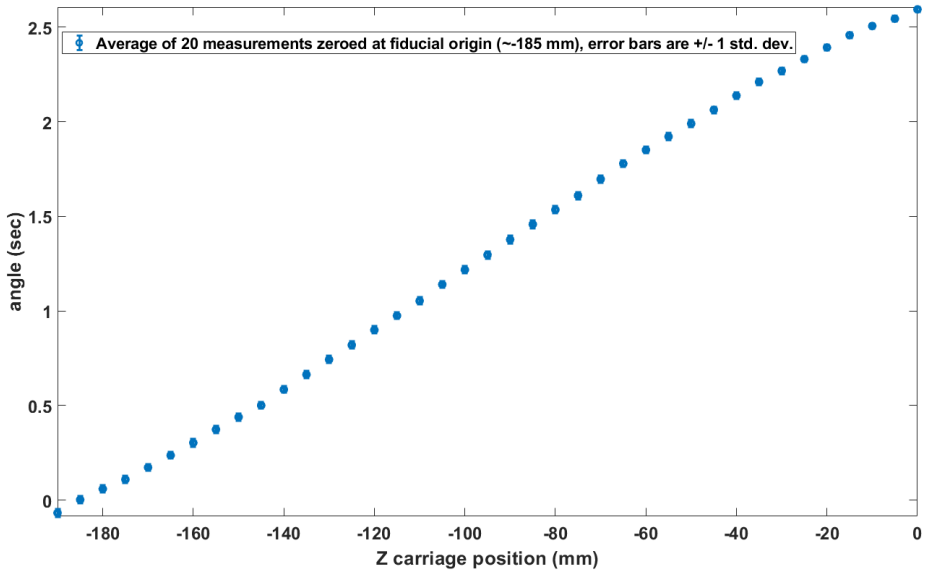

Figure 5.29: Pitch in Z carriage after the enclosure was installed measured with the electronic levels.

The uncertainty evaluation of the levels measurements is shown below.

5.22 Laser Interferometric Measurements

The Agilent laser system was used for the laser interferometric measurements. The Agilent laser is a helium-neon two frequency laser. The displacement laser readings were corrected for temperature, humidity, and pressure over the measurement distance. The angular measurement did not require the same compensation. The displacement setup is sometimes called a displacement measuring interferometer (DMI). Before using the Agilent laser system, it is important to deflate the vibration isolation air bags.

5.23 Linear Displacement Measurement

The Agilent Laser System was used to measure the linear displacement or positioning error. The optics used for the measurement included an interferometer (beam splitter) and two retroreflectors. The interferometer was placed at the origin of the carriage being measured. The measurement was automated using the Agilent software. The positions are entered into the software and a threshold is set around each position. Once the position is within that threshold, the software waits a specified amount of time then records the displacement.

5.24 Optical Setup

The optical setup for measuring linear displacement can be seen in Figure 5.30. The linear displacement measurements all used this orientation although the reference retroreflector/interferometer assembly was not in the vertical position when measuring the Z carriage.

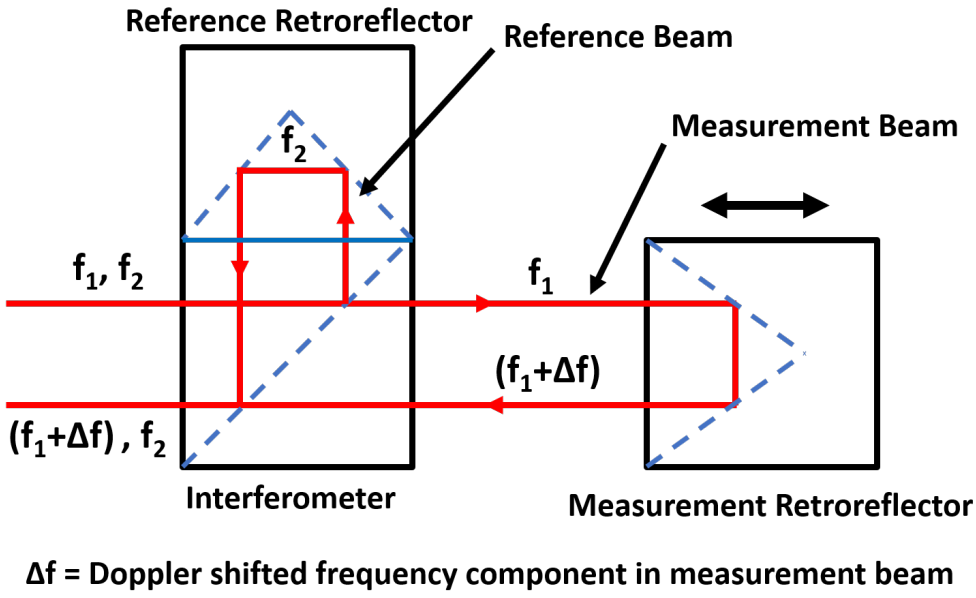

Figure 5.30: Linear displacement optical setup for laser interferometer [9].

Care was taken to ensure that the center of the cube corner on the Z carriage was centered on the rotational axis of the C carriage. This was done by rotating the C

carriage by 180 degrees and watching the return beam as it moves. When centered the return beam will not move off the crosshairs on the laser when rotated. The laser aperture was on small and the target was on the crosshairs. Figure 5.31 shows the front of the laser where the selection for beam size and target are located. The front of the laser also has a selection for straight or other. Other was selected for the linear displacement measurement.

Figure 5.31: Agilent laser system alignment using the crosshairs to align the optics to return the laser to the inlet.

A fixture was placed on the C carriage to place the retroreflector on as seen in Figure 5.32. The center of this retroreflector is placed so the center of the cube corner is at the center of the axis of rotation of the C carriage. A compliant material was used to protect the retroreflector from the C-clamp which was loosely tightened to hold the retroreflector to the mount on the C carriage.

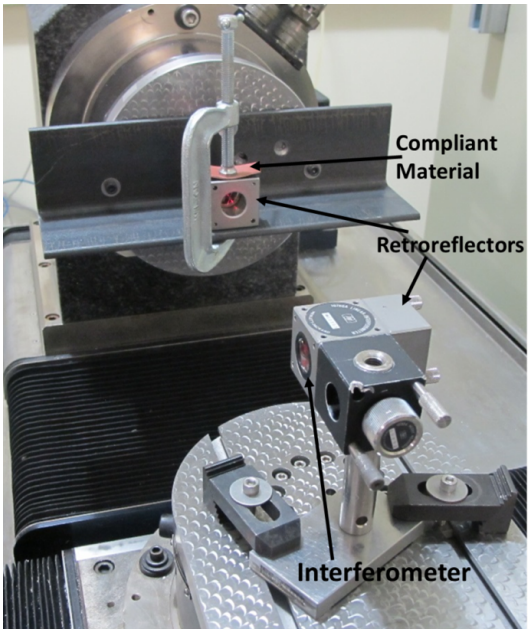

Figure 5.32: Optical setup for the linear displacement measurement of the Z carriage.

The laser sits on a tripod which has six degrees of freedom for adjusting the laser to get the desired alignment. The height of the laser is set to the height of the center of the C spindle axis of rotation plus half the distance of the separation of the output of the laser and the inlet. This relationship can be seen in Figure 5.33.

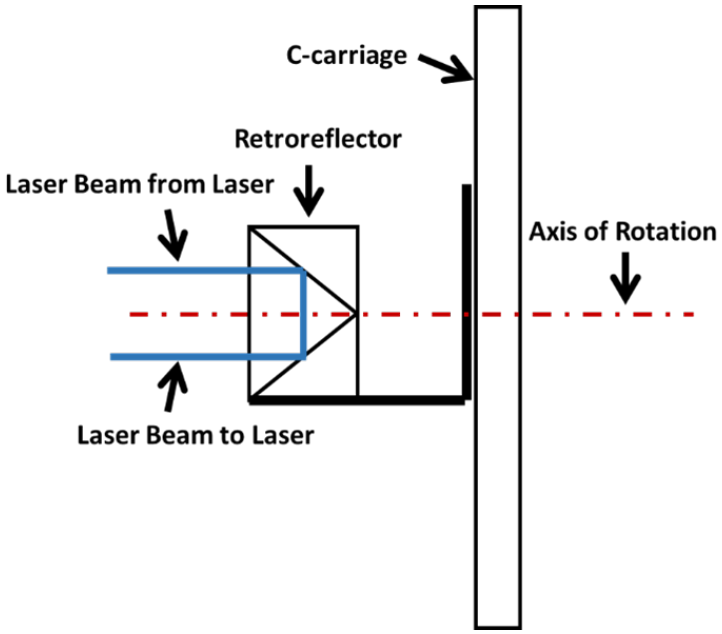

Figure 5.33: Aligning the laser with the center of rotation of the C carriage.

Once the height was found the laser was locked down for that vertical direction and not moved. The laser is also aligned to the motion of the X carriage and Z carriage using the gunsight method to align the laser. The position of the laser with respect to the 100UMM can be seen in Figure 5.34.

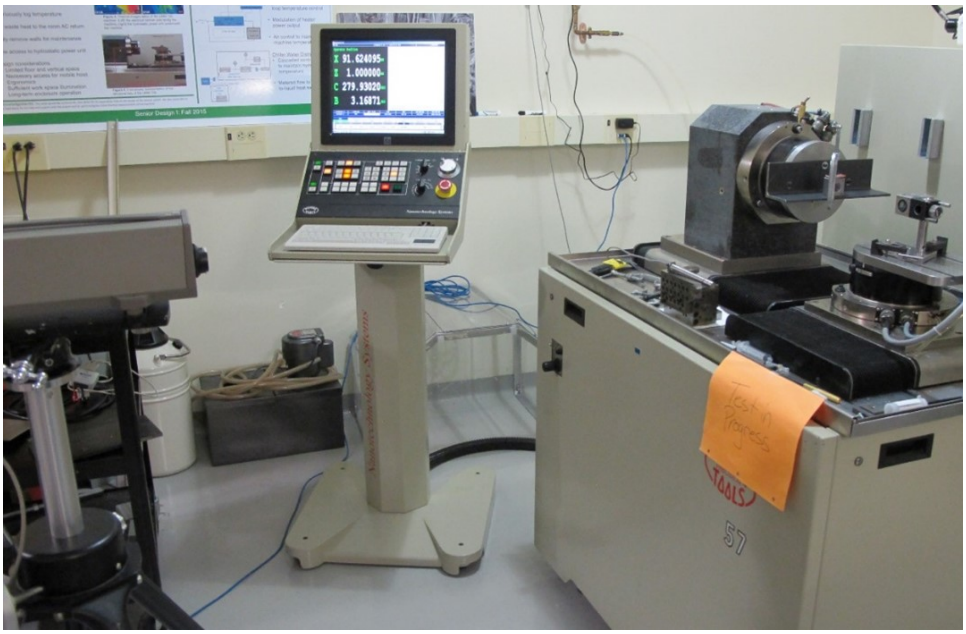

Figure 5.34: Optical setup for the linear displacement measurement of the Z carriage including the laser.

When measuring the linear displacement of the X carriage the interferometer and reference retroreflector were placed on the C carriage and the measurement retroreflector was placed on the B carriage. This arrangement can be seen in Figure 5.35.

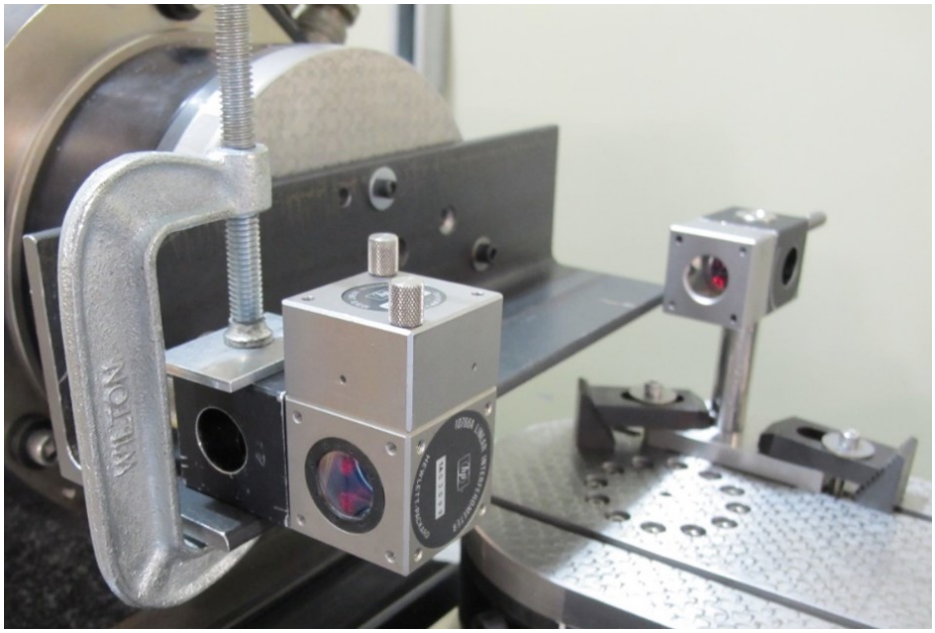

Figure 5.35: Laser interferometer setup for measuring the linear displacement error in the X carriage including the optical setup.

The laser setup for measuring the linear displacement error in the X carriage is shown in Figure 5.36. In Figure 5.36 the X carriage is in the home position. The measured distance is between the interferometer and the measurement retroreflector which means that at X_M equal to zero the measurement distance is the largest for the setup shown in Figure 5.36. When doing the laser corrections care was taken to ensure that the correction was applied to the measurement distance not to the machine position beings it would be backwards.

Figure 5.36: Laser interferometer setup for measuring the linear displacement error in the X carriage.

5.25 Laser and Scale Corrections

To decrease the uncertainty in the measurements taken with the laser interferometer the measurements are corrected for the temperature, humidity, and pressure while the machine scales are corrected for temperature (thermal expansion). Temperature, pressure and humidity were measured using a probe that transmits over the internet so the data could be stored and accessed remotely. The data was saved to an excel sheet and imported into MATLAB for processing.

5.26 Laser Corrections

The laser measurements were corrected for temperature, humidity, and pressure using the modified Edlen's equation. Equation 5.6 was used to calculate the correction [41].

$$L_C = L_R(1 + K_T(T_A - 20\,^\circ C) - K_P(P_A - 760\,mmHg) + K_H(V_A - 10\,mmHg)) \quad (5.6)$$

Where: L_C is the corrected laser reading

L_R is the laser display reading

K_T is the temperature coefficient (0.93 ppm/$^\circ C$)

K_P is the pressure coefficient (0.36 ppm/mmHg)

K_H is the humidity coefficient (0.05 ppm/mmHg)

T_A is the ambient temperature ($^\circ C$)

P_A is the ambient pressure (mmHg)

V_A is the ambient vapor pressure (mmHg of H_2O)

$$V_A = \%R.H. * V_{psat}@T_A \tag{5.7}$$

The table used to look up the vapor pressure at saturation can be found in Appendix C.

5.27 Machine Scale Corrections

The machine scales are made by Sony and are glass scales. The effective thermal expansion coefficient of the machine scales is assumed to be $-0.7\,x10^{-6}\,ppm$ based on the manual for the linear encoders from Sony [42]. To correct the machine scales equation 5.8 was used [41].

$$CMR = MDR[1 + \alpha_S(T_A - 20\,^\circ C)] \tag{5.8}$$

Where CMR is the corrected machine reading, MDR is the machine display reading, α_S is the effective thermal expansion coefficient of the machine scales and T_A is the scale temperature during measurements ($^\circ C$).

5.28 Angular Interferometer

The angular interferometer uses a double retroreflector and an angular interferometer. The setup uses two beam paths with the retroreflectors separated by a known distance. The change in relative path lengths between the two beams causes a "doppler-shifted frequency change [9]" in the return beam from the interferometer into the receiver photodetector. The frequency change will "result in an indicated change in path length [9]" shown in Figure 5.37.

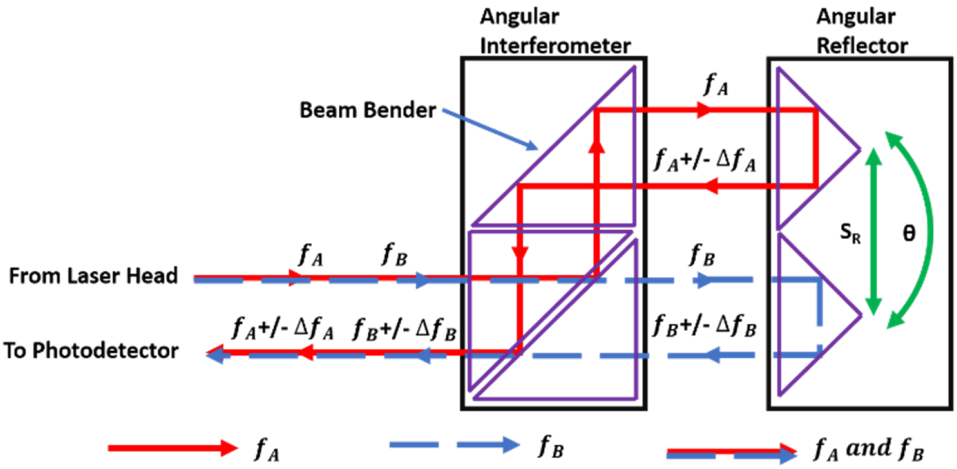

Figure 5.37: Operating principle of the angular interferometer [9].

A correction for the temperature, humidity and pressure is not required since the measurements are common path, and the difference in environment is minimal. The manual from Agilent describes the ability to solve for the angle of rotation using the change in relative path length with the following equation [9].

$$\theta = \frac{D}{S_R} \tag{5.9}$$

Where: θ is the angle of rotation of the retroreflector, D is the indicated change in relative path length, S_R is the spacing of the retroreflectors in the angular reflector, and between the parallel beam paths from the angular interferometer to the retroreflectors [9].

5.29 Linear Displacement Results

The linear displacement results are reported in the ISO 230-2 2014 format [4]. The standard is used for the determination of accuracy and repeatability for positioning of numerically controlled axes. The graph shown in Figure 5.39 shows the bidirectional errors and repeatability example chart adapted from the standard.

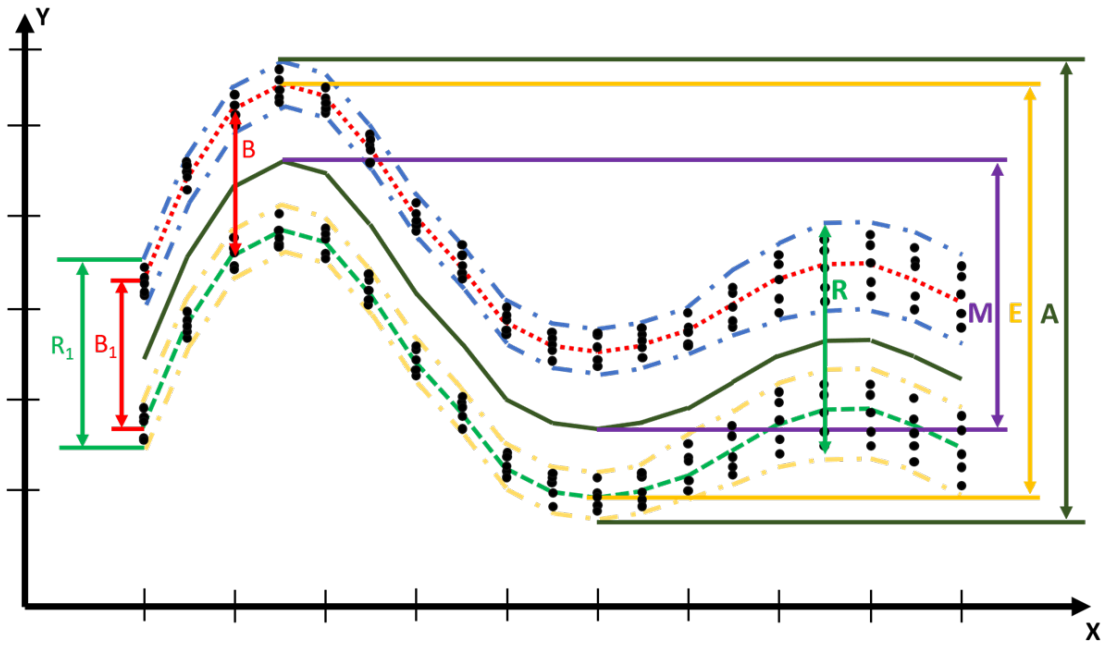

Figure 5.38: ISO 230-2 2014 bi-directional errors and positioning repeatability [4].

The values for A, E, M, R, and B are reported for the X and Z carriages with descriptions of their meaning below. A solid line shows the forward, reverse and total average. The total average is a heavier weighted line. The dashed line is the two standard deviations above and below the forward average and reverse average.

5.30 Z Carriage Displacement Before the Enclosure

The test took about 1.5 hours to collect the five sets of measurements. Looking at Figure 5.39 there is a noticeable amount of drift as the carriage moves back and forth. Starting with the first forward measurement the value is about 0.4 μm, as the test progresses and the carriage moves across the ways, heating them up, the variation between the runs decreases until the first measurement on fifth run is about -0.2 μm. This discrepancy is hypothesized to be from the hydraulic oil, in the hydrostatic bearing, heating up the ways as it moves back and forth as the hydraulic oil is at a higher temperature than the ways. As the temperature of the ways stabilizes, the measurements are closer together.

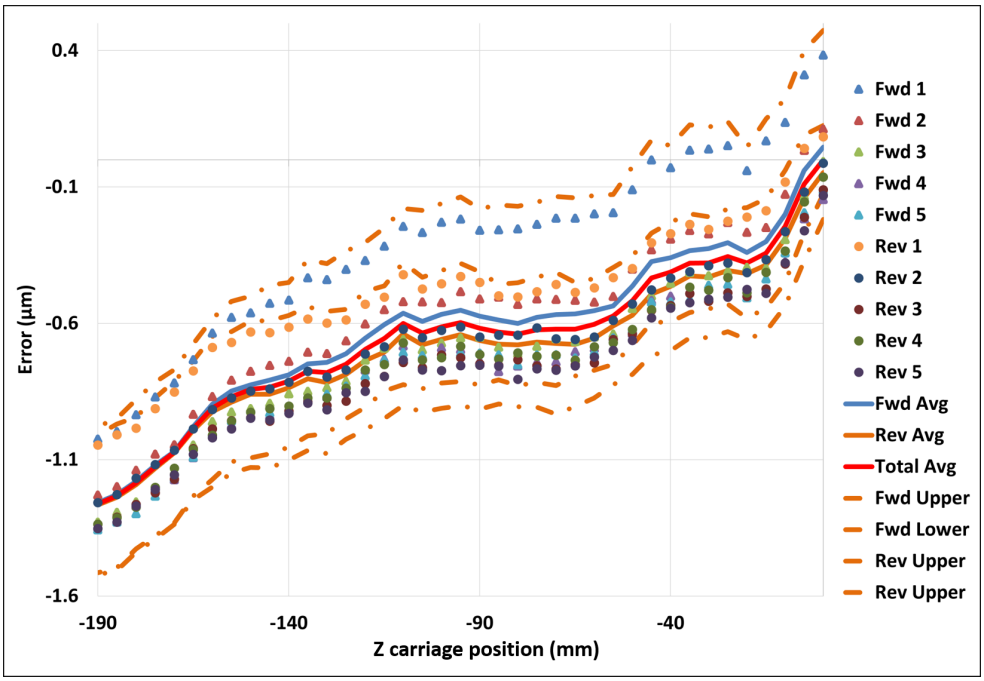

Figure 5.39: Linear displacement (positioning) error for the Z carriage in the ISO 230-2 2014 format [4].

In Table 5.3 and Table 5.4 the up arrow denotes the forward direction while the down arrow denotes the reverse direction. The tables include the values calculated using ISO 230-2 2014 for bi-directional accuracy, repeatability, reversal error, systematic positioning and mean positioning error [4]. The values for accuracy, repeatability and systematic positioning are shown for the forward and reverse directions as well as a total average.

Table 5.3: ISO 230-2 2014 bi-directional accuracy, repeatability, reversal error, systematic positioning, and mean positioning error for the Z carriage [4].

	μm
Accuracy (A)	1.996
Accuracy (A)↑	1.988
Accuracy (A)↓	1.648
Repeat (R)	0.923
Repeat (R)↑	0.923
Repeat (R)↓	0.552
Reversal Error (B)	0.118
Mean Reversal Error (B)	0.071
Sys. Dev. Pos. (E)	1.311
Sys. Dev. Pos. (E)↑	1.303
Sys. Dev. Pos. (E)↓	1.218
Mean (M)	1.261

From the ISO 230-2 2014 the accuracy was determined to be around 2 μm [4].

5.31 X Carriage Displacement Before the Enclosure

Like the Z carriage there is a similar trend in the variation of the measurements between the runs. This trend can be seen in Figure 5.40.

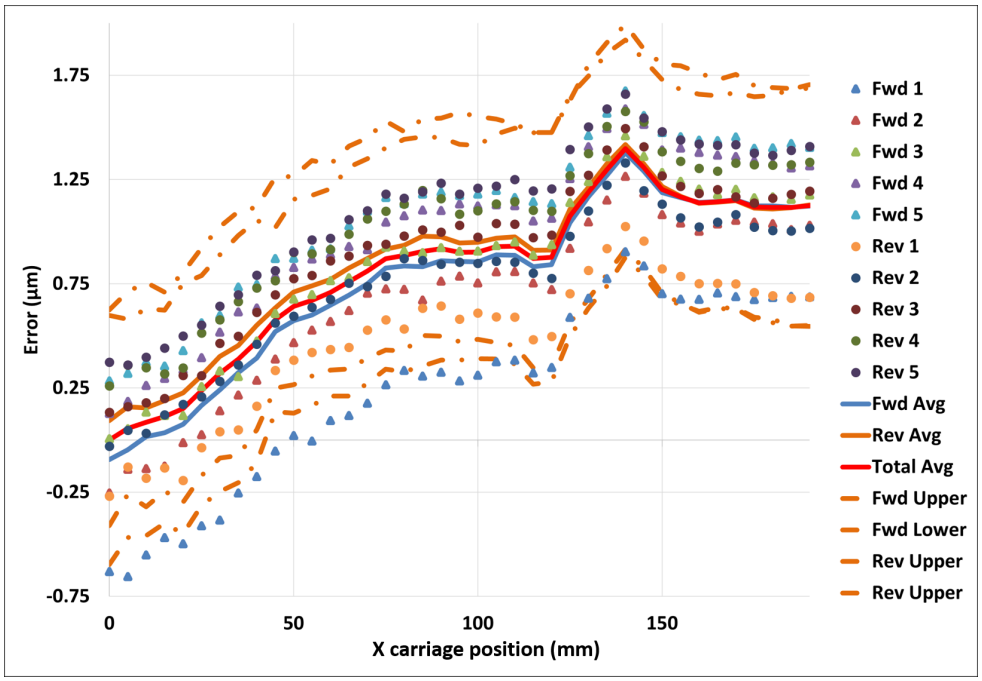

Figure 5.40: Linear displacement (positioning) error for the X carriage in the ISO 230-2 2014 format [4].

The ISO 230-2 bi-directional accuracy, repeatability, reversal error, systematic positioning and mean positioning error for the X carriage can be found in Table 5.4 [4]. The accuracy value is reported at 2.591 μm.

Table 5.4: ISO 230-2 2014 bi-directional accuracy, repeatability, reversal error, systematic positioning, and mean positioning error for the X carriage [4].

	μm
Accuracy (A)	2.591
Accuracy (A)↑	2.591
Accuracy (A)↓	2.330
Repeat (R)	1.565
Repeat (R)↑	1.565
Repeat (R)↓	1.155
Reversal Error (B)	0.206
Mean Reversal Error (B)	0.088
Sys. Dev. Pos. (E)	1.510
Sys. Dev. Pos. (E)↑	1.472
Sys. Dev. Pos. (E)↓	1.324
Mean (M)	1.398

5.32 Displacement Measurements After the Enclosure

After the environmentally controlled enclosure was installed around the 100UMM the linear carriage positioning errors were re-measured. These are the measurements that are used in the error compensation and Monte Carlo simulation. Since the error measurements are used in the mathematical model the interferometer was placed on the fiducial origin. The positioning errors should mirror the pitch error of the carriage and the sign convention should make sense. For instance, a positive pitch error in the X carriage would result in a negative positioning error assuming that most of the positioning error is due to the angular errors and not other factors like the linear encoder. Figure 5.41 shows the inferferometer setup for the Z carriage displacement error measurement.

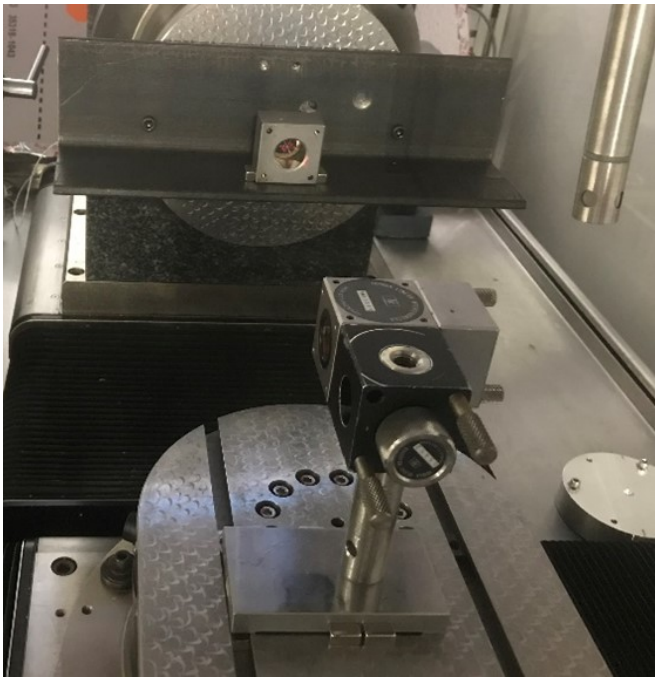

Figure 5.41: Agilent laser interferometer setup for measuring the positioning error in the Z carriage after the environmentally controlled enclosure was installed.

Magnets were used to hold the optics and fixturing to the carriage face and bracket during alignment. Not shown in Figure 5.41, a c-clamp was used to secure the retroreflector to the steel angle bracket. The same setup process was followed as before the enclosure when aligning the optics with the machine and laser. Figure 5.42 shows the optical setup for measuring the positioning error in the X carriage using the laser interferometer.

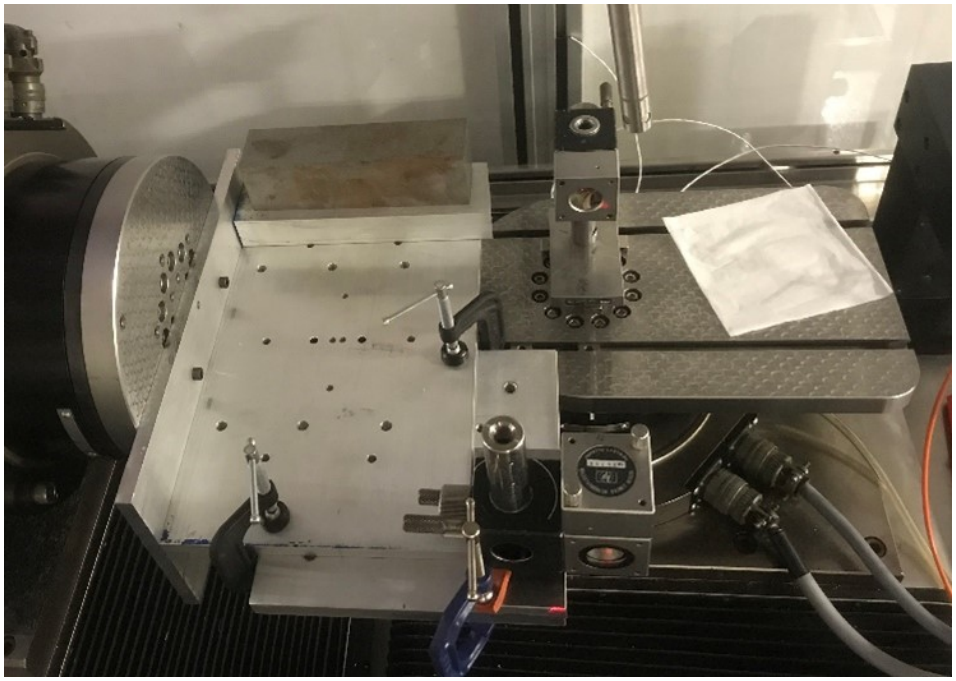

Figure 5.42: Interferometry setup for measuring the positioning error in the X carriage after the enclosure was installed.

As before, the measurement results were corrected using Edlen's equation for the temperature, humidity, and pressure differences. The probe for measuring the environmental conditions can be seen in 5.41 and 5.42. Figure 5.43 shows the X carriage positioning error.

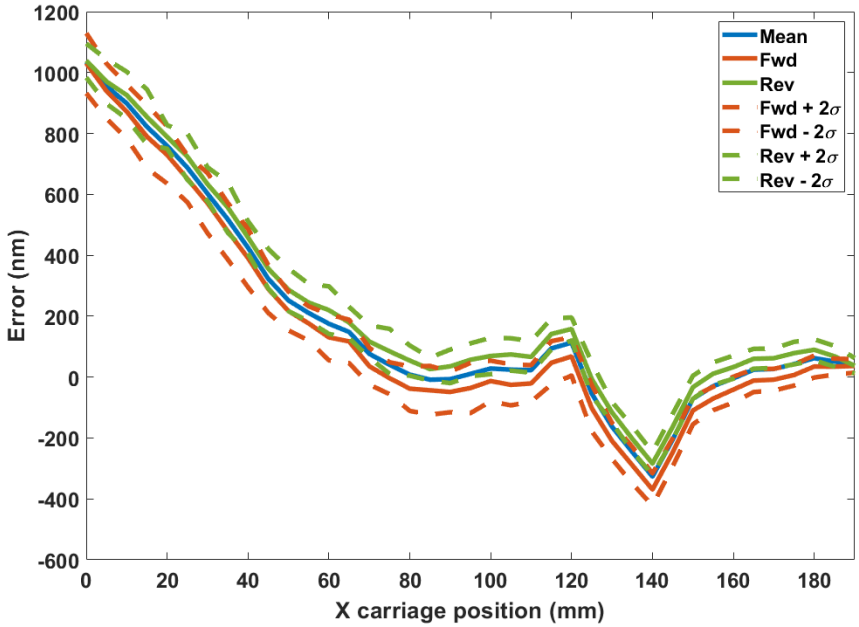

Figure 5.43: X carriage positioning error on the Nanotech 100UMM measured with the Agilent laser system.

The error in the X carriage position is in a non-sensitive direction for measuring the AFRL optics. It is like the Y direction errors where the error contribution of the X carriage positioning in the Z height is a function of the part slope. The sign convention is switched from the measurement above that was done before the enclosure was installed. There may have been an error during the subsequent measurements, however, the sign was checked during the measurement setup. The sign convention was checked again during the measurement after the enclosure and the result was an opposite sign on the measurement result. Somewhere there is a discrepancy.

The sign convention of the second set of measurements matches the assumption that the positioning error is largely due to the X carriage pitch and the measurement result from the X carriage pitch error measurements. A misalignment of the machine scales or a calibration error could also cause an error in the X carriage position. The magnitude of the positioning error compared to the pitch in the X carriage is larger than would be expected for the distance of the interferometer from the assumed center

of rotation of the carriage, between the ways.

The Z carriage positioning error is shown in Figure 5.44.

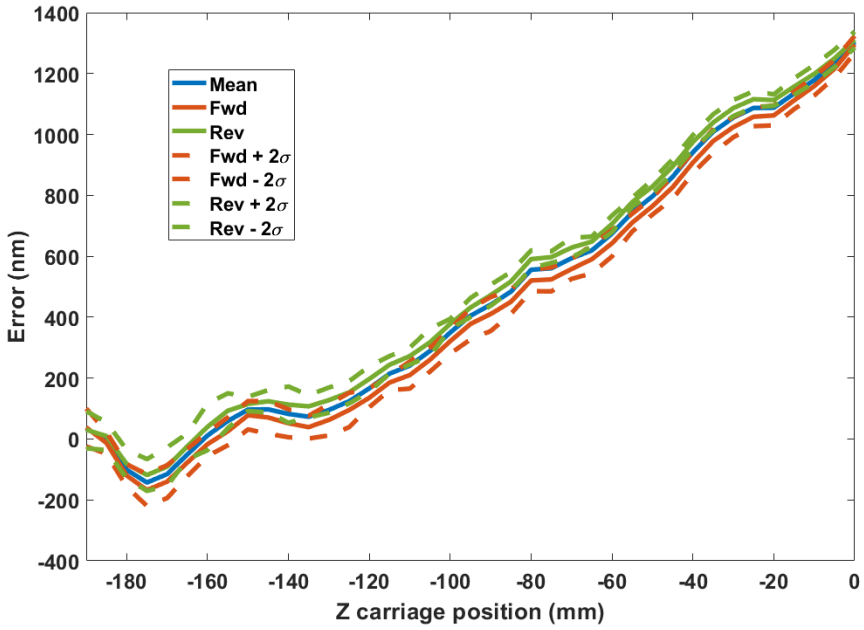

Figure 5.44: Z carriage positioning error on the Nanotech 100UMM measured with the Agilent laser system.

The error may look alarming at first but remember the error is being compensated and the Z carriage is only used over a small range near the flat region.

5.33 Pitch and Positioning Error Relationship

The pitch error motion in a linear carriage will manifest in the position error as well. Like the X carriage roll and horizontal straightness of the X carriage, this relationship is accounted for in the model. It is informative to understand this relationship as the measurement plan is being developed for a machine that may have large pitch errors.

5.34 Yaw Measurements

The yaw measurements using the Agilent angular interferometer are relatively straight forward since the Agilent laser system comes with software. The spray mist machine codes were used to trigger the measurement in the Agilent software like

other measurements on the 100UMM. The laser reading was not compensated for the measurements for temperature, humidity, and pressure since the laser path is nearly balanced. The fiducial origin is at the carriage position Z = -185.158175 mm. The yaw in the Z carriage is shown in Figure 5.45.

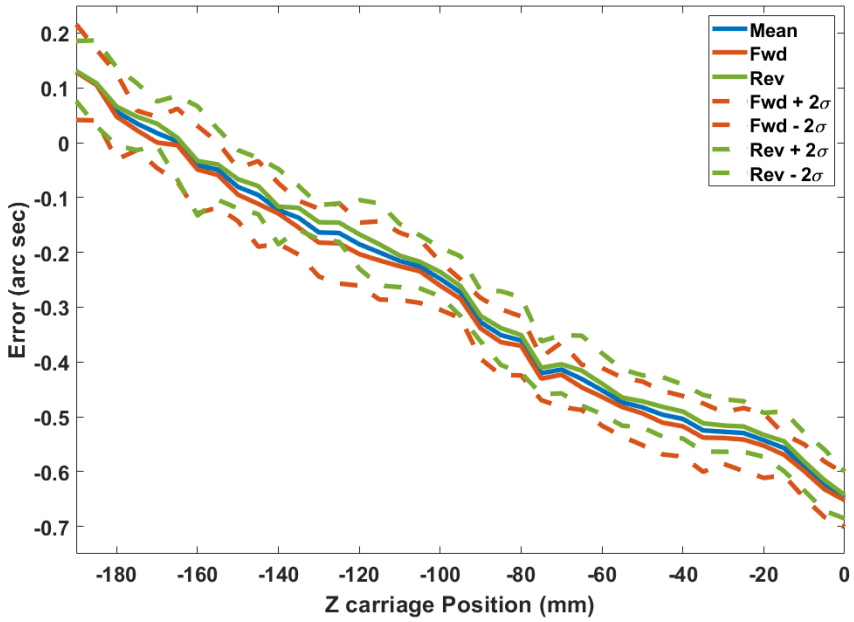

Figure 5.45: Yaw in Z carriage of the Nanotech 100UMM measured with the Agilent laser system angular interferometer.

The yaw in the X carriage is shown in Figure 5.46.

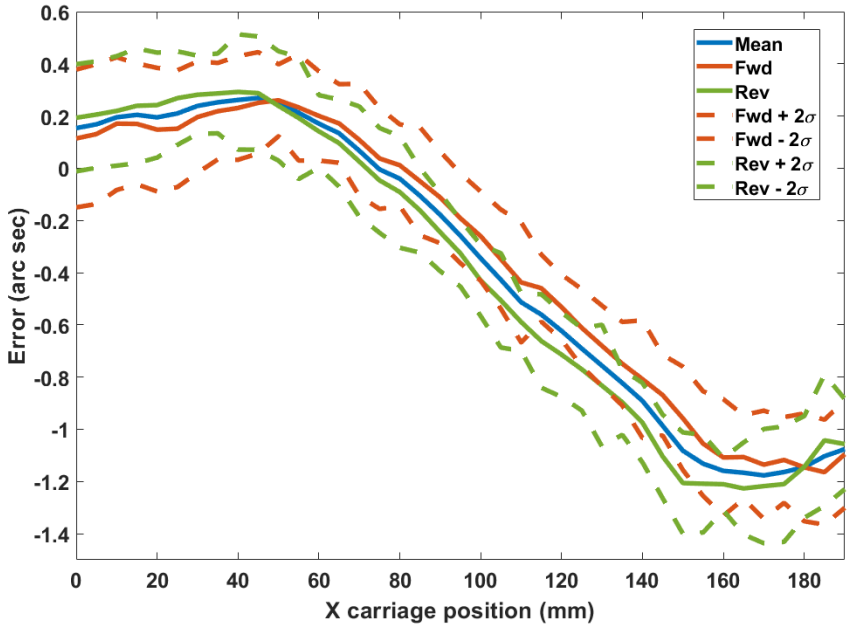

Figure 5.46: Yaw in X carriage of the Nanotech 100UMM measured with the Agilent laser system angular interferometer.

5.35 Measuring Straightness

The X carriage horizontal straightness was measured before and after the environmental enclosure was installed. It was measured using a capacitance gage and a fiber optic intensity probe on a mirrored surface with a glass substrate. The straightness measurements use reversal techniques to subtract out the error of the mirrored surface or artifact. The ISO 230-1 standard was referenced for guidance in measuring straightness. ISO 230-1 defines 'straightness deviation' in a linear carriage as the "distance of the functional point from the reference straight line fitting its trajectory, measured in one of the two directions orthogonal to the direction commanded (nominal) straight-line trajectory [30]." In NOTE 3 of the definition it states that the 'least squares reference straight line' can be used. The 'least squares reference straight line' is defined as the "straight line, where the sum of the squares of the measured straightness deviations is minimum [30]."

5.36 Horizontal Straightness in the X carriage

For the measurement of freeform optics on the 100UMM with the part mounted on the C carriage and the probe on the B carriage the X carriage horizontal straightness is one of the most sensitive errors in the part measurement. As with the other straightness and linear carriage positioning errors, the X carriage horizontal straightness is measured at the origin of the X carriage coordinate system. Initial measurements were made in the Fall of 2016 using the Philtec fiber optic probe and the measurement was repeated in the Spring of 2019 using a capacitance gage with special care taken to measure at the X carriage origin.

5.37 Measurand

The horizontal straightness of the X carriage is measured as a function of the carriage position. An uncertainty evaluation for the measurements will be conducted to complete the measurement and for use in the Monte Carlo simulation. The coordinate systems and mathematical solution is shown below for the final measurements. It is important to work through the coordinate systems of the probe, machine carriages and straightedge orientation to ensure the correct sign conventions.

5.38 Initial Measurements

Initial measurements were made using the Philtec fiber optic probe and an aluminum mirror on glass. These measurements were made before the environmentally controlled enclosure was installed. Pins and magnets were used to locate the mirror during the reversal. A custom probe holder was fit to the tool post that also allowed for reversal of the probe. The specifications for the Philtec probe are shown in Table 5.5.

Table 5.5: Philtec fiber optic probe specifications [5].

Model Number	muDMS-RC25
Serial Number	2126
Range (mm)	0.76
Fiber Optic Area (mm)	0.64 x 3.175

The Philtec probe works by detecting the intensity of reflected light off the measurement object. The fiber optic bundle in the probe tip has two detectors where "the light reflected off a surface follows two separate paths back to the electronics where a ratiometric calculation provides the distance measurement which is independent of varying surface reflectance [5]", what they call reflectance compensation. The sensor is calibrated for the surface being measured and the calibration is stored onboard the sensor. During a measurement, the sensor takes the dynamic light signals reflected from the surface and converts it to a distance by comparing to the calibration data. The probe tip is shown in Figure 5.47.

Figure 5.47: Philtec fiber optic probe configuration showing the sensor tip [5].

The measurement setup is shown in Figure 5.48 with the custom probe holder for reversal and the mirror mounted on the fixture.

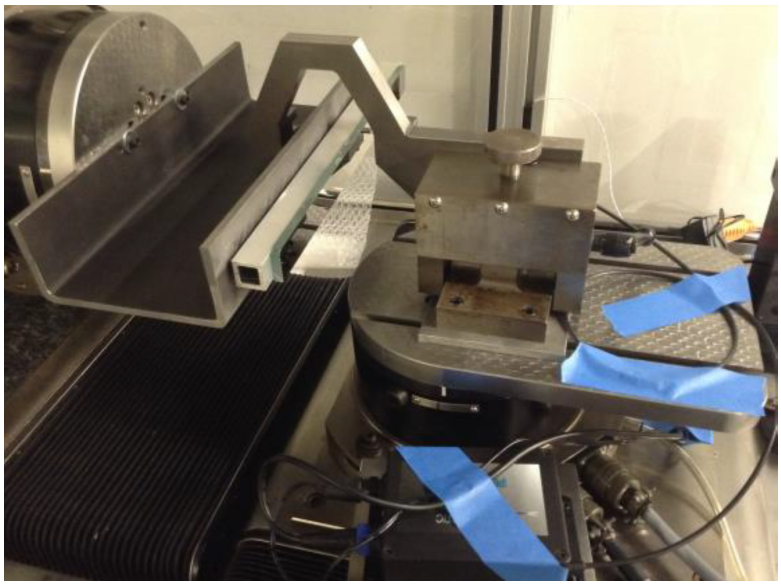

Figure 5.48: Using the Philtec fiber optic probe to measure X carriage horizontal straightness with an aluminum mirror on glass as the artifact.

Measurements were taken every five millimeters along the travel of the X carriage. A measurement was triggered for one second using the machine code for spray mist on/off and the opto-coupler connected to the spray mist solenoid. The opto-coupler sends a digital signal to the DAQ when actuated which can be interrogated in the LabVIEW code to determine when to initiate a measurement.

Twenty measurements were taken for each direction of the X carriage and on each side of the straightedge for 80 total measurements. The probe was recalibrated each time the setup was changed as any movement in the fiber optic cable would change the calibration. For this reason, the sensor unit was placed on the X carriage. Before taking a measurement a three second wait was implemented to allow for any dynamics to settle out.

The probe uses dynamic light signals reflected from the target surface which converted to distance by comparing the sensor signal to gap calibration tables stored on-board the sensor control box. The manual for the probe recommends using the probe in its optimum performance range where the RC function or ratio has the steepest slope. The signal is near linear over a range of 0.2 μm to 0.4 μm and has the

steepest slope. This can be seen in the calibration data shown in Figure 5.49.

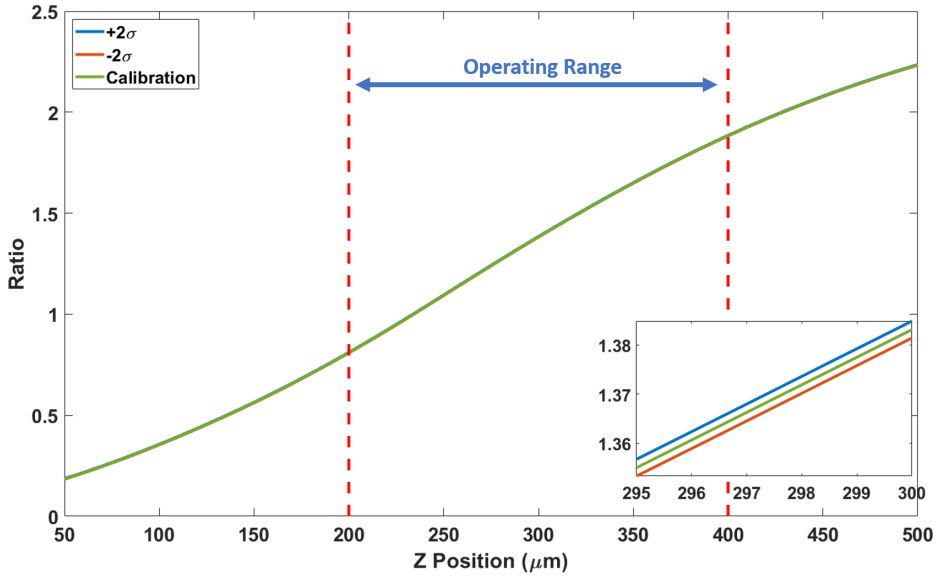

Figure 5.49: Calibration data for the Philtec fiber optic probe using the Nanotech 100UMM as a reference.

Possible sources of uncertainty were reduced after the initial measurements. The amount of settle out time was increased to three seconds from two seconds after moving to a new position. The mirror was mounted on a piece of box tube to reduce the amount of bending due to uneven mounting surfaces. The mirror was moved so that the middle of the mirror was being measured since the ends of the mirror have larger slopes.

When the mirror is flipped for the reversal it is assumed that the same place on the mirror is being measured on each side. There is some uncertainty associated with the reversal due to not knowing the exact height and in this case angle at which the mirror needs to be, to measure the same line. It was estimated with a type B uncertainty estimation that the amount of variation could be up to 250 nm or +/- 125 nm. This was done by looking at an interferogram of the mirror surface and estimating that the height of the mirror is likely no more than 1 mm different from side to side.

After setup, the machine and enclosure were left for a minimum of 30 minutes to

allow for the setup to reach a thermal equilibrium to reduce the thermal drift during the measurement. The control box was moved onto the X carriage so that the fiber optic cable would no longer be moved between measurement points.

The DC offset and tilt were removed by calculating a least squares linear fit to the measurement data for the nominal (forward) and reverse measurements and subtracting the line from the measurement data for each set of measurements. The result can be seen in Figure 5.50.

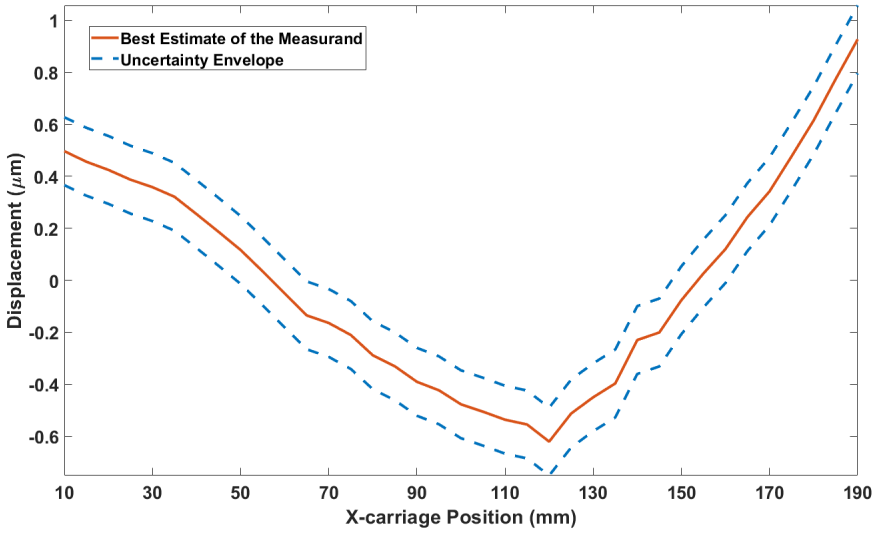

Figure 5.50: Measurement result for X carriage horizontal straightness with uncertainty statement with a coverage factor of 2.

The shape of the mirror can also be found using the measurement results. The shape of the mirror is shown in Figure 5.51.

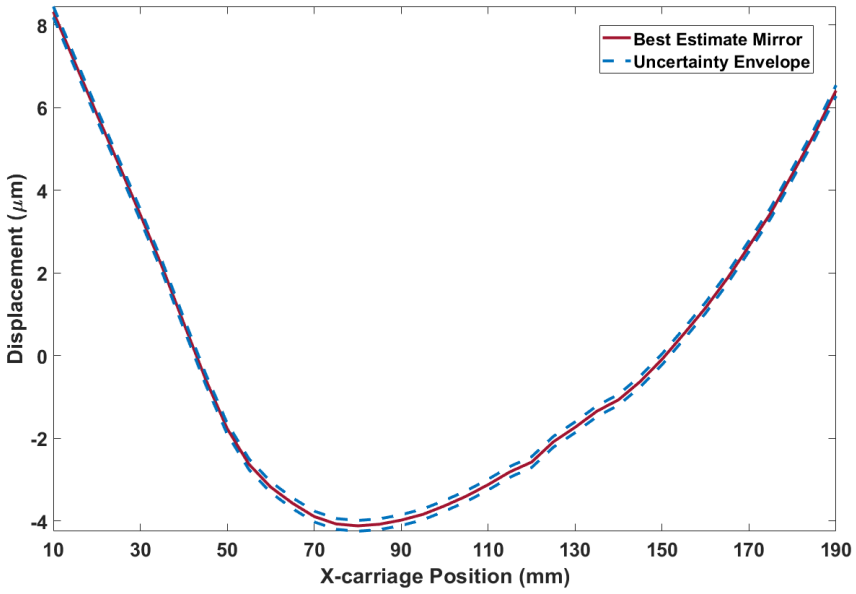

Figure 5.51: The straightedge measurement and uncertainty envelope for a coverage factor of 2.

5.39 Final Measurements

A final set of X carriage horizontal straightness measurements was conducted using a kinematically mounted mirrored artifact and a capacitance gage with special care taken to locate the measurement point on the origin of the X carriage in the mathematical model. Since the first set of measurements before the enclosure was installed, the oil temperature in the hydrostatic bearings was reduced such that the temperature exiting the bearing was nominally 20 °C. The probe used in the final measurement is more repeatable and has a higher resolution.

5.40 Instruments and Equipment

The Lion Precision Spindle Error Analyzer (SEA) with the Elite series capacitive displacement sensor system was used for the X carriage horizontal straightness measurements after the enclosure was installed. The capacitive displacement sensor modules were the CPL 290 which has a dual range and the MM190 signal processing and meter module. To hold and position the probe a Mahr indicator stand was used

with an adapter that a colleague Alex Blum manufactured. A NI USB-6001 DAQ and NI LabVIEW were used to acquire and average data.

Measurements were triggered on/off using the spray mist on/off command in the machine code as described above. By triggering the measurement, separating the data the between individual traces is much easier and it also allows for a soak out time to be programmed into the machine controller before the measurement is begun.

5.41 Measurement Artifacts

An aluminum mirror on glass with a kinematic mount was used as the measurement artifact. Using reversal techniques, the shape of the mirror and the straightness measurement are calculated. Precision ground shafts and machinist squares were used to align the probe to the rotational axes of the B and C carriages.

Fiducials were used to locate the straightedge in the machine coordinates such that the machine error measurements were taken in the same location on the straightedge (between the fiducials). The fiducials consist of laser cut dots that have an adhesive backing. The fiducials can be found in the measurement data as the capacitance gage goes over them. The fiducials are shown in Figure 5.52.

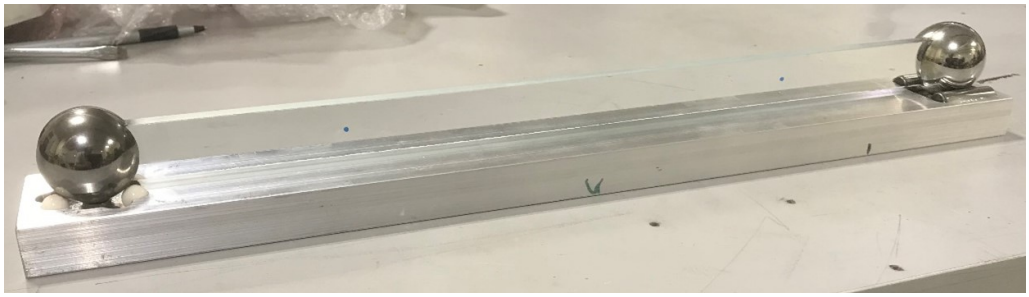

Figure 5.52: Straightedge mounted in kinematic mounted balls showing the fiducials used in alignment of the straightedge to the machine carriage and probe.

A kinematic mounting system was designed and assembled by Nicholas Horvath at UNCC. The straightedge was placed in two spheres cut on the wire EDM as shown. This allows for the reversal of the straightedge without imposing a moment causing deflection. The metal spheres are pre-loaded using neodymium magnets and are

supported on two cylindrical pins on one end and three alumina ceramic spheres on the other shown in Figure 5.53.

Figure 5.53: Close up of the kinematic mounted ball on two cylinders on the left and three balls on the right with a magnet for preload. The blue dot fiducials used to align the measurement results are also shown.

The preload helps with repeatability and stability in the kinematic mount. The spheres were cut on a wire electro discharge machine (EDM) to allow for the center of the straightedge to be placed at nominally the center of the sphere. Epoxy was used to assemble the kinematic mounting hardware into the aluminum bar.

Precision ground shafts with a diameter of 0.25 inches were used with precision squares to align the rotational axis of the C carriage with the rotational axis of the B carriage. This location will be checked again when the X-C squareness is measured. The mathematical model is built based on this location.

5.42 Measurement Setup

The feed rate used in the measurement was 20 mm/min. In LabVIEW, the analog measurement was averaged to reduce noise in the measurement. For each point recorded in the measurement 100 samples from the DAQ were taken and averaged. Data was taken from the DAQ using DAQ assistant in LabVIEW with continuous sampling of 100 samples at a rate of 4 kHz. The DAQ was read RSE or single ended at 10 V to -10 V. To connect the DAQ to the Lion Precision system a BNC connector to bare wire that connects to the screw terminal on the DAQ was used. The SEA system is shown in Figure 5.54.

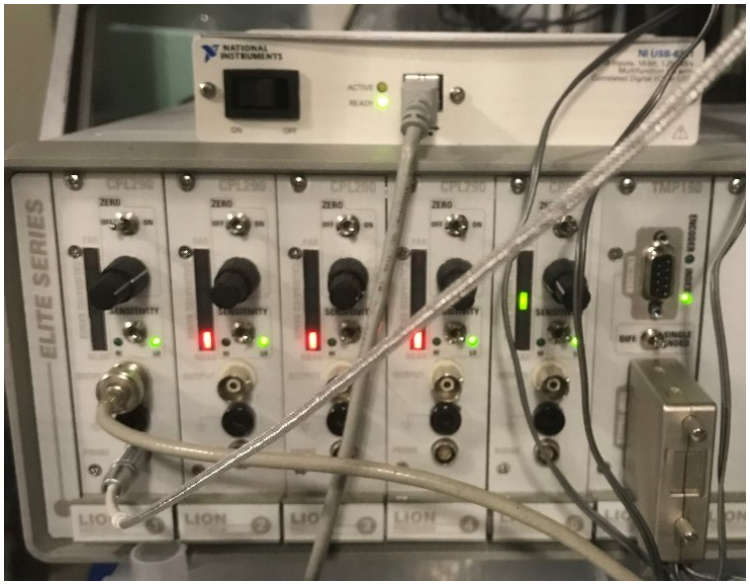

Figure 5.54: Lion Precision Elite Series capacitive displacement sensor system.

To read the probe the analog out was used from the SEA system. The probe was calibrated against the machine scales. It was assumed that over the range of the capacitance probe the positioning error in the Z carriage was negligible.

5.43 Aligning the Probe

The capacitance gage was aligned with precision ground shafts that were used to establish the fiducial origin shown above. The shafts were squared to the face of the C and B carriages using precision machinists squares and magnets. It was assumed that the hole in the centers of the B and C carriages where nominally in the center of the carriage and located on the axis of rotation for each carriage. For each shaft, two squares were placed perpendicular to one another and held into place with magnets. The squares were then brought into contact with the shaft. The probe was placed over the shaft that was centered on the B carriage and positioned such that the end of the capacitance gage was at the diameter of the top of the shaft as shown in Figure 5.55.

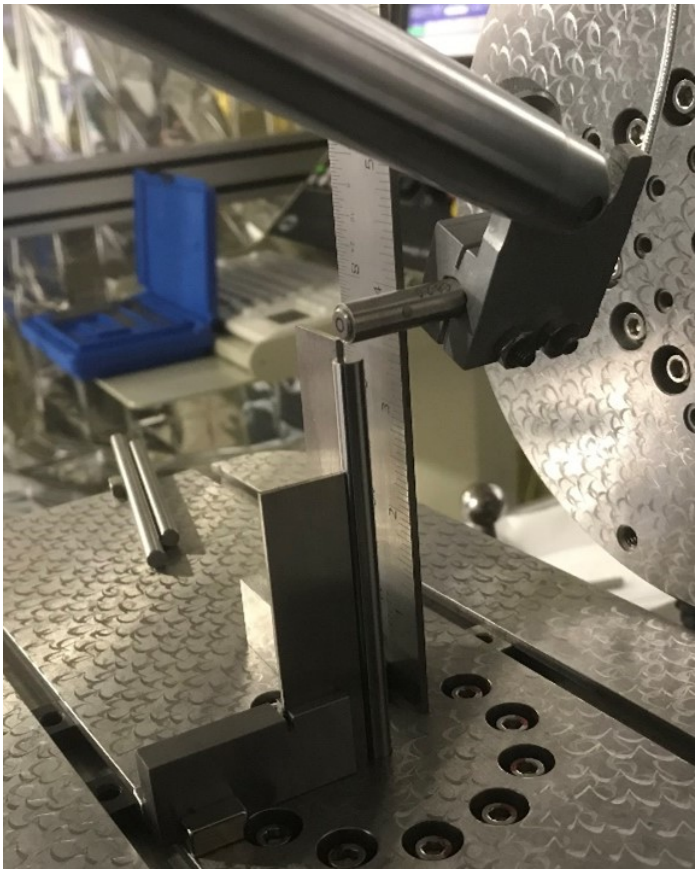

Figure 5.55: Aligning the probe with the rotational axis of the B carriage.

The height of the probe was found using a ruler as shown in the figure. Once the probe was aligned, the straightedge mounting bracket and straightedge were placed on the machine. The machine was moved back and forth over the measurement line with the fiducials placed at each end of the travel. By watching the probe displacement while moving over the measurement line the straightedge was situated to reduce the tilt, thus using less of the measurement range of the probe and reducing any error due to non-linearity in the probe.

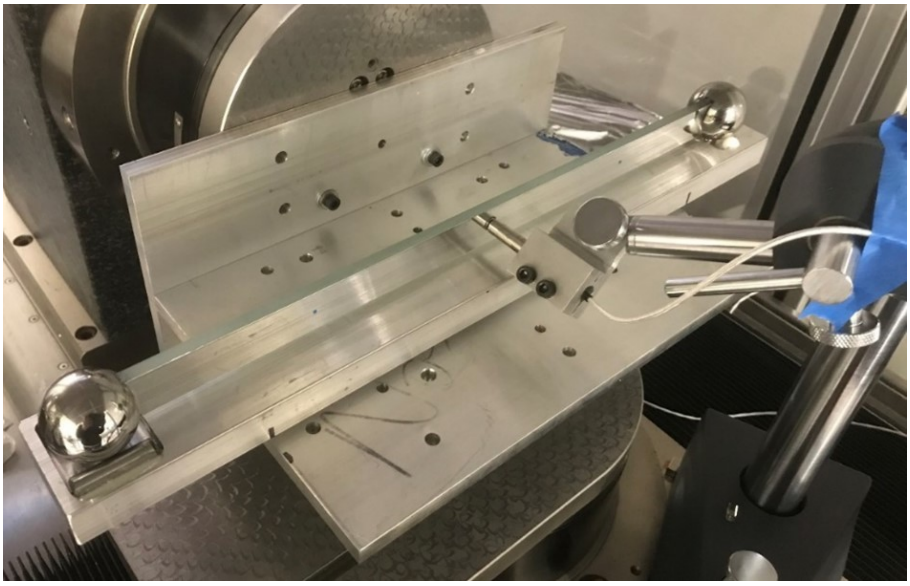

Figure 5.56: Final setup for measuring the straightedge with a capacitance gage on the -Z side of the straightedge after reversal.

A bracket was used to support the straightedge assembly on the C carriage. The straightedge was supported on gage blocks to raise it to where the fiducials were at the height of the probe and origin of the X carriage. To roughly align the straightedge in the same position in the X direction a mark was made on the aluminum bar with a permanent marker and aligned to the bracket edge. The final alignment was found using the fiducials and the capacitance gage.

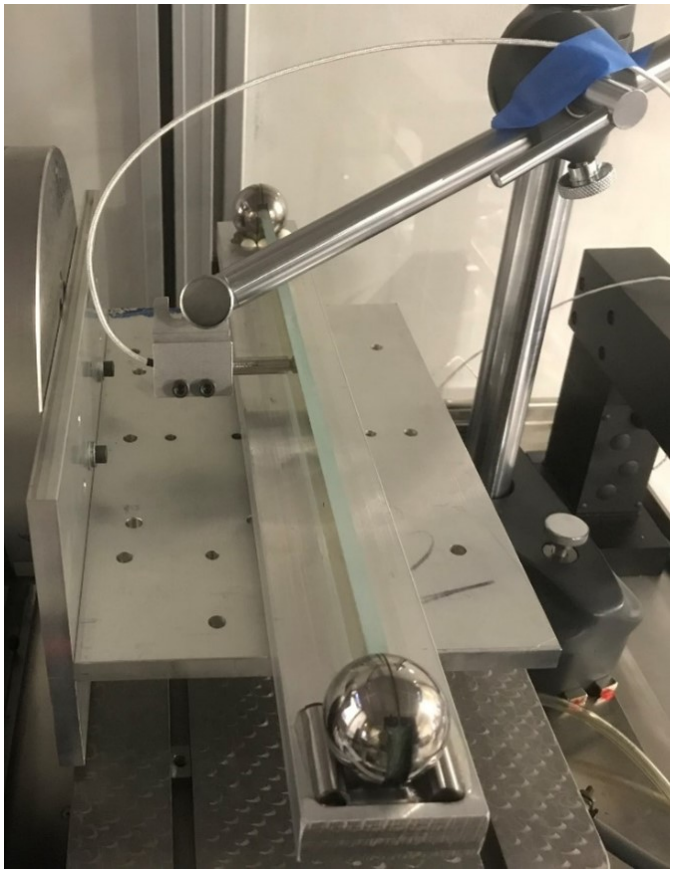

Figure 5.57: Measuring straightness using the capacitance gage on the +Z side of the straightedge before reversal.

5.44 Measurement Process

The scanning mode was used for the measurements. The artifact was measured in both directions to reduce the data age uncertainty in the measurement. That created four sets of data, one for each direction on the X axis and one for each direction on the Z axis. The two sets of data for each direction on the Z axis is the reversal used to separate out the error in the carriage from that of the artifact.

Care must be taken during the reversal such that the straightedge is not under stress after reversal. After reversal, lightly tapping on the assembly with something metallic can help the kinematic mount overcome stiction. The assembly was also let to soak out and come to equilibrium after the reversal and alignment. The contact areas between the artifact and fixture are made from smooth hard surfaces to reduce

the amount of friction.

A diagram was made for each orientation of the straightedge and probe to ensure that the coordinate systems and sign convention were correct. The diagrams encompass the reversal technique. The first orientation is referred to the 'normal' orientation in Reference [15]. A bump or positive feature on the straightedge aids in determining the behavior and sign convention of the probe in the specific orientation. The normal orientation is shown in Figure 5.58.

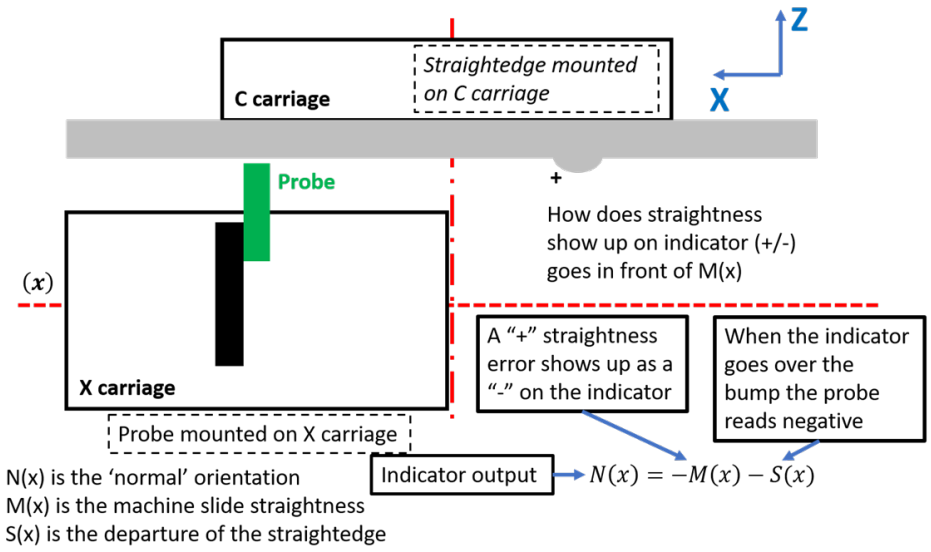

Figure 5.58: Measuring the X carriage horizontal straightness using the reversal technique, determining sign convention and coordinate systems of the measurement for the 'normal' orientation.

The indicator output is broken into the two influences, the shape of the artifact and the X carriage horizontal straightness. The reversal technique allows the two to be separated. For each orientation, the sign is chosen for the straightness and artifact (straightedge) as shown in the figure. The output of the probe is shown in the lower right of the figure. The same type of diagram is made for the reverse orientation with the output equation in the lower right in Figure 5.59.

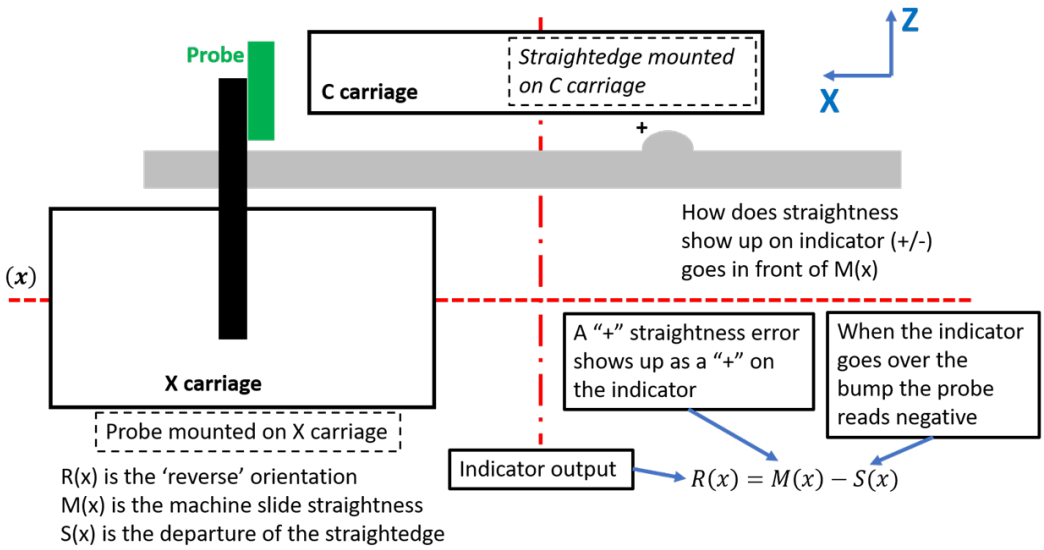

Figure 5.59: Measuring the X carriage horizontal straightness using the reversal technique, determining sign convention and coordinate systems of the measurement for the 'reverse' orientation.

The output equations are used in the data processing to calculate the measurement result separating the shape of the artifact from the X carriage horizontal straightness.

5.45 Data Processing

The measurement data was collected using the scanning LabVIEW program which records the carriage positions and probe displacement continuously while the measurements is activated in the machine code. MATLAB was used to process the measurement data. The equations used to calculate the shape of the artifact and the horizontal straightness of the X carriage are shown in equation 5.10 to 5.13 [15].

$$N(x) = -M(x) - S(x) \tag{5.10}$$

$$R(x) = M(x) - S(x) \tag{5.11}$$

$$M(x) = \frac{R(x) - N(x)}{2} \tag{5.12}$$

$$S(x) = \frac{-N(x) - R(x)}{2} \tag{5.13}$$

Where: M(x) is the straightness as a function of the X position, S(x) is the artifact

measurement as a function of the X position, R(x) is the reverse direction probe reading and N(x) is the normal direction probe reading.

The linear fit, subtraction and plotting were all done in MATLAB. Since the data was not in the same positions using 'scanning mode', the MATLAB function 'interp1' was used to create a set of data that had the same X carriage values to allow for the averaging and subtractions. The interpolation was done using the method of modified Akima in the interp1 function. The measurement data was interpolated at a spacing of 0.1 mm over the X carriage travel. Each measurement was interpolated separately then averaged and the standard deviation calculated.

5.46 Results

A line was fit to the data and subtracted to take out the tilt in the straightedge. The measurements were taken while moving the X carriage in the positive direction and in the negative direction to determine if the direction of travel effected the measurement. Some small discrepancies were noticed in the result but for the most part they are agreeable. The measurement result can be seen in Figure 5.60.

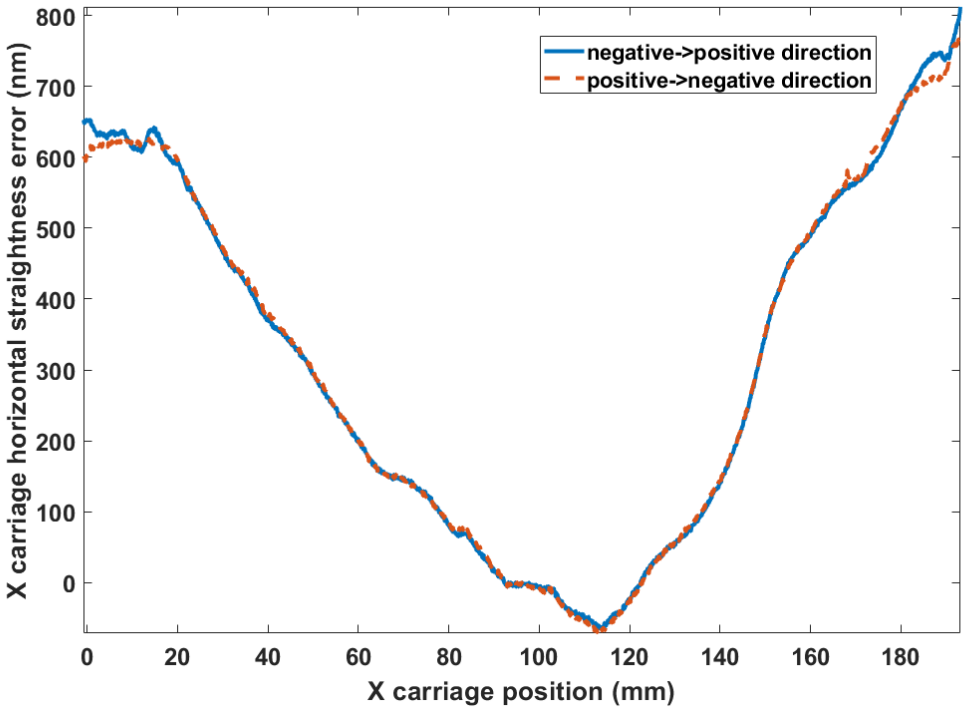

Figure 5.60: The X carriage horizontal straightness error on the Moore Nanotech 100UMM.

The measurement of the straightedge is shown in Figure 5.61.

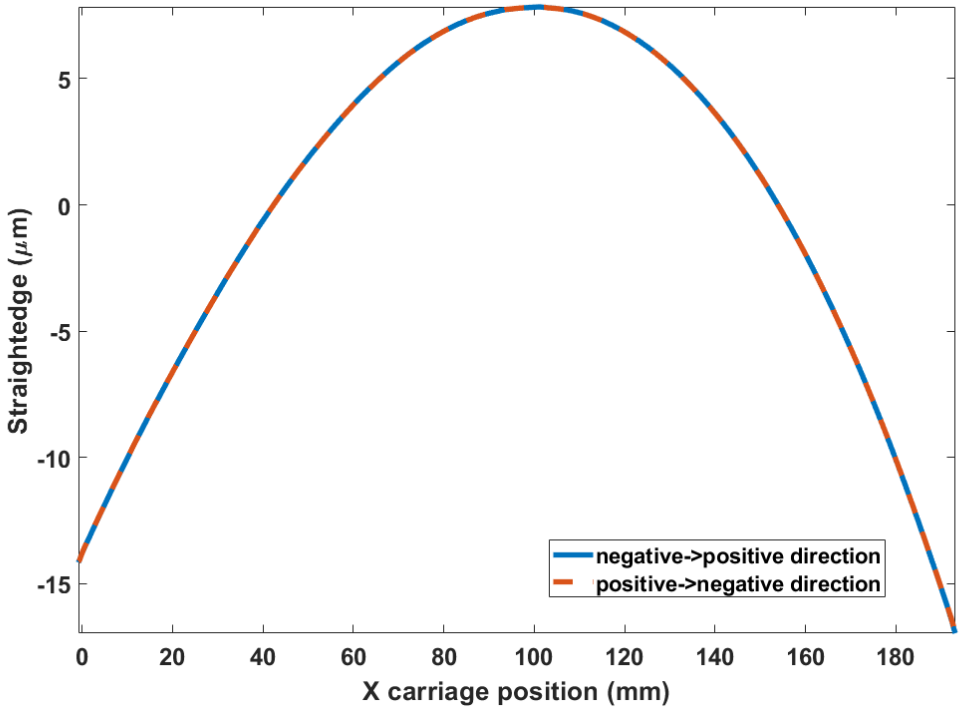

Figure 5.61: Measurement of the straightedge used to measure the X carriage horizontal straightness error on the Moore Nanotech 100UMM using reversal.

The straightedge measurement is found using equation 5.13 above. There is agreement between positive X carriage direction measurement and the negative X carriage direction measurement. The X carriage horizontal straightness will be used with the mathematical model of the 100UMM for error compensation. Uncertainty contributions are to be considered as they will be used in determining the task specific uncertainty in parts measured on the 100UMM after the error compensation has be completed. The measurement result from the initial measurements before the enclosure are roughly twice the magnitude of the final measurements. The discrepancies could be the location of the measurement as much of the straightness error is due to roll in the X carriage. Further work in tracking and correcting this discrepancy will be conducted.

5.47 X Carriage Squareness Measurement

For the optics measured in this research, the measurement result is sensitive to the X carriage squareness or the squareness of the X carriage in the Z direction. This could also be called the C-X carriage squareness since the rotational axis of the C carriage establishes the Z axis of the frame coordinate system in the mathematical model. To measure the X carriage squareness a 1-inch precision steel ball was used on an aluminum standoff. The C carriage on the 100UMM has two 1/4-20 threaded holes used for securing the air bearing during shipping and when the air bearing does not have air. The aluminum standoff has a threaded stud that is screwed into one of these threaded holes. The precision steel ball is also attached with a threaded rod. The setup can be seen in Figure 5.62 with both measurement positions.

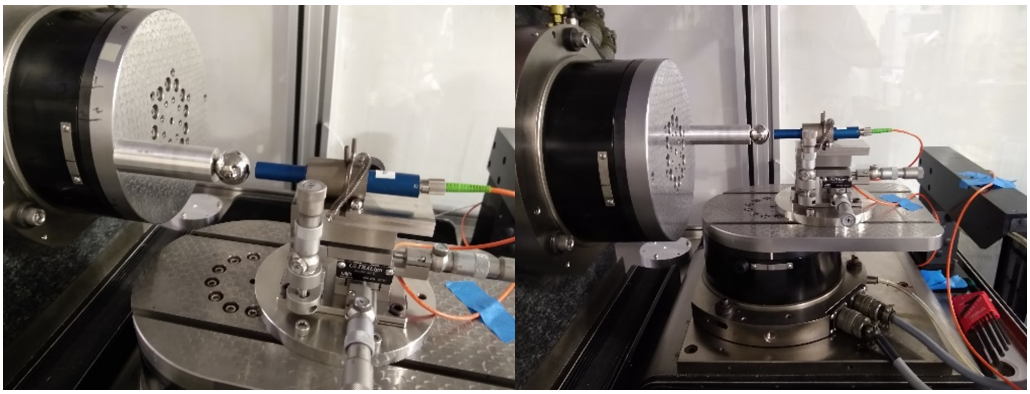

Figure 5.62: Setup for measuring X carriage squareness using a 1-inch steel ball and chromatic confocal probe showing both measurement positions.

Since the rotational axis of the C carriage establishes the Z axis of the frame coordinate system, the X carriage squareness will then be measured and modeled with respect to the Z axis. The measurement will be corrected for the X carriage horizontal straightness as it will be present in the measurement.

To find the center of the steel ball, it was 'crowned' using the Precitec chromatic confocal probe. To reduce any error from the height of the probe or positioning error of the C carriage the center of the ball was found on the "left" and "right" side of

the measurement. Ideally the rotation would be 180° but in reality, if the probe is below the axis of rotation of the C carriage the rotation would be more than 180° and if it is above, the rotation will be less than 180°. The process of crowning by moving the C and X carriages to minimize the displacement on the probe was done by switching back and forth between the two carriage movements during crowning until the center is found. This may take a few changes between manipulating the two carriage positions. The pitch and/or roll in the X carriage could also affect the measurement result. The squareness measurement is shown in Figure 5.63 with the two positions.

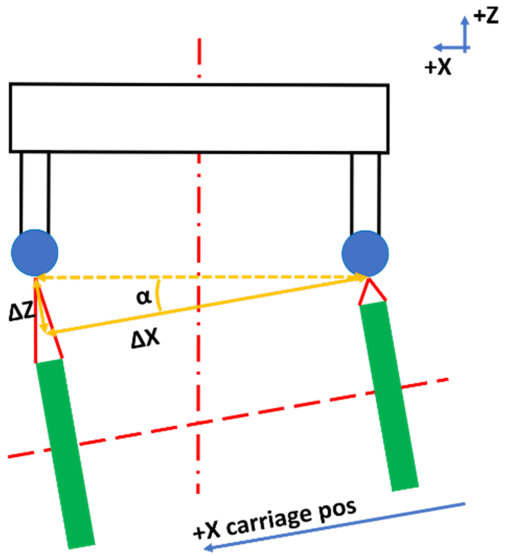

Figure 5.63: X carriage squareness on the Moore Nanotech 100UMM showing the two measurement positions and the geometry of a squareness error.

Equation 5.14 was used to calculate the X carriage squareness.

$$\alpha = tan^{-1}\frac{\Delta Z}{\Delta X} \tag{5.14}$$

The result is used in the model with the units of radians. A squareness error will show up in the measurement as a cone shape when using one radial direction. The squareness error of the 100UMM is shown below in two of the probe paths used for this research.

5.48 Uncertainty in the Measurement of Machine Errors

From the GUM, "the result of a measurement after correction for recognized systematic effects is still only an estimate of the value of the measurand because of the uncertainty arising from random effects and from imperfect correction of the result for systematic effects." A common mistake, uncertainty is the property of a measurement, not a machine or instrument. The GUM defines uncertainty of measurement as "the parameter associated with the result of a measurement, that characterizes the dispersion of the values that could reasonably be attributed to the measurand [12], [13]."

The machine error measurement uncertainty is used in a Monte Carlo simulation to evaluate the task specific uncertainty of parts measured on the 100UMM. An uncertainty evaluation is conducted with guidance from the Guide to Uncertainty in Measurement (GUM) [12]. The GUM divides uncertainty evaluation into Type A and Type B. For each of the machine error measurements measured, the uncertainty is evaluated and becomes a part of the uncertainty budget. The GUM explains "Type A standard uncertainty is obtained from a probability density function derived from an observed frequency distribution, while a Type B standard uncertainty is obtained from an assumed probability density function based on the degree of belief that an event will occur [12]." In other words, a Type A uncertainty evaluation is of statistical means while a Type B uncertainty evaluation encompasses all other means and may be based on the experience of the metrologist. The GUM points out that while "the purpose of the Type A and Type B classification is to indicate the two different ways of evaluating uncertainty components and is for convenience of discussion only; the classification is not meant to indicate that there is any difference in the nature of the components resulting from the two types of evaluation [12]."

In the machine model, the standard uncertainty and combined standard uncertainty will be used for the uncertainty in the machine error measurements. Standard

uncertainty is defined as the "uncertainty of the result of a measurement expressed as a standard deviation [12]." The combined standard uncertainty is "standard uncertainty of the result of a measurement when that result is obtained from the values of a number of other quantities, equal to the positive square root of a sum of terms, the terms being the variances or covariances of these other quantities weighted according to how the measurement result varies with changes in these quantities [12]." There is too much information to go into here, but the GUM clearly lays out the nuances and procedures for evaluating uncertainty.

Two more important terms are the expanded uncertainty and coverage factor. Expanded uncertainty is the "quantity defining an interval about the result of a measurement that may be expected to encompass a large fraction of the distribution of values that could reasonably be attributed to the measurand [12]." The coverage factor is a "numerical factor used as a multiplier of the combined standard uncertainty in order to obtain an expanded uncertainty [12]." Simply put, to calculate the expanded uncertainty the coverage factor is multiplied by the standard uncertainty. The coverage factor increases the amount of certainty that the value will fall between the values of the measurement result when properly stated.

5.49 Probability Distribution for Measurement Uncertainty

It may be informative to discuss the type A or statistical evaluation of measurement uncertainty. If we think of a measurement as producing a single value, we can build the groundwork for evaluating and thinking about measurement uncertainty and be able to expand that understanding to a more complex measurements or measurands such as those in this research. If a measurement is repeated many times and the results are recorded, a data set is built that can be statistically evaluated. The distribution of these measurement results will likely (but not always) trend toward a normal distribution.

To better visualize the type A uncertainty the probability density function of a

normal distribution is shown in Figure 5.64.

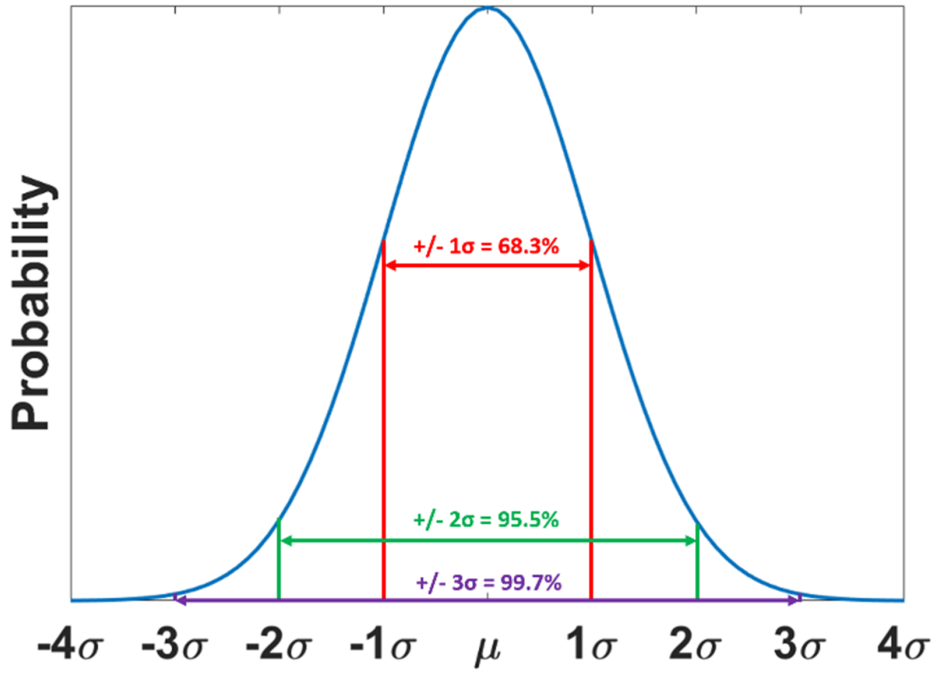

Figure 5.64: Probability density function of the normal distribution with the expectation value (μ) and the standard deviation (σ).

Note that the area under the curve represents the probability. We can estimate the measurement result, sometimes called the expectation (μ), by using the mean of the repeated measurements. The experimental standard deviation is used to evaluate the uncertainty in the mean or the experimental standard deviation of the mean. The coverage factor increases the amount of certainty in the estimation of the expectation value and is multiplied by the standard uncertainty or combined standard uncertainty.

5.50 Sources of Uncertainty

For measurements on the Nanotech 100UMM some of the sources of uncertainty are shown in an Ishikawa diagram which was adapted from Reference [43]. The Ishikawa diagram (Figure 5.65) provides a visual representation of the influence of uncertainty contributors organized by categories.

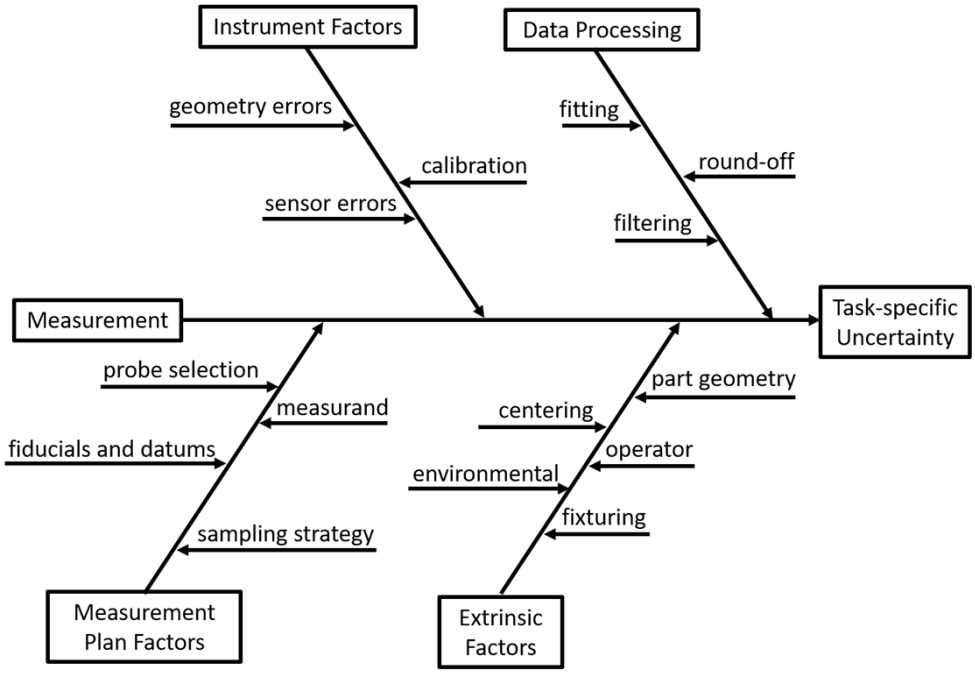

Figure 5.65: Ishikawa diagram for the uncertainty contributions for a measurement on the Nanotech 100UMM.

This is meant as a broad collection of the uncertainty influences. For a more detailed diagram of the uncertainty sources used in the Monte Carlo simulation see the mind map in Appendix D.

5.51 Electronic Levels Measurements

The differential levels were used in the angular measurements of roll and pitch of the linear carriages. The measurement uncertainty was evaluated using the GUM Type A uncertainty.

The best estimate of the variance of the mean, s, is shown in equation 5.15 [12]. Where the variance of the mean, σ is given by equation 5.16.

$$s^2(\overline{q}) = \frac{s^2(q_k)}{n} \tag{5.15}$$

$$\sigma^2(\overline{q}) = \frac{\sigma^2}{n} \tag{5.16}$$

Where n is the independent repeated observations and q_k is the individual obser-

vations. The GUM states that the experimental standard deviation of the mean, $s(\overline{q})$, estimates the expectation value μ_q of q, and may be used as a measure of the uncertainty of $\overline{q}$ [12]. For the measurements in this research that are evaluated using the Type A uncertainty the equation 5.17 will be used.

$$s(\overline{q}) = \frac{s(q_k)}{\sqrt{n}} \tag{5.17}$$

It may have been noticed that the uncertainty goes down with an increase in the number of measurements. The uncertainty in the X carriage roll measurement is shown in Figure 5.66.

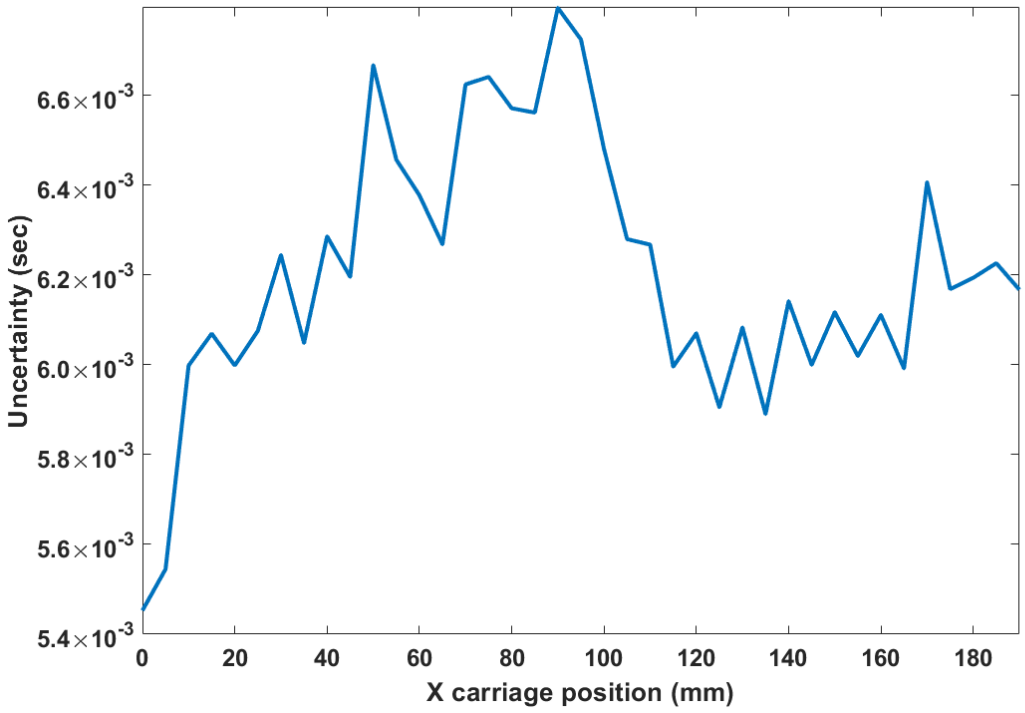

Figure 5.66: X carriage roll error measurement uncertainty.

The uncertainty in the X carriage pitch measurement is shown in Figure 5.67.

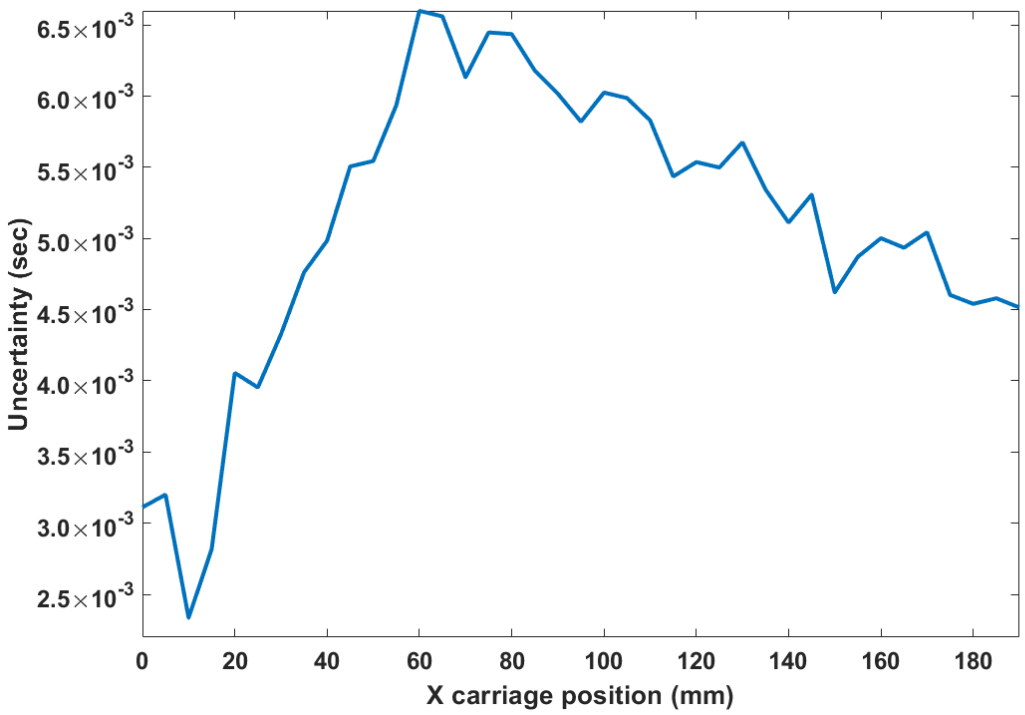

Figure 5.67: X carriage pitch error measurement uncertainty.

The uncertainty in the Z carriage roll measurement is shown in Figure 5.68.

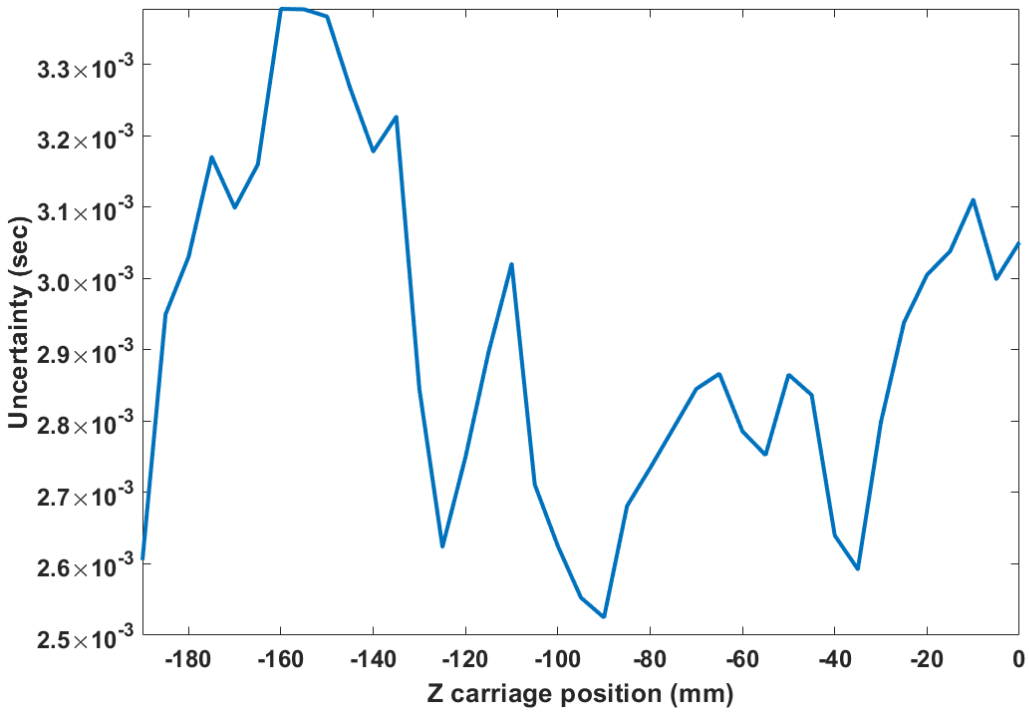

Figure 5.68: Z carriage roll error measurement uncertainty.

The uncertainty in the Z carriage pitch measurement is shown in Figure 5.69.

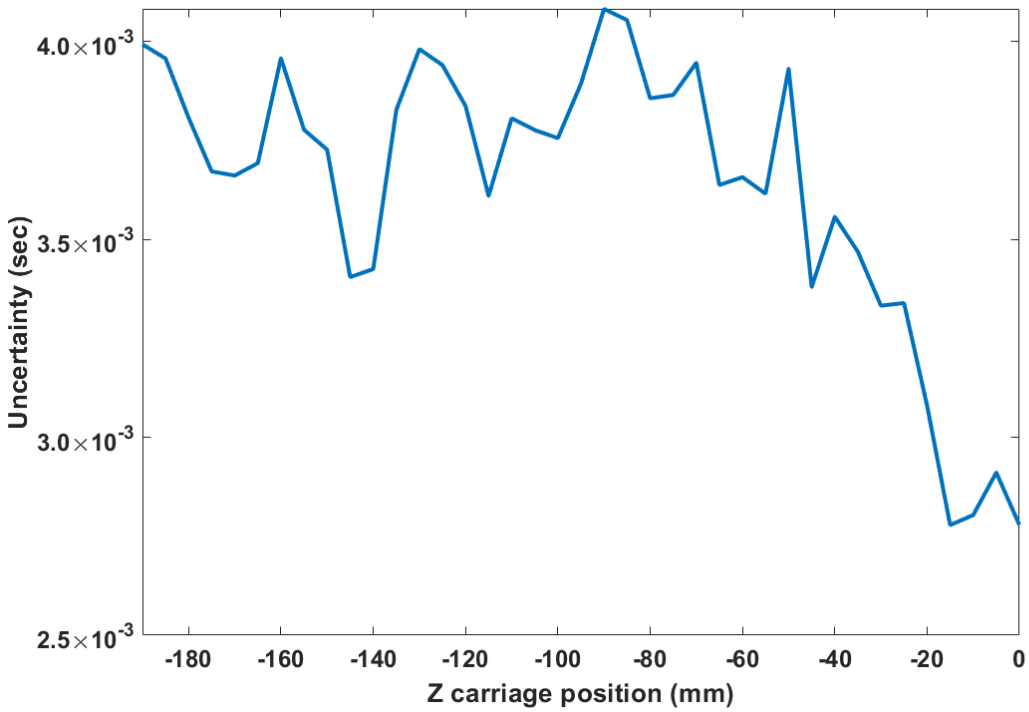

Figure 5.69: Z carriage pitch error measurement uncertainty.

5.52 Agilent Laser System Measurements

The laser measurements are like the level measurements and will also be a Type A evaluation following the GUM. There is an uncertainty contribution due to the correction for temperature, pressure, and humidity that will not be considered. The uncertainty in the X carriage positioning error measurement is shown in Figure 5.70.

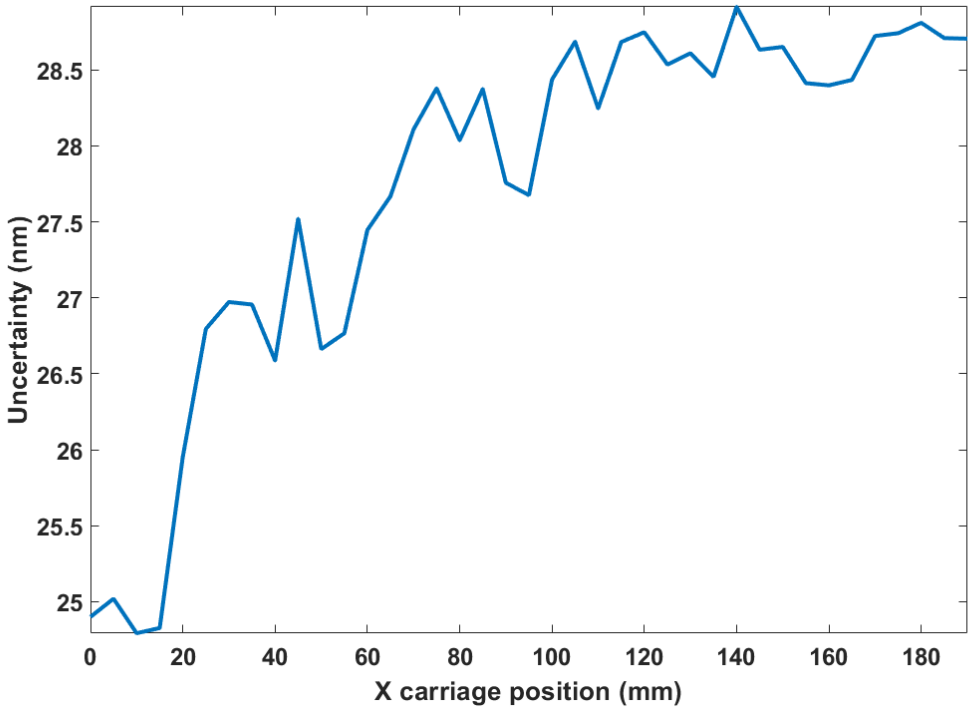

Figure 5.70: X carriage positioning error measurement uncertainty.

The uncertainty in the Z carriage positioning error measurement is shown in Figure 5.71.

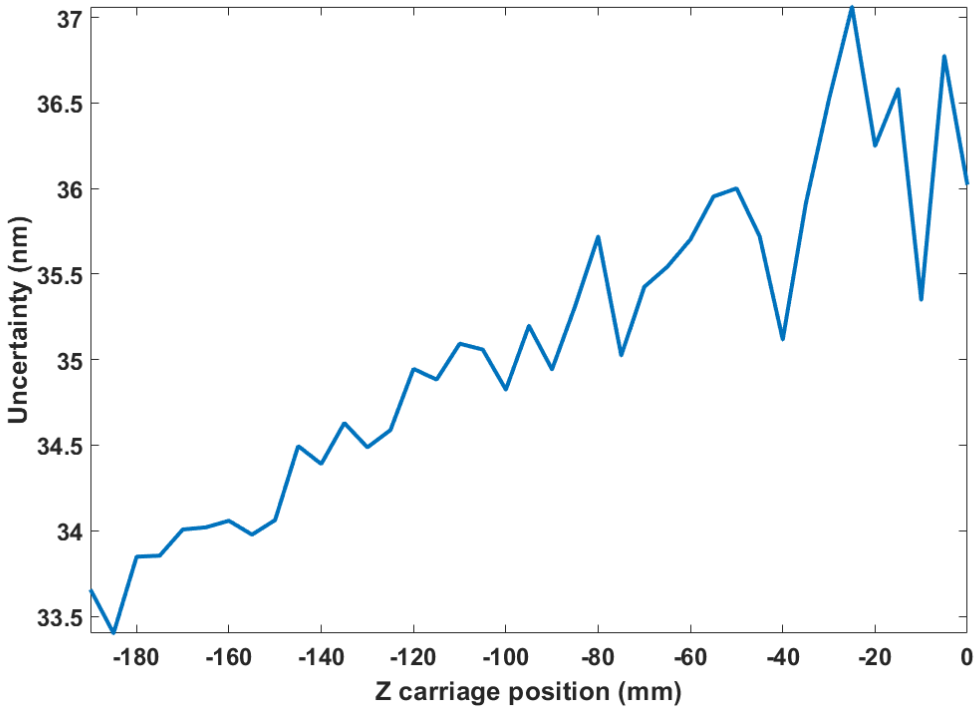

Figure 5.71: Z carriage positioning error measurement uncertainty.

The uncertainty in the X carriage yaw measurement is shown in Figure 5.72.

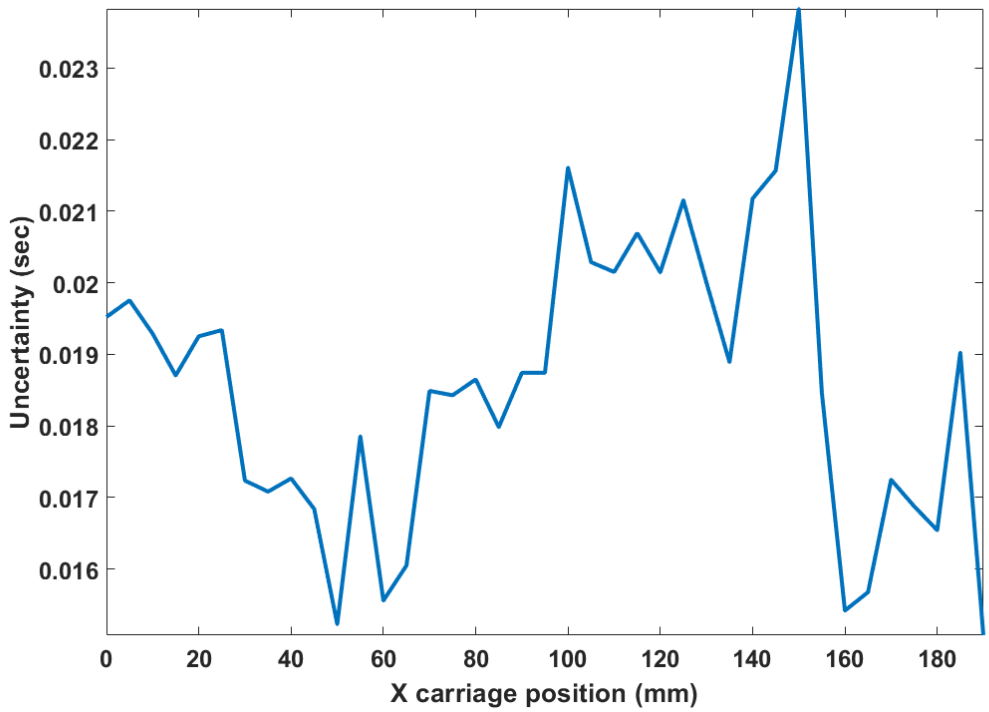

Figure 5.72: X carriage yaw error measurement uncertainty.

The uncertainty in the Z carriage yaw measurement is shown in Figure 5.73.

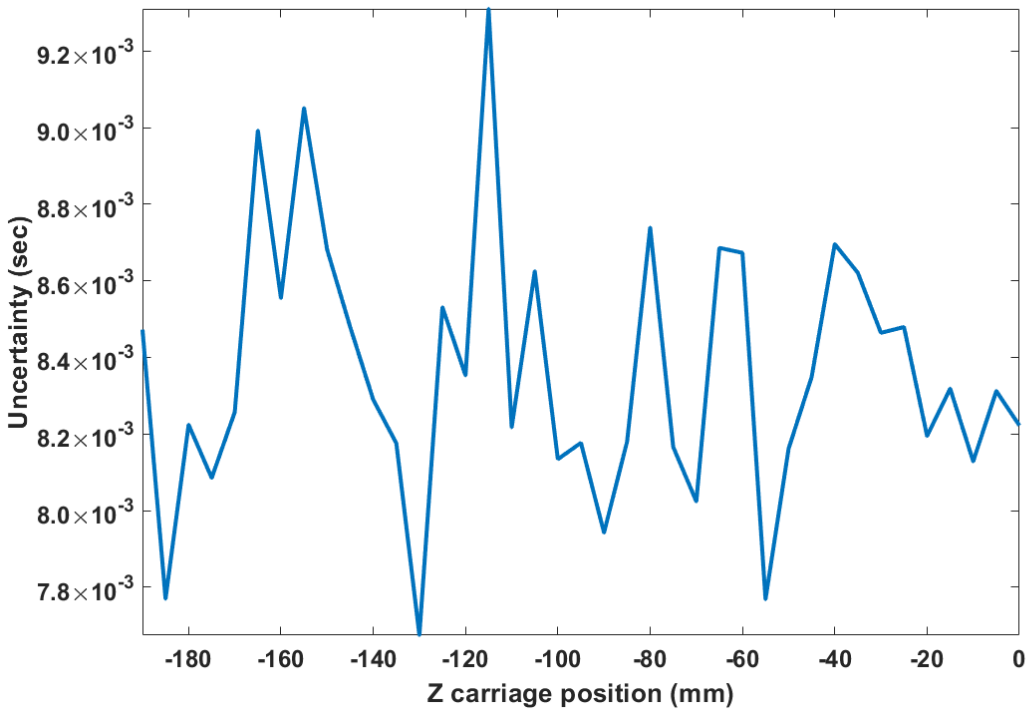

Figure 5.73: Z carriage yaw error measurement uncertainty.

5.53 Probe Noise Uncertainty Contribution

The probe noise uncertainty contribution changes depending on the averages and rate of data collection, so the uncertainty is evaluated for each measurement. To quantify the Type A probe noise uncertainty in each measurement the probe calibration is used. This process is done for every measurement. The calibration has 21 points where the probe displacement is recorded for a stationary position through the probe range used in the measurement. Each position records the probe displacement for 5 seconds. The standard deviation is taken for each of those 21 positions and the uncertainty is calculated using equation 5.17. The uncertainty contribution from probe noise was found to be sub-nanometer so was deemed negligible for the measurements of the half scale tertiary.

5.54 X Carriage Horizontal Straightness

The uncertainty in the X carriage horizontal straightness is found using the combined standard uncertainty since the measurement result has multiple inputs. The inputs are assumed to be uncorrelated (independent). The GUM lays out the procedure for combining the standard uncertainties for independent data with equation 5.18 [12].

$$u_c^2(y) = \sum_{i=1}^{N} \left(\frac{\partial f}{\partial x_i} \right)^2 u^2(x_i) \tag{5.18}$$

Where f is the function, y is the estimate of the measurand, x_i is the input estimates, $u^2(x_i)$ is the standard uncertainty, $u_c^2(y)$ is the combined standard uncertainty and $\frac{\partial f}{\partial x_i}$ is the sensitivity coefficient.

For the X carriage horizontal straightness, the function is given by equation 5.12. The standard uncertainties are found using the same Type A method as the levels and interferometer. Calculating the sensitivity coefficients is done in equation 5.19 and 5.20.

$$\frac{\partial M(x)}{\partial R(x)} = \frac{1}{2} \tag{5.19}$$

$$\frac{\partial M(x)}{\partial N(x)} = -\frac{1}{2} \tag{5.20}$$

To find the combined standard uncertainty equation 5.21 is used.

$$u_c(M(x)) = \sqrt{\left(-\frac{1}{2}\right)^2 (u(N(x)))^2 + \left(\frac{1}{2}\right)^2 (u(R(x)))^2} \tag{5.21}$$

The computation of the combined standard uncertainty as a function of the X carriage position was done in MATLAB. A more comprehensive estimation of the uncertainty would include thermal considerations, the ability to reposition the probe after the reversal and the distortion in the mirror after reversal. Using an artifact with less deviation could also reduce the amount of uncertainty. The results of the measurement uncertainty evaluation are shown in Figure 5.74.

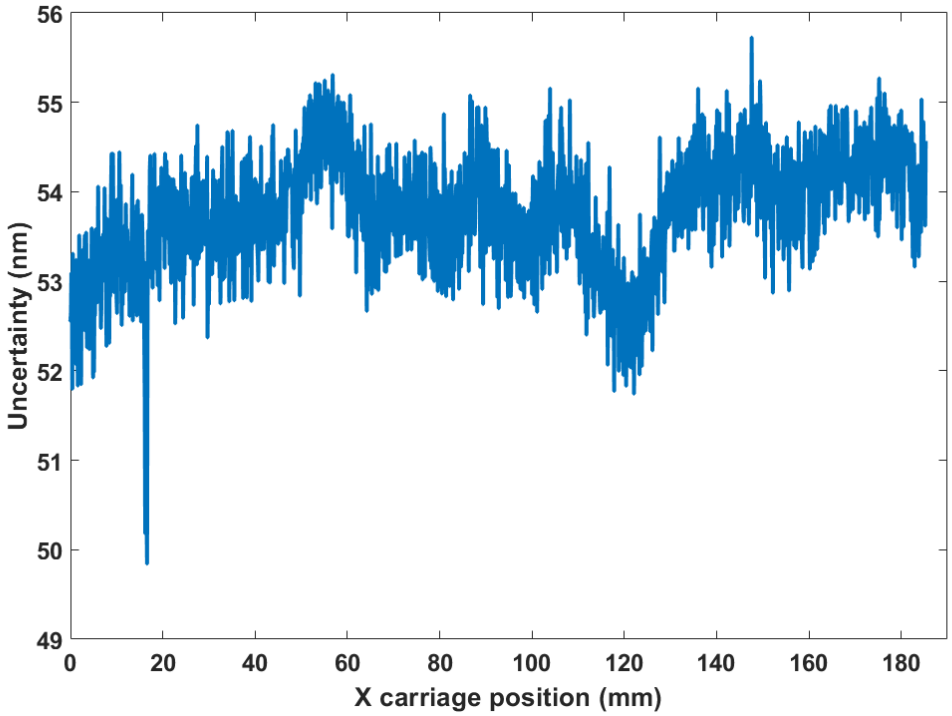

Figure 5.74: Uncertainty in the X carriage horizontal straightness measurements used in the Monte Carlo simulation.

5.55 X Carriage Squareness

For the parts measured in this research the X carriage squareness is one of the most sensitive error motions. For the Monte Carlo simulation this makes the uncertainty evaluation of the X squareness error measurement important. The equation used to the determine the squareness is shown in equation 5.22.

$$\alpha = tan^{-1}\frac{\Delta Z}{\Delta X} \tag{5.22}$$

Where the combined standard uncertainty is shown in equation 5.23.

$$u_c(\alpha) = \sqrt{(u_{\Delta X})^2\left(\frac{\partial \alpha}{\partial \Delta X}\right)^2 + (u_{\Delta Z})^2\left(\frac{\partial \alpha}{\partial \Delta Z}\right)^2} \tag{5.23}$$

With the partial derivatives or sensitivities shown in equation 5.24 and equation 5.25.

$$\frac{\partial \alpha}{\partial \Delta X} = -\frac{\Delta Z}{\Delta X^2 + \Delta Z^2} \tag{5.24}$$

$$\frac{\partial \alpha}{\partial \Delta Z} = \frac{\Delta X}{\Delta X^2 + \Delta Z^2} \tag{5.25}$$

The combined standard uncertainty for each variable is shown in equation 5.26 and equation 5.27.

$$u_{\Delta X} = \sqrt{(920\,nm)^2 + (10\,\mu m)^2} = 10.042\,\mu m \tag{5.26}$$

$$u_{\Delta Z} = \sqrt{(10\,nm)^2 + (5\,nm)^2 + (40\,nm)^2 + (5\,nm)^2} = 41.8\,nm \tag{5.27}$$

The estimated uncertainty contributions to the ΔX variable are shown in Table 5.6.

Table 5.6: Contributions to the uncertainty in the ΔX variable for calculating the X carriage squareness error.

Uncertainty Contribution	Value
Positioning Error	920 nm
Crowing (re-finding center of ball) x2	10 μm
Std Dev. of Scales	~

The estimated uncertainty contributions to the ΔZ variable are shown in Table 5.7.

Table 5.7: Contributions to the uncertainty in the ΔZ variable for calculating the X carriage squareness error.

Uncertainty Contribution	Value
Probe Noise	0.125 nm
Probe Calibration Error	10 nm
Crowning (in Z direction) x2	5 nm
X Carriage Horizontal Straightness (corrected)	40 nm
Std Dev. of Probe	5 nm

The results of the uncertainty evaluation are shown in equation 5.28.

$$u_c(\alpha) = 2.43\, x10^{-7}\, radians \tag{5.28}$$

5.56 Estler's Face Motion Reversal

The uncertainty in the Estler's face motion reversal was evaluated using a Type A measurement uncertainty. The measurement was repeated 5 times for each setup. The uncertainty is evaluated following the GUM for combined standard uncertainty [12]. The symbol T is used for the face motion. The measurement equation is shown in equation 5.29.

$$T(R,\theta) = \frac{1}{R}\left(\frac{I_2'(\theta) - I_1'(\theta)}{2} - I_3'(\theta)\right) \tag{5.29}$$

The sensitivity factors are calculated in equation 5.30 through 5.32.

$$\frac{\partial T}{\partial I_1'} = -\frac{1}{2R} \tag{5.30}$$

$$\frac{\partial T}{\partial I_2'} = \frac{1}{2R} \tag{5.31}$$

$$\frac{\partial T}{\partial I_2'} = -\frac{1}{R} \tag{5.32}$$

The uncertainty in the Estler face motion reversal components is shown in equation

5.33 through 5.35.

$$u_{I_1'} = \frac{s(I_1')}{\sqrt{n}} \tag{5.33}$$

$$u_{I_2'} = \frac{s(I_2')}{\sqrt{n}} \tag{5.34}$$

$$u_{I_3'} = \frac{s(I_3')}{\sqrt{n}} \tag{5.35}$$

The combined standard uncertainty is shown in equation 5.36.

$$u_c(T) = \sqrt{\left(u_{I_1'}\right)^2 \left(\frac{\partial T}{\partial I_1'}\right)^2 + \left(u_{I_2'}\right)^2 \left(\frac{\partial T}{\partial I_2'}\right)^2 + \left(u_{I_3'}\right)^2 \left(\frac{\partial T}{\partial I_3'}\right)^2} \tag{5.36}$$

Figure 5.75 shows the combined standard uncertainty in the Estler's face motion reversal.

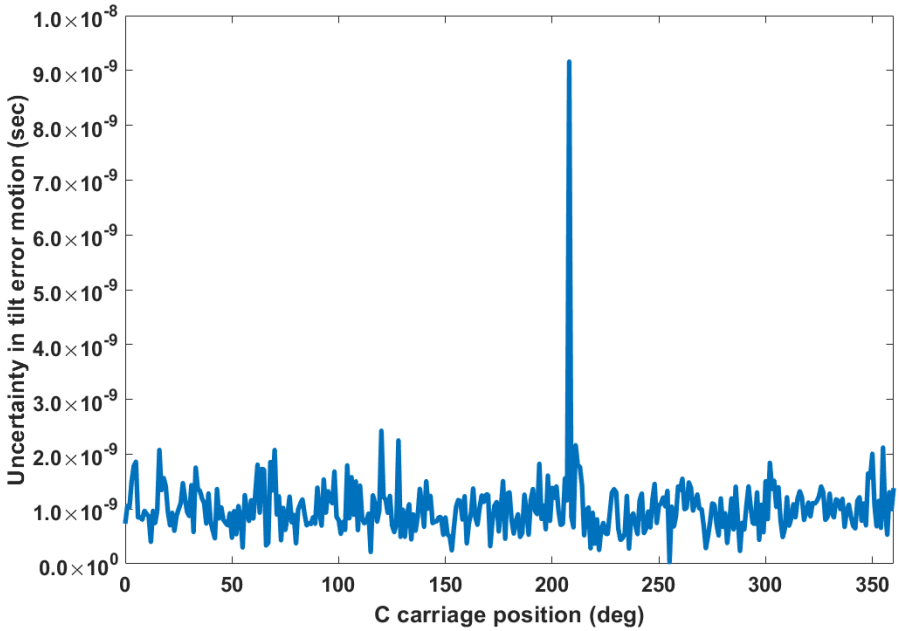

Figure 5.75: Combined standard uncertainty of the Estler's face motion reversal measurement on the C carriage of the Nanotech 100UMM.

CHAPTER 6: THERMAL DRIFT

It became clear while characterizing the 100UMM that thermal drift needed to be addressed to get the performance required. This began with the environmentally controlled enclosure and removing unnecessary heat loads from around the machine. Even with these improvements it was found that the probe displacement follows the enclosure temperature in the plenum which follows the temperature of the surrounding laboratory. Thermal coupling could be coming from the probe, sensor box, carriages of the machine, electronics in scales, etc. To illustrate the problem, results from a drift test inside the enclosure using the chromatic confocal probe are shown below.

6.1 Drift Tests

Drift tests were used to quantify the thermal stability of the 100UMM. They were conducted using the differential levels, capacitance gauges and the chromatic confocal probes for displacement sensors and thermistors as temperature sensors.

6.2 Dynamic Position Drift Test

Before the enclosure was installed a positioning drift test was conducted to determine the effect of the hydrostatic bearing heating up the ways of a carriage after it had been in one position at the end of the ways for an extended amount of time then moved to the opposite end of the ways. The electronic levels were used to quantify this effect with one level on the carriage of interest and one on a stationary carriage for reference. The angle between the differential levels was recorded after moving to the second position. The angular measurements shown in Figure 6.1 and Figure 6.2 are the result of this test for a 20 minute interval. For the X carriage pitch dynamic drift test the electronic level configuration shown in Figure 6.1.

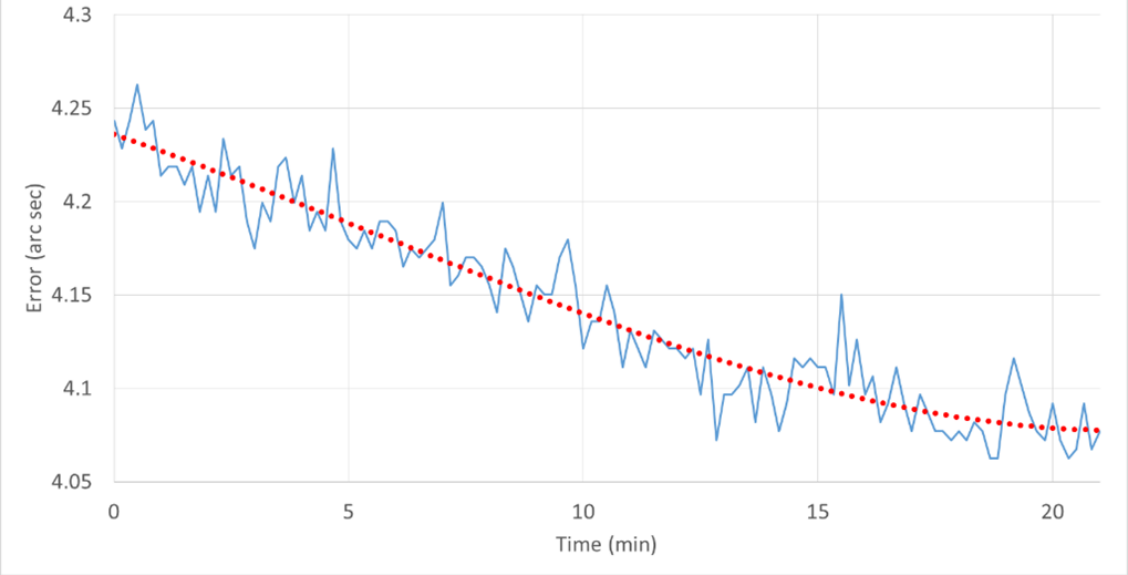

Figure 6.1: Drift in the X carriage pitch during the dynamic positioning test on the Nanotech 100UMM.

The trend of the measurement data showing an exponential decay is customary of thermal drift. Drift in the differential levels for the Z carriage roll orientation during the dynamic drift test can be seen in Figure 6.2.

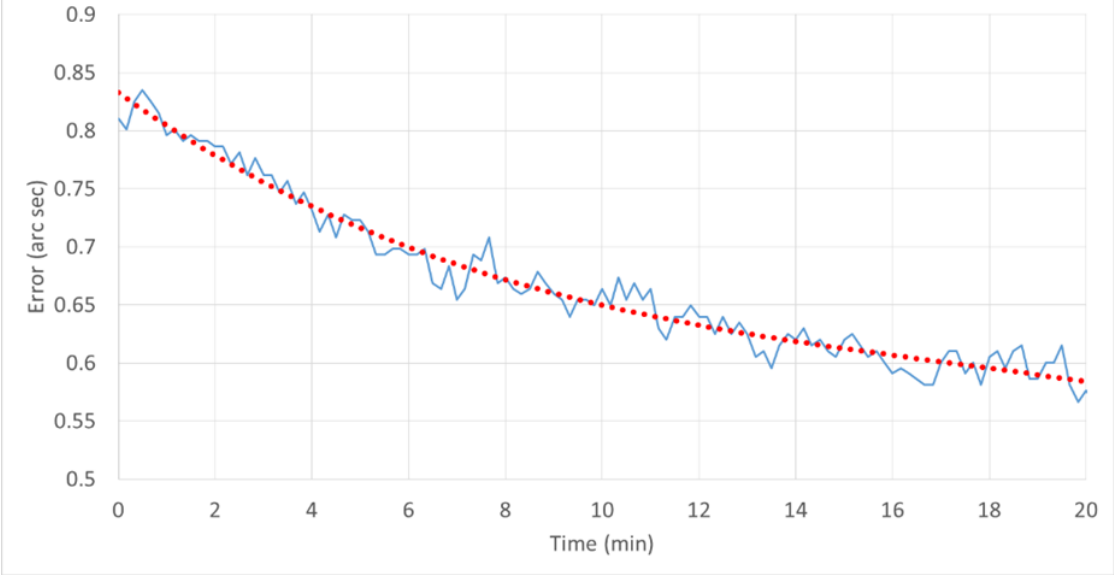

Figure 6.2: Drift in the Z carriage roll during the dynamic positioning test on the Nanotech 100UMM.

It was not expected that the roll would be affected as much by heating of the ways

as the ways are symmetric in the roll direction. The thermal drift shown here led to further investigations into the drift in the machine due to the hydrostatic bearings.

6.3 Thermal Drift Test Before the Environmental Enclosure

A thermal drift test was conducted using a precision steel sphere, three capacitance gauges made by Lion Precision and seven thermistors. The system is an older model of the Lion Precision SEA used in the X carriage horizontal straightness measurements. It comes with software for thermal drift testing. A fixture is provided to align the capacitance gauges in orthogonal directions. The fixture was held to the B carriage using magnets. The setup can be seen in Figure 6.3.

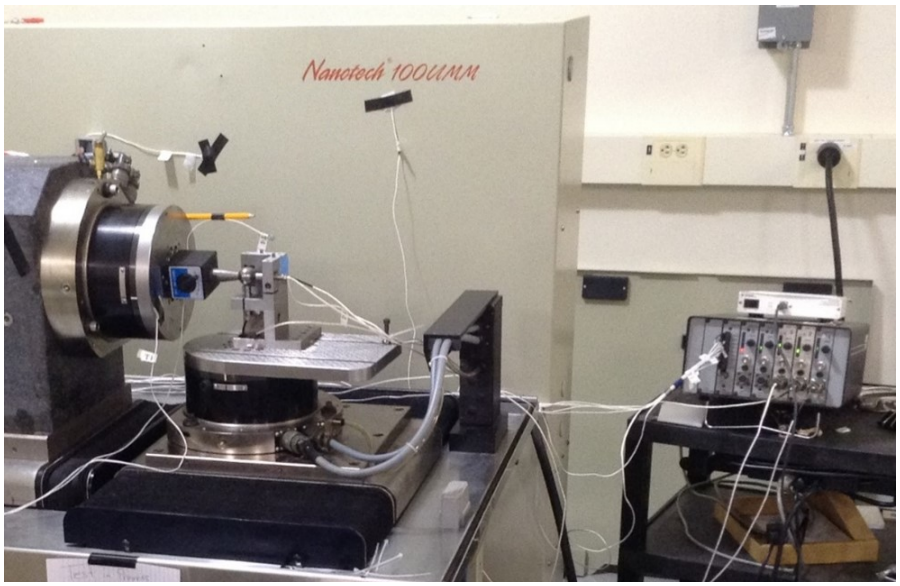

Figure 6.3: Thermal drift test using three capacitance gauges and seven thermistors from the Lion Precision SEA system.

The test was conducted over a 24-hour period. The sphere used is no longer a precision sphere due to rough handling however it was decided that for this test the sphere would be sufficient. A close-up of the capacitance gauge setup and fixture is shown in Figure 6.4.

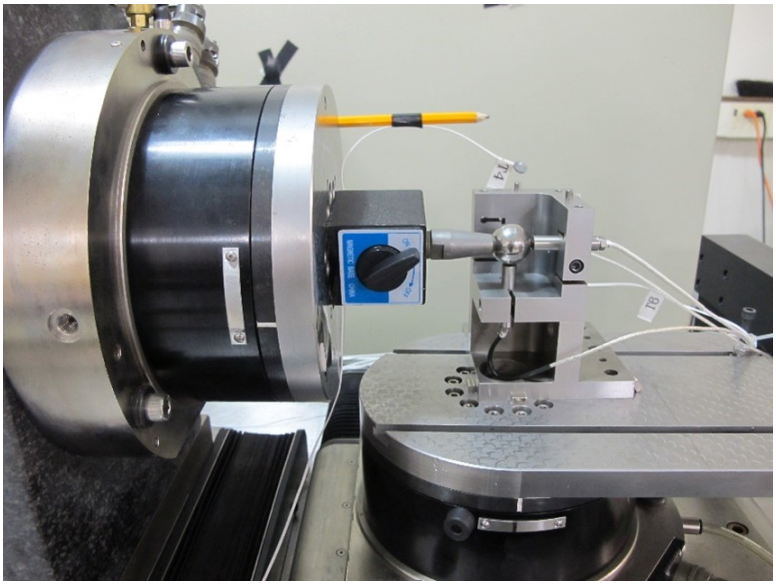

Figure 6.4: Capacitance gage setup for the thermal drift test using a steel ball and fixture for 3 capacitance gages orthogonal to one another.

The capacitance gauges were centered by moving the axis perpendicular to the one being test by the capacitance gauge and looking for a minimum in the gap distance. This process is illustrated in Figure 6.5.

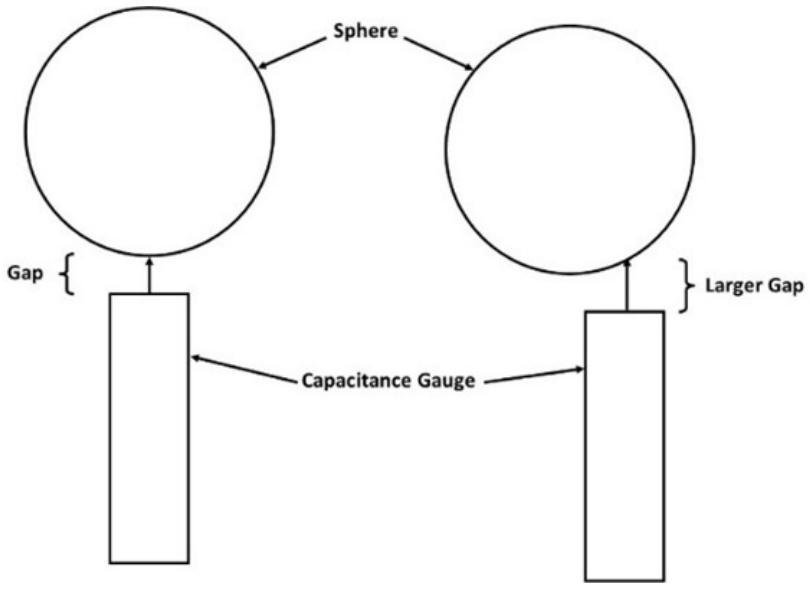

Figure 6.5: Centering the capacitance gauges on the sphere.

The first axes to be centered were the x and z axis probes. Since the y axis cannot

be controlled by the machine the magnetic base with the sphere attached was raised and lowered to find the minimum distance. Once the y direction height was centered the x axis probe was centered by moving the Z carriage in and out to find the minimum distance. The same process is used for the z axis probe moving the X carriage and finding the minimum. The process is then repeated to make sure nothing changed while aligning the other directions. See also probe setting and alignment (Section 4.8)

The metal side of the thermistor was placed on the surface of interest. A piece of foam insulation was placed on top of the thermistor and taped to the surface. The thermistors were placed in areas of interest around the machine to both better understand the change in temperature of the areas used in measurements and to find the areas of heat generation on the machine. The thermistors were placed according to the positions indicated in Table 6.1.

Table 6.1: Thermistor temperature probe placement on Nanotech 100UMM during drift test before the enclosure was installed.

Sensor	Location
T1	face of C carriage
T2	electronics cabinet (upper right)
T3	top of hydraulic pump motor shroud
T4	air temp. above sphere
T5	air temp. below machine
T6	capacitance gauge fixture
T7	electronics cabinet (upper left)

Figure 6.6 shows the 24-hour drift test with the seven thermistors and the three capacitance gauges.

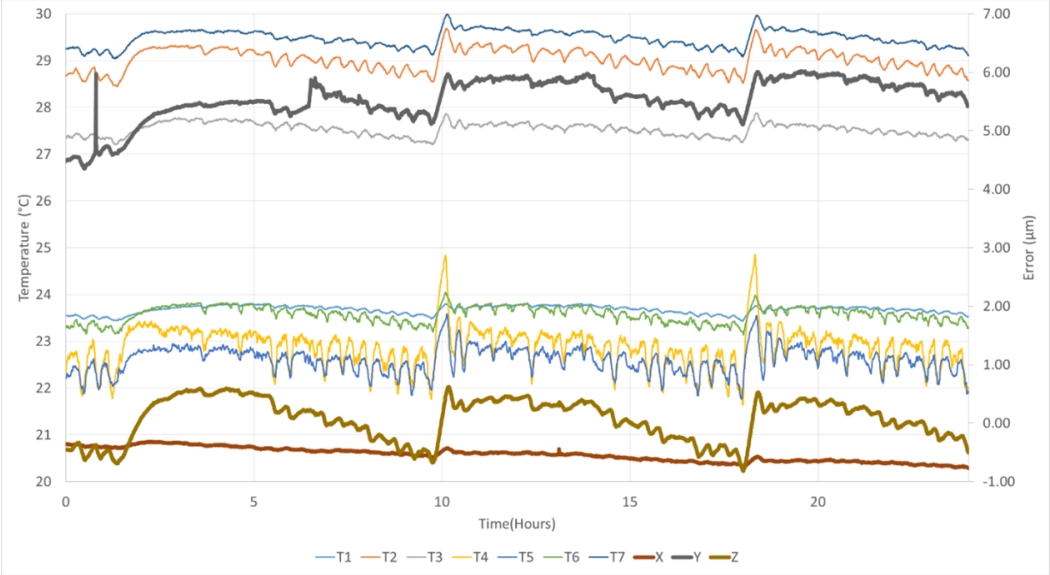

Figure 6.6: Drift test using three capacitance gauges and seven thermistors from the Lion Precision SEA.

The scale on the left is temperature in Celsius while the right scale is the error or change in position in micrometers. It is evident that the position of the sphere changes with the change in temperature of the room. The Z axis is the most affected while the Y axis is less affected. The X axis is considerably less affected by the temperature change. There is a noteworthy event in the laboratory temperature every 8-10 hours. The temperature increases suddenly then slowly drifts back down until it increases suddenly again. This is referred to as a sawtooth effect and is due to the temperature control in the surrounding laboratory.

6.4 Chromatic Confocal Drift Tests After the Environmental Enclosure

To quantify the thermal stability of the machine and chromatic confocal probe after the environmentally controlled enclosure was installed a drift test is used. This allows abnormalities, patterns, or correlation in the change of temperature and displacement of the probe to be identified. If problems are identified that could affect the measurement, it is decided whether they can be avoided or if they need to be addressed. Drift tests were conducted using the newer model of the Lion Precision SEA and the

Precitec chromatic confocal probe. The SEA has five capacitance gages and seven thermistors. Drift tests were conducted over 48 hours to identify any abnormalities and trends that may affect measurements of varying length. The setup for the drift test can be seen in Figure 6.7.

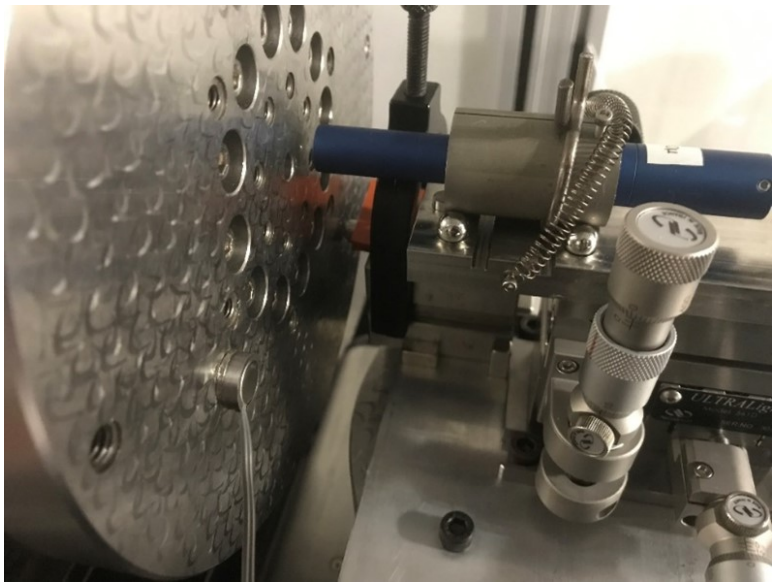

Figure 6.7: Drift test using thermistors and measuring the face of the C carriage with the Precitech chromatic confocal probe and capacitance gauge from the Lion Precision Spindle Error Analyzer (SEA).

The capacitance gage and chromatic confocal probe were set up to measure the face of the C carriage. Thermistors were placed around the machine and outside the enclosure to identify possible problem areas and establish the temperature in the surrounding laboratory. The test was conducted to identify any correlation between the temperature of the air in the enclosure and components of the machine with displacement in the probes and between the air temperature in the enclosure and outside the enclosure. In this case, both were found. Figure 6.8 shows the temperature outside the enclosure and the chromatic confocal probe displacement.

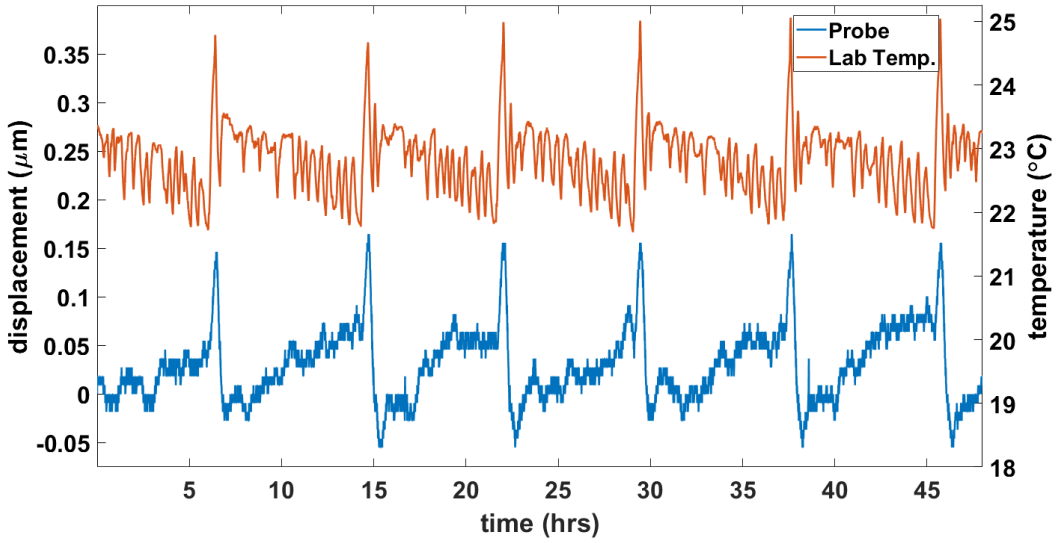

Figure 6.8: Drift test with temperature outside the enclosure and the Precitec chromatic confocal probe over 48 hours.

The probe displacement generally follows the inverse of the enclosure temperature except for when there is a spike in the temperature which happens roughly every eight hours. The chromatic confocal probe is of interest since that is the probe that will be used in measuring the mirrors. The capacitance gage offers a comparison to ensure that the drift is in the machine and not in the chromatic confocal probe. An area of interest for measurements is the air temperature near the part. Figure 6.9 shows the air temperature inside the enclosure just above where the part would be mounted on the C carriage along with the chromatic confocal probe displacement.

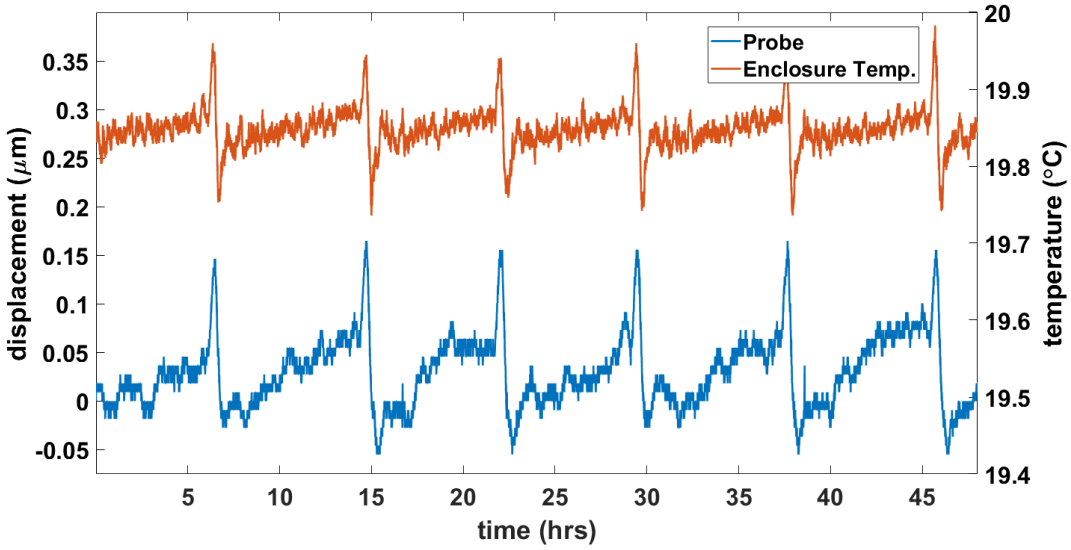

Figure 6.9: Drift test with temperature inside the enclosure and the Precitec chromatic confocal probe over 48 hours.

This is also where one of the feedback thermistors for the control system of the enclosure is located. Notice that the probe displacement follows the enclosure temperature closely including during the spike in temperature. It is noted that the drift in temperature inside the enclosure is generally inverse of the drift outside the enclosure with a different magnitude.

There is a need for a soak out period before measuring begins. Prior to a measurement a 2-hour dwell is included allowing time for the part, machine, fixturing and probe to come to temperature and equilibrium. Measurements are avoided during the rapid change in temperature if possible. The anomaly occurs roughly every 8 hours meaning that measurements longer than that amount of time will not be able to avoid it. The temperature of interest is near the part, other areas of the machine can be a different temperature if they are stable and do not affect the probe or part.

CHAPTER 7: FREEFORM OPTICS METROLOGY

The freeform optics measured in the probe path experiments are part of a project funded through the Center for Freeform Optics (CeFO) by the Air Force Research Laboratory (AFRL). The optics are part of a design, manufacture and metrology project of a 250 mm class three mirror anastigmat (TMA) telescope [44], [45], [46]. For this research, half-scale tertiary mirrors were made from an aluminum substrate with a Nickel Phosphorus coating for durability. The tertiary mirror is the third mirror in the system, just before the detector. The general shape is a concave mirror with a sag of 3.65 mm. Two of the half scale tertiary mirrors were manufactured by diamond turning. A half scale tertiary mirror is shown being measured in Figure 7.1.

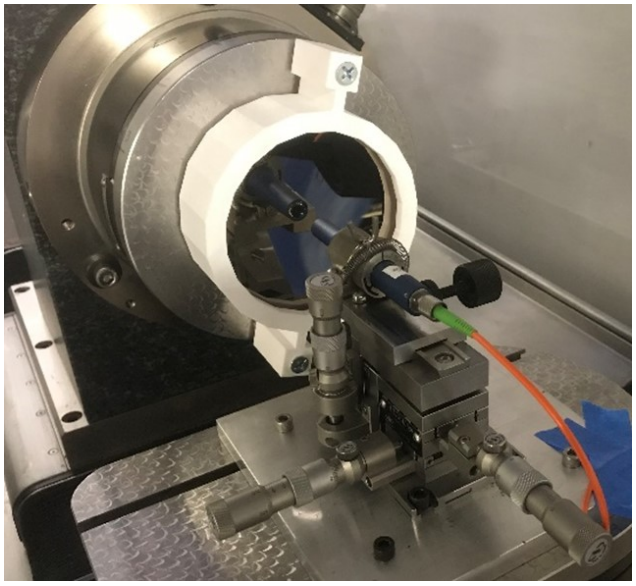

Figure 7.1: Half scale tertiary mirror mounted on the 100UMM showing the Precitec chromatic confocal probe and 3 degree of freedom probe holder.

The form of the optical surface is specified or prescribed with a base asphere and 21 Zernike polynomial coefficients with a normalization radius. Often Zernike polyno-

mials are normalized over the unit circle but the prescription for the AFRL telescope optics are specified at a specific normalization radius. The Zernike polynomials are what specify the freeform shape of the mirror or the departure from the base asphere. The prescribed shape is found by adding the base asphere and surface generated by the Zernike polynomials. Tolerancing of the prescription will not be discussed in this paper. Key attributes of the half scale tertiary can be found in Table 7.1.

Table 7.1: Characteristics of the half scale tertiary mirror.

Characteristic	Value
max slope	9°
clear aperture	92 mm
max sag	3.653 mm

A safety collar is used when mounting the part with vacuum in case the power is shut off or vacuum is lost. The vacuum safety is rapid prototyped plastic that does not touch the part but is close enough that if the vacuum fails, the safety will catch the part before the probe is damaged. An experiment was done to determine the effect of the vacuum on the shape of the part since it was used during manufacture and metrology. The vacuum was increased while recording the displacement on the probe, measuring the center of the part. It was found that over the range of the vacuum possible the part deflected 200 nm. The back of the part has been light weighted and there is a rim around the outside of the back of the part to ensure a good seal on the face of the C carriage. The data from the test is shown in Table 7.2.

Table 7.2: Testing the effect of vacuum during mounting of the half scale tertiary mirror from the AFRL optics on the C carriage of the Nanotech 100UMM.

Vacuum ($in - Hg$)	Displacement (μm)
-10	100.460
-11	100.483
-12	100.501
-13	100.530
-14	100.552
-15	100.570
-16	100.583
-17	100.603
-18	100.623
-19	100.635
-20	100.649
-21	100.660

If the mirror is deflecting during manufacturing and metrology, when the vacuum is removed the shape reflected in the measurement or intended to manufacture will differ. To ensure the change in displacement was not due to the spindle air bearing, a similar test was conducted where the spindle face was measured with a vacuum pulled against a diamond turned aluminum disc shown in Figure 7.2.

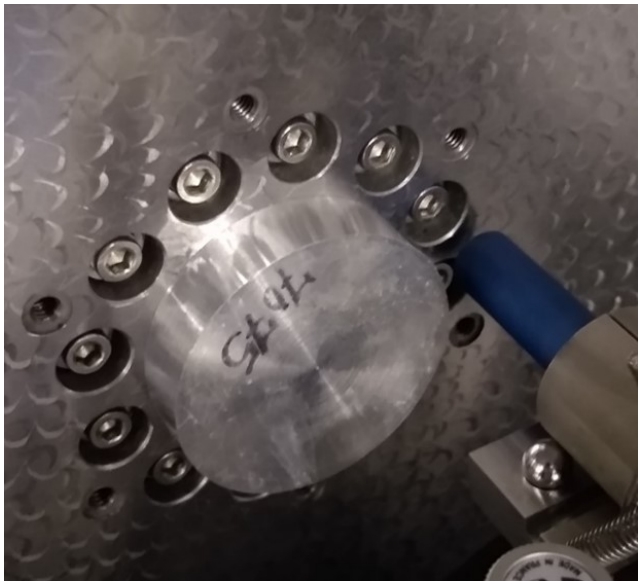

Figure 7.2: Testing the effect of vacuum on the air bearing of the C carriage.

The results of the test shown in Figure 7.2 are shown in Table 7.3.

Table 7.3: Results from a test to measure the effect of vacuum on the air bearing spindle of the C carriage.

Vacuum $(in - Hg)$	Displacement (μm)
-10	136.110
-21	136.131

Based on the results in Table 7.3, it was concluded that most of the change in displacement was due to the mirror deflecting. To eliminate the deflection, it is possible to attach the mirror to a mounting plate or intermediary piece that attaches to the face of the C carriage. This can be done by using a tapped hole in the back of the mirror primarily used for shipping or using a glue or wax to attach the mirror. These mounting techniques can also distort the mirror and should be investigated further if used. With some difficulty it is possible to measure the mirror in a different orientation by placing the mirror on the B carriage and the probe on the C carriage. There are instruments that operate in this fashion such as the Optipro UltraSurf [35].

A full scale of the primary mirror was made with a light weighted aluminum substrate with a Nickel Phosphorus coating. The mirror was roughed on a CNC mill before plating then finished on a diamond turning machine. A mounting system was designed by the manufacturing group of the AFRL project to decrease deflection during manufacturing, metrology, and final system assembly. The mounting chassis can be seen in Figure 7.3 [47].

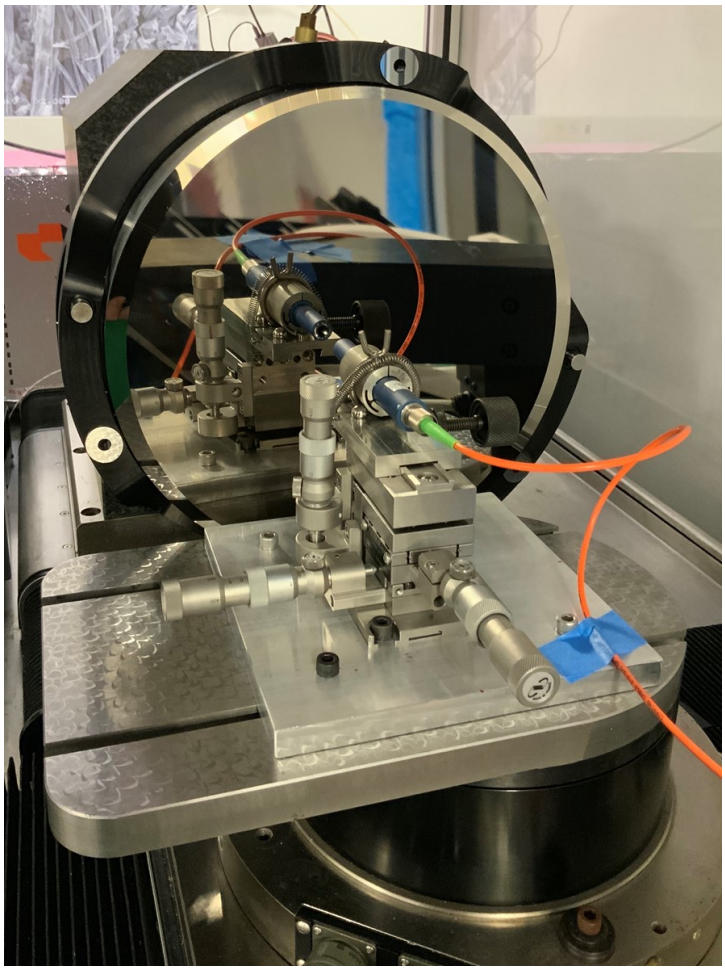

Figure 7.3: Full scale primary mirror for Air Force Research Laboratory, three mirror anastigmat telescope optics. (Photo credit: Laura Hopper)

The full-scale primary was measured using the Mahr LD260 profilometer fitted with an air bearing linear stage and rotary stage. The LD260 offers a contact measurement using a 1 mm diameter stylus. The measurement setup is shown in Figure 7.4.

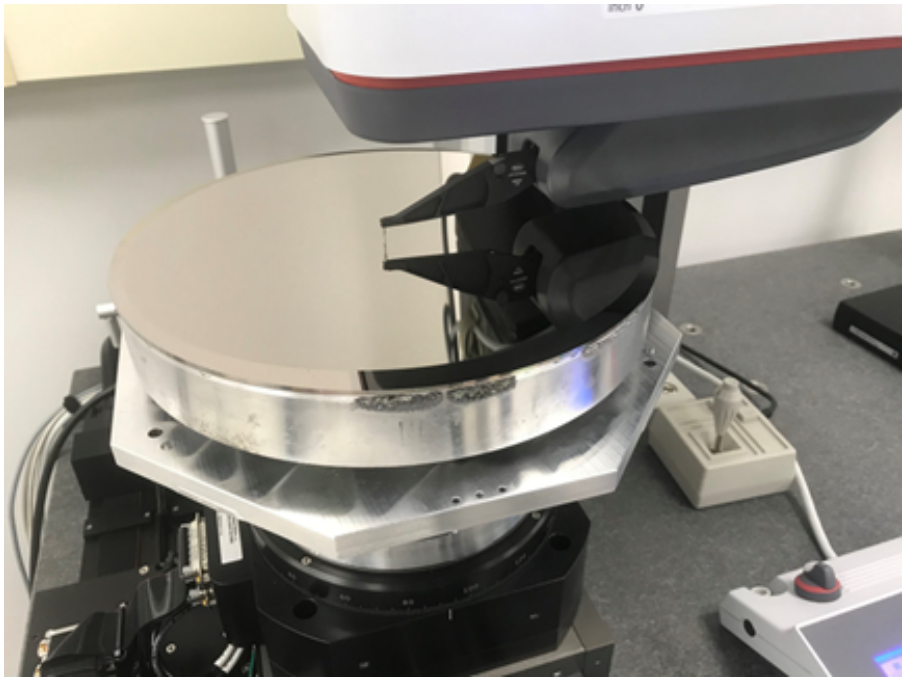

Figure 7.4: Full scale primary mirror being measured on Mahr LD 260 profilometer.

7.1 Datums and Fiducials

Datums and fiducials were used to locate features or the prescription on the parts measured in this research. Fiducials can be as simple as the edge of the part or as complex as spheres machined into the part. In this research fiducials will be considered as features on a part that define a datum or datums that are used to locate the prescription on the part.

This is done by centering the part on an instrument, determining the tilt in the measurement coordinate system and the 'clocking' of the part. Once the part is oriented in the measurement coordinate system the measurement result can be used to realize the datums. For example, three spheres around the clear aperture of a part can be used to establish the tilt and plane of the prescription. Fiducials not in the measurement result such as the outside diameter are used in setting up the part like centering on the outside diameter.

For parts with tilt in the prescription it is important to incorporate a fiducial or

fiducials to locate the plane of the prescription. It is common to remove a plane from the measurement result to remove tilt in the measurement from mounting or the measurement process but without fiducials it is impossible to differentiate between tilt in mounting from that in the prescription.

There is a contribution in the measurement uncertainty from locating the fiducials and datums. This includes the ability to locate the prescription using the datums. This contribution can be reduced by properly defining the measurand and thoughtfully locating the fiducials. Freeform optics often require fiducials to locate the optical reference axis for incorporating a lens or mirror into a system as the shape of the optic alone is not sufficient.

ISO 10110-19 stipulates the use of the same fiducials and datums during design, manufacturing and metrology of a lens or system. This requires a more thoughtful approach as the fiducials will need to be accessible by the manufacturing system and metrology instrument. One approach is to cut the fiducials during manufacturing in the same setup as cutting the prescription. This could be cutting the outside diameter on an ultra-precision lathe or milling spheres outside the clear aperture during manufacturing of the optical surface. Fiducials and datums are also used in molding freeform surfaces.

Datums were used in locating the prescription on the part while measuring the half scale tertiary mirror on the 100UMM. Fiducials cut into the part during manufacturing were used to locate the datums. The clocking and centering fiducials were cut while roughing the part on the mill after plating and used in orienting the part on the diamond turning machine for manufacture. While set up on the diamond turning machine the centering fiducial was re-cut to ensure that the prescription and the outside diameter (OD) of the part were concentric. An annulus outside the clear aperture (CA) of the part can be cut in a facing process to establish the tilt in the part. The diamond turned OD was used to center the part and the flat milled in the

top of the part to clock the part on the 100UMM. A drawing of the half scale tertiary is shown in Figure 7.5.

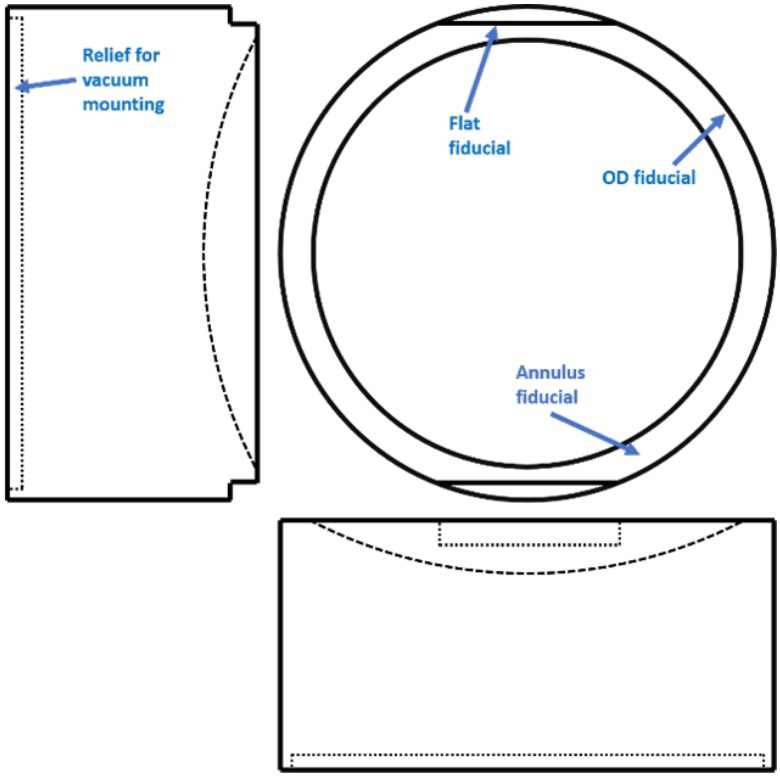

Figure 7.5: Half scale tertiary test part drawings (not to scale) showing the fiducials for manufacturing and metrology.

Figure 7.6 shows the fiducials and the use of the electronic indicator to clock the mirror on the 100UMM.

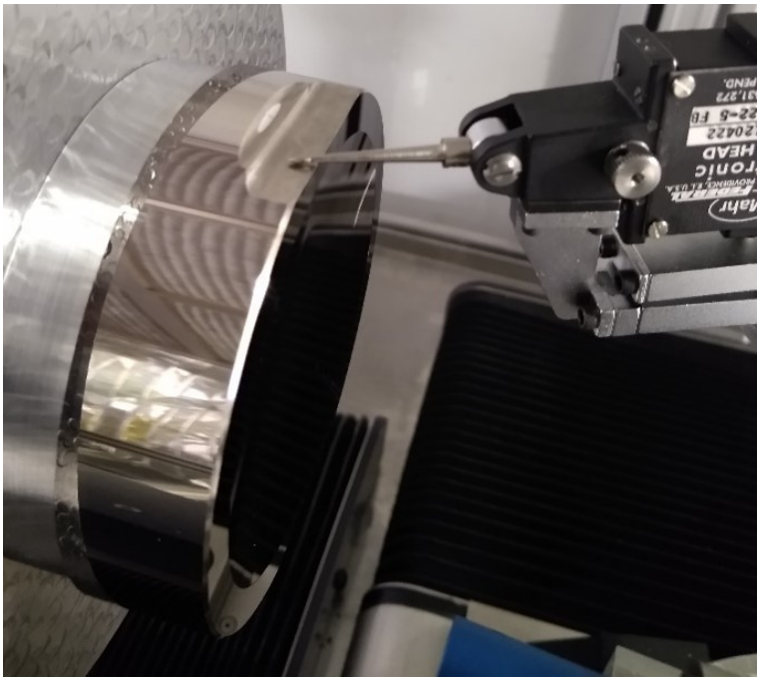

Figure 7.6: During setup, 'clocking' the half scale tertiary mirror using a flat as a datum milled in the part during roughing.

There is a tilt term in the prescription requiring a fiducial to differentiate tilt from mounting the part and the tilt in the prescription. The annulus around the clear aperture was designed to differentiate between the two tilts in the measurement. Three points are required to define a plane so there are other ways of developing a tilt datum using fiducials. Three spheres could be cut into the part or attached to define the plane [36], [48]. To locate the top of the prescription there are marks on one of the flats to signify the top of the part as a flat was milled on the top and bottom of the part.

7.2 Part Mounting

The three fiducials described above are used in orienting the AFRL half scale tertiary mirror on the 100UMM and setting the G-54 offsets in the controller interface for measuring the part and locating the prescription. When mounting the part, the clocking and centering fiducials are used while the tilt fiducial is used in post processing.

The base of the electronic indicator is placed on a stable part of the machine that can be assumed to be fixed. The indicator is moved into range on the OD of the part. If the part is far enough out of center that the indicator does not have sufficient range, it may be necessary to leave the indicator just off the part and rotate the part while tapping to center by "eyeballing" the distance between the OD and the indicator. That should get the part centered enough to use the coarse range on the indicator. The indicator is then brought into contact with the part OD and adjusted into range by tapping with the rubber handled screwdriver. The indicator may need to be flipped if the direction that it measures is incorrect. This can be checked by gently pressing on the probing part of the indicator and feeling for the spring to depress and watching the dial to show a reading. There are also adjustments on the base, indicator readout/electronics box and electronic indicator mount for fine adjustment. Figure 7.7 and Figure 7.8 show the centering process.

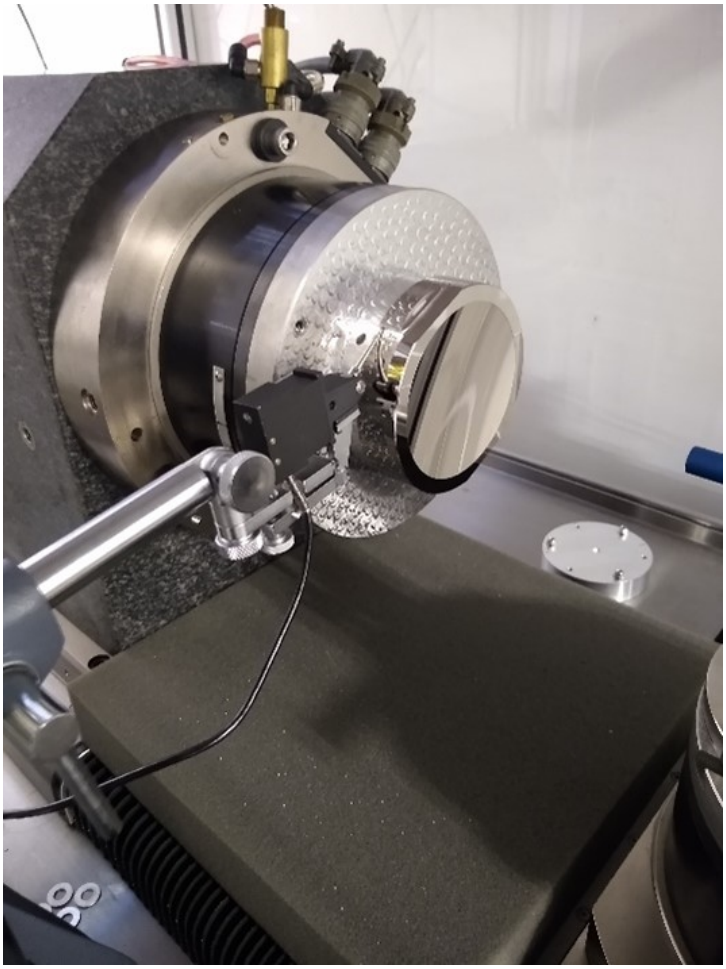

Figure 7.7: Using an electronic indicator to center the part on the rotational axis of the C carriage using the diamond turned outer diameter. Foam is used to avoid damage if the part falls during centering.

Foam is placed under the optic as a safety in case the vacuum fails due to centering. To tap the part to center, a permanent marker was used on the aluminum section of the optic as to not disturb the diamond turned Nickel Phosphorus OD. There is not enough clearance to tap directly with the screwdriver. Figure 7.8 shows the permanent marker being used.

Figure 7.8: Centering the part using a permanent marker to keep from damaging the diamond turned outer diameter.

The flat is shown in Figure 7.6 with the electronic indicator. The indicator stand is placed on the X carriage as shown in Figure 7.9.

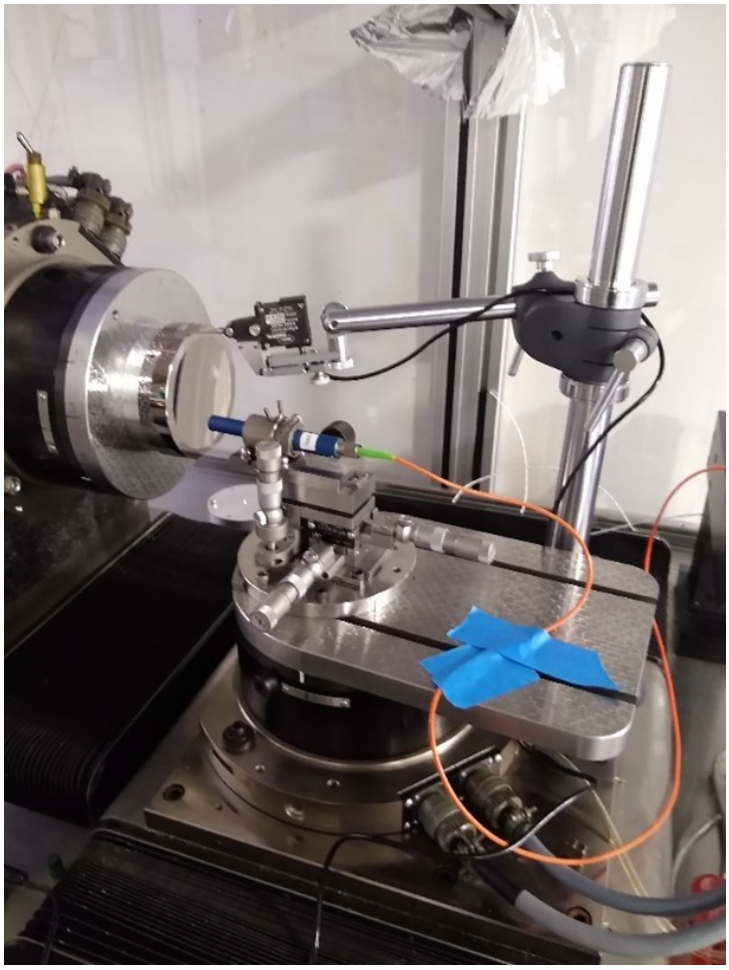

Figure 7.9: Placing the electronic indicator on the X carriage for clocking the half scale tertiary optics of the Air Force Research Lab three mirror anastigmat.

To establish clocking the indicator is placed in contact with the flat on the 'top' of the mirror. The 'top' is indicated with a mark on the flat since there are two flats. The X carriage is jogged back and forth while watching the readout on the electronic indicator for variation. The optic is rotated using the C carriage until the readout is at a minimum deviation. There is a mild bow to the flat fiducial on the 'top' of the optic. This was overcome by matching the displacement on of the indicator on either side of the flat a given distance in X from the minimum displacement.

7.3 Point by Point Measurements

This research started with point to point measurements where the machine was moved to a measurement point and allowed to settle out before taking a few seconds of data while quasi-static then moving to the next measurement point. The prescription was overlaid with a cartesian grid of measurement points equally spaced in the X-Y plane, with Z being the sag of the mirror. The Z height was calculated for each of these measurement points. The X, Y and Z coordinates of the measurement point, in the supporting carriage coordinate system (C carriage), were input into the mathematical model which was solved for the carriage positions at each of these points. The machine movements were written to G-code that the machine can understand using MATLAB. Figure 7.10 shows the measurement points for the point by point measurements in the X-Y plane.

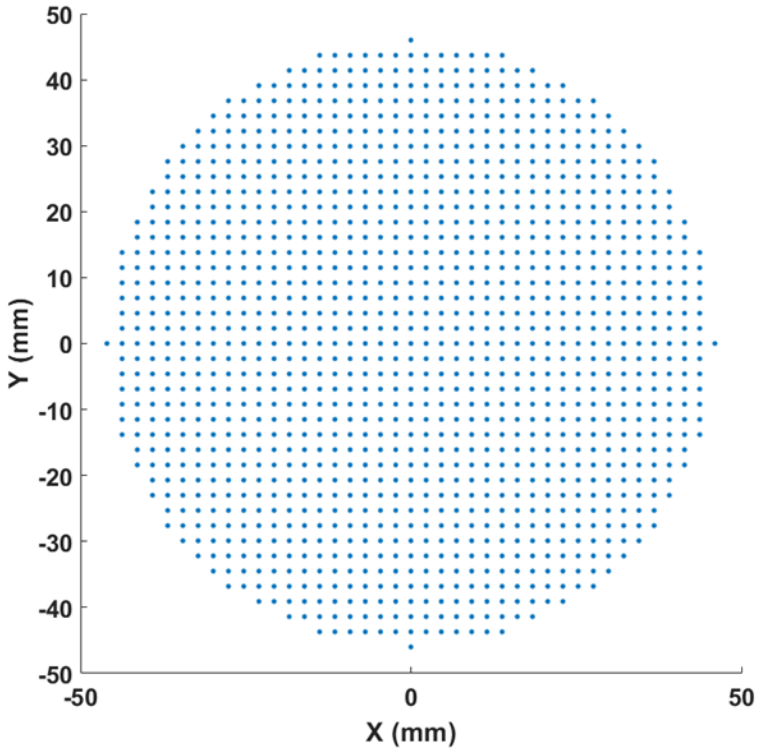

Figure 7.10: Measurement points for the point by point probe path showing the X-Y grid with equal data spacing.

Using G01 or the linear interpolation mode, the controller moves the carriages to follow a straight path between the measurement points. To keep on the line, the carriages move at different feed rates stopping at the same time once they have reached the next point.

Every eight hours the temperature in the laboratory changes rapidly which is affecting the measurement result, as stated above. The carriage positions were organized to either reduce the amount of measurement time (total distance traveled) or reduce the amount of a specific carriage's motion to reduce carriage related thermal drift. The rotary carriages are more thermally stable than the linear carriages. This is primarily due to the linear carriages heating the supporting ways as they move.

It could be possible that more carriage motion would decrease the amount of thermal drift. A strategy where the X carriage is moved back and forth across the part for several hours before the measurement to allow for any thermal drift due to the carriage motion to come to an equilibrium before starting the measurement was discussed but never implemented. In this case, it may be that the probe path would incorporate larger movements in X to keep the ways at the elevated temperature.

For the half scale tertiary mirror, the total measurement time for a point to point measurement was roughly 6.5 hours to 11.25 hours depending on the order the points were measured. The measurement time needed to be reduced significantly to both avoid the spike in temperature every eight hours and to minimize other thermal effects. To reduce the measurement time, the measurement points were organized to minimize the distance traveled. One way of doing this was to organize the points in a raster scan pattern. The traveling salesman problem (TSP) was also used to reduce the distance traveled. Since linear interpolation was being used, the probe path is a series of straight lines between measurement points making the TSP a way to reduce measurement time.

7.4 Traveling Salesman Problem

To reduce the measurement time or total distance traveled by the machine, the traveling salesman problem was investigated. The traveling salesman problem refers to a set of optimization algorithms and solutions used to minimize the distance traveled for a salesman that has multiple cities to visit and is looking for the shortest route possible saving them time and money. The traditional traveling salesman problem starts and stops at the same point or city. For this application that is not necessary. The goal is to distribute the measurement points in an equally spaced cartesian grid and reduce the measurement time by reducing the overall distance traveled. By having equally spaced data, the fitting of orthogonal polynomials such as the Zernike polynomials is more reliable.

7.5 Traveling Salesman Problem Comparison

MATLAB has examples of solutions for the TSP on their website [49], [50]. The first TSP algorithms explored were from those examples. The examples include what they call the 'problem based' and the 'solver based' approaches. Although the code was adapted for use with the probe path generation, they still started and stopped at the same measurement point.

Due to time constraints, and upon a searching of the MathWorks website a program was found that does not start and stop at the same point [51]. The author refers to this as an open variation of the TSP and uses a "genetic algorithm." The "genetic algorithms work with a population of solutions that are combined and modified to produce new solutions, the best of which are selected for the next generation of the population. The general scheme is modeled after evolutionary processes in nature [52]." In the code it is also pointed out that the output path is a 'best estimate' of the shortest overall distance. The program has an input for the locations, number of iterations and population size. With 10^7 iterations using a point cloud of x, y, z

coordinates the algorithm produced a total distance of 2591.21 mm. Run time for the optimization program was about 5 days. Figure 7.11 shows the probe path in the X-Y plane of the part coordinate system.

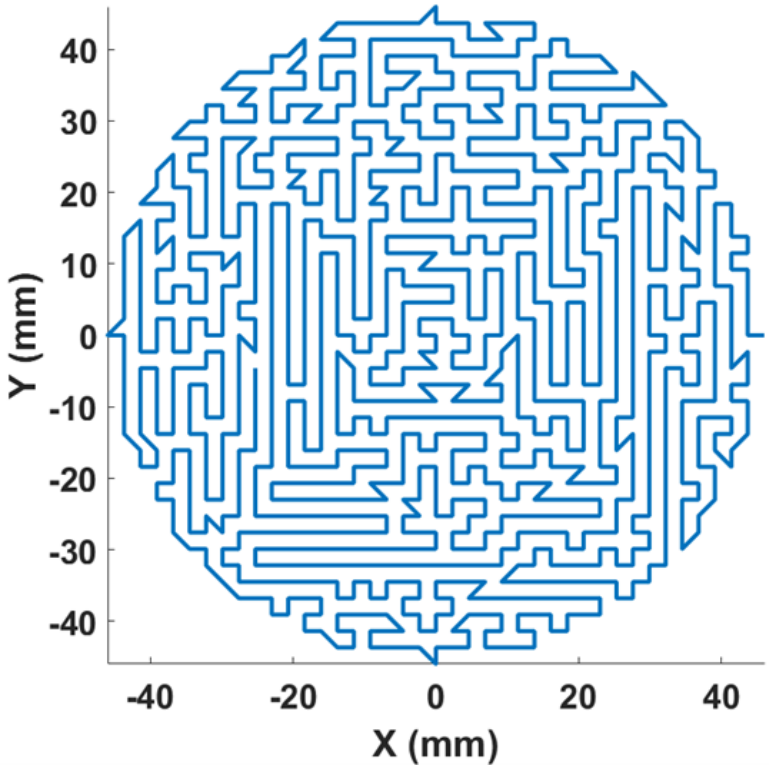

Figure 7.11: Traveling salesman problem solution starting and stopping at different locations using the X, Y, and Z coordinates for measuring the half scale tertiary mirror.

Following the optimization above, a new approach was used with the same algorithm where only the x, y coordinates were used. The total distance was calculated using the path or measurement point ordering from the x, y optimization but using the x, y, z coordinates. The total distance reduced to 2913.22 mm. The probe path is shown in Figure 7.12.

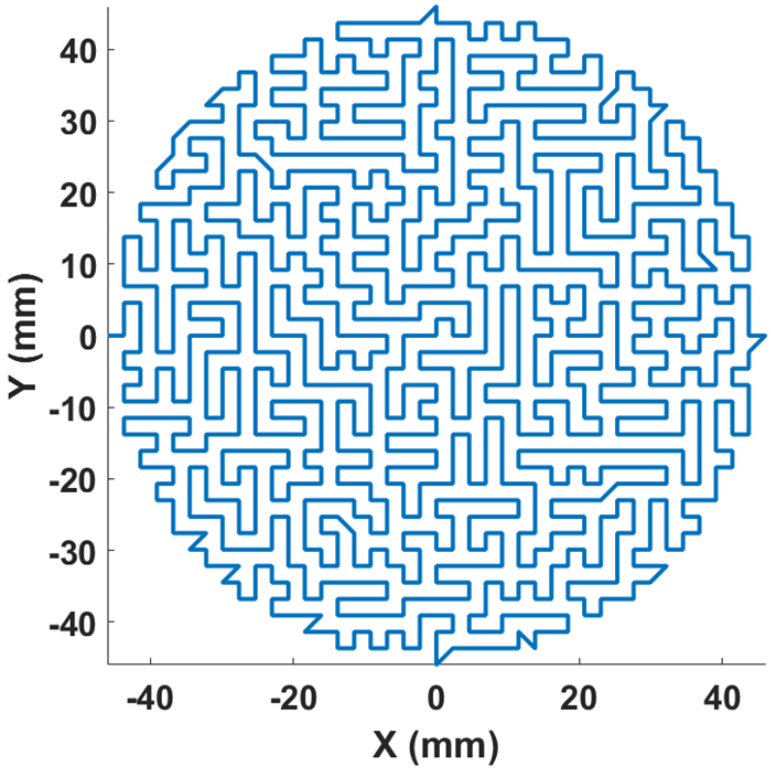

Figure 7.12: Solution to the Traveling Salesman Problem algorithm in the X-Y plane for measuring the half scale tertiary mirror.

To make sure that the TSP algorithms are reducing the distance traveled a brute force or "common sense" approach was taken to developing a probe path. The raster scan approach had a total distance 2931.55 mm. The raster scan probe path is shown in Figure 7.13.

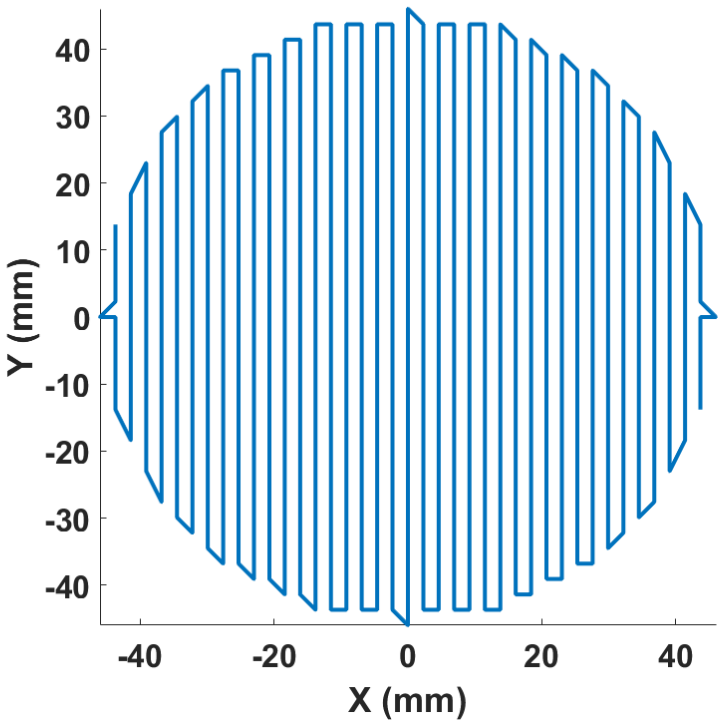

Figure 7.13: Raster scan probe path for the half scale tertiary mirror with a total distance of 2931.55 mm, shown in the X-Y plane.

The raster scan approach was shorter than the genetic algorithm solution that used the x, y, z in the optimization but not shorter than using just the x, y coordinates. Further optimization could be done, and the program could be run for more iterations. There are also many more algorithms used to solve the TSP. Even with reducing the distance traveled and overall measurement time to further reduce the thermal effects it was decided that a scanning measurement mode was required.

7.6 Scanning Measurement Mode

To further reduce the amount of time to complete a measurement, reducing thermal drift, a scanning measurement mode was implemented. The scanning mode eliminates the need to stop and wait for the machine to settle out or dwell at a measurement point. The scanning mode is implemented by recording the probe displacement at nominally the same time as the carriage positions while the probe is moving over the

surface being measured. This began by reading the machine scales (linear encoders) directly before they entered the machine controller. Although the measurement time is reduced the scanning mode introduces a data age uncertainty due to the inability to record the measurement data at precisely the same time.

Due to the carriage orientation on the 100UMM and the shape of the part, it made sense to work in polar coordinates. A probe path was developed to reduce X carriage movements and allow for an estimation of the thermal drift in the measurement. X carriage movements were also eliminated while recording data.

The probe path developed in the traveling salesman algorithm was used with continuous scanning to further reduce the measurement time while getting a pseudo equally spaced data set. This does make filtering more difficult. The mechanism for estimating the drift in the measurement with this probe path is limited to the diametral measurements before and after the measurement.

7.7 Concentric Circle Probe Path

To quantify and compensate for drift during the measurement a probe path using concentric circles was developed. Measurements were also made across the diameter before and after the concentric circles at 0° and 90° to quantify the drift over the entire measurement. The measurement starts by measuring the center of the part and rotating 370°. The probe is then stepped over X direction the desired data spacing and another measurement is triggered while rotating the part 370°, recording probe displacement and carriage positions. By having an overlapping region of the circular measurement at the beginning and end, a comparison can be made looking for any discrepancy or drift. This could be considered an application of closure, discussed further in Reference [15]. The X carriage (probe) is stationary while the C carriage (part) rotates during the circular measurement. The Z carriage also moves to keep the probe in range. The probe path is shown in Figure 7.14.

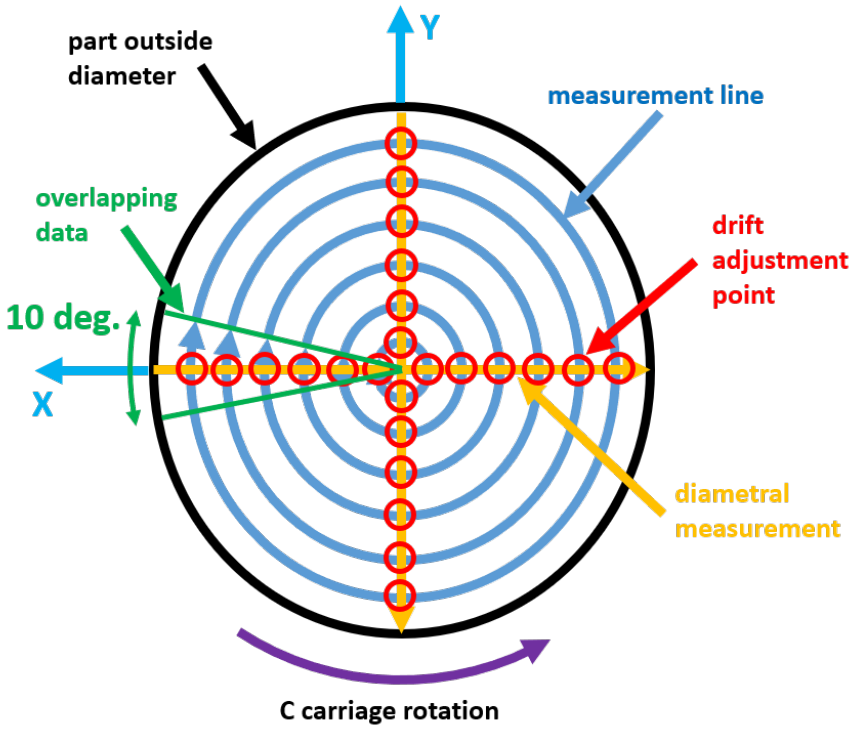

Figure 7.14: Probe path with concentric circles showing the diametral measurement and overlapping data [10].

The concentric circle probe path also reduces the amount of X carriage movement (see above). The air bearings of the C carriage are assumed to be more stable than the hydrostatic bearings in the linear carriages. Movements in the Z direction are much smaller compared to the X carriage movements. This probe path has sparse data in the radial direction which can be changed by reducing the step over in the X direction between rotations.

Different probe paths were considered such as the wagon wheel or a series of diametral measurements taken at different rotations, a spiral moving outward from the center, and the paths described in the TSP section above. Some of these probe paths are also discussed in Reference [53].

The data spacing for measuring form was determined by deciding what spatial frequencies were enough to define form. It was then a decision of what sampling would be adequate for those spatial frequencies. There is a tradeoff between being

able to fully identify the form and the amount of time it takes for a measurement. The longer a measurement, the more thermal drift. It is possible to down sample and filter the measurement data to separate the mid spatial frequencies and roughness. The nominal spot size of the chromatic confocal probe ($8\,\mu m$) is larger than the default wavelength ($\lambda_s = 2\mu m$) in ISO 10110-8 making spatial content in the roughness range not reliable.

7.8 Positive and Negative Side of Part

To identify some of the issues or errors in the machine, prove that the error compensation is working and for repeatability, the half scale tertiary mirrors were measured at radial distances in the X direction on the positive and negative sides of the part using the concentric circle probe path. Figure 7.15 shows the probe positions for the positive and negative side measurements.

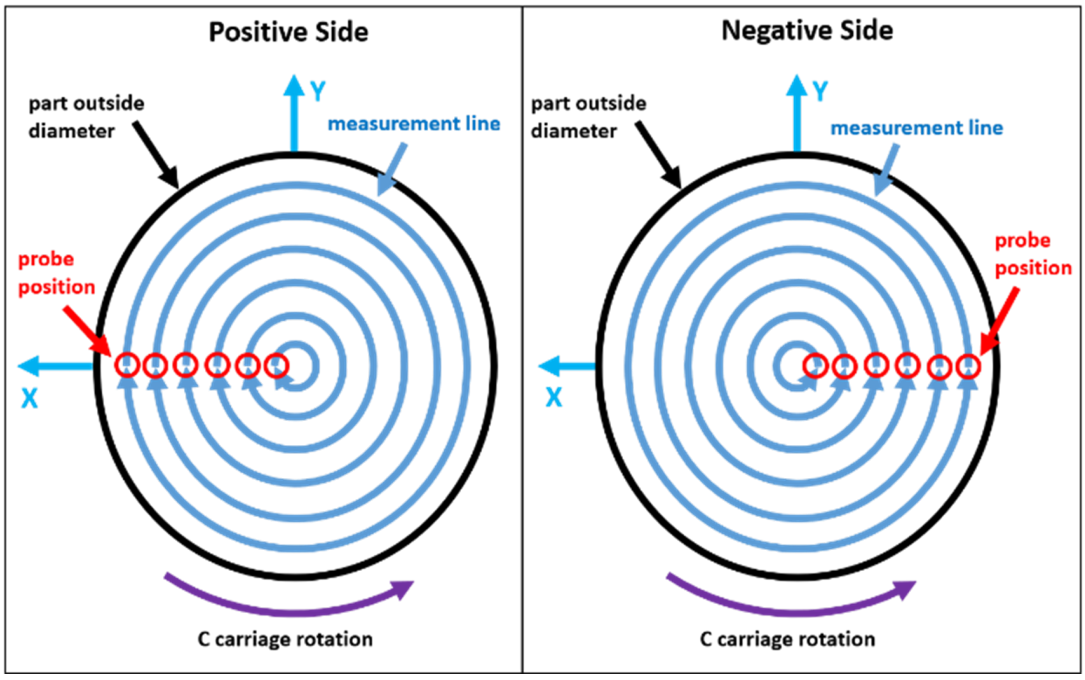

Figure 7.15: Probe positions for the positive and negative side of the part in the X direction using the concentric circle probe path.

The result is measuring the same point on the part using different X carriage and C carriage positions. This is only possible since the size of the mirror allowed for

full access to the diameter. For parts where the probe is placed off center on the B carriage, it will likely not be possible to measure both sides of the part. The point by point measurements also measure points on the part near one another but using different X carriage positions. The resulting measurement results tell a lot about the error compensation and machine error measurements (see results below).

7.9 Writing Part Programs

Once a probe path is decided, the measurement points and path that the probe will take are determined mathematically. This is done using the prescription of the optic being measured, the sampling strategy and the desired data spacing. The measurement points and probe path are input into the mathematical model of the machine to generate the machine carriage positions required to follow the probe path. These calculations and solutions are done in MATLAB. Point by point goes to a measurement point and stops while a scanning mode goes between points without stopping at the measurement point. The measurement triggering and dwells are programmed into the machine code.

7.10 Probe Path Generation

For a given measurement point there will likely be two solutions in the mathematical model. It is then decided which of the sets of positions to use based on how the machine is set up. The set of positions chosen should be checked for continuity as there may be a position in the other set that is better suited for the probe path. This usually happens at a zero crossing or on an axis of the coordinate system.

The mathematical model and part prescription are used to generate the G-code for the part programs to measure optics on the 100UMM. A flow chart, shown in Figure 7.16, was developed to show the part program code.

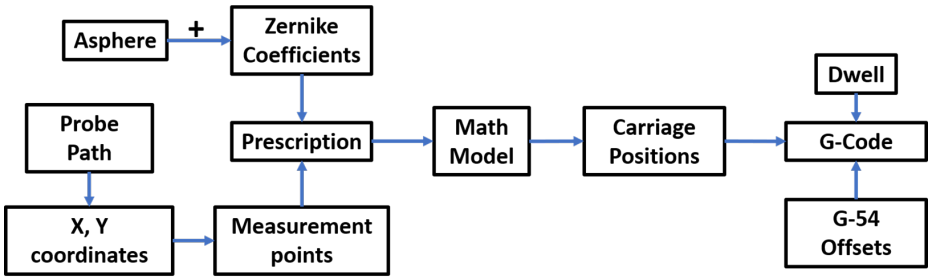

Figure 7.16: Flow chart showing the probe path generation for G-code program writing.

A previous measurement result could also be used to include the part error and tilt. This would be used for a nulling probe path where a minimal amount of the probe range would be used. This may also be useful if measuring with probe normal to the part surface. In an iterative fashion the process should converge on a null probe path.

7.11 Generating Machine Carriage Positions

From the mathematical model above, equation 3.30 is used to generate the machine carriage positions. The model is solved for the C, X, Z carriage positions using the MATLAB function 'solve'. Depending on the size of the part there are likely going to be two solutions to a given measurement point as the part can be rotated 180 degrees and the X carriage can be moved to the other opposite side. This process is reverse of solving for the part coordinates in the C carriage coordinate system. The model is used for the relationship of the carriages as the machine errors and offsets are not considered. The tilt in the part can be entered into the part prescription for nulling the probe or if the tilt exceeds the probe range.

7.12 Measurement Setup

For taking measurements, after homing the machine, the carriages are moved such that the probe is in the center of the part and is at the desired displacement in the probe range. In the machine code the G54 work offsets are used to establish a new zero for the machine during measurements. The C carriage is rotated such that the

'clocking' is known using the fiducials located on the part. The error measurements are based on the machine coordinates, making a conversion necessary and noting the G54 offsets a critical step.

7.13 Nulling Measurement Mode

The machine and probe were used in a nulling mode to reduce the range of the probe required. The nulling mode uses the machine carriages to move the probe along the surface of the part, based on the prescription, minimizing the error due to the non-linearity in the probe. The range of the probe needed is reduced to the deviation from the prescription due to errors in the part, errors in the machine carriages, non-linearity of the probe, mounting distortion and tilt, and thermal drift. The nulling mode is used assuming that the machine is more repeatable than the non-linearity in the probe. In scanning mode, the less dense the measurement points are the more of the probe range is used due to the sag between measurement points because the machine is set to linear interpolation. A point in the probe range is chosen to be the null location that is stable and is in the linear part of the range. A trade off using the nulling mode is that the Z carriage travels continuously (for a freeform surface) over a larger range and could be introducing some thermal drift.

CHAPTER 8: DATA PROCESSING

Following the measurement, the data processing is done in MATLAB. LabVIEW saves the data in the native format TDMS. A MATLAB converter changes the TDMS format into the double data type. Data processing also includes fitting polynomials, filtering, interpolating, rotations, and prescription subtraction. These processes allow for the data to be interpreted for the extraction of useful information for designers, engineers and metrologists.

8.1 Fitting to Measurement Data

In processing measurement data or running simulations it is often necessary to fit to a set of data in two or three dimensions. Data fitting is used to remove a certain shape, determine the slope of a line, interpolate data, and to compare with the prescription or sets of data with different data spacing. Interpolation was used to reduce the data to equal data spacing and to filter outliers. There are many built in functions in MATLAB that will fit to a set of data, but it is important to know how the fit was calculated and how it may affect the data.

8.2 Algebraic Fitting and Geometrical Fitting

An important distinction is made between algebraic and geometric fitting to data. Depending on what information is being extracted from the data or the definition of the measurand, a choice may be made between the two. Algebraic fitting is considered easier to implement and is commonly used. When fitting to the surface using algebraic fitting there will be an added bias in the "estimated fitting parameters [11]." Geometric fitting is also known as orthogonal distance fitting which better explains the function [54]. Geometric fitting "intends to minimize the sum of the squared or-

thogonal distances from the measurement points to the nominal surface [11]." When fitting to simple shapes, the orthogonal distances may be easy to calculate with a closed form solution but for freeform surfaces this becomes more challenging [11]. Figure 8.1 shows a comparison between the two methods.

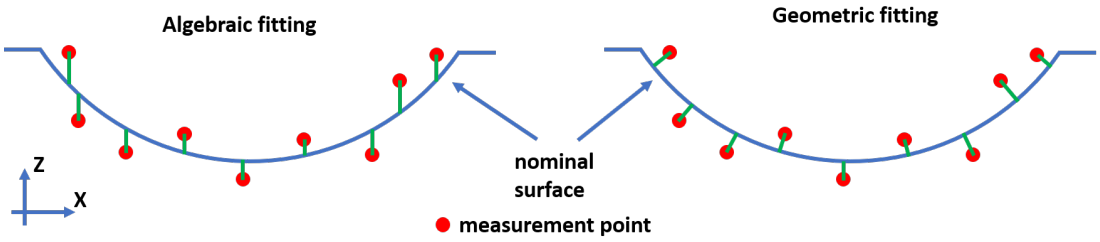

Figure 8.1: Showing the difference between algebraic and geometric fitting [11].

When fitting to data, a plot of the fit residuals shows how good the fit is visually. This is simply calculated by solving the fit for each measurement point and taking the difference. There is an uncertainty contribution to fitting that may need to be considered.

8.3 Removing Tilt

A common issue with measurement data is tilt induced by setup, fixturing or the measuring process. An easy way to remove tilt is to fit a line or a plane and subtract the line or plane from the data set. This method effects the spatial content of the surface. If the object being measured is a sphere it will change the shape of the sphere and reduce the diameter. If the surface has a sine wave, the period of the sign wave will be reduced. Figure 8.2 shows fitting a line to measurement data with the green lines representing the height of the best fit line at the x coordinate of a measurement point.

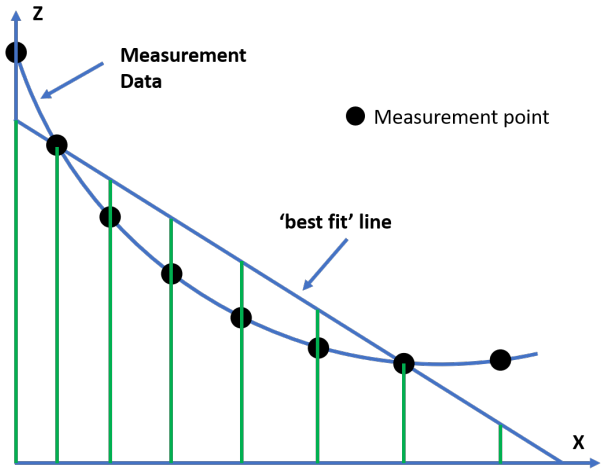

Figure 8.2: Fitting a line to measurement data.

For a given measurement point, the height of the best fit line at the x coordinate of the measurement point is subtracted. That height is then subtracted from the measurement point. Figure 8.3 shows this process with the subtracted line in red.

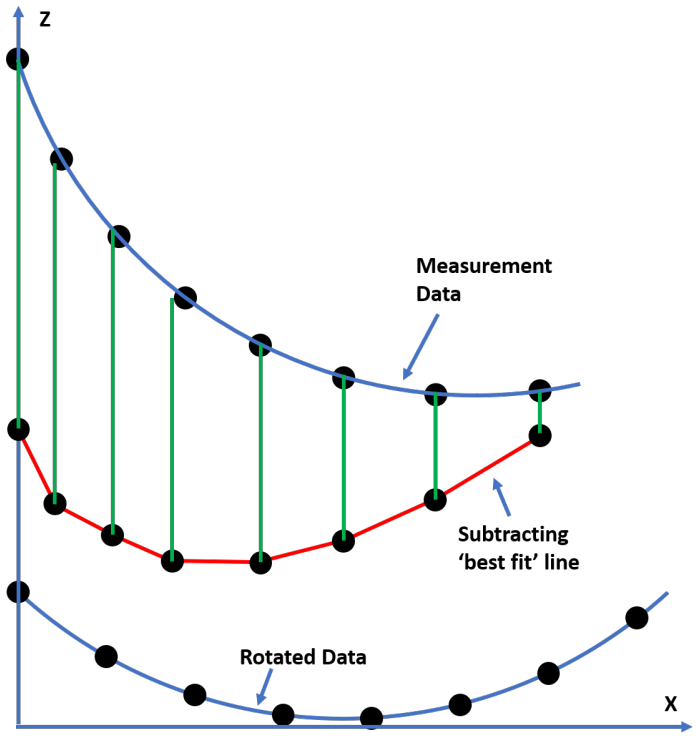

Figure 8.3: Removing a line from data using a rotation rather than best fit line subtraction.

When compared to the measurement data that has been rotated "flat" the subtracted data has lost the original shape. The arc or part of a circle is no longer circular, but the measurement data is "flat" to the X axis. For some shapes and applications this may be acceptable but for this research the amount error was significant, so a method was used that rotates the data to a flat position.

8.4 Fitting Zernike Polynomials

The Zernike fitting code developed for this research uses the backslash operator in MATLAB to solve for the Zernike coefficients. The code from Reference [25] was used as a starting point to build the subfunction. A function from MathWorks central called "Zernfun" was used to calculate the polynomials although I would use caution when using the Zernfun function. It is important to understand the normalization, ordering and coordinate system that Zernfun and MATLAB use. A function that calculated the Zernike polynomials based on the equation for each term was used to check the Zernfun function to ensure the correct output was given. The Zernfun function can calculate any of the terms without having to type in each equation. Zernike polynomials are orthogonal over the unit circle, but some prescriptions are normalized over a different radius. The backslash operator solves the common equation:

$$Ax = b \tag{8.1}$$

Where to solve for x:

$$x = A\backslash b \tag{8.2}$$

In solving for the Zernike coefficients, A is the solved Zernike polynomial for the given (rho, theta), x is the Zernike coefficient, and b is the height of the surface being fit to. The coefficients can be used to later solve for a new rho, theta set or to compare with a specification or prescription. The set up for the equation is shown in Figure 8.4.

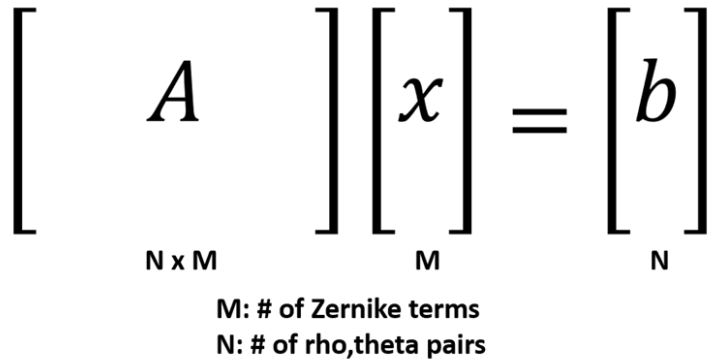

Figure 8.4: Fitting Zernike polynomials using the backslash operator in MATLAB.

There is a brief section in Reference [11] about calculating Zernike polynomials and the orthogonality. For a more in-depth discussion Reference [55] is a great reference. In Reference [11] the authors describe the Zernike polynomials as "sag orthogonal to each other over the unit disk." Another set of what is called "Zernike difference polynomials" is discussed as a "slope-orthogonal representation" that may be a more representative of the "imaging functionalities of optical components" and "from the viewpoint of fabrication [11]." This is a similar idea to geometrical fitting.

8.5 Sine Wave Fitting

A sine wave fit was used in Estler's face motion reversal to remove tilt in the measurement. The system of linear equations in the matrix equation Ax = b, shown in equation 8.3 is used to solve for the coefficients of equation 8.4.

$$\begin{bmatrix} 1 & cos\theta_1 & sin\theta_1 \\ 1 & cos\theta_2 & sin\theta_2 \\ 1 & cos\theta_3 & sin\theta_3 \\ \vdots & \vdots & \vdots \\ 1 & cos\theta_n & sin\theta_n \end{bmatrix} \begin{bmatrix} \beta_1 \\ \beta_2 \\ \beta_3 \end{bmatrix} = \begin{bmatrix} A_1 \\ A_2 \\ A_3 \\ \vdots \\ A_n \end{bmatrix} \tag{8.3}$$

Where A is the amplitude, β is the set of coefficients, and θ is the angle. The sine wave used in fitting is shown in Figure 8.5.

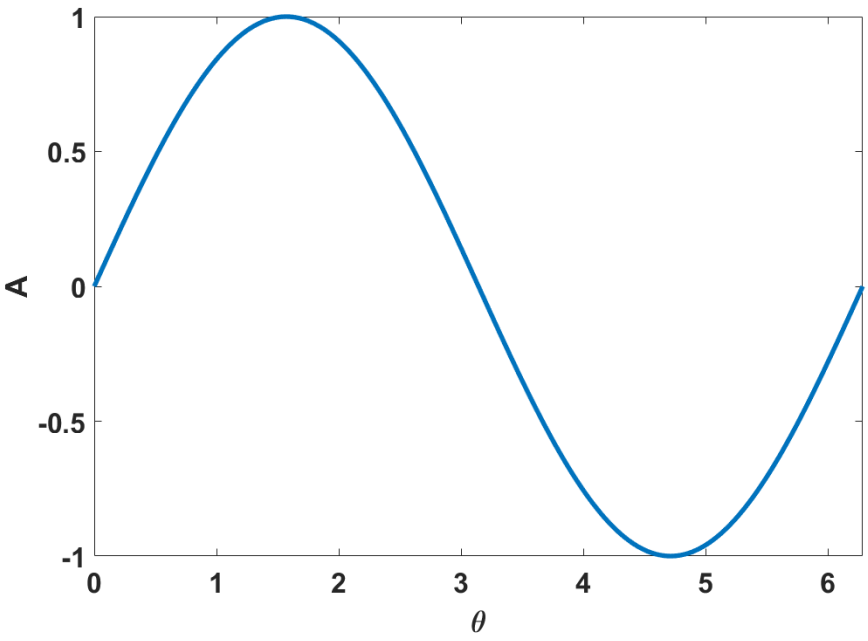

Figure 8.5: Sine wave in the form used for fitting.

Solving for β gives the coefficients for the sine wave fit. To solve for the fit line use equation 8.4.

$$A = \beta_1 + \beta_2 cos(\theta) + \beta_3 sin(\theta) \tag{8.4}$$

The solution is then used for subtraction from the initial dataset.

8.6 Filtering and Interpolating

MATLAB has many built in functions for filtering and interpolating data sets. Several methods and algorithms were tried for this research to find one that was suitable. The functions and algorithms were selected by fitting or interpolating the data then looking at the error when plotting a subtraction of the fit data from the initial data set.

The functions vary between fitting and interpolating in what MATLAB calls 1D, 2D and 3D. The MATLAB functions used for fitting and interpolating for this research are considered 1D. The 2D fitting and interpolating was done by functions that were written specifically for this research to remove tilt from a measurement or to fit the

Zernike polynomials. The fitting and interpolating functions in MATLAB allow the user to select between algorithms which they call 'methods.' Of the methods used the modified Akima method was found to be most suitable. The full name is modified Akima piecewise cubic Hermite interpolation [56]. The description provided by MATLAB states: "the interpolated value at a query point is based on a piecewise function of polynomials with degree at most three evaluated using the values of neighboring grid points in each respective dimension ... the Akima formula is modified to avoid overshoots." When compared to the other methods, the modified Akima was shown to have less residual error. For more on interpolating, see Section 8.7. The key properties according to Cleve Moler, the author of the first MATLAB and their chief mathematician, are [56]:

- It produces undulations which find a nice middle ground between 'spline' and 'p-chip'
- It is a local cubic interpolant which generalizes to 2-D grids and higher dimensional n-D grids
- It increases the robustness of Akima's formula in the edge case of equal side slopes
- It eliminates a special type of overshoot arising when the data is constant for more than two consecutive nodes

For more information on the modified Akima, see [57] and [58].

8.7 Reducing to Psuedo Equal Data Spacing

The scanning mode provides dense data spacing in the direction of travel. The data may need to be filtered or interpolated to provide a nearly uniform data spacing for fitting polynomials. Data from this sampling strategy is dense in the circumferential direction and sparse in the radial direction. The data is interpolated to the same data spacing in the circumferential direction as the radial direction to achieve nominally uniform spacing. This provides a more precise fitting of the Zernike polynomials [59]

while also filtering the data for noise and outliers, further improving the Zernike fit. For the AFRL half scale tertiary mirrors the aspheric surface is subtracted before the Zernike polynomials are calculated.

For interpolating, the circular measurement is "unwound" into a line. The beginning and end or the overlapping region are then compared. If there is a discrepancy in the overlapping region it can be corrected as discussed below. To match the data spacing in the radial and circumferential data, the circular measurement is divided by the radial spacing which will give a number and a remainder. The circular measurement can then be divided by the number, ignoring the remainder, and that number is used as the circumferential spacing for that set of measurement data at that radial position. This method provides an approximation of equal data spacing without leaving any large gaps or unequal data spacing in the circumferential measurements.

8.8 Measurement Data Processing

The measurement data is recorded in LabVIEW. The measurement process and data discussed here are specific to the half scale tertiary mirrors measured on the Nanotech 100UMM using the concentric circles probe path with a diametral measurement before and after the circular measurements.

8.9 Measurement Data

The data recorded in LabVIEW using the TDMS format is:

- Start date and time
- Time in sec
- X carriage position in counts
- Z carriage position in counts
- B carriage position in counts
- C carriage position in counts
- Probe displacement in digital format

8.10 Measurement Data Processing Program

In MATLAB the data processing program follows the following steps:

1. Convert TDMS data type to the double data type
2. Probe data is converted to micrometers from the digital format
3. Time is zeroed by subtracting the first time recorded
4. Time is converted to minutes
5. Remove zeroes from data (if a zero is in any element of the set of data, entire set is removed)
6. Split data by gaps in time (index start/stop of measurement)
7. Calibrate Z carriage and Probe based on calibration routine at end of measurement
8. Separate diametral measurements before and after measurement
9. Separate circular measurements into positive/negative direction for each radial position
10. Calibrate C carriage and convert from degrees to radians
11. Calibrate X carriage
12. Use X calibration on diametral measurements and center
13. Put X, C, Z, and probe data into machine coordinates using G54 offsets
14. Send X, C, Z, and probe data for each measurement point to error compensation
15. Return the compensated X, Y, Z coordinates in the C carriage coordinate system
16. Center the measurement data in X, Y, Z to center of the part
    (a) Calculate prescription for each x, y position of measurement data (rotate by C carriage G54 offset)
    (b) Subtract prescription from error compensated measurement data
    (c) Combine subtraction data from separate circular measurements to three vectors (X, Y, Z)
    (d) Rotate subtraction data to X-Y plane by fitting a plane to the X, Y, Z

data, finding normal to the plane, calculating angle to rotate to X-Y plane and using rotation matrices to rotate around X and Y axes.

17. Send X, C, Z, and probe data to Monte Carlo simulation
18. Return the possible surface X, Y, Z coordinates in the C carriage coordinate system for each iteration of the Monte Carlo simulation
19. Center each possible surface to the middle of the part measured
20. Subtract prescription from each iteration or possible surface of the Monte Carlo simulation
21. Subtract error compensated data with prescription subtracted from each possible surface with prescription subtracted

A flow chart for the data processing program can be found in Appendix B.

8.11 Probe and Scale Calibration

The probe and Z carriage scales are calibrated immediately following each part measurement. This ensures that the calibration did not change and allows a comparison of calibrations between different measurements. The probe and scale calibrations are done to determine the non-linearity in the probe and to convert counts from interpolating the machine scales to displacement. The calibration routine moves the Z carriage over the range of the probe used in the measurement. The calibration is conducted over 10 μm divided into 21 positions or every 0.5 μm. The calibration starts at -5 μm in the Z carriage position from the "zero" position of the Z, C and X carriages in the G-54 offset coordinates. The part is then pulled away from the probe with the Z carriage through the calibration routine in the positive direction through zero and ending at 5 μm in the G-54 coordinates.

The calibration repeatability depends on the positioning error of the machine carriages. This is acceptable since the positioning error of the carriage is negligible over 10 μm. The calibrations are plotted in data processing for the Z carriage machine scales and for the probe. The intended motion is plotted against the displacement

of the probe or Z carriage scales. A line is fit to the data to use the slope for the calibration. The linearity is determined by subtracting the line from the data to see the residual error. The calibration data to determine the conversion factor to displacement from counts of the interpolator is shown in Figure 8.6 with the residual from the fit.

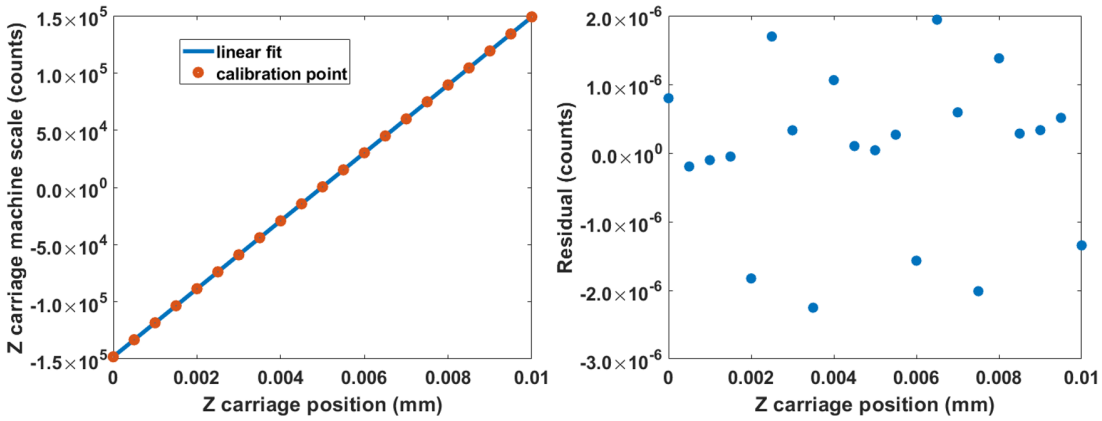

Figure 8.6: Calibrations of the Z carriage with a linear fit to the data for determining the slope (left) and the residual error (right).

The calibration data to determine the conversion factor for the probe based on the commanded machine carriage position is shown in Figure 8.7 with the residual from the fit.

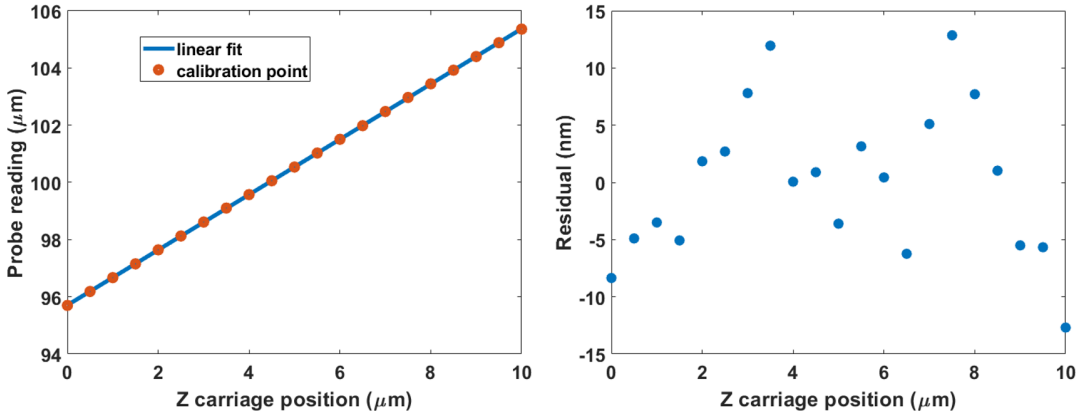

Figure 8.7: Calibrations of the probe with a linear fit to the data for determining the slope (left) and the residual error (right).

The probe has a conversion factor to go from the digital output to micrometers,

but the probe output needs to be further calibrated for each surface and portion of the probe range used in the measurement. The residuals from the calibration can be used in the Monte Carlo uncertainty evaluation.

CHAPTER 9: RESULTS AND DISCUSSION

The half scale tertiary mirrors for the AFRL TMA telescope and a spherical glass mirror were measured to validate and investigate the ideas discussed above. The two half scale tertiary mirrors from the AFRL project were measured in two setups each. For each setup, the optics were measured several times with different probe paths and settings for comparison. Repeatability and reproducibility tests were also conducted. The time to take a measurement was compared as it can be used to estimate the possible thermal drift. Problems that came up during data processing and in the measurement result were addressed. Often further testing was conducted.

9.1 Measurement Time

The probe paths discussed above were used to measure the half scale tertiary mirror from the AFRL TMA. The time to take each measurement was calculated to determine which probe path would have less thermal drift from the influence of the surrounding laboratory. The tradeoff could be the amount of travel of each carriage and the thermal drift that may result. Due to the time savings, the scanning mode and traveling salesman approaches are more suitable. The concentric circles also allowed for the estimation of the thermal drift during the measurement and for any anomalies to be identified. The measurements were each conducted several times to find any discrepancies as well. As stated above, it is important to keep the measurement time under 8 hours or between the sharp temperature change in the laboratory outside the enclosure.

Table 9.1: Probe path elapsed measurement time comparison.

Probe Path	Coordinate System	Elapsed Time	Mode
Concentric circles	Cylindrical	39m 27s	Scanning
X-Y grid (minimizing X movement)	Cartesian	11h 18m 49s	Pt. to Pt.
X-Y grid (minimizing C movement)	Cartesian	6h 28m 42s	Pt. to Pt.
X-Y grid (traveling salesman)	Cartesian	2h 11m 27s	Pt. to Pt.
X-Y grid (traveling salesman)	Cartesian	26m 20s	Scanning

For all the measurements the same feed rate was used in linear interpolation mode. The feed rate was set to 200 mm/min for the linear carriages and 200 deg./min for the rotary carriages. Although the traveling salesman with the scanning mode is faster, it does not allow for the drift estimation that the concentric circles probe path enables.

9.2 Overlapping Region

For the concentric circle probe path, the overlapping region allows for an estimation of the thermal drift during the time that it takes for a full rotation or a single circle in the measurement. The overlapping region does include an acceleration and deceleration which are discarded, due to their unstable nature, by only using 6 degrees of the 10 degrees in the overlapping region. To estimate the drift, lines are fit to the overlapping data at the beginning and the end of the rotation. Since the overlap is in degrees, the length of the line will change as the radial distance increases.

A correction could be implemented where the drift is linearized over the measurement and used to compensate the measurement data. The drift is thought to be

dominated by thermal drift but changes in humidity, hydrostatic bearing pressure, air pressure and the high-pressure air used in the air bearings could also cause a drift. Each 370° rotation takes 1.885 minutes at the 200 deg./min feed rate used. Figure 9.1 shows the overlapping region for the 2 mm radial position.

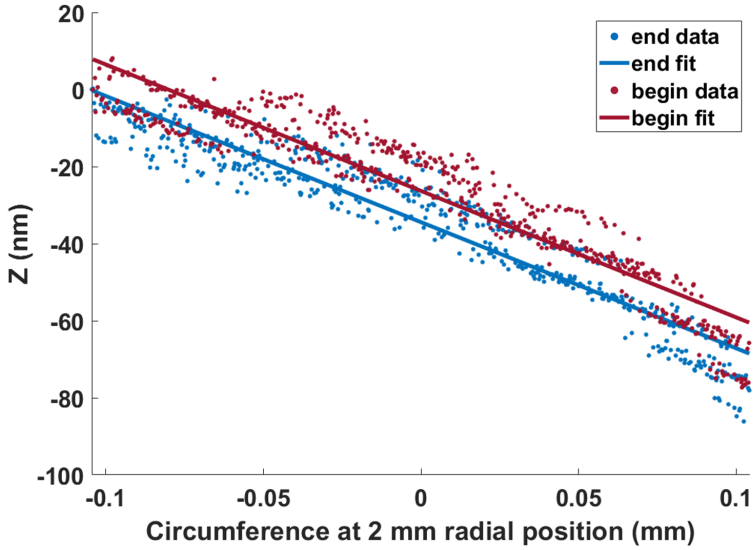

Figure 9.1: Overlapping region of the concentric circle probe path for the 2 mm radius.

The six degrees of overlap is approximately 200 μm. The figure shows the two sets of point data from the beginning and end of the rotation. A line is fit to each set of data. To quantify the drift, the linear fits are subtracted. Figure 9.2 shows the subtraction.

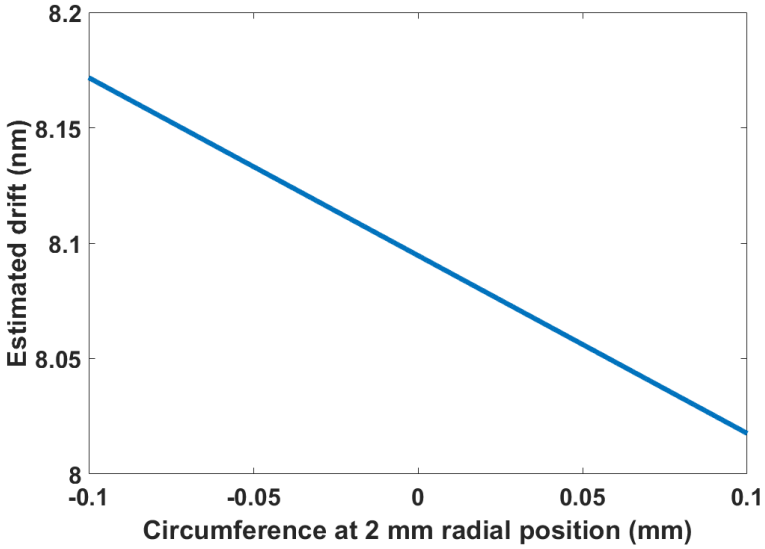

Figure 9.2: Subtraction of the fit lines to the overlapping data at the 2 mm radial position to determine drift.

The drift is determined at the zero position, or the middle of the overlapping region. This process is repeated for each of the radial positions. A summary of the results for a set of concentric circles is shown in Figure 9.3.

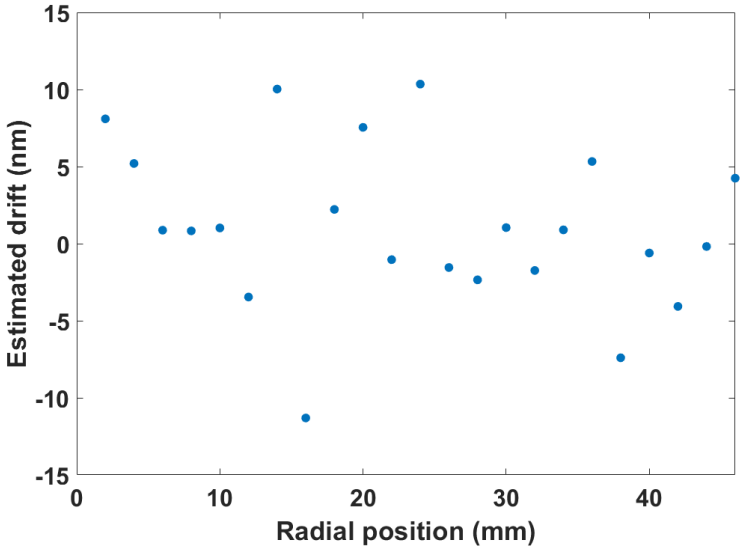

Figure 9.3: Drift estimate for each of the radial positions using the subtraction of the fit lines on the X axis.

There is not a noticeable trend in the drift for each of the radial positions. The

rotation of the C carriage is a fixed feed rate, so the same time has elapsed for each of the radial positions. The range of drift is around +/- 10 nm, which will be added to the uncertainty or error budget and can be fed into the Monte Carlo simulation.

9.3 Diametral Measurements

Measurements were made across the diameter of the part before and after each measurement to estimate the thermal drift over the entire measurement. The diameter measurements were taken at 0° and 90°. Figure 9.4 shows the measurement data and two diametral measurements.

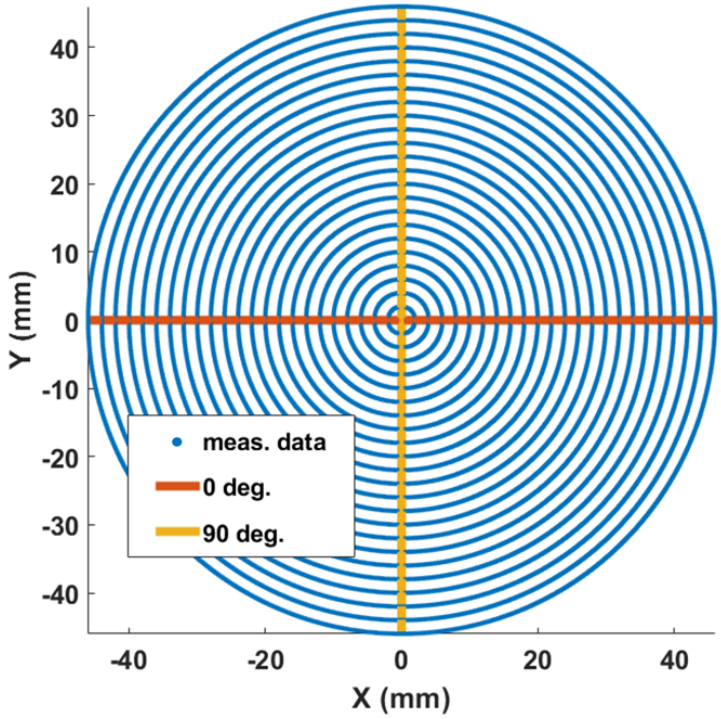

Figure 9.4: Measurement data on the X-Y plane showing the diametral measurements before and after the measurement.

To gage the effect of thermal drift during the measurement the before and after measurements were subtracted for the 0° and 90° orientations. A spline fit was used to get the data into uniform spacing for the subtraction. Figure 9.5 shows the subtraction for the 0° orientation.

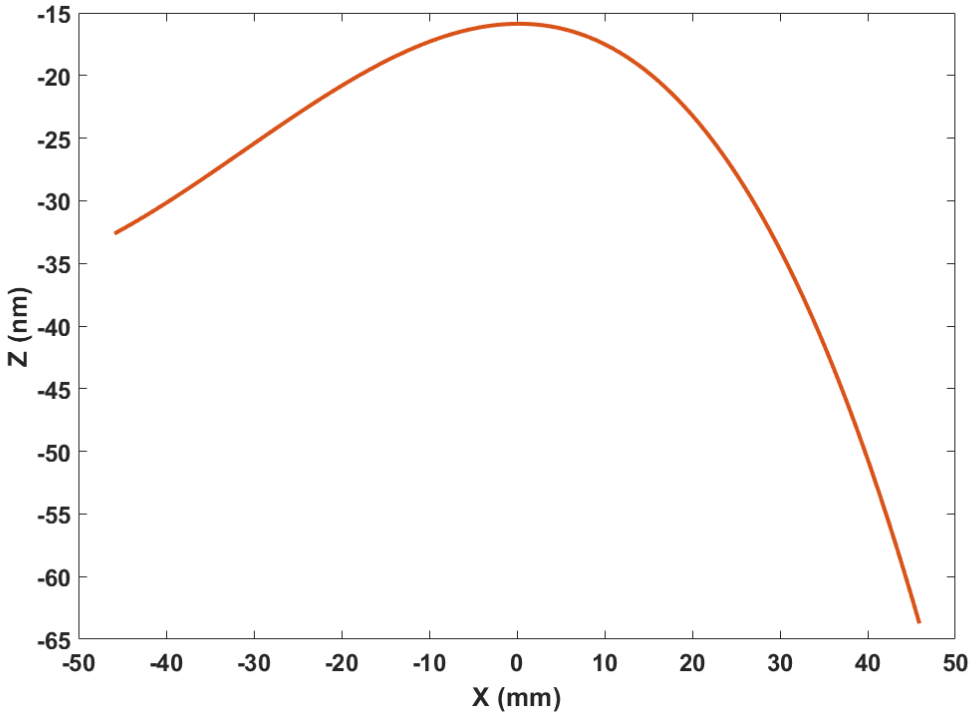

Figure 9.5: Subtraction of the diametral traces before and after at 0 degrees or the X axis.

While looking at these figures it is important to remember the aspect ratio of the data. With the Z direction in nanometers and the X direction in millimeters the extremes portrayed may in fact be less drastic. With the noise filtered out, maximimum thermal drift in the measurement is around 65 nm. Since the part is being measured for form using this probe path, the noise can be disregarded and will be dealt with using filtering and fitting of the polynomials. Figure 9.6 shows the subtraction for the 90° orientation.

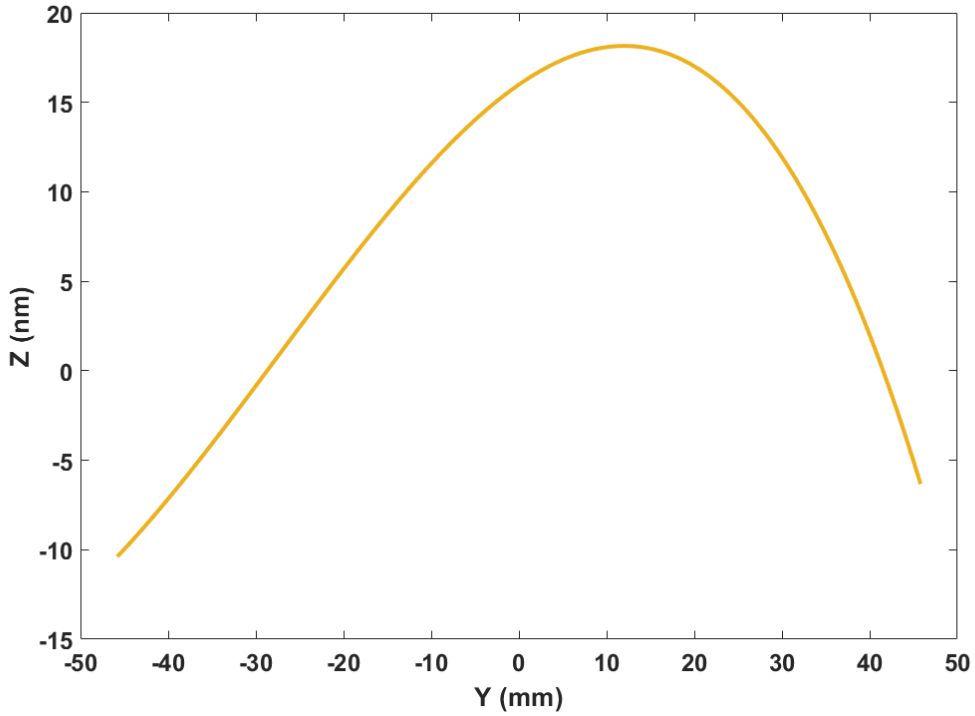

Figure 9.6: Subtraction of the diametral traces before and after at 90 degrees or the Y axis.

Again, disregarding the noise, maximum thermal drift is around 18 nm. For the full-scale TMA optics, a full diameter measurement will not be possible so either a radial measurement or a portion of the diameter will be measured.

9.4 Repeatability

To test the repeatability of the 100UMM, the half scale tertiary mirror was measured 3 times with the same program and the same mounting. Repeatability is defined in the GUM as the "closeness of the agreement between results of successive measurements of the same measurand carried out under the same conditions of measurement [12]." The same offsets and probe settings were used with the concentric circles probe path. Astigmatism shown in the part, could be from mounting in metrology or manufacturing. The measurement is of an 88 mm sub aperture since the edge was trimmed due to the annulus extending slightly into the clear aperture. The data spacing in

the radial direction for the measurements was 2 mm. Successive measurements a few hours apart were used for the repeatability test.

Repeatability conditions from the GUM [12]:

- The same measurement procedure
- The same observer
- The same measuring instrument, used under same conditions
- The same location
- Repetition over a short period of time

"Repeatability may be expressed quantitatively in terms of the dispersion characteristics of the results [12]." The repeatability in the second tertiary, the second time it was mounted is shown in Figure 9.7.

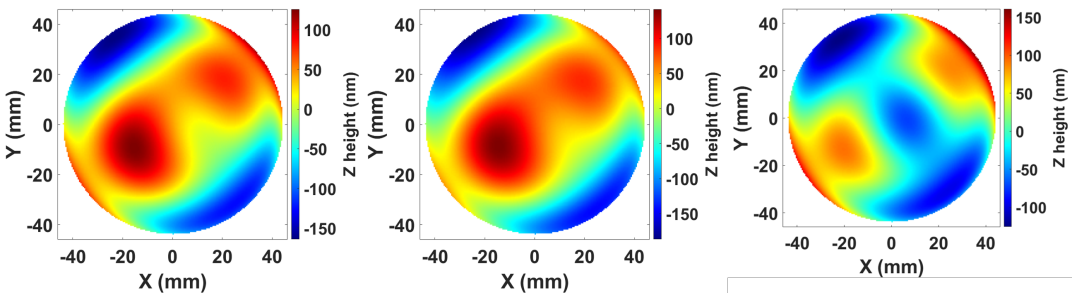

Figure 9.7: Repeatability with no error compensation on the Nanotech 100UMM showing 3 measurements with the prescription subtracted and then rotated flat.

There is a strong agreement between the first two measurements and a slight disagreement in the third measurement. To calculate the repeatability, the measurement data was brought into the MATLAB program in X, Y, Z coordinates without being compensated for the machine errors. The two measurements are fit to Zernike polynomials. The Zernike polynomials are used to get the data into the same X, Y coordinates so that a subtraction of the height data (Z coordinates) is possible. The data has the same radial spacing but varies along the azimuthal direction due to the scanning mode. The Zernike polynomial terms used are shown in Table 9.2.

Table 9.2: Zernike terms used to fit the data to get matching x, y coordinates for subtraction of the height data (z).

Zernike Polynomials							
n	m	n	m	n	m	n	m
0	0	4	-4	5	5	7	-3
1	1	4	-2	6	-6	7	-1
1	-1	4	0	6	-4	7	1
2	0	4	2	6	-2	7	3
2	2	4	4	6	0	7	5
2	-2	4	-5	6	2	7	7
3	-1	5	-3	6	4	8	0
3	1	5	-1	6	6	10	0
3	-3	5	1	7	-7	12	0
3	3	5	3	7	-5	14	0

When fitting to an asphere, which the makes up most of the sag of the half scale tertiary, it is important to use enough of the spherical terms to fully capture the shape. It could be thought of like the Fourier series, it requires a certain amount of Cos/Sin waves to define a wave or shape. The fit was subtracted from the initial surface to see how good the fit was. The spherical Zernike terms have a m value of zero. In Table 9.2, there are four spherical terms added at the end to fully characterize the asphere. Another way to get around that issue is to subtract the base asphere first then fit to the freeform plus any error in the base asphere and tilt. It is possible to add too many spherical terms and may cause a ripple in the radial direction of the fit.

9.5 Reproducability

The 2nd half scale tertiary mirror was measured in two different setups to determine the reproducibility. Each setup followed the same alignment and mounting procedure as described above (Sections 4.8, 7.2). The radial data spacing was 2.3 mm. Reproducibility of the results of measurements is defined in the GUM as "closeness of the agreement between the results of measurements of the same measurand carried out under changed conditions of measurement [12]." The conditions changed for the reproducibility of the half scale tertiary mirror where: the time, part mounting, C carriage location, centering of part and probe, and the datum location. To show the reproducibility, the two measurements were subtracted.

The changed conditions may include [12]:

- principle of measurement
- method of measurement
- observer
- measuring instrument
- reference standard
- location
- conditions of use
- time

Note: Reproducibility may be expressed quantitatively in terms of the dispersion characteristics of the results. Results are usually understood to be corrected results. The difference for determining the reproducibility is shown in Figure 9.8.

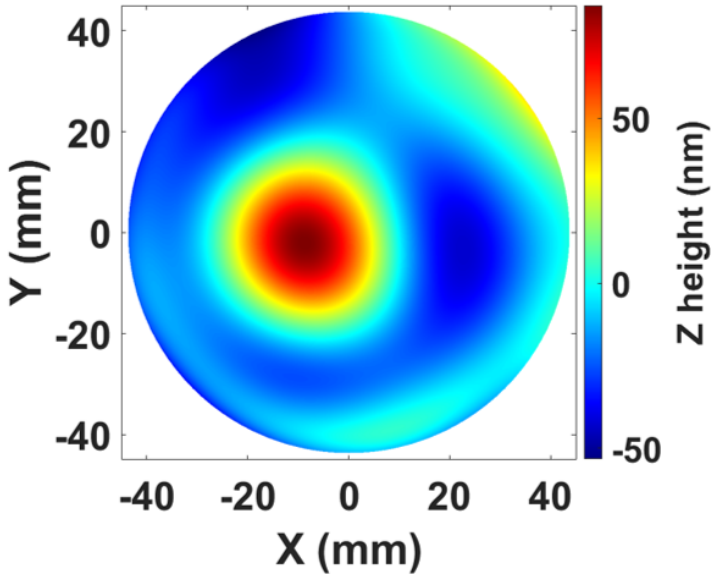

Figure 9.8: Reproducibility measurements on the Nanotech 100UMM of the 2nd half scale tertiary mirror with a 2.3 mm radial data spacing.

The same fitting and subtraction procedure were followed in MATLAB as was described for the repeatability. The difference is the data sets were from different setups rather than repeat measurements in the same setup.

9.6 Positive and Negative Sides of Part (Results)

The discrepancies in measuring the optics using different X and C carriage positions is examined. As discussed above, it is possible to measure the half scale tertiary using different X and C carriage positions to reach the same position on the part. If the center of the part is at zero, the X carriage could be moved in the positive direction or negative direction for the concentric circle probe path. The difference between the positive and negative side measurements after subtracting the prescription but before error compensation is shown in Figure 9.9.

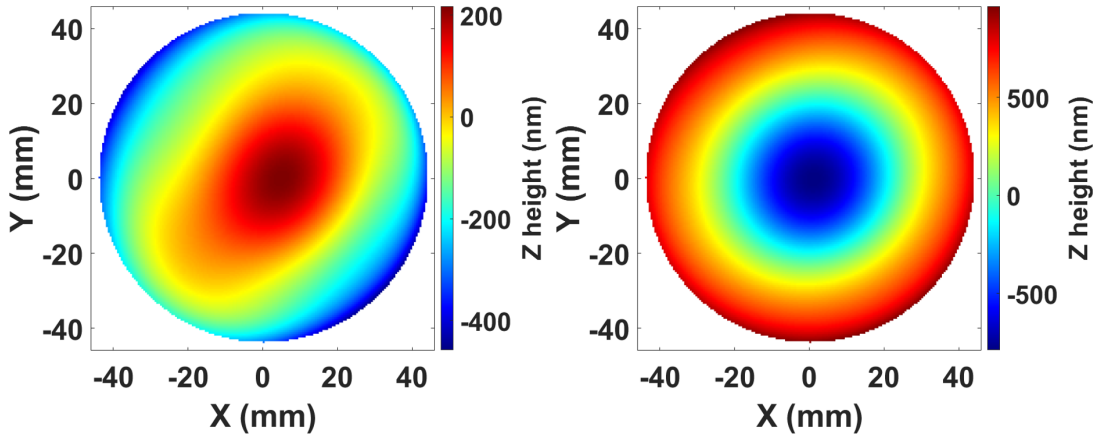

Figure 9.9: Positive side (left) and negative side (right) concentric circle measurements before error compensation.

There is a roughly 2 μm cone shape to the negative side where the positive side has a PV around 600 nm. Cone is a common symptom of out of squareness of the X carriage and the C carriage however it would appear on both measurements. There is a possibility that the X carriage horizontal straightness and X squareness are combining to produce the effect shown. Another possibility is the shape of the part being such that cone in the part is adding to negative side measurement and subtracting the positive side leaving the actual part shape in between the two measurement results. The squareness error of the machine that manufactured the part could be of the same magnitude as that of the 100UMM. This would also mean that the squareness measurement used in the error compensation is incorrect. The error compensated measurement results are shown in Figure 9.10.

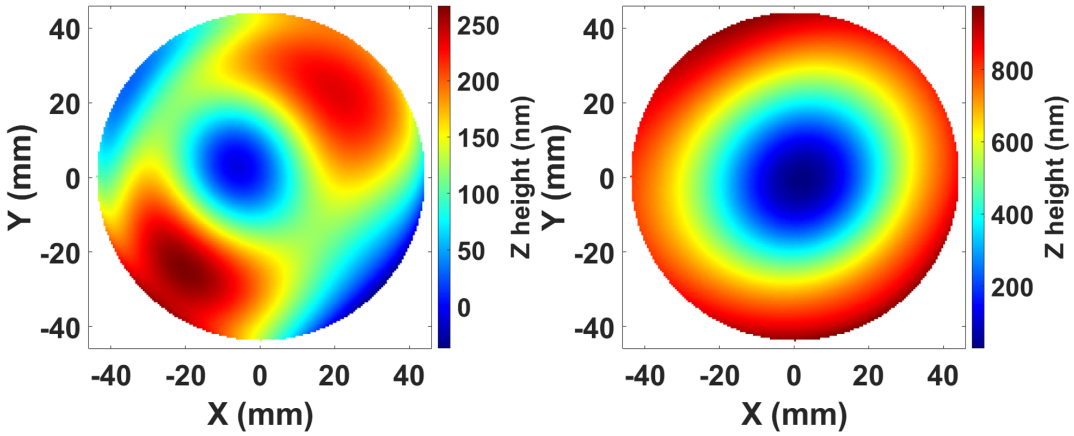

Figure 9.10: Positive side (left) and negative side (right) concentric circle measurements after error compensation.

After compensation, the cone reduced to 1 μm on the negative side and the PV reduced to about 250 nm on the positive side. The amount of error compensation for both measurement sides is shown in Figure 9.11.

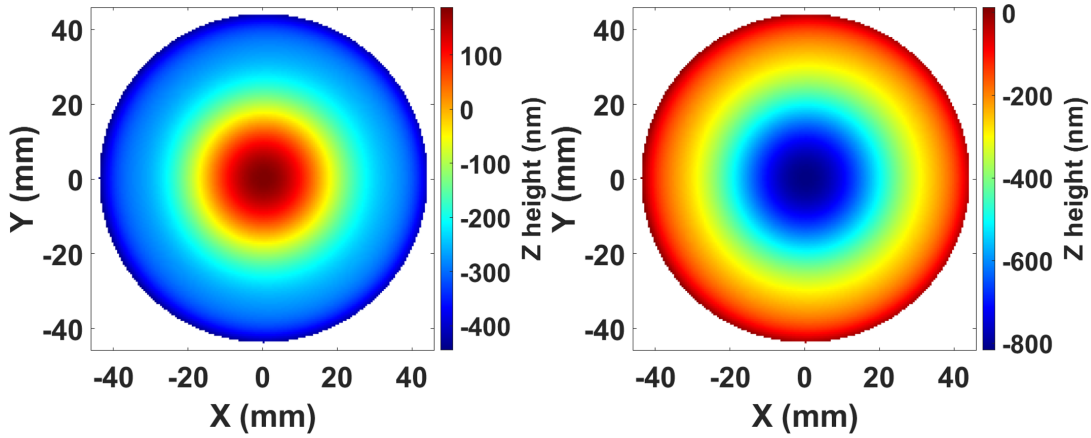

Figure 9.11: Amount of error compensation for the half scale tertiary measurements for the positive side (left) and negative side (right).

The subtraction of the two measurements from the positive and negative measurements is shown in Figure 9.12.

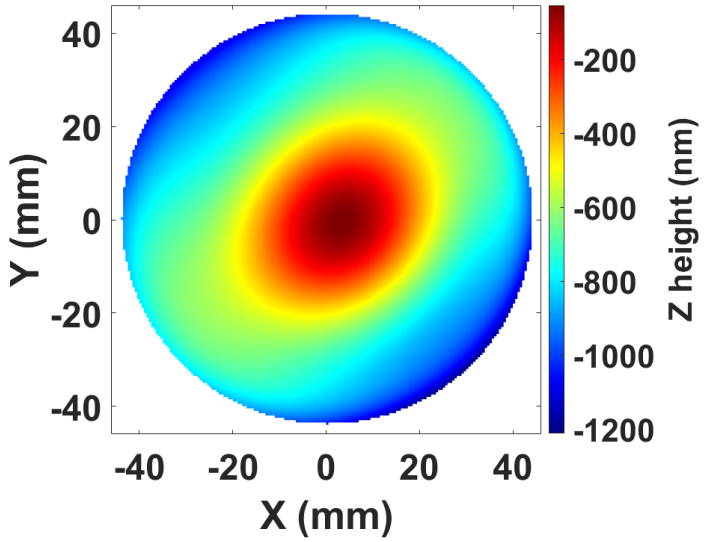

Figure 9.12: Subtraction of the negative and positive X carriage direction measurements.

The subtraction shows a substantial amount of discrepancy between the two measurement results.

9.7 Adjusted Squareness Measurements

By multiplying the X carriage horizontal squareness by a correction factor of 1.3 it was possible to balance out the amount of cone on the positive and negative X carriage direction measurements. The amount of cone on each measurement equaled out at around 600 nm. The measurement results with the correction factor are shown in Figure 9.13.

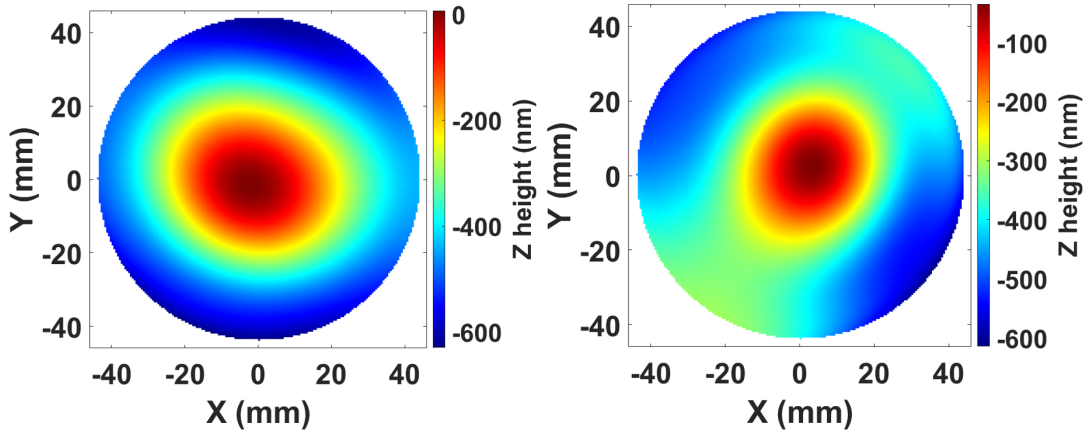

Figure 9.13: The squareness error was multiplied by a correction factor of 1.3 to equal out the amount of cone in each measurement (left) after compensation negative side, (right) after compensation positive side.

The resulting shapes show the same amount of cone and each has a slight amount of astigmatism. Astigmatism is common in mounting a part. The amount of compensation to each measurement is shown in Figure 9.14.

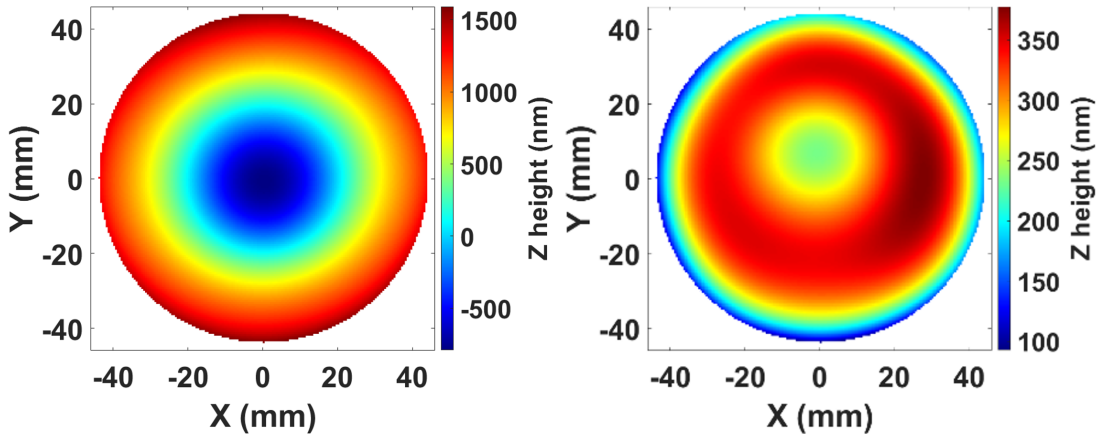

Figure 9.14: The squareness error was multiplied by a correction factor of 1.3 to equal out the amount of cone in each measurement (left) amount of compensation negative side, (right) amount of compensation positive side.

up to about 1500 nm of correction to the measurement is shown using the negative side of the X carriage and about 250 nm on the positive side. The subtraction of the positive and negative side measurements is shown in Figure 9.15.

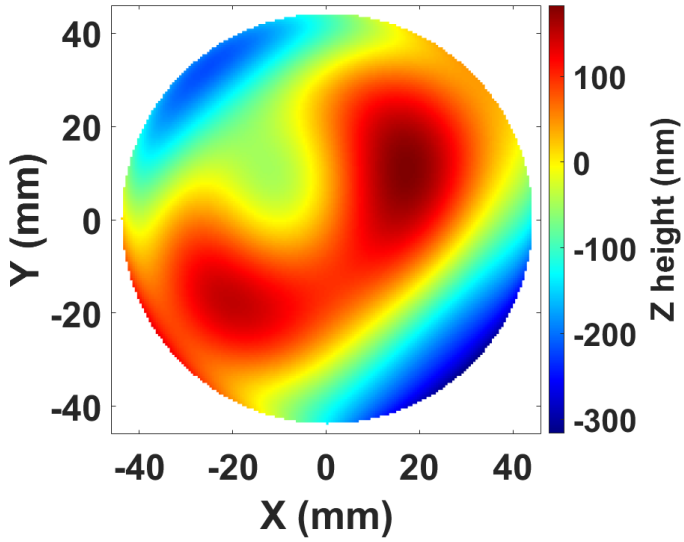

Figure 9.15: Subtraction of the negative and positive X carriage direction measurements after the squareness correction factor of 1.3.

The amount of difference between the two measurements is decreased to about 450 nm.

9.8 Point by Point Measurements (TSP)

The same discrepancy was noticed in the TSP raster measurements. The probe path of the measurement uses a larger portion of the X carriage. In the concentric circle measurements, the range of the X carriage is equal to the radius while in the TSP measurements the range of the X carriage is equal to the diameter. It is possible to use only the X carriage range equal to the radius on the TSP measurements however that does not illuminate issues with the error compensation. The resulting plot of the data is interesting since there is data taken at opposite ends of the X carriage range that appear adjacent in the plot of the measurement data. The figures may look pixelated as Delaunay triangulation was used for plotting. Figure 9.16 shows the measurement plotted before error compensation.

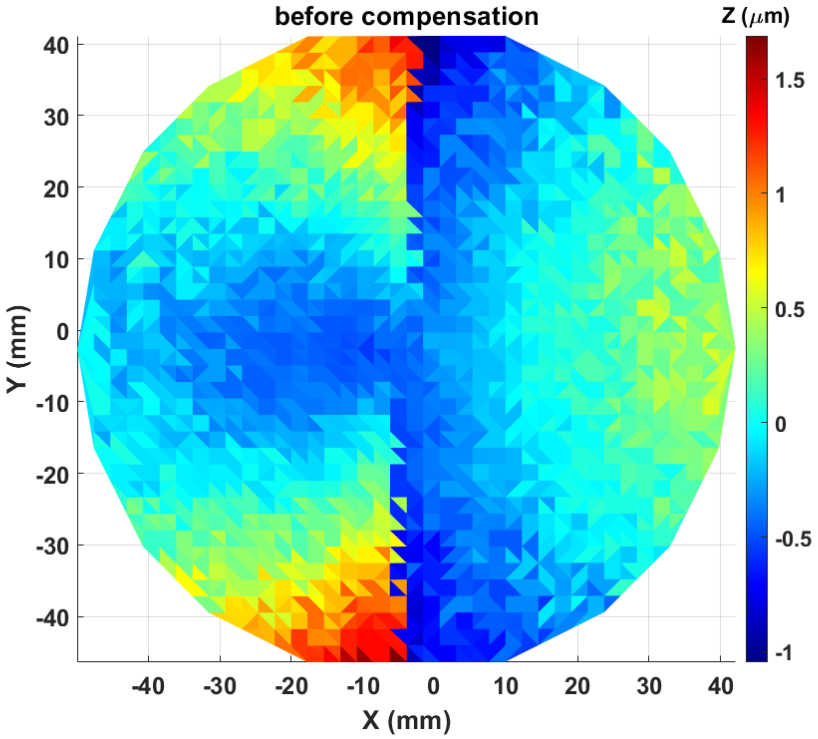

Figure 9.16: Measurement of the second half scale tertiary using the raster pattern before compensation.

Notice the vertical discontinuity in the middle of the part. The point by point TSP raster path is followed by moving the C, X and Z carriages, taking measurements on a grid pattern shown in Figure 7.13. Since it goes past the zero mark, the shape changes with the machine errors at opposite ends of the X carriage positions. The measurement is a point by point measurement. It may look like a scanning measurement in the figure, but the intent is to show the direction and order the data was taken. The path shown in Figure 9.17 shows the path of the probe in the X-Y plane.

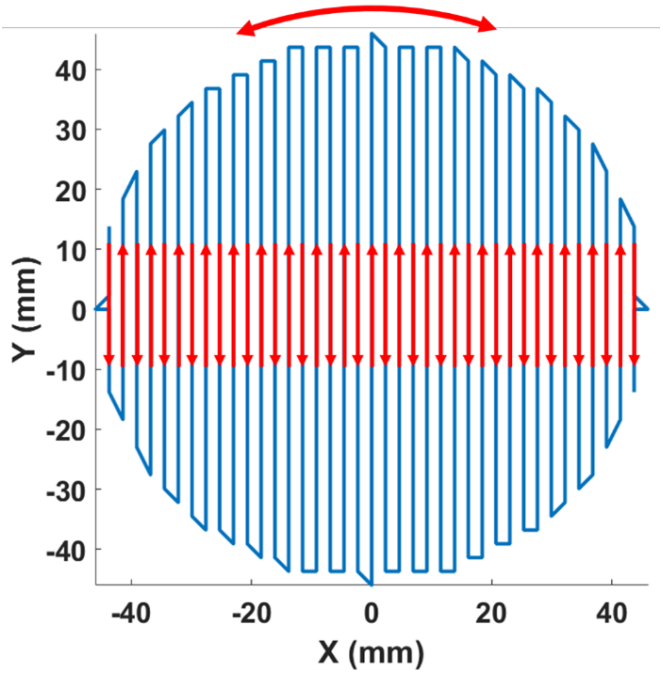

Figure 9.17: Probe path for the traveling salesman problem raster measurement.

The motion of the C carriage is shown in Figure 9.18.

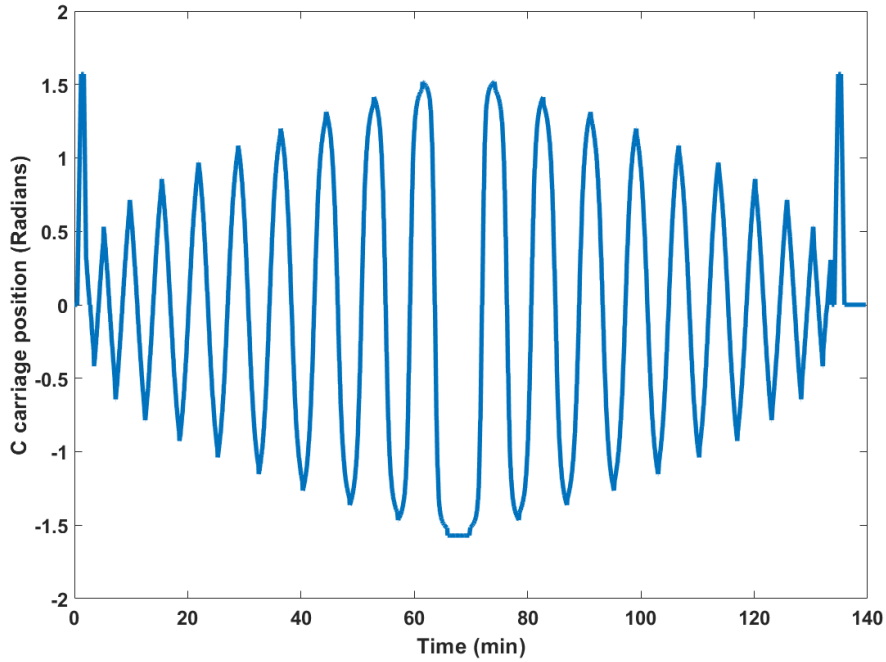

Figure 9.18: C carriage position over time while measuring the half scale tertiary using the traveling salesman problem raster probe path.

As the probe moves across the part on the X carriage the C carriage is rotated between $\pi/2$ and $-\pi/2$ so the probe can reach the measurement points. The X carriage motion is shown in Figure 9.19.

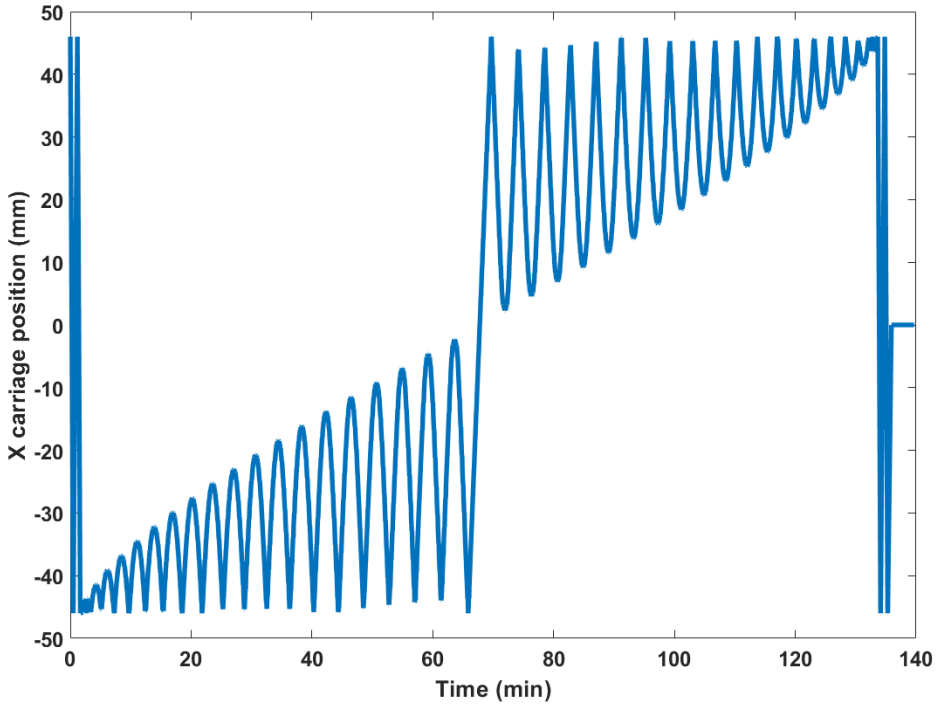

Figure 9.19: X carriage position over time while measuring the half scale tertiary using the traveling salesman problem raster probe path.

The X carriage moves back and forth in the negative direction of the part coordinate system then moves to the positive direction halfway through the measurement. This is the reason why two points that are next to each other on the part use opposite ends of the X carriage range. Ideally, error compensation should eliminate the discontinuity of the measurement result however the error compensation reduced the error roughly by half.

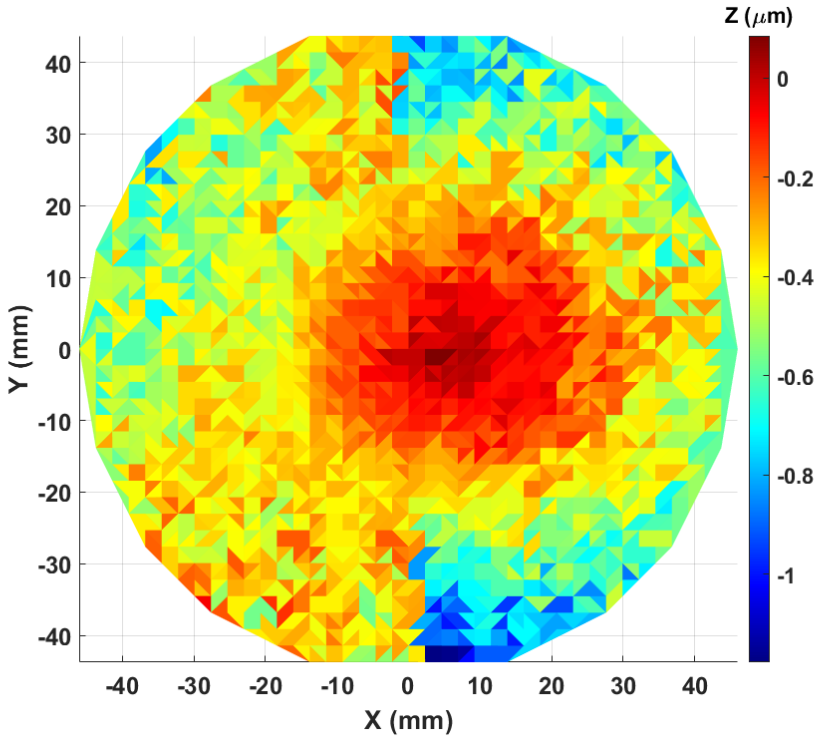

Figure 9.20: Measurement of the second half scale tertiary using the raster pattern after compensation.

After error compensation the discontinuity reduced from about 2 μm to about 1 μm. A similar reduction in the discrepancy between the positive and negative side measurements discussed above. Dulaney triangulation and 'trisurf' MATLAB functions were used because they gave a more accurate representation of the surface than fitting to Zernike polynomials and replotting. With the discontinuity in the data a fitting algorithm would smooth out the surface and some fidelity would be lost.

9.9 Half Scale Tertiary Measurements

The measurement result is combined with an uncertainty statement. The measurement will inform the designers and manufacturers how close the mirror is to the prescription so that assumptions of the system performance can be made. It is possible that the mirror can be re-machined to correct the measured errors. The measurement result can be entered into the optical design software to re-evaluate

positioning of an optic in the imaging system. The half scale tertiary prescription is defined by the asphere and 21 Zernike coefficients of which a few are zero. The first three Zernike terms can be disregarded as the piston and tilt terms are removed from the measurement data.

9.10 Monte Carlo Simulation

The Monte Carlo simulation was run for measurements of the half scale tertiary mirror from the AFRL optics. The entire data set was run through the simulation with each measurement point being evaluated every iteration. The result is a complete set of measurement points for every iteration, resulting in a large data set. The data from the Monte Carlo simulation is statistically evaluated for the task specific uncertainty.

A histogram of the Z height of a single measurement point as it goes through the Monte Carlo simulation was plotted to determine the distribution. For a given measurement point, the mean of the Monte Carlo simulation data should trend to the value for the same measurement point of the error compensated data. A histogram for a measurement point in the 0 mm radial direction is shown in Figure 9.21.

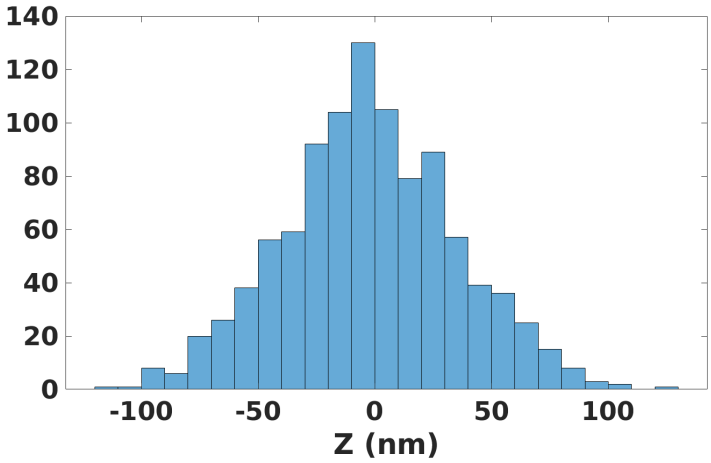

Figure 9.21: Z height histogram from the Monte Carlo simulation at the center of the part (1000 iterations).

It is expected to continue to take a Gaussian shape as more iterations are completed. A histogram for a measurement point in the 40 mm radial direction is shown in Figure

9.22.

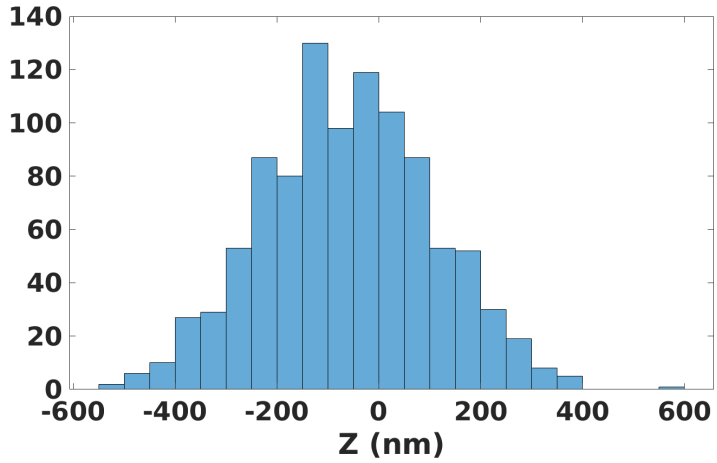

Figure 9.22: Z height histogram from the Monte Carlo simulation at the 40 mm radial position toward the middle of the circular measurement (1000 iterations).

The uncertainty map or standard deviation of the data in the Monte Carlo simulation is shown in Figure 9.23.

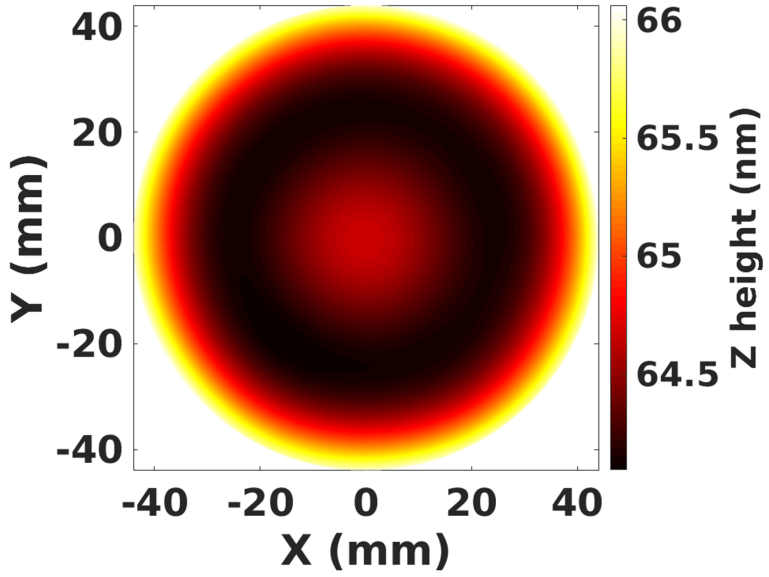

Figure 9.23: Uncertainty map of the Monte Carlo simulation with 1000 iterations for the AFRL TMA half scale tertiary measured on the Nanotech 100UMM.

9.11 Spherical Mirror Measurements

A glass spherical mirror was measured using a Fizeau interferometer and the 100UMM to compare the measurement results. The Fizeau measurements were made by an associate at UNCC named Kumar Arumugam and the 100UMM measurements were made by a research partner Laura Hopper. The errors in the transmission sphere were separated out of the measurement result by Kumar using ball averaging and the n-rotation method [60], [61]. Table 9.3 shows the specifications from the supplier of the spherical mirror.

Table 9.3: Spherical mirror specifications.

Specification	
Substrate	BOROFLOAT®
Diameter	76.20 +1.0/-0 mm
Effective Focal Length	152.4 mm
Surface Accuracy	$\lambda/4$
Focal Length Tolerance	+/- 2%

A F/1.5 transmission sphere was used in the measurement. The Fizeau measurement has the Zernike polynomial terms for piston, tilt and power removed. The Fizeau measurement does not provide useful information about the piston, tilt or power. The result shows a slight astigmatism with a peak to valley around 100 nm. The Fizeau measurement are shown in Figure 9.24.

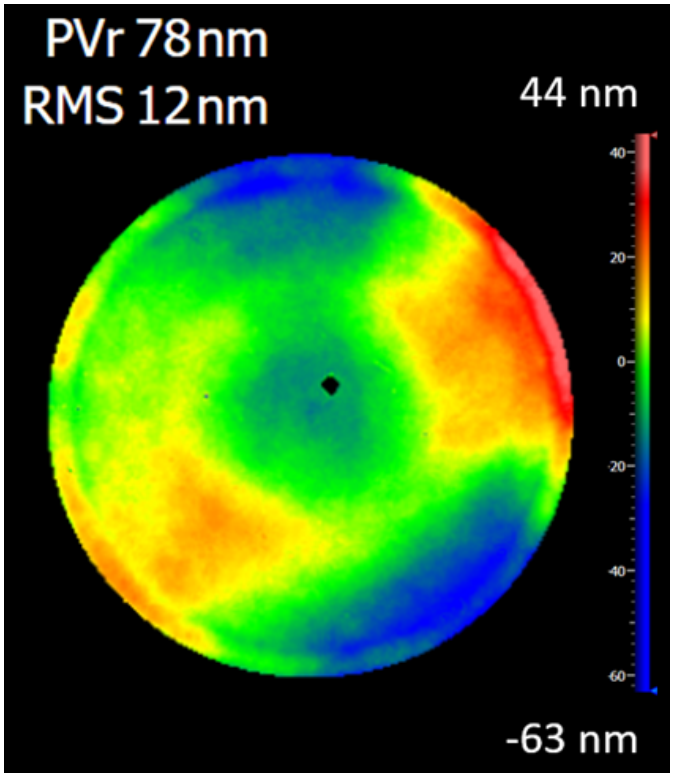

Figure 9.24: Laser Fizeau measurement of the spherical mirror used as an artifact to measure on the Nanotech 100UMM (Source: Kumar Arumugam).

The spherical mirror was chosen as an optical surface, that could be measured with a well-known instrument and technique (Fizeau interferometer), to serve as an artifact to be measured on the 100UMM. The spherical mirror does not require any movement in the Z carriage while data is being recorded, reducing possible error contributions. The measurements on the 100UMM were compensated for the geometric machine errors. The optic was mounted using a vacuum chuck and measured with the concentric circle probe path described above with radial spacings of 1.905 mm and 3.81 mm. The part was small enough that the measurement could be done on the positive and negative sides in the X direction of the part like the half scale tertiary measurements. The measurement result without error compensation, measured at the 3.81 mm radial spacing, is shown in Figure 9.25.

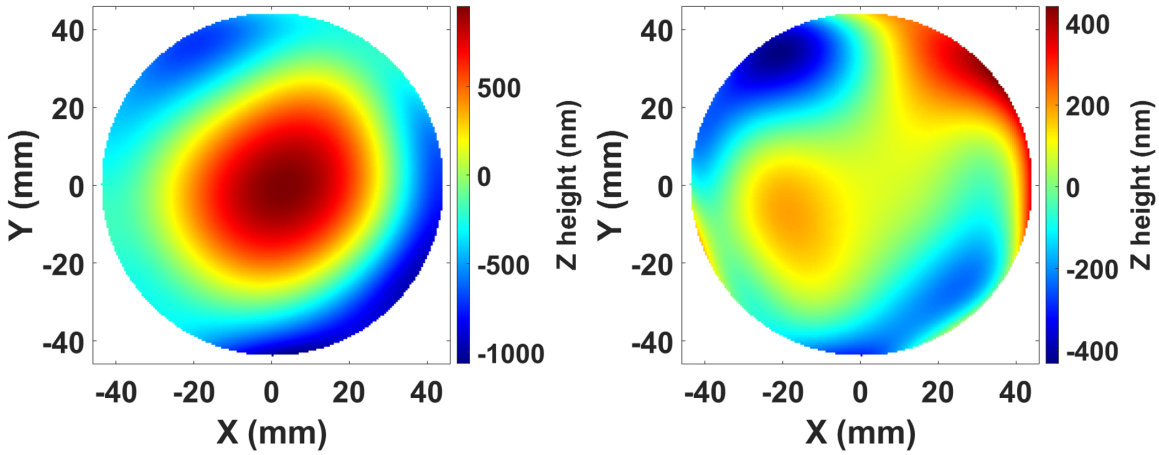

Figure 9.25: Spherical optic measurements without error compensation with the positive side (left) and negative side (right) in the X direction.

For plotting, the measurement result was fit to the first 36 Zernike terms in the Fringe set. To compare directly with the Fizeau measurement, the Zernike terms for piston, tilt and power were removed for plotting. The measurement results after error compensation are shown in Figure 9.26.

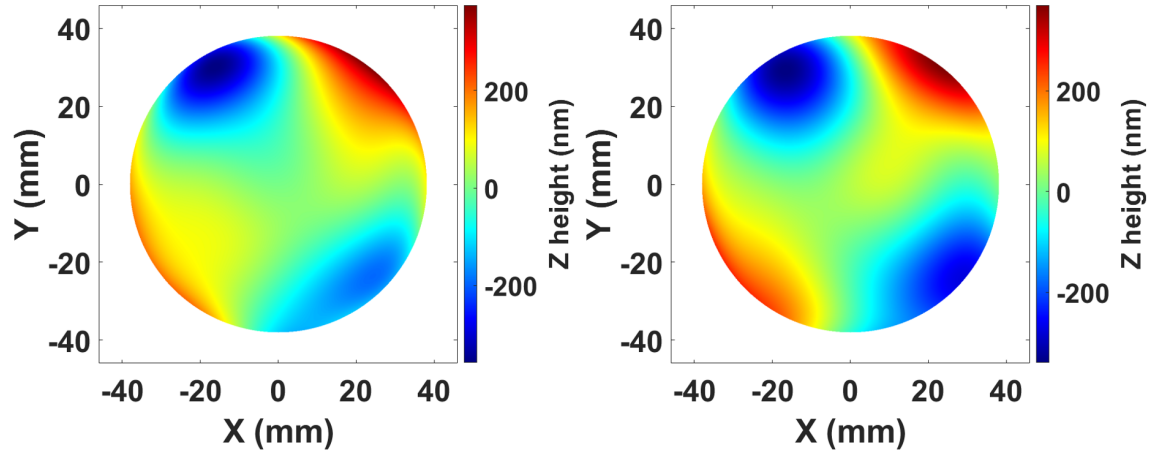

Figure 9.26: Spherical optic measurement result after error compensation with the positive side (left) and negative side (right) in the X direction.

The amount of error compensation is shown in Figure 9.27.

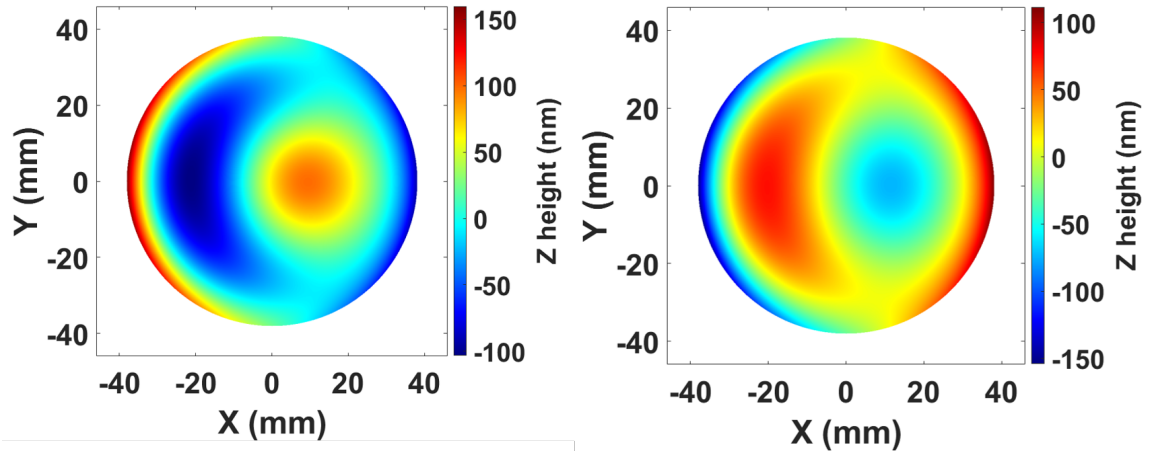

Figure 9.27: Amount of error compensation for the spherical optic measurements showing the positive (left) and negative (right) side in the X direction measured at the 3.81 mm radial spacing.

The subtraction of the positive and negative side measurements is shown in Figure 9.28.

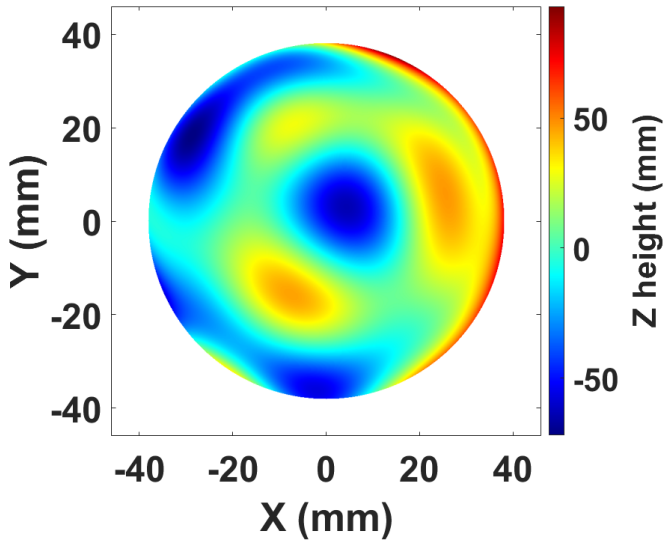

Figure 9.28: Subtraction of the positive and negative measurements (in the X direction) of the spherical optic measured at a data spacing of 3.81 mm.

The measurement using the 3.81 mm radial data spacing had less of a discrepancy between the measurements on the positive and negative side of the X carriage than the 1.905 mm radial spacing measurements. This is likely due to the some abnormalities

on the edge of the measurement for the 1.905 mm radial data spacing.

A colleague Laura Hopper conducted testing to investigate the effect of mounting using vacuum on the spherical mirror. The probe was placed at the center of the part and measurements were taken at varying levels of vacuum to determine the change in displacement or deflection of the mirror due to a change in vacuum. It was assumed to be a linear relationship and by extrapolating to zero we can estimate the amount of deflection at the vacuum used in the measurement (10 in-Hg). Figure 9.29 shows the experimental data and the linear fit.

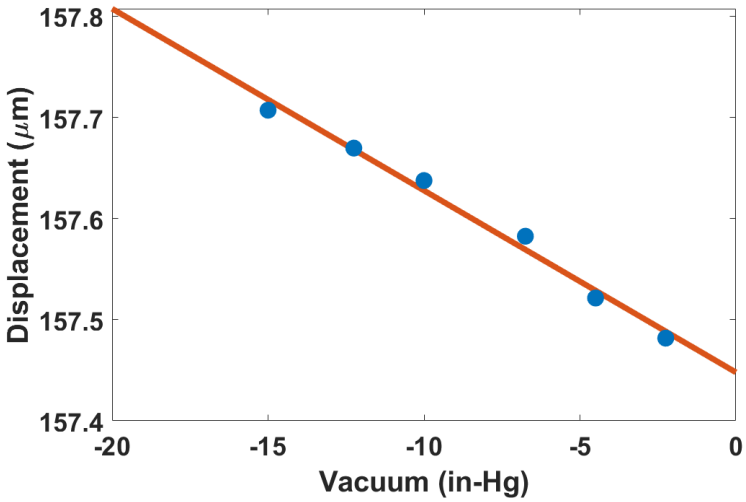

Figure 9.29: Testing the effect of vacuum on the spherical mirror using a vacuum chuck for mounting.

The estimated deflection was about 190 nm. With a deviation of about 500 nm from the Fizeau measurement to the 100UMM measurements, the vacuum does not explain all of the discrepancy but accounts for a large portion.

Deflection of a uniformly loaded, elastically isotropic, and simply supported circular window was calculated to estimate the amount of deflection from the vacuum chuck. The equation was found in Reference [62] and is shown in 9.1.

$$w = \frac{3\Delta p(1-\nu^2)}{16Et^3}\left[\frac{5+\nu}{1+\nu}\left(\frac{D}{2}\right)^2 - r^2\right]\left[\left(\frac{D}{2}\right)^2 - r^2\right] \tag{9.1}$$

Where w is the deflection, ν is Poisson's ratio, E is the Young's modulus, t is the thickness, D is the diameter, Δp is the change in pressure and r is the radial value. The estimated value of deflection for a circular window of the same material as the spherical mirror was 220 nm using the same thickness.

CHAPTER 10: CONCLUSIONS

A 4-axis coordinate measurement machine (Nanotech 100UMM) was acquired for measurements of freeform reflective optics from a three mirror anastigmat telescope in the 250 mm class. Freeform optics allow designers greater freedom to innovate however they require some additional considerations during metrology such as large slopes, a lack of an axis of symmetry and difficulties in locating the prescription. These limitations were overcome by using a chromatic confocal probe, compensating the geometric machine errors in the CMM, probe path planning, and fiducials manufactured into the mirrors.

A method was developed to measure freeform optics on the Nanotech 100UMM and to provide a task specific uncertainty statement. The method utilizes a mathematical model of the machine for error compensation and a Monte Carlo simulation for the task specific uncertainty evaluation. The geometric machine errors sensitive to the parts measured for the AFRL project were measured for use in the mathematical model. The uncertainty in those measurements was added to the model for the Monte Carlo simulation.

Two of the half scale tertiary mirrors were manufactured for testing. The mirrors were used in repeatability and reproducibility measurements and for experiments with probe paths. The probe paths were designed to estimate thermal drift over the measurement and to check the machine error compensation. Discrepancies were found when measuring the optics due to the geometric machine errors. The task specific uncertainty in the half scale tertiary measurements was evaluated using the Monte Carlo simulation showing an uncertainty of about 65 nm for the form measurement.

Through careful probe path planning it is possible to estimate and possibly com-

pensate for thermal drift in measurements. The measurement time is also decreased, further reducing thermal drift. Many factors effecting the uncertainty of the measurement were discussed, and solutions suggested. Although some of the issues are machine specific, many of the same issues arise when measuring freeform optics in general. The greater the repeatability required, the more thought and testing must go into the measurement process including the machine and temperature stability. Ways of quantifying the thermal drift can be incorporated into the measurement using closure and repeat measurements. The use of fiducials and datums reduce the uncertainty contribution from locating the prescription on a part for measurement, manufacturing, and system alignment.

A glass spherical mirror was measured on the 100UMM to compare with measurements from a Fizeau interferometer. The discrepancy in the measurements was partly due to mounting the spherical mirror on the 100UMM with a vacuum chuck. Analysis showed that the deflection in the center of the mirror due to vacuum is about 190 nm.

10.1 Future Work

As with any research project, there are still avenues that could be explored. Often more discovery leads to more questions. Some of the areas left to be researched will be discussed here. The Nanotech 100UMM used for this research will remain operational and will be used to measure the final AFRL optics as they become available.

Further measurements will be conducted on the half-scale mirrors and the techniques discussed will be expanded to measurements of the full-scale mirrors. A compensation for the data age and non-linearity in the probe is being researched. The data acquisition and chromatic confocal probe testing is a primary focus. The full scale AFRL optics will be measured using the concentric circle probe path, error compensation and Monte Carlo simulation.

A lot of the groundwork was done to perform probe normal measurements, but it

was decided that probe normal was not necessary to achieve the level of uncertainty required with the chromatic confocal probe. Probe normal could allow for the use of contact probes or probes that did not have a large angle of acceptance. Parts with a steep slope outside of the angle of acceptance for the chromatic confocal probes could also be measured.

The point by point measurements using the traveling salesman algorithms could be re-measured. Two sets of measurements with a 180-degree flip in the C carriage between them would help establish a reproducibility. The squareness error could be estimated using this method. It is a similar idea to a reversal, but the part is not flipped. The same measurement point will be measured at the same distance from the fiducial origin on the X carriage but on the opposite side.

To fully characterize the 100UMM, the machine error measurements should be completed. If parts with different geometry are to be measured on the 100UMM the sensitivity to the machine errors should be evaluated and sensitive errors should be considered in the model. If the errors cannot be directly measured, an estimation of the uncertainty contribution can be entered into the model for the Monte Carlo simulation.

Most of the testing was done on the half scale tertiary mirror for the AFRL telescope. As the AFRL project progresses, larger optics will be available to measure. The full-scale optics will be tested as a full-scale system. The measurement data for each of the mirrors can be entered into the optical design software to optimize the alignment and estimate the wavefront.

The LabVIEW program for data acquisition could be improved to reduce the data age uncertainty. There may be a better way to read the scale data and do the interpolation that is faster and easier to control the data rate. The system in place uses a buffer to collect the carriage positions and clears the buffer every time it is interrogated. The system is first in first out (FIFO) which means that the data that

is used is oldest data in the buffer. The LabVIEW program is set up to keep that buffer as small as possible, but it is not perfect. A system that is last in first out would be better, so the data represents the latest position. This would match the probe data acquisition better. A system without the buffer could be faster and have more recent data.

For optics that a contact probe could be used, it would be interesting to use an optical probe and a contact probe with the same probe path and compare the results. The contact measurement would have to probe normal to surface. The probes available at UNCC have the required repeatability and provide mechanical averaging due to the size of the stylus.

The machine error measurements could be re-measured as the machine was shut down for an extended amount of time. The temperature control in the surrounding laboratory has also been improved. Some manufacturers recommend re-calibrating the machine every year to ensure that the machine has not fallen out of specification.

REFERENCES

[1] R. J. Hocken and P. H. Pereira, *Coordinate Measuring Machines and Systems*. CRC Press, 2 ed., 2012.

[2] G. Zhang, R. Ouyang, and B. Lu, "A displacement method for machine geometry calibration," *Annals of CIRP*, vol. 37, pp. 515–518, 1988.

[3] T. Noste, L. Hopper, J. Miller, and C. Evans, "Task specific uncertainty in measurement of freeform optics," in *EUSPEN - 19th International Conference Proceedings*, 2019.

[4] ISO 230-2-2014, "Test code for machine tools - part 2: Determination of accuracy and repeatability of positioning of numerically controlled axes," 2014.

[5] Philtec Inc., *Fiberoptic Displacement Sensor PHILTEC® Model DMS-RC25*, 2018.

[6] Precitec Group, "Chromatic confocal principle for distance measurements." https://www.precitec.de/en/products/optical-measuring-technology/how-it-works/, 2 2020.

[7] E. R. Marsh, *Precision Spindle Metrology*. DEStech Publications, Inc., 2008.

[8] Mahr Federal, *Mahr - Millimar Electronic Levels Flyer*, 2005.

[9] Hewlett Packard, *5528A Laser Measurement System Users Manual*, 1988.

[10] L. Hopper, T. Noste, J. Miller, and C. Evans, "Error sources, compensation, and probe path optimization for on-machine metrology of freeform optics," in *Optical Manufacturing and Testing XIII* (R. Rascher and D. W. Kim, eds.), p. 7, SPIE, 8 2020.

[11] J. X. Jiang and P. J. Scott, *Advanced Metrology - Freeform Surfaces*. Elsevier Science, 2020.

[12] Joint Committee for Guides in Metrology, "Evaluation of measurement data - guide to the expression of uncertainty in measurement," 2008.

[13] Joint Committee for Guides in Metrology (JCGM), "International vocabulary of metrology - basic and general concepts and associated terms (vim)," 2012.

[14] F. Z. Fang, X. D. Zhang, A. Weckenmann, G. X. Zhang, and C. Evans, "Manufacturing and measurement of freeform optics," *CIRP Annals - Manufacturing Technology*, vol. 62, pp. 823–846, 2013.

[15] C. J. Evans, R. J. Hocken, and W. T. Estler, "Self-calibration: Reversal, redundancy, error separation, and 'absolute testing'," *CIRP Annals - Manufacturing Technology*, 1996.

[16] C. J. Evans and A. D. Davies, "Certification, self-calibration and uncertainty in optical surface testing," *International Journal of Precision Technology*, vol. 3, p. 388, 2013.

[17] R. G. Wilhelm, R. Hocken, and H. Schwenke, "Task specific uncertainty in coordinate measurement," *CIRP Annals - Manufacturing Technology*, 2001.

[18] J. B. Bryan, "The power of deterministic thinking in machine tool accuracy," in *First International Machine Tool Engineers Conference*, Lawrence Livermore National Labratory, 1984.

[19] J. B. Bryan, "International status of thermal error research," in *17th General Assembly of CIRP*, 1967.

[20] J. Bryan, T. Charlton, D. DeBra, U. Dea, R. R. Donaldson, J. Roblee, U. H. Harary, C. Evans, R. Hocken, J. N. Raja, U. Humanistic, U. Ingenieurburo, L. Sauge, J. Janeczko, L. F. D. Lac, W. R. U. Kegg, C. Milacron, U. H. Kun, E. T. Waldele, G. Llnl, C. E. U. Loewen, M. Roy, A. Mottu, S. J. Petavel, S. H. Renker, F. A. S. Thun, S. S. Sartori, lnstituto di Metrologia, I. T. Sata, I. Saitama, J. H. Sato, Y. Su, O. ACooper, J. Pack, D. Cogdell, H. Trumphold, T. A. K. M. S. G. V. D. Wolf, and P. Schellekens, "International status of thermal error research," *Annals of the CIRP*, vol. 39, pp. 645–656, 1990.

[21] W. Brewer, J. B. Bryan, E. R. McClure, and J. W. Pearson, "Thermal effects in dimensional metrology," tech. rep., University of California Ernest O. Lawrence Radiation Laboratory, 1966.

[22] E. B. Mcclure, *Manufacturing Accuracy through Control of Thermal Effects*. PhD thesis, University of California Berkeley, 6 1969.

[23] J. M. Beaman, *A PROCESS TO EVALUATE COMMERCIAL SOFTWARE PACKAGES THAT ESTIMATE MEASUREMENT UNCERTAINTY THROUGH SIMULATION*. PhD thesis, University of North Carolina at Charlotte, 2011.

[24] L. C. Hale, *Principles and Techniques for Designing Precision Machines*. PhD thesis, Massachusetts Institute of Technology, 1999.

[25] M. Uwakwe, *MINIMIZING TASK-SPECIFIC UNCERTAINTY IN CMM-BASED FREEFORM OPTICS METROLOGY*. PhD thesis, University of North Carolina at Charlotte, 2018.

[26] K. P. Thompson and J. P. Rolland, "Freeform optical surfaces: A revolution in imaging optical design," *Optics and Photonics News*, vol. 23, p. 30, 6 2012.

[27] W. B. Rowe, *Hydrostatic, Aerostatic and Hybrid Bearing Design*. Butterworth-Heinemann, 2012.

[28] H. J. Hansen, "Techniques for precision air temperature control," *Contemporary Methods of Optical Manufacturing and Testing*, 1983.

[29] J. W. Roblee, "Precision temperature control for optics manufacturing," in *2nd International Technical Symposium on Optical and Electro-Optical Applied Science and Engineering*, 1985.

[30] ISO 230-1-2012, "Test code for machine tools - part 1: Geometric accuracy of machines operating under no-load or quasi-static conditions," 2012.

[31] Joint Committee for Guides in Metrology, "Evaluation of measurement data - supplement 1 to the "guide to the expression of uncertainty in measurement" - propagation of distributions using a monte carlo method," 2008.

[32] T. Blalock, M. Brunelle, I. Ferralli, and B. Myer, "Metrology of freeform optics," in *Optical Design and Fabrication*, Optical Society of America, 2017.

[33] M. Khreishi, R. Ohl, J. Howard, J. Papa, C. Hovis, A. Howe, T. Hadjimichael, P. Thompson, R. Shiri, G. West, A. Phenis, and R. Liang, "Freeform surface characterization and instrument alignment for freeform space applications," in *Design and Fabrication Congress 2019*, OSA, 2019.

[34] M. Brunelle, J. Yuan, K. Medicus, and J. D. Nelson, "Importance of fiducials on freeform optics," in *Optifab 2015*, vol. 9633, p. 963318, SPIE, 10 2015.

[35] S. DeFisher, G. Matthews, and J. Ross, "New advancements in freeform optical metrology," in *Window and Dome Technologies and Materials XV*, vol. 10179, 2017.

[36] A. Beutler, "Strategy for a flexible and noncontact measuring process for freeforms," *Optical Engineering*, vol. 55, p. 071206, 4 2016.

[37] ISO 1:2016, "Geometrical product specifications (gps) - standard reference temperature for the specification of geometrical and dimensional properties," 2016.

[38] M. A. V. Chapman, "Calibration of machine squareness," tech. rep., Renishaw, 5 2013.

[39] Lion Precision, "C-LVDT Bandwidth-Response Speed." www.lionprecision.com, 2013.

[40] J. G. Salsbury, "Implementation of the Estler face motion reversal technique," *Precision Engineering*, 2003.

[41] ASME B5.57-2012, "Methods for performance evaluation of computer numerically controlled lathes and turning centers," 2012.

[42] Magnescale Co., *LASERSCALE - Scale Unit: BS78*, 10 2014.

[43] M. O. Valdez, *TASK-SPECIFIC UNCERTAINTY FOR INDUSTRIAL MEASUREMENTS*. PhD thesis, University of North Carolina at Charlotte, 2015.

[44] T. Noste, C. Evans, J. Miller, and L. Hopper, "Concurrent engineering of a next-generation freeform telescope: metrology and test," in *Advanced Optics for Imaging Applications: UV through LWIR IV*, p. 36, SPIE-Intl Soc Optical Eng, 5 2019.

[45] N. W. Horvath and M. A. Davies, "Concurrent engineering of a next-generation freeform telescope: mechanical design and manufacture," in *Advanced Optics for Imaging Applications: UV through LWIR IV*, p. 35, SPIE-Intl Soc Optical Eng, 5 2019.

[46] A. M. Bauer, E. M. Schiesser, and J. P. Rolland, "Concurrent engineering of a next-generation freeform telescope: optical design," in *Advanced Optics for Imaging Applications: UV through LWIR IV*, p. 34, SPIE-Intl Soc Optical Eng, 5 2019.

[47] N. W. Horvath, M. A. Davies, and S. R. Patterson, "Kinematic mirror mount design for ultra-precision manufacturing, metrology, and system level integration for high performance visible spectrum imaging systems," *Precision Engineering*, vol. 60, pp. 535–543, 11 2019.

[48] A. Beutler, "Strategy for non-contact freeform measurements with a cylinder coordinate measuring instrument," in *Optifab 2015*, vol. 9633, p. 963319, SPIE, 10 2015.

[49] MathWorks - Help Center, "traveling salesman problem: Problem-based - matlab and simulink example." https://www.mathworks.com/help/optim/examples/travelling-salesman-problem.html, 2020.

[50] MathWorks - Help Center, "Traveling salesman problem: Solver-based - matlab and simulink." https://www.mathworks.com/help/optim/ug/travelling-salesman-problem.html, 2020.

[51] J. Kirk, "Open traveling salesman problem - genetic algorithm - file exchange - matlab central." https://www.mathworks.com/matlabcentral/fileexchange/21196-open-traveling-salesman-problem-genetic-algorithm, 2020.

[52] D. L. Applegate, R. E. Bixby, V. Chvatal, and W. J. Cook, *The traveling salesman problem: A computational study*. 2011.

[53] D. Li, X. Jiang, Z. Tong, and L. Blunt, "Development and application of interferometric on-machine surface measurement for ultraprecision turning process," *Journal of Manufacturing Science and Engineering, Transactions of the ASME*, vol. 141, 1 2019.

[54] S. J. Ahn, W. Rauh, H. S. Cho, and H.-J. E. R. Warnecke, "Orthogonal distance fitting of implicit curves and surfaces," *IEEE TRANSACTIONS ON PATTERN ANALYSIS AND MACHINE INTELLIGENC*, vol. 24, 2002.

[55] D. Malacara, *Optical Shop Testing*. John Wiley & Sons, Inc., 3 ed., 2007.

[56] C. Moler, "Makima piecewise cubic interpolation," 4 2019. MATLAB Central.

[57] H. Akima, "A new method of interpolation and smooth curve fitting based on local procedures," *Journal of the Association for Computing Machinery*, vol. 17, pp. 589–602, 1970.

[58] H. Akima, "A method of bivariate interpolation and smooth surface fitting based on local procedures," *Communications of the ACM*, vol. 17, pp. 18–20, 1974.

[59] J. Y. Wang and D. E. Silva, "Wave-front interpretation with zernike polynomials," *Applied Optics*, vol. 19, pp. 1510–1518, 1980.

[60] R. E. Parks, C. Evans, and L. Shao, "Calibration of interferometer transmission spheres." https://www.researchgate.net/publication/253884546, 1998.

[61] C. J. Evans and R. N. Kestner, "Test optics error removal," *Applied Optics*, vol. 35, 1996.

[62] C. A. Klein, B. diBenedetto, and J. Pappis, "ZnS, ZnSe, and ZnS/ZnSe windows: their impact on FLIR system performance," *Optical Engineering*, vol. 25, 4 1986.

APPENDIX A: LIST OF VARIABLES

A detailed definition of the variables used in the mathematical model is provided for clarity.

A.1 Rotational Error Terms

$\varepsilon_x(\beta)$ - Measurement of the B carriage coordinate system rotation about the x-axis of the frame coordinate system with respect to the frame coordinate system ($_{CS}F$)

$\varepsilon_y(\beta)$ - Measurement of the B carriage coordinate system rotation about the y-axis of the frame coordinate system with respect to the frame coordinate system ($_{CS}F$)

$\varepsilon_z(\beta)$ - Measurement of the B carriage coordinate system rotation about the z-axis of the frame coordinate system with respect to the frame coordinate system ($_{CS}F$)

$\varepsilon_x(\theta)$ - Measurement of the C carriage coordinate system rotation about the x-axis of the frame coordinate system with respect to the frame coordinate system ($_{CS}F$)

$\varepsilon_y(\theta)$ - Measurement of the C carriage coordinate system rotation about the y-axis of the frame coordinate system with respect to the frame coordinate system ($_{CS}F$)

$\varepsilon_z(\theta)$ - Measurement of the C carriage coordinate system rotation about the z-axis of the frame coordinate system with respect to the frame coordinate system ($_{CS}F$)

$\varepsilon_x(Z)$ - Measurement of the Z carriage coordinate system rotation about the x-axis of the frame coordinate system with respect to the frame coordinate system ($_{CS}F$)

$\varepsilon_y(Z)$ - Measurement of the Z carriage coordinate system rotation about the y-axis of the frame coordinate system with respect to the frame coordinate system ($_{CS}F$)

$\varepsilon_z(Z)$ - Measurement of the Z carriage coordinate system rotation about the z-axis of the frame coordinate system with respect to the frame coordinate system ($_{CS}F$)

$\varepsilon_x(X)$ - Measurement of the X carriage coordinate system rotation about the x-axis of the frame coordinate system with respect to the frame coordinate system ($_{CS}F$)

$\varepsilon_y(X)$ - Measurement of the X carriage coordinate system rotation about the y-axis of the frame coordinate system with respect to the frame coordinate system ($_{CS}F$)

$\varepsilon_z(X)$ - Measurement of the X carriage coordinate system rotation about the z-axis of the frame coordinate system with respect to the frame coordinate system ($_{CS}F$)

A.2 Linear Error Terms

$\delta_X(\theta)$ - Measurement of the translation of the origin of the C carriage coordinate system in the x-axis of the Z coordinate system with respect to the Z coordinate system

$\delta_Y(\theta)$ - Measurement of the translation of the origin of the C carriage coordinate system in the y-axis of the Z coordinate system with respect to the Z coordinate system

$\delta_Z(\theta)$ - Measurement of the translation of the origin of the C carriage in the z-axis of the Z coordinate system with respect to the Z coordinate system

$\delta_X(\beta)$ - Measurement of the translation of the origin of the B carriage in the x-axis of the X coordinate system with respect to the X coordinate system

$\delta_Y(\beta)$ - Measurement of the translation of the origin of the B carriage in the y-axis of the X coordinate system with respect to the X coordinate system

$\delta_Z(\beta)$ - Measurement of the translation of the origin of the B carriage in the z-axis of the X coordinate system with respect to the X coordinate system

$\delta_X(X)$ - Measurement of the translation of the origin of the X carriage in the x-axis of the frame coordinate system with respect to the frame coordinate system

$\delta_Y(X)$ - Measurement of the translation of the origin of the X carriage in the y-axis of the frame coordinate system with respect to the frame coordinate system

$\delta_Z(X)$ - Measurement of the translation of the origin of the X carriage in the z-axis of the frame coordinate system with respect to the frame coordinate system

$\delta_X(Z)$ - Measurement of the translation of the origin of the Z carriage in the x-axis of the frame coordinate system with respect to the frame coordinate system

$\delta_Y(Z)$ - Measurement of the translation of the origin of the Z carriage in the y-axis of the frame coordinate system with respect to the frame coordinate system

$\delta_Z(Z)$ - Measurement of the translation of the origin of the Z carriage in the z-axis

of the frame coordinate system with respect to the frame coordinate system

A.3 Squareness and Parallelism Terms

$\alpha_{B.X}$ - The non-perpendicularity of the B axis of rotation with respect to the frame coordinate system in the x direction

$\alpha_{X.Z}$ - The non-perpendicularity of the X carriage with respect to the frame coordinate system in the z direction

$\alpha_{X.Y}$ - The non-perpendicularity of the X carriage with respect to the frame coordinate system in the y direction

$\alpha_{Z.X}$ - The non-parallelism of the Z carriage with respect to the z axis of the frame coordinate system in the x direction

$\alpha_{Z.Y}$ - The non-parallelism of the Z carriage with respect to the z axis of the frame coordinate system in the y direction

APPENDIX B: DATA PROCESSING FLOW CHART

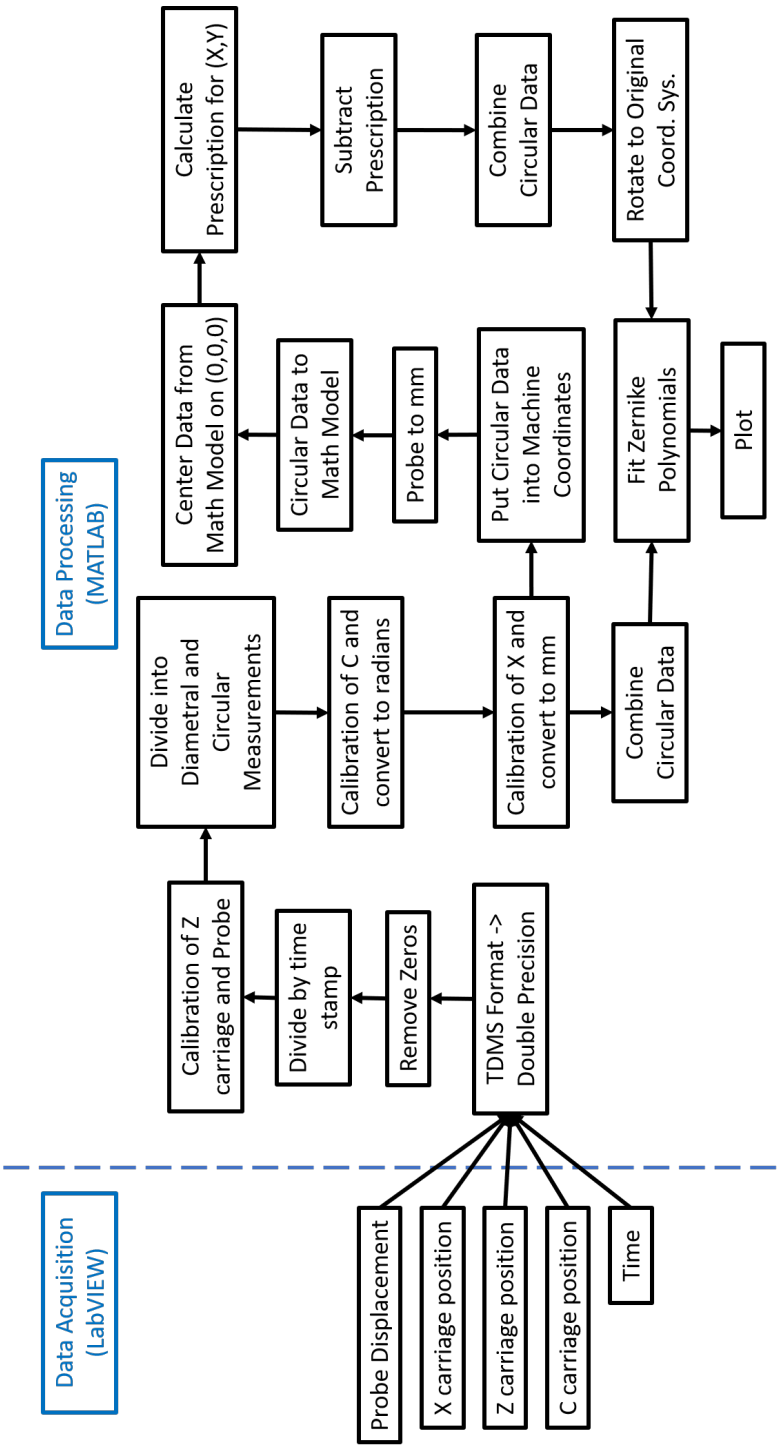

Figure B.1: Data processing flow chart for measurements made on the Nanotech 100UMM with the concentric circle probe path.

APPENDIX C: VAPOR PRESSURE

VAPOR PRESSURE OF WATER

T	P	T	P	T	P	T	P
°C	torr	°C	torr	°C	torr	°C	torr
19.1	16.581	22.1	19.948	25.1	23.897	28.1	28.514
19.2	16.685	22.2	20.070	25.2	24.039	28.2	28.680
19.3	16.789	22.3	20.193	25.3	24.182	28.3	28.847
19.4	16.894	22.4	20.316	25.4	24.326	28.4	29.015
19.5	16.999	22.5	20.440	25.5	24.471	28.5	29.184
19.6	17.105	22.6	20.565	25.6	24.617	28.6	29.354
19.7	17.212	22.7	20.690	25.7	24.764	28.7	29.525
19.8	17.319	22.8	20.815	25.8	24.912	28.8	29.697
19.9	17.427	22.9	20.941	25.9	25.060	28.9	29.870
20.0	17.535	23.0	21.068	26.0	25.209	29.0	30.043
20.1	17.644	23.1	21.196	26.1	25.359	29.1	30.217
20.2	17.753	23.2	21.324	26.2	25.509	29.2	30.392
20.3	17.863	23.3	21.453	26.3	25.660	29.3	30.568
20.4	17.974	23.4	21.583	26.4	25.812	29.4	30.745
20.5	18.085	23.5	21.714	26.5	25.964	29.5	30.923
20.6	18.197	23.6	21.845	26.6	26.117	29.6	31.102
20.7	18.309	23.7	21.977	26.7	26.271	29.7	31.281
20.8	18.422	23.8	22.110	26.8	26.426	29.8	31.461
20.9	18.536	23.9	22.243	26.9	26.582	29.9	31.642
21.0	18.650	24.0	22.377	27.0	26.739	30.0	31.824
21.1	18.765	24.1	22.512	27.1	27.897	30.1	32.007
21.2	18.880	24.2	22.648	27.2	27.055	30.2	32.191
21.3	18.996	24.3	22.785	27.3	27.214	30.3	32.376
21.4	19.113	24.4	22.922	27.4	27.374	30.4	32.561
21.5	19.231	24.5	23.060	27.5	27.535	30.5	32.747
21.6	19.349	24.6	23.198	27.6	27.696	30.6	32.934
21.7	19.468	24.7	23.337	27.7	27.858	30.7	33.122
21.8	19.587	24.8	23.476	27.8	28.021	30.8	33.312
21.9	19.707	24.9	23.616	27.9	28.185	30.9	33.503
22.0	19.827	25.0	23.756	28.0	28.349	31.0	33.695

Figure C.1: Vapor pressure table used in Edlen's equation for compensating the laser interferometer readings.

APPENDIX D: MIND MAPS

A mind map is used to show how the inputs to the mathematical model used in error compensation and the Monte Carlo simulation.

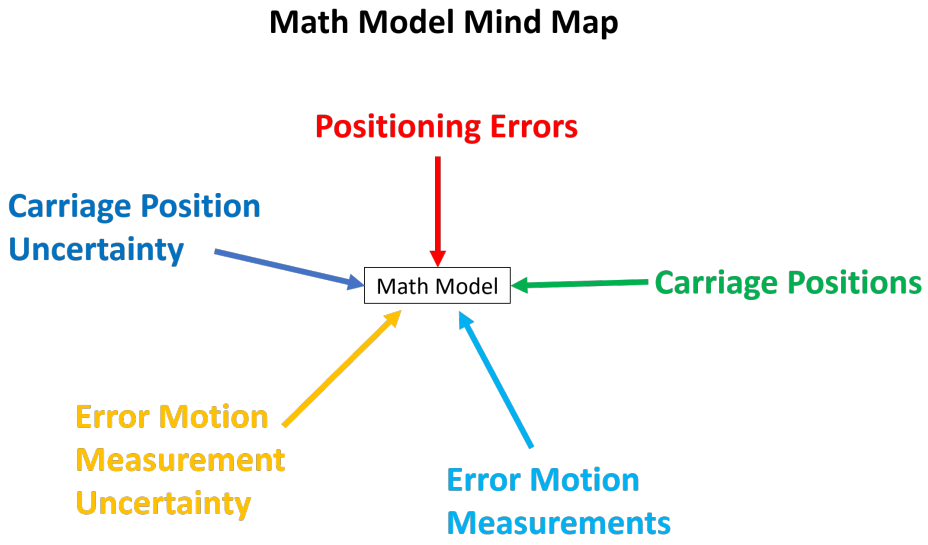

Figure D.1: Mind map for the mathematical model showing the groups of inputs.

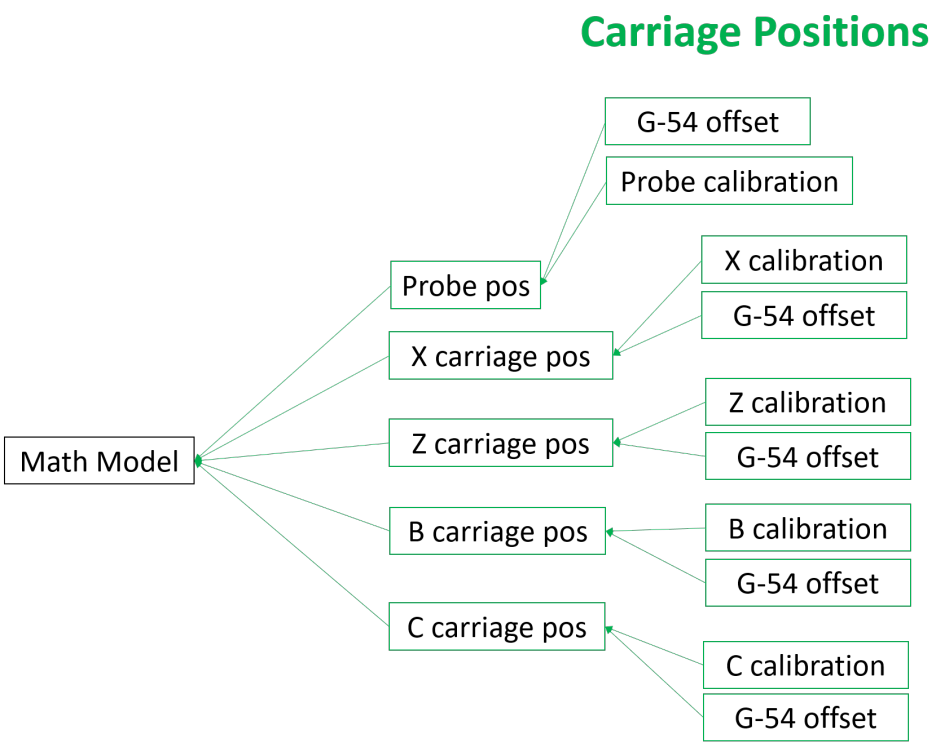

Figure D.2: Mind map for the mathematical model showing the carriage positions.

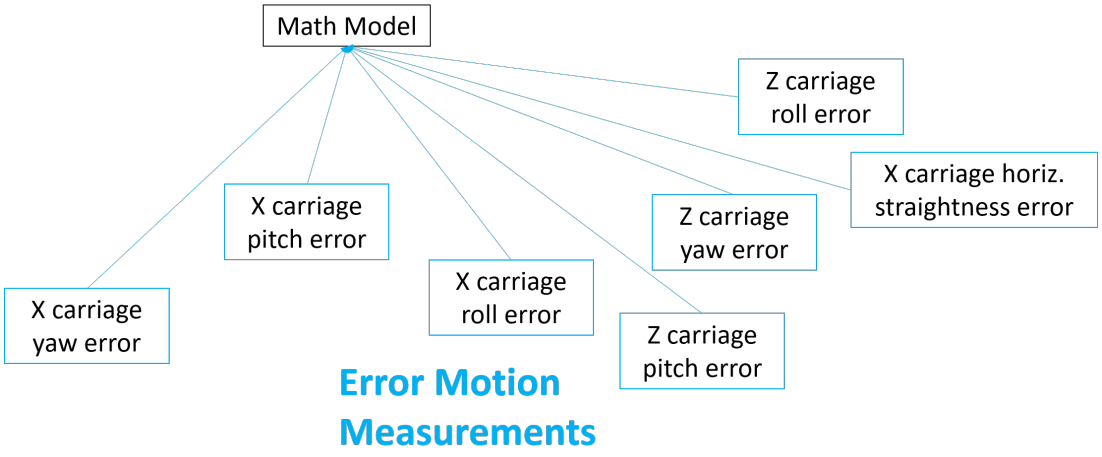

Figure D.3: Mind map for the mathematical model showing the error motion measurements.

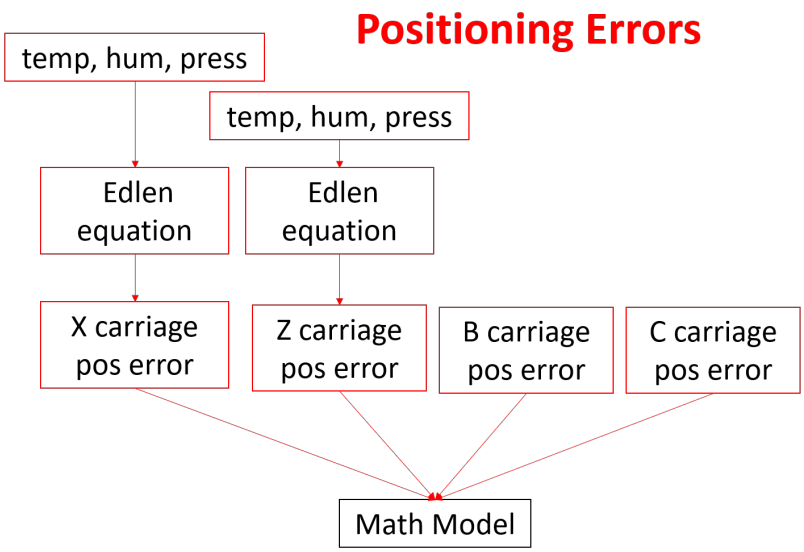

Figure D.4: Mind map for the mathematical model showing the positioning errors.

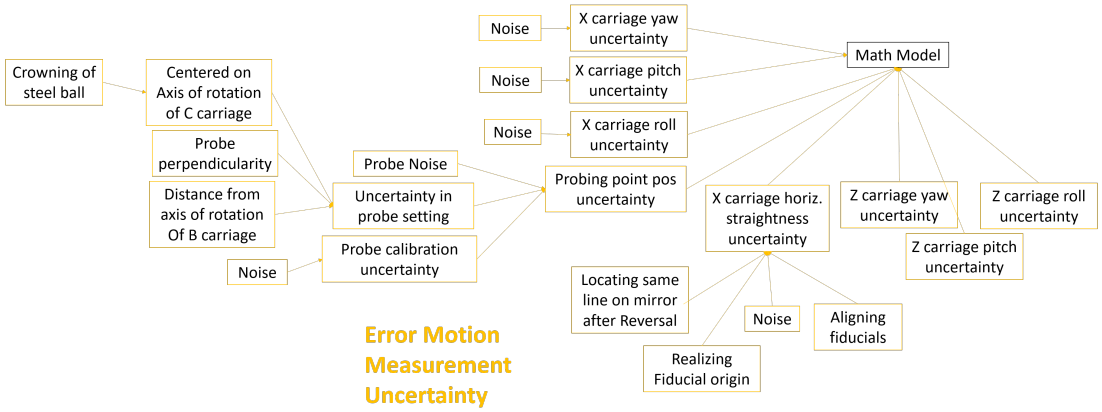

Figure D.5: Mind map for the mathematical model showing the error motion measurement uncertainty.

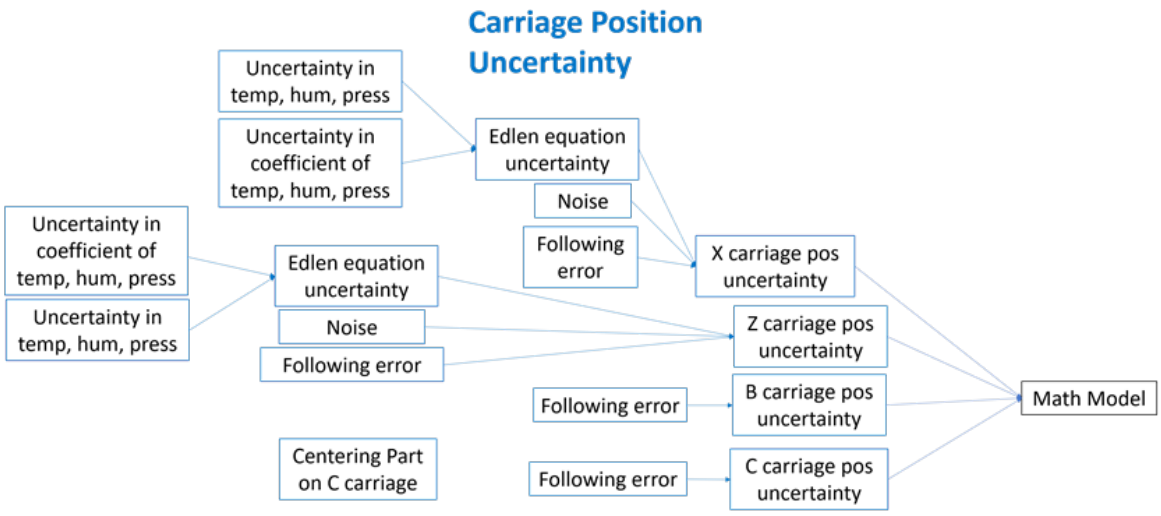

Figure D.6: Mind map for the mathematical model showing the carriage position uncertainty.

APPENDIX E: MATLAB CODES

MATLAB codes used in this research.

E.1 Probe Path Generation

Code used to generate the probe path with inputs: X,Y,Z.

```
clc;
close all;
clear all;

% measurement of the 3 inch spherical optic
% probe path generation
% Z(s) =sqrt(R^2-s^2)
% Z - sag
% s - radial distance from optical axis
% R - radius of curvature

% diameter is 76.2 mm (3 inches)

% UNITS IN MM

% constants
R = 304.8; % in mm

rho = 0:76.2/2/20:76.2/2; % sets radial spacing
theta = (-5:365)*pi/180; % 10 deg. overlapping region (in radians)
theta = theta';

[¬,tt] = size(rho);
[ss,¬] = size(theta);

```

```
26 rho = repmat(rho,ss,1); % radial distance
27 theta = repmat(theta,1,tt);
28
29 rho = reshape(rho,[],1);
30 theta = reshape(theta,[],1);
31
32 % spherical equation for a given radius
33 Z_sphere = sqrt(R^2-rho.^2);
34
35 [x,y] = pol2cart(theta,rho);
36
37 Z_sphere = Z_sphere - R; % zero out data
38
39 %% Should be in machine coordinates
40 figure
41 plot3(x,y,Z_sphere,'o')
42 %Z = reshape(Z,11,11);
43
44
45 %% Part to Measure (Nominal)
46 % As long as probe is able to handle deviation from Nominal.
47 % Input Tilt if needed.
48 % Input Center of part to work offsets (G54)
49
50 %% Setting up the code (prepratory code)
51 % Using the zero position for B
52 Bm = 0;
53
54 % Nominal points of measurement
55 % nominal = [x,y,z];
56
57 % Part Coordinates to be entered into model
58 Xt = x;
```

```
59 Yt = y;
60 Zt = Z_sphere;
61
62 %%%%%%%%%%%%%%%%%%%%%%%%%%%%%%%%%%%%%%%%%%%%%%%%%%%%%%%%%%%%%%%%%%%%%%%%%%%%
63 %% Error Terms
64 %%%%%%%%%%%%%%%%%%%% Angular errors %%%%%%%%%%%%%%%%%%%%%%%%%%
65 Exb = 0;
66 Eyb = 0;
67 Ezb = 0;
68 Exc = 0;
69 Eyc = 0;
70 Ezc = 0;
71 Exx = 0;
72 Eyx = 0;
73 Ezx = 0;
74 Exz = 0;
75 Eyz = 0;
76 Ezz = 0;
77
78 %%%%%%%%%%%%%%%%%%%% Linear errors %%%%%%%%%%%%%%%%%%%%%%%%%%
79 Dxb = 0;
80 Dyb = 0;
81 Dzb = 0;
82 Dxc = 0;
83 Dyc = 0;
84 Dzc = 0;
85 Dxx = 0;
86 Dyx = 0;
87 Dzx = 0;
88 Dxz = 0;
89 Dyz = 0;
90 Dzz = 0;
91
```

```
92  [m,¬] = size(Xt);
93
94  syms Xm Zm Cm % for using symbols
95
96  % j is for the number of measurement points
97
98  % pre initiate
99  Xmach = zeros(2,m);
100 Zmach = zeros(2,m);
101 Cmach = zeros(2,m);
102
103 for j = 1:m
104
105 %% Machine Motions
106 %%%%%%%%%%%%%%%%%%%% Rotational axis motion %%%%%%%%%%%%%%%%%
107
108 % Commanded position of the B axis
109 % What we need to find for each measurement point
110 % Calculated through the normal of the part on the machine
111 Bm = 0;
112
113 % Commanded position of the C axis
114 % What we need to find for each measurement point
115 % we will get this from the sampling strategy
116 % Cm = Tr_sorted(j);
117 % Added a negative here since it is position
118
119 %% Linear axis Motion
120
121 %%%%%%%%% Machine Position of Z axis at Part Origin %%%%%%%
122 % Machine Position of Z axis at Origin of part
123 Zm0 = 0;
124
```

```
125 %%%%%%%%%%%%%%%%%%%%%% Machine Position of Z axis %%%%%%%%%%%%%%%
126 % What we need to find for each measurement point
127 %Zm = 0;
128 %ZmArray = Zm;
129
130 %%%%%%%%% Machine Position of X axis at Part Origin %%%%%%%%%%%%%
131 %Machine Position of Z axis at Origin of part
132 Xm0 = 0;
133
134 %%%%%%%%%%%%%%%%%% Machine Position of X axis %%%%%%%%%%%%%%%%%%%
135 % What we need to find for each measurement point
136 %Xm = 0;
137 %XmArray = Xm;
138
139 % Probe Position in the C coordinate system
140 % This is what we will iterate through....
141
142 %% Vectors and Matrices
143
144 % Part Vector
145 PartVectorInC = [Xt(j); Yt(j); Zt(j)];
146
147 % Tool Vector
148 ToolVectorInB = [0;0;0];
149
150 % Nominal Rotation Matrices
151 Rot_BX_Nom = [cos(Bm) 0 sin(Bm); 0 1 0; -sin(Bm) 0 cos(Bm)];
152
153 Rot_ZF_Nom = [1 0 0; 0 1 0; 0 0 1];
154
155 Rot_CZ_Nom = [cos(Cm) -sin(Cm) 0; sin(Cm) cos(Cm) 0; 0 0 1];
156
157 Rot_XF_Nom = [1 0 0; 0 1 0; 0 0 1];
```

```
158
159
160 % Error Rotation Matrices
161 Rot_BX_Error = [1 -Ezb Eyb; Ezb 1 -Exb; -Eyb Exb 1];
162
163 Rot_ZF_Error = [1 -Ezz Eyz; Ezz 1 -Exz; -Eyz Exz 1];
164
165 Rot_CZ_Error = [1 -Ezc Eyc; Ezc 1 -Exc; -Eyc Exc 1];
166
167 Rot_XF_Error = [1 -Ezx Eyx; Ezx 1 -Exx; -Eyx Exx 1];
168
169 %%%%%%%%%%%%%%%% Combining Nominal and Error Matrices %%%%%%%%%%%
170 % For the two rotational axes, the nominal and error rotation ...
      matrices need
171 % to be combined. This is done differently for the two axes since ...
      one is
172 % inversed when solving for the part and tool vectors. Since the ...
      rotation
173 % matrices are symmetric the inverse is also the transpose which ...
      equates to
174 % changing the sign of the off diagonal terms or reflecting about the
175 % diagonal.
176
177 % Part vector in C coordinate frame
178 % Inverse of Rcz with error and nominal rotation matrices combined
179 rot_zc_comb = inv(Rot_CZ_Error)*inv(Rot_CZ_Nom); % There's a ...
      better way of doing this if entering errors
180 rot_fz = inv(Rot_ZF_Error); % MATLAB recommends using backslash ...
      operator instead of inv()
181 rot_bx_comb = inv(Rot_BX_Nom)*inv(Rot_BX_Error); % There's a ...
      better way of doing this if entering errors
182
183 % Matrices with translational error terms
```

```
184 Origin_BinX = [Dxb; Dyb; Dzb];
185
186 Origin_CinZ = [Dxc; Dyc; Dzc];
187
188 Origin_XinF = [(Dxx + Xm - Xm0); Dyx; Dzx];
189
190 Origin_ZinF = [Dxz; Dyz; (Dzz + Zm - Zm0)];
191
192 %% Solving Matrix Math
193
194 % Solving for the Nominal Position Vector in C coordinate frame
195 S = (PartVectorInC == (rot_zc_comb)*(-Origin_CinZ + ...
        ((rot_fz)*(-Origin_ZinF + Origin_XinF + ...
        Rot_XF_Nom*(Origin_BinX+Rot_BX_Nom*ToolVectorInB)))));
196
197 [Sx, Sz, Sc] = solve([S(1,1) S(2,1) S(3,1)],[Xm Zm Cm]);
198
199 Xpos = double(Sx);
200 Zpos = double(Sz);
201 Cpos = double(Sc);
202
203 % machine coordinates
204 Xmach(:,j) = Xpos;
205 Zmach(:,j) = Zpos;
206 Cmach(:,j) = Cpos*180/pi; % change to radians from degrees
207
208 end
```

E.2 Plane Rotation

See above description of plane subtraction issues.

```
function [plane_sub] = plane_sub_issue_func2(X,Y,f)

% plane sub is a (x,y,z)
[X_plane, Y_plane, Z_plane] = planefit(X,Y,f);

%% Finding normal to plane
PQ = [X_plane(2,1)-X_plane(1,1),Y_plane(2,1)-Y_plane(1,1)...
,Z_plane(2,1)-Z_plane(1,1)];
PR = [X_plane(1,3)-X_plane(1,1),Y_plane(1,3)-Y_plane(1,1)...
,Z_plane(1,3)-Z_plane(1,1)];

normal = cross(PQ,PR);
normal = -normal;

theta_y = pi/2-atan2(normal(3),normal(2));

%% Rotate plane about X using angle of Y
R_x = [1 0 0; 0 cos(theta_y) -sin(theta_y); 0 sin(theta_y) ...
    cos(theta_y)];
M = [X_plane(:), Y_plane(:), Z_plane(:)];
[n,¬] = size(M);

for i = 1:n
M(i,:) = R_x*M(i,:)';
end

[n,m] = size(X_plane);
M(:,3) = M(:,3)-mean(M(:,3));
X_plane = reshape(M(:,1),n,m);
Y_plane = reshape(M(:,2),n,m);
Z_plane = reshape(M(:,3),n,m);

% figure
```

```
% surfnorm(X_plane,Y_plane,Z_plane)
% ylabel('y')
% xlabel('x')
% zlabel('z')
% xlim([-15 15])
% ylim([-15 15])

[n,¬] = size(M);

PQ = [X_plane(2,1)-X_plane(1,1),Y_plane(2,1)-Y_plane(1,1)...
,Z_plane(2,1)-Z_plane(1,1)];

PR = [X_plane(1,3)-X_plane(1,1),Y_plane(1,3)-Y_plane(1,1)...
,Z_plane(1,3)-Z_plane(1,1)];


normal = cross(PQ,PR);
normal = -normal;

theta_x = atan2(normal(3),normal(1))-pi/2;

%% Rotate plane about Y using angle of X
R_y = [cos(theta_x) 0 sin(theta_x); 0 1 0;-sin(theta_x)  0  ...
    cos(theta_x)];

for i = 1:n
M(i,:) = R_y*M(i,:)';
end

% Plotting
% [n,m] = size(X_plane);

% X_plane = reshape(M(:,1),n,m);
```

```
% Y_plane = reshape(M(:,2),n,m);
% Z_plane = reshape(M(:,3),n,m);

% figure
% surf(X_plane,Y_plane,Z_plane)
% ylabel('y')
% xlabel('x')
% zlabel('z')
% zlim([-1 1])
% xlim([-30 30])
% ylim([-30 30])


%% Rotate data
M_data = [X(:), Y(:), f(:)];

[n,~] = size(M_data);

for i = 1:n
M_data(i,:) = R_x*M_data(i,:)';
end

for i = 1:n
M_data(i,:) = R_y*M_data(i,:)';
end

X_data = M_data(:,1);
Y_data = M_data(:,2);
Z_data = M_data(:,3);

plane_sub = [X_data,Y_data,Z_data];

end
```

```
98
99  function [X_plane, Y_plane, Z_plane] = planefit(X,Y,Z)
100 % Fitting a plane to X,Y,Z data
101 xx = reshape(X,[],1);
102 yy = reshape(Y,[],1);
103 zz = reshape(Z,[],1);
104 % [n,m] = size(X);
105
106 S = [xx, yy, zz];
107
108 [N,¬] = size(xx);
109
110 % Assuming that yourData is N-by-3 numeric array
111 B = [ones(N,1), S(:,1:2)] \ S(:,3);
112
113 a = B(2); b = B(3); c = B(1);
114
115 x = -5:5;
116 y = -5:5;
117 y = y';
118 x = repmat(x,11,1);
119 y = repmat(y,1,11);
120
121
122 Z_sub = x.*a+y.*b+c;
123 Z_plane = reshape(Z_sub,[11,11]);
124 X_plane = x;
125 Y_plane = y;
126
127 end
```

E.3 Monte Carlo Simulation

```
1  function [PinC_Monte]= ...
       MooreUMM100HTM_MonteCarlo_func(Xmach,Zmach,Cmach,Probe, ...
       Exx_X_unc,Exx_X_pos,Ezx_X,Ezz_C,Eyz_B_error,Ezx_C, ...
       Ezz_Z,Dzz_Z_unc,Dzz_Z_pos...
2  ,Dxx_X_unc,Dxx_X_pos,Ezz_Z_unc,Ezz_Z_pos,Eyz_Z_unc, ...
       Eyz_Z_pos,Exz_Z_unc,Exz_Z_pos...
3  ,Eyx_X_unc,Eyx_X_pos,Ezx_X_unc,Ezx_X_pos,Dxx_X_error, ...
       Dzx_x_pos,Exx_A,Exz_Z,Eyx_B_error,Dzx_z_error, ...
       Dzz_Z_error,Exx_X,Exz_A, Dzx_z_unc)
4
5  %% NOTES
6  % need to decide coverage factor
7
8  % compensate measurement with the machine error measurements and use
9  % uncertainty in machine error measurements in Monte Carlo for task
10 % specific uncertainty
11
12 %% UNITS in mm and Radians
13
14 % Moore Nanotech UMM 100 Task Specific Uncertainty
15
16 % sets the number of measurements
17 [m,¬] = size(Xmach);
18
19 % since the B carriage doesn't move, Bmach uncertainty is ...
       probably just the
20 % following error.
21 % Bmach = 0;
22
23 method = 'makima';
24
25 %%%%%%%%%%%%%%%%%%%%%%%%%%%%%%%%%%%%%%%%%%%%%%%%%%%%%%%%%%%%%%%%%%%%%%%%%%%
```

```
26 %%%%%%%%%%%%%%%%%%%%%%%% GUM sampling methods %%%%%%%%%%%%%%%%
27 % Normal Distribution
28 % For the normal distribution the standard deviation and mean are ...
       needed to
29 % sample the distribution
30
31 % Triangle Distribution
32 % For the triangle distribution the upper and lower limits are needed
33
34 % Uniform Distribution
35 % For the uniform distribution the upper and lower limits are needed
36
37 %%%%%%%%%%%%%%%%%%%%%% Sampling Strategy %%%%%%%%%%%%%%%%%%%%%%
38 % Some errors are sampled every monte carlo iteration while ...
       others are
39 % sampled every "measurement".
40
41 % Per iteration of the Monte Carlo errors
42 % The idea is that for every iteration of the Monte Carlo there ...
       will be a
43 % "new machine".  This means that the machine errors won't change ...
       at every
44 % measurement point.
45
46 %% errors considered for correction and uncertainty evaluation
47 % first remove bias then consider uncertainty
48
49 %% Monte Carlo
50 parfor j = 1:m % m is number of measurements in point cloud
51
52 %% Error Terms
53
54 %%%%%%%%%%%%%%%%%%%% Angular errors in the B axis %%%%%%%%%%%%%%
```

```
55 % Measurement of the rotation of the B carriage about the x axis ...
       of the Z
56 % coordinate system with respect to the Z coordinate system
57 % Exb = normrnd(0,0.00005);
58 Exb = 0;
59
60 % Measurement of the rotation of the B carriage about the y axis ...
       of the Z
61 % coordinate system with respect to the Z coordinate system
62 Eyb = 0; % Keep Zero due to how the errors are measured
63
64 % Measurement of the rotation of the B carriage about the z axis ...
       of the Z
65 % coordinate system with respect to the Z coordinate system
66 % Ezb = normrnd(0,0.00005);
67 Ezb = 0;
68
69 %%%%%%%%%%%%%%%%%%% Angular errors in the C axis %%%%%%%%%%%%%%%
70
71 % Measurement of the rotation of the C carriage about the x axis ...
       of the Y
72 % coordinate system with respect to the Y coordinate system
73 % Exc = normrnd(0,0.00005);
74 Exc = 0;
75
76 % Measurement of the rotation of the C carriage about the y axis ...
       of the Y
77 % coordinate system with respect to the Y coordinate system
78 % Eyc = normrnd(0,0.00005);
79 Eyc = 0;
80
81 % Measurement of the rotation of the C carriage about the z axis ...
       of the Y
```

```
82 % coordinate system with respect to the Y coordinate system
83 Ezc = 0; % Keep Zero due to how the errors are measured
84
85 %%%%%%%%%%%%%%%%% Angular errors in the X axis %%%%%%%%%%%%%%%
86
87 % Measurement of the rotation of the X carriage about the x axis ...
       of the frame
88 % coordinate system with respect to the frame coordinate system
89
90 Exx_std = interp1(Exx_X_pos,Exx_X_unc,Xmach(j),method);
91 Exx = normrnd(0,Exx_std);
92 Exx = Exx + interp1(Exx_X,Exx_A,Xmach(j),method);
93 Exx = Exx *pi/(180*3600); % Change to radians from arc-sec
94
95 % Measurement of the rotation of the X carriage about the y axis ...
       of the frame
96 % coordinate system with respect to the frame coordinate system
97 Eyx_std = interp1(Eyx_X_pos,Eyx_X_unc,Xmach(j),method);
98 Eyx = normrnd(0,Eyx_std);
99 Eyx = Eyx + interp1(Eyx_X_pos,Eyx_B_error,Xmach(j),method);
100 Eyx = Eyx *pi/(180*3600); % Change to radians from arc-sec
101
102 % Measurement of the rotation of the X carriage about the z axis ...
       of the frame
103 % coordinate system with respect to the frame coordinate system
104 Ezx_std = interp1(Ezx_X_pos,Ezx_X_unc,Xmach(j),method);
105 Ezx = normrnd(0,Ezx_std);
106 Ezx = Ezx + interp1(Ezx_X,Ezx_C,Xmach(j),method);
107 Ezx = Ezx *pi/(180*3600); % Change to radians from arc-sec
108
109 %%%%%%%%%%%%%%%%%%%%%% Angular errors in the Z axis %%%%%%%%%%
110
```

```
111 % Measurement of the rotation of the Z carriage about the x axis ...
       of the frame
112 % coordinate system with respect to the frame coordinate system
113 Exz_std = interp1(Exz_Z_pos,Exz_Z_unc,Zmach(j),method);
114 Exz = normrnd(0,Exz_std);
115 Exz = Exz + interp1(Exz_Z,Exz_A,Zmach(j),method);
116 Exz = Exz *pi/(180*3600); % Change to radians from arc-sec
117
118 % Measurement of the rotation of the Z carriage about the y axis ...
       of the frame
119 % coordinate system with respect to the frame coordinate system
120 Eyz_std = interp1(Eyz_Z_pos,Eyz_Z_unc,Zmach(j),method);
121 Eyz = normrnd(0,Eyz_std);
122 Eyz = Eyz + interp1(Eyz_Z_pos,Eyz_B_error,Zmach(j),method);
123 Eyz = Eyz *pi/(180*3600); % Change to radians from arc-sec
124
125 % Measurement of the rotation of the Z carriage about the z axis ...
       of the frame
126 % coordinate system with respect to the frame coordinate system
127 Ezz_std = interp1(Ezz_Z_pos,Ezz_Z_unc,Zmach(j),method);
128 Ezz = normrnd(0,Ezz_std);
129 Ezz = Ezz + interp1(Ezz_Z,Ezz_C,Zmach(j),method);
130 Ezz = Ezz *pi/(180*3600); % Change to radians from arc-sec
131
132 %%%%%%%%%%%%%%%%%%%% Linear errors in the B axis %%%%%%%%%%%%
133
134 % Measurement of the translation of the origin of the B ...
       coordinate system along
135 % the x axis of the Z coordinate system with respect to the Z ...
       coordinate system
136 % Dxb = normrnd(0,0.00005);
137 Dxb = 0;
138
```

```
139 % Measurement of the translation of the origin of the B ...
       coordinate system along
140 % the y axis of the Z coordinate system with respect to the Z ...
       coordinate system
141 % Dyb = normrnd(0,0.00005);
142 Dyb = 0;
143
144 % Measurement of the translation of the origin of the B ...
       coordinate system along
145 % the z axis of the Z coordinate system with respect to the Z ...
       coordinate system
146 % Dzb = normrnd(0,0.00005);
147 Dzb = 0;
148
149 % Linear errors in the C axis
150
151 % Measurement of the translation of the origin of the C ...
       coordinate system along
152 % the x axis of the Y coordinate system with respect to the Y ...
       coordinate system
153 % Dxc = normrnd(0,0.00005);
154 Dxc = 0;
155
156 % Measurement of the translation of the origin of the C ...
       coordinate system along
157 % the y axis of the Y coordinate system with respect to the Y ...
       coordinate system
158 % Dyc = normrnd(0,0.00005);
159 Dyc = 0;
160
161 % Measurement of the translation of the origin of the C ...
       coordinate system along
```

```
% the z axis of the Y coordinate system with respect to the Y ...
    coordinate system
% Dzc = normrnd(0,0.00005);
Dzc = 0;

% Linear errors in the X axis

% Measurement of the translation of the origin of the X ...
    coordinate system along
% the x axis of the frame coordinate system with respect to the ...
    frame coordinate system

Dxx_std = interp1(Dxx_X_pos,Dxx_X_unc,Xmach(j),method);
Dxx = normrnd(0,Dxx_std);
Dxx = Dxx + interp1(Dxx_X_pos,Dxx_X_error,Xmach(j),method);

% Measurement of the translation of the origin of the X ...
    coordinate system along
% the y axis of the frame coordinate system with respect to the ...
    frame coordinate system
% Dyx = normrnd(0,0.00005);
Dyx = 0;

% Measurement of the translation of the origin of the X ...
    coordinate system along
% the z axis of the frame coordinate system with respect to the ...
    frame coordinate system
% Dzx = normrnd(0,0.00005);

% X carriage horizontal straightness
Dzx_std = interp1(Dzx_x_pos,Dzx_z_unc,Xmach(j),method);
Dzx = normrnd(0,Dzx_std);
Dzx = Dzx + interp1(Dzx_x_pos,Dzx_z_error,Xmach(j),method);
```

```
188
189 % Linear errors in the Z axis
190
191 % Measurement of the translation of the origin of the Z ...
       coordinate system along
192 % the x axis of the frame coordinate system with respect to the ...
       frame coordinate system
193 % Dxz = normrnd(0,0.00005);
194 Dxz = 0;
195
196 % Measurement of the translation of the origin of the Z ...
       coordinate system along
197 % the y axis of the frame coordinate system with respect to the ...
       frame coordinate system
198 % Dyz = normrnd(0,0.00005);
199 Dyz = 0;
200
201 % Measurement of the translation of the origin of the Z ...
       coordinate system along
202 % the z axis of the frame coordinate system with respect to the ...
       frame coordinate system
203
204 Dzz_std = interp1(Dzz_Z_pos,Dzz_Z_unc,Zmach(j),method);
205 Dzz = normrnd(0,Dzz_std);
206 Dzz = Dzz + interp1(Dzz_Z_pos,Dzz_Z_error,Zmach(j),method);
207
208 %% Squareness Error Uncertainty
209 Axz_unc = normrnd(0,2.43e-07); % in mm
210 Axz = -1.6599e-5 + Axz_unc; % in radians for small angle ...
       approximation
211
212 %% Probe Noise
213 pnoise  = normrnd(0,1.25e-4/1000); % in mm
```

```
214
215 %% Machine Motions
216 %%%%%%%%%%%%%%%%%%%%%% Rotational axis motion %%%%%%%%%%%%%%%%%%
217
218 % Commanded position of the B axis
219 % Following error for uncertainty in commanded position
220 % Bm = normrnd(0,0.000005);
221 Bm = 0;
222
223 % Commanded position of the C axis
224 % Following error for uncertainty in commanded position
225 % Cmach3
226 % Cm = normrnd(Cmach(j,1),0.000005);
227 Cm = Cmach(j);
228
229 %%%%%%%%%%%%%%%%%%%%%%%%% Linear axis Motion %%%%%%%%%%%%%%%%%%
230 %%%%%%%%%%%%% Machine Position of Z axis at Fiducial Origin %%%%%%%
231 % Zm0 = normrnd(-185.158175,0.000005);
232 Zm0 = -185.158175;
233
234 %%%%%%%%%%%%%%%%%%%%%% Machine Position of Z axis %%%%%%%%%%%%%%%%%
235 % Zm = normrnd(Zmach(j,1),0.000005);
236 Zm = Zmach(j);
237
238 %%%%%%%%% Machine Position of X axis at Fiducial Origin %%%%%%%%%
239 % Xm0 = normrnd(92.222,0.000005);
240 Xm0 = 92.222;
241
242 %%%%%%%%%%%%%%%%%%% Machine Position of X axis %%%%%%%%%%%%%%%%%%
243 % Xm = normrnd(Xmach(j,1),0.000005);
244 Xm = Xmach(j);
245
246 % Probe Position in the B coordinate system
```

```
% Xprobe = normrnd(-1*(94.1818-92.222),0.0005);
Xprobe = -1*(94.1818-92.222);
% Yprobe = normrnd(0,0.0005);
Yprobe = 0;
Zprobe = 75-Probe(j)+pnoise; % mm

%% Vectors and Matrices
% Probe Vector
ProbeVectorInB = [Xprobe; Yprobe; Zprobe];

% Nominal Rotation Matrices
Rot_BX_Nom = [cos(Bm) 0 sin(Bm); 0 1 0; -sin(Bm) 0 cos(Bm)];

% Rot_CZ_Nom = [cos(Cm) -sin(Cm) 0; sin(Cm) cos(Cm) 0; 0 0 1];

% Error Rotation Matrices
% Rot_BX_Error = [1 -Ezb Eyb; Ezb 1 -Exb; -Eyb Exb 1];

Rot_ZF_Error = [1 -Ezz Eyz; Ezz 1 -Exz; -Eyz Exz 1];

% Rot_CZ_Error = [1 -Ezc Eyc; Ezc 1 -Exc; -Eyc Exc 1];

Rot_XF_Error = [1 -Ezx Eyx; Ezx 1 -Exx; -Eyx Exx 1];

%%%%%%%%%%%%%%%% Combining Nominal and Error Matrices %%%%%%%%%%%
% For the two rotational axes, the nominal and error rotation ...
    matrices need
% to be combined. This is done differently for the two axes since ...
    one is
% inversed when solving for the part and tool vectors.  Since the ...
    rotation
% matrices are symmetric the inverse is also the transpose which ...
    equates to
```

```
% changing the sign of the off diagonal terms or reflecting about the
% diagonal.

% Part vector in C coordinate frame
% Inverse of Rcz with error and nominal rotation matrices combined
rot_zc_comb = [cos(Cm+Ezc) sin(Cm+Ezc) -Eyc; -sin(Cm+Ezc) ...
    cos(Cm+Ezc) Exc;...
     (Eyc*cos(Cm)+Exc*sin(Cm+Ezc)) (-Exc*cos(Cm)+Eyc*sin(Cm+Ezc)) 1];
% rot_fz = inv(Rot_ZF_Error);
% rot_bx_comb = inv(Rot_BX_Nom)*inv(Rot_BX_Error);

% Matrices with translational error terms
Origin_BinX = [Dxb; Dyb; Dzb];

Origin_CinZ = [Dxc; Dyc; Dzc];

Origin_XinF = [(Dxx + Xm - Xm0); Dyx; Dzx + (Xm - Xm0)*Axz];

Origin_ZinF = [Dxz; Dyz; (Dzz + Zm - Zm0)];

%% Solving Matrix Math
% Solving for the Nominal Position Vector in C coordinate frame
PinC = (rot_zc_comb)*(-Origin_CinZ + (Rot_ZF_Error\(-Origin_ZinF ...
    + Origin_XinF + Rot_XF_Error*(Origin_BinX + ...
    Rot_BX_Nom\ProbeVectorInB))));

PinC_meas(j,:) = PinC';

end

PinC_Monte(:,:) = PinC_meas;

end
```

E.4 Error Compensation

```
1
2  function [PinC] = Nanotech100UMM_error_comp_func(Xmeas, Cmeas, ...
       Zmeas, Probe)
3  %% Error Compensation using mathematical model
4
5  %% NOTES
6  % compensate measurement with the machine error measurements and use
7  % uncertainty in machine error measurements in Monte Carlo for task
8  % specific uncertainty
9
10 % Input into this program will be the measurement data
11
12 % Error measurements will be in machine coordinates
13
14 %% Moore Nanotech UMM 100 Error Compensation
15 %% Measurement Data
16 % sets the number of measurements
17
18 Bmeas = 0; % Don't use the B axis for these measurements
19
20 %%%%%%%%%%%%%%%%%%%%%%%%%%%%%%%%%%%%%%%%%%%%%%%%%%%%%%%%%%%%%%%%%%%%%%%%%%%
21 %% Load Machine Tool Metrology Data
22 load 'Dxx'
23 load 'Dzx4'
24 load 'Dzz'
25
26 load 'Exx'
27 load 'Exz'
```

```
load 'Eyx'

load 'Eyz'
load 'Ezx'
load 'Ezz'

% load 'Eyc_doub'
% load 'Dzc_doub'

%% %%%%%%%%%%%%%%%%%%%%%%%%%%%%%%%%%%%%%%%%%%%%%%%%%%%%%%%%%%%%%%%%%%%%%%%
%% %%%%%%%%%%%%%%%%%%%% Error Compensation %%%%%%%%%%%%%%%%%%%%%%%% %%
%% Per measurement point errors
% Probe noise - each measurement point will have a different noise.

%% Per "machine" errors
% For each iteration

% Have the origin of the coordinate systems, the G-54 offsets and the
% machine coordinate system.

%% Interpolation method
method = 'makima'; % have had luck with the modified akima ...
    before, also used modified akima to zero out the error ...
    measurements at the fiducial origin

%% Size of data (number of measurement points)
[m,¬] = size(Xmeas);

for j=1:m % m is number of measurement points in point cloud

%% Error Terms
%%%%%%%%%%%%%%%%%%%% Angular errors in the B axis %%%%%%%%%%%%%%%%%
```

```
58 % Measurement of the rotation of the B carriage about the x axis ...
       of the Z
59 % coordinate system with respect to the Z coordinate system
60 Exb = 0; % not measured
61
62 % Measurement of the rotation of the B carriage about the y axis ...
       of the Z
63 % coordinate system with respect to the Z coordinate system
64 Eyb = 0; % Keep Zero due to how the errors are measured
65
66 % Measurement of the rotation of the B carriage about the z axis ...
       of the Z
67 % coordinate system with respect to the Z coordinate system
68 Ezb = 0; % not measured
69
70
71 %%%%%%%%%%%%%%%%%%% Angular errors in the C axis %%%%%%%%%%%%%%%
72 % Measurement of the rotation of the C carriage about the x axis ...
       of the Y
73 % coordinate system with respect to the Y coordinate system
74 Exc = 0; % not measured
75
76 % Measurement of the rotation of the C carriage about the y axis ...
       of the Y
77 % coordinate system with respect to the Y coordinate system
78 % Eyc = interp1(Eyc_pos,Eyc_err,Cmeas(j),method); %
79 Eyc = 0;
80
81 % Measurement of the rotation of the C carriage about the z axis ...
       of the Y
82 % coordinate system with respect to the Y coordinate system
83 Ezc = 0; % Keep Zero due to how the errors are measured
84
```

```
85 %%%%%%%%%%%%%%%%% Angular errors in the X axis %%%%%%%%%%%%%%%%%%
86 % Measurement of the rotation of the X carriage about the x axis ...
       of the frame
87 % coordinate system with respect to the frame coordinate system
88 Exx = interp1(Exx_X,Exx_A,Xmeas(j),method);
89 Exx = Exx *pi/(180*3600); % Change to radians from arc-sec
90
91 % Measurement of the rotation of the X carriage about the y axis ...
       of the frame
92 % coordinate system with respect to the frame coordinate system
93 Eyx = interp1(Eyx_X_pos,Eyx_B_error,Xmeas(j),method);
94 Eyx = Eyx *pi/(180*3600); % Change to radians from arc-sec
95
96 % Measurement of the rotation of the X carriage about the z axis ...
       of the frame
97 % coordinate system with respect to the frame coordinate system
98 Ezx = interp1(Ezx_X,Ezx_C,Xmeas(j),method);
99 Ezx = Ezx *pi/(180*3600); % Change to radians from arc-sec
100
101 %%%%%%%%%%%%%%%%%%%% Angular errors in the Z axis %%%%%%%%%%%%%%%%
102 % Measurement of the rotation of the Z carriage about the x axis ...
       of the frame
103 % coordinate system with respect to the frame coordinate system
104 Exz = interp1(Exz_Z,Exz_A,Zmeas(j),method); % Pitch of Z carriage
105 Exz = Exz*pi/(180*3600); % Change to radians from arc-sec
106
107 % Measurement of the rotation of the Z carriage about the y axis ...
       of the frame
108 % coordinate system with respect to the frame coordinate system
109 Eyz = interp1(Eyz_Z_pos,Eyz_B_error,Zmeas(j),method); % Yaw of Z ...
       carriage
110 Eyz = Eyz*pi/(180*3600); % Change to radians from arc-sec
111
```

```
112 % Measurement of the rotation of the Z carriage about the z axis ...
       of the frame
113 % coordinate system with respect to the frame coordinate system
114 Ezz = interp1(Ezz_Z,Ezz_C,Zmeas(j),method); % Roll of Z carriage
115 Ezz = Ezz*pi/(180*3600); % Change to radians from arc-sec
116
117 %%%%%%%%%%%%%%%%%%%% Linear errors in the B axis %%%%%%%%%%%%%%%%%
118 % Measurement of the translation of the origin of the B ...
       coordinate system along
119 % the x axis of the Z coordinate system with respect to the Z ...
       coordinate system
120 Dxb = 0;
121
122 % Measurement of the translation of the origin of the B ...
       coordinate system along
123 % the y axis of the Z coordinate system with respect to the Z ...
       coordinate system
124 Dyb = 0;
125
126 % Measurement of the translation of the origin of the B ...
       coordinate system along
127 % the z axis of the Z coordinate system with respect to the Z ...
       coordinate system
128 Dzb = 0;
129
130 %%%%%%%%%%%%%%%%%%%% Linear errors in the C axis %%%%%%%%%%%%%%%%%
131 % Measurement of the translation of the origin of the C ...
       coordinate system along
132 % the x axis of the Y coordinate system with respect to the Y ...
       coordinate system
133 Dxc = 0;
134
```

```
135 % Measurement of the translation of the origin of the C ...
       coordinate system along
136 % the y axis of the Y coordinate system with respect to the Y ...
       coordinate system
137 Dyc = 0;
138
139 % Measurement of the translation of the origin of the C ...
       coordinate system along
140 % the z axis of the Y coordinate system with respect to the Y ...
       coordinate system
141 % Dzc = interp1(Dzc_pos,Dzc_err,Cmeas(j),method); %
142 Dzc = 0;
143
144 %% Linear errors in the X axis
145 % Measurement of the translation of the origin of the X ...
       coordinate system along
146 % the x axis of the frame coordinate system with respect to the ...
       frame coordinate system
147 Dxx = interp1(Dxx_X_pos,Dxx_X_error,Xmeas(j),method);
148
149 % Measurement of the translation of the origin of the X ...
       coordinate system along
150 % the y axis of the frame coordinate system with respect to the ...
       frame coordinate system
151 Dyx = 0;
152
153 % Measurement of the translation of the origin of the X ...
       coordinate system along
154 % the z axis of the frame coordinate system with respect to the ...
       frame coordinate system
155 Dzx = interp1(Dzx_x_pos,Dzx_z_error,Xmeas(j),method);
156
157 %% Linear errors in the Z axis
```

```
158 % Measurement of the translation of the origin of the Z ...
       coordinate system along
159 % the x axis of the frame coordinate system with respect to the ...
       frame coordinate system
160 Dxz = 0;
161
162 % Measurement of the translation of the origin of the Z ...
       coordinate system along
163 % the y axis of the frame coordinate system with respect to the ...
       frame coordinate system
164 Dyz = 0;
165
166 % Measurement of the translation of the origin of the Z ...
       coordinate system along
167 % the z axis of the frame coordinate system with respect to the ...
       frame coordinate system
168 Dzz = interp1(Dzz_Z_pos,Dzz_Z_error,Zmeas(j),method);
169
170 %% Squareness Error
171 Axz = -1.6599e-05; % in radians for small angle approximation
172
173 %% Machine Motions
174 %%%%%%%%%%%%%%%%%%%%% Rotational axis motion %%%%%%%%%%%%%%%%%%%%%
175 % Commanded position of the B axis
176 Bm = Bmeas; % set to zero
177
178 % Commanded position of the C axis
179 Cm = Cmeas(j);
180
181 %% %%%%%%%%%%%%%%%%%%%%% Linear axis Motion %%%%%%%%%%% %%
182 %%%%%%%%%%%%% Machine Position of Z axis at Fiducial Origin %%%%%%%%%
183 Zm0 = -185.158175;
184
```

```
185 %%%%%%%%%%%%%%%%%%%%% Machine Position of Z axis %%%%%%%%%%%%%%%%%%%
186 Zm = Zmeas(j);
187
188 %%%%%%%%% Machine Position of X axis at Fiducial Origin %%%%%%%%%%
189 Xm0 = 92.222;
190
191 %%%%%%%%%%%%%%%%%% Machine Position of X axis %%%%%%%%%%%%%%%%
192 Xm = Xmeas(j);
193
194 % Probe Position in the B coordinate system
195 Xp = 94.1818-92.222; % (mm) Change to X position of centered probe
196 Yp = 0;
197 Zp = 75-Probe(j); % (mm) Position of the probe measurement point ...
       from the rotational axis of the B carriage in Z direction
198
199 %% Vectors and Matrices
200
201 % Probe Vector
202 ProbeVectorInB = [Xp; Yp; Zp];
203
204 % Nominal Rotation Matrices
205 Rot_BX_Nom = [cos(Bm) 0 sin(Bm); 0 1 0; -sin(Bm) 0 cos(Bm)];
206
207 % Rot_ZF_Nom = [1 0 0; 0 1 0; 0 0 1];
208
209 % Rot_CZ_Nom = [cos(Cm) -sin(Cm) 0; sin(Cm) cos(Cm) 0; 0 0 1]; % ...
       Combined with
210 % nominal based on Hocken's book
211
212 % Rot_XF_Nom = [1 0 0; 0 1 0; 0 0 1];
213
214
215 % Error Rotation Matrices
```

```
% Rot_BX_Error = [1 -Ezb Eyb; Ezb 1 -Exb; -Eyb Exb 1]; % Not measured

Rot_ZF_Error = [1 -Ezz Eyz; Ezz 1 -Exz; -Eyz Exz 1];

% Rot_CZ_Error = [1 -Ezc Eyc; Ezc 1 -Exc; -Eyc Exc 1]; % Combined ...
    with
% nominal based on Hocken's book

Rot_XF_Error = [1 -Ezx Eyx; Ezx 1 -Exx; -Eyx Exx 1];

%%%%%%%%%%%%%%%% Combining Nominal and Error Matrices %%%%%%%%%%%%%
% For the two rotational axes, the nominal and error rotation ...
    matrices need
% to be combined. This is done differently for the two axes since ...
    one is
% inversed when solving for the part and tool vectors.  Since the ...
    rotation
% matrices are symmetric the inverse is also the transpose which ...
    equates to
% changing the sign of the off diagonal terms or reflecting about the
% diagonal.

%% Part vector in C coordinate frame
% Inverse of Rcz with error and nominal rotation matrices ...
    combined (From
% Hocken's Book)
rot_zc_comb = [cos(Cm+Ezc) sin(Cm+Ezc) -Eyc; -sin(Cm+Ezc) ...
    cos(Cm+Ezc) Exc;...
     (Eyc*cos(Cm)+Exc*sin(Cm+Ezc)) (-Exc*cos(Cm)+Eyc*sin(Cm+Ezc)) 1];

% rot_fz = inv(Rot_ZF_Error); % Didn't use (better for MATLAB to use
% backslash operator than inv())

```

```
242 % rot_bx_comb = inv(Rot_BX_Nom); % Didn't measure the error ...
       motions for
243 % the B carriage but would need to do the same as (rot_zc_comb) ...
       also (better
244 % for MATLAB to use backslash operator than inv())
245
246 % Matrices with translational error terms
247 Origin_BinX = [Dxb; Dyb; Dzb];
248
249 Origin_CinZ = [Dxc; Dyc; Dzc];
250
251 Origin_XinF = [(Dxx + Xm - Xm0); Dyx; Dzx + (Xm - Xm0)*Axz];
252
253 Origin_ZinF = [Dxz; Dyz; (Dzz + Zm - Zm0)];
254
255 %% Solving Matrix Math
256 % Solving for the Position Vector in C coordinate frame
257 PinC(j,:) = rot_zc_comb*(-Origin_CinZ + ...
       (Rot_ZF_Error\(-Origin_ZinF...
258     + Origin_XinF + Rot_XF_Error*(Origin_BinX + ...
           Rot_BX_Nom\ProbeVectorInB))));
259
260
261 end
262
263 end
```

E.5 Fitting Zernike Polynomials

```
1 function [Zernike_coefficients] = zern_fit_func(X,Y,Z)
2
3 %normalization radius
```

```
4  norm_rad = 44;
5
6  [n,¬] = size(Z);
7
8  [theta,rho] = cart2pol(X,Y); % converting cartesian coords. to ...
       polar coords.
9
10 rho = rho/norm_rad;
11
12 Z_fit=zeros(n,36);
13
14 for i=1:n
15     Z_fit(i,:)=[zernfun(0,0,rho(i),theta(i)),...
16     zernfun(1,1,rho(i),theta(i)),zernfun(1,-1,rho(i),theta(i)),...
17     zernfun(2,0,rho(i),theta(i)),zernfun(2,-2,rho(i),theta(i)),...
18     zernfun(2,2,rho(i),theta(i)),zernfun(3,-1,rho(i),theta(i)),...
19     zernfun(3,1,rho(i),theta(i)),zernfun(3,-3,rho(i),theta(i)),...
20     zernfun(3,3,rho(i),theta(i)),zernfun(4,-4,rho(i),theta(i)),...
21     zernfun(4,-2,rho(i),theta(i)),zernfun(4,0,rho(i),theta(i)),...
22     zernfun(4,2,rho(i),theta(i)),zernfun(4,4,rho(i),theta(i)),...
23     zernfun(5,-5,rho(i),theta(i)),zernfun(5,-3,rho(i),theta(i)),...
24     zernfun(5,-1,rho(i),theta(i)),zernfun(5,1,rho(i),theta(i)),...
25     zernfun(5,3,rho(i),theta(i)),zernfun(5,5,rho(i),theta(i)),...
26     zernfun(6,-6,rho(i),theta(i)),zernfun(6,-4,rho(i),theta(i)),...
27     zernfun(6,-2,rho(i),theta(i)),zernfun(6,0,rho(i),theta(i)),...
28     zernfun(6,2,rho(i),theta(i)),zernfun(6,4,rho(i),theta(i)),...
29     zernfun(6,6,rho(i),theta(i)),zernfun(7,-7,rho(i),theta(i)),...
30     zernfun(7,-5,rho(i),theta(i)),zernfun(7,-3,rho(i),theta(i)),...
31     zernfun(7,-1,rho(i),theta(i)),zernfun(7,1,rho(i),theta(i)),...
32     zernfun(7,3,rho(i),theta(i)),zernfun(7,5,rho(i),theta(i)),...
33     zernfun(7,7,rho(i),theta(i))];
34 end
35
```

```
Zernike_coefficients=Z_fit\Z;

end
```

E.6 Write to NC Code

```
clc;
close all;
clear all;

%%%%%%%%%%%%%%%%%%%%%%%%%%%%%%%%%%%%%%%%%%%%%%%%%%%%%%%%%%%%%%%%%%%%%%%%%%%%
% Problem in ninety degree diametral trace at the zero, zero, ...
    zero position
load 'sphere_orthog_traces.mat'

Xmach_trace = Xmach(1,:);
Zmach_trace = Zmach(1,:);
Cmach_trace = Cmach(1,:); %

load 'mach_sphere_1_905.mat' % replaces Cmach

rad_dist = 21; % number of radial distances

[¬,jj] = size(Xmach);

% pre allocating vectors
Xmach_sort = zeros(1,jj);
Zmach_sort = zeros(1,jj);
Cmach_sort = zeros(1,jj);

Xmach_sortplus = zeros(1,jj);
Zmach_sortplus = zeros(1,jj);
```

```
26 Cmach_sortplus = zeros(1,jj);
27
28 % for the negative side of the X carriage from X=0 in G54 offsets
29 for ii = 1:jj
30
31     if Xmach(1,ii) < 0 % there is no negative Xmach when Cmach is ...
           zero, also the move from 179 to zero to -179 is no good.
32         Xmach_sort(ii) = Xmach(1,ii);
33         Zmach_sort(ii) = Zmach(1,ii);
34         Cmach_sort(ii) = Cmach(2,ii);
35     elseif Xmach(2,ii) ≤0
36         Xmach_sort(ii) = Xmach(2,ii);
37         Zmach_sort(ii) = Zmach(2,ii);
38         Cmach_sort(ii) = Cmach(1,ii);
39     else
40         Xmach_sort(ii) = -1*Xmach(2,ii);
41         Zmach_sort(ii) = Zmach(2,ii);
42         Cmach_sort(ii) = Cmach(2,ii);
43     end
44
45 end
46
47 % for the positive side of the X carriage from X=0 in G54 offsets
48 for iii = 1:jj
49
50     if Xmach(1,iii) ≥0
51         Xmach_sortplus(iii) = Xmach(1,iii); % change to sort negative
52         Zmach_sortplus(iii) = Zmach(1,iii);
53         Cmach_sortplus(iii) = Cmach(1,iii);
54     elseif Xmach(2,iii) ≥0
55         Xmach_sortplus(iii) = Xmach(2,iii);
56         Zmach_sortplus(iii) = Zmach(2,iii);
57         Cmach_sortplus(iii) = Cmach(2,iii);
```

```
58      end
59
60  end
61
62
63
64  %% Moore Nanotech UMM 100 Measurement G-Code Generator
65  %% G-Codes
66  % G00 - Rapid Positioning
67  % G01 - Linear Interpolation
68  % G02 - Circular Interpolation, clockwise
69  % G03 - Circular Interpolation, counterclockwise
70  % G04 - Dwell
71  % G18 (XZ - PLANE) Letter address I for X Letter address K for Z
72  % G53 Machine Coordinate Selection
73  % G90 Absolute Mode
74  % G91 Incremental Mode
75  % M26 Spray Mist Nozzle #1 On
76  % M29 Spray Mist Nozzles #1 and #2 Off
77  % M30 END OF PROGRAM (AND REWIND)
78  % G54-59 Work Coordinate System 1 - 6 Selection
79  %       Set these in the F4 menu?
80
81  fileID = fopen('cnc_sphere_test.nc','a');
82
83  % negative x positions
84  Xmachn = Xmach_sort';
85  Zmachn = Zmach_sort';
86  Cmachn = Cmach_sort';
87
88  % positive x positions
89  Xmachp = Xmach_sortplus';
90  Zmachp = Zmach_sortplus';
```

```
91  Cmachp = Cmach_sortplus';
92
93  Bm = 0;  % Set Bm in work offsets
94
95  [n,¬] = size(Xmachn);
96
97  % Prepratory code
98  fprintf(fileID,'G90 G55 G01; \n');
99  fprintf(fileID,'F200 X%4.4f Z%4.4f B%4.4f C%4.4f; \n',0,0,Bm,0);  ...
        % set Bm
100 fprintf(fileID,'\r\n');
101 fprintf(fileID,'\r\n');
102
103 %% Diameter traces before
104
105 [¬,e] = size(Xmach_trace);
106
107 %% at Zero degrees
108 % fprintf(fileID,'X%4.6f Z%4.6f C%4.4f; ...
        \r\n',Xmach_trace(1),Zmach_trace(1), ...
109 Cmach_trace(1));  % positioning
110 fprintf(fileID,'X%4.6f Z%4.6f C%4.4f; ...
        \r\n',Xmach_trace(1),Zmach_trace(1),0);  % hard coding the C ...
        carriage position
111 fprintf(fileID,'\r\n');
112
113 fprintf(fileID,'G04 X1; \r\n');  %dwell
114 fprintf(fileID,'M26; \r\n');  % flood coolant #1 on
115 fprintf(fileID,'G04 X1; \r\n');  %dwell
116 fprintf(fileID,'\r\n');
117
118 % at zero degrees
119 for h = 2:e/2
```

```
120
121 % fprintf(fileID,'X%4.6f Z%4.6f C%4.4f; ...
       \r\n',Xmach_trace(h),Zmach_trace(h),Cmach_trace(h));  % ...
       positioning
122 fprintf(fileID,'X%4.6f Z%4.6f C%4.4f; ...
       \r\n',Xmach_trace(h),Zmach_trace(h),0);  % hard coding the C ...
       carriage position
123 fprintf(fileID,'\r\n');
124
125 end
126
127 fprintf(fileID,'G04 X1; \r\n');  %dwell
128 fprintf(fileID,'M29; \r\n');  % flood coolant #1 and #2 off
129 fprintf(fileID,'G04 X1; \r\n');  %dwell
130 fprintf(fileID,'\r\n');
131
132 %% at 90 degrees
133 % fprintf(fileID,'X%4.6f Z%4.6f C%4.4f; ...
       \r\n',Xmach_trace(e/2+1),Zmach_trace(e/2+1), ...
       ...Cmach_trace(e/2+1));  % positioning start at (e/2+1)
134 fprintf(fileID,'X%4.6f Z%4.6f C%4.4f; ...
       \r\n',Xmach_trace(e/2+1),Zmach_trace(e/2+1),90);  % ...
       positioning start at (e/2+1)% hard coding the C carriage position
135 fprintf(fileID,'\r\n');
136
137 fprintf(fileID,'G04 X1; \r\n');  %dwell
138 fprintf(fileID,'M26; \r\n');  % flood coolant #1 on
139 fprintf(fileID,'G04 X1; \r\n');  %dwell
140 fprintf(fileID,'\r\n');
141
142 % at ninety degrees
143 for hh = e/2+2:e
144
```

```
145 % fprintf(fileID,'X%4.6f Z%4.6f C%4.4f; ...
       \r\n',Xmach_trace(hh),Zmach_trace(hh),Cmach_trace(hh));  % ...
       positioning
146 fprintf(fileID,'X%4.6f Z%4.6f C%4.4f; ...
       \r\n',Xmach_trace(hh),Zmach_trace(hh),90);  % positioning % ...
       hard coding the C carriage position
147 fprintf(fileID,'\r\n');
148
149 end
150
151 fprintf(fileID,'G04 X1; \r\n');  %dwell
152 fprintf(fileID,'M29; \r\n');  % flood coolant #1 and #2 off
153 fprintf(fileID,'G04 X1; \r\n');  %dwell
154 fprintf(fileID,'\r\n');
155
156 %% at 180 degrees
157
158 % fprintf(fileID,'X%4.6f Z%4.6f C%4.4f; ...
       \r\n',Xmach_trace(1),Zmach_trace(1),Cmach_trace(1));  % ...
       positioning
159 fprintf(fileID,'X%4.6f Z%4.6f C%4.4f; ...
       \r\n',-Xmach_trace(1),Zmach_trace(1),180);  % hard coding the ...
       C carriage position % switch the X direction of travel for ...
       data age
160 fprintf(fileID,'\r\n');
161
162 fprintf(fileID,'G04 X1; \r\n');  %dwell
163 fprintf(fileID,'M26; \r\n');  % flood coolant #1 on
164 fprintf(fileID,'G04 X1; \r\n');  %dwell
165 fprintf(fileID,'\r\n');
166
167 % at zero degrees
168 for h = 2:e/2
```

```
169
170 % fprintf(fileID,'X%4.6f Z%4.6f C%4.4f; ...
       \r\n',Xmach_trace(h),Zmach_trace(h),Cmach_trace(h));  % ...
       positioning
171 fprintf(fileID,'X%4.6f Z%4.6f C%4.4f; ...
       \r\n',-Xmach_trace(h),Zmach_trace(h),180);  % positioning % ...
       hard coding the C carriage position % switch the X direction ...
       of travel for data age
172 fprintf(fileID,'\r\n');
173
174 end
175
176 fprintf(fileID,'G04 X1; \r\n');  %dwell
177 fprintf(fileID,'M29; \r\n');  % flood coolant #1 and #2 off
178 fprintf(fileID,'G04 X1; \r\n');  %dwell
179 fprintf(fileID,'\r\n');
180
181 %% at 270 degrees
182 % fprintf(fileID,'X%4.6f Z%4.6f C%4.4f; ...
       \r\n',Xmach_trace(e/2+1),Zmach_trace(e/2+1),... ...
       Cmach_trace(e/2+1));  % positioning start at (e/2+1)
183 fprintf(fileID,'X%4.6f Z%4.6f C%4.4f; ...
       \r\n',-Xmach_trace(e/2+1),Zmach_trace(e/2+1),270);  % ...
       positioning start at (e/2+1) % hard coding the C carriage ...
       position % switch the X direction of travel for data age
184 fprintf(fileID,'\r\n');
185
186 fprintf(fileID,'G04 X1; \r\n');  %dwell
187 fprintf(fileID,'M26; \r\n');  % flood coolant #1 on
188 fprintf(fileID,'G04 X1; \r\n');  %dwell
189 fprintf(fileID,'\r\n');
190
191 % at ninety degrees
```

```
192 for hh = e/2+2:e
193
194 % fprintf(fileID,'X%4.6f Z%4.6f C%4.4f; ...
       \r\n',Xmach_trace(hh),Zmach_trace(hh),Cmach_trace(hh));  % ...
       positioning
195 fprintf(fileID,'X%4.6f Z%4.6f C%4.4f; ...
       \r\n',-Xmach_trace(hh),Zmach_trace(hh),270);  % positioning % ...
       hard coding the C carriage position % switch the X direction ...
       of travel for data age
196 fprintf(fileID,'\r\n');
197
198 end
199
200 fprintf(fileID,'G04 X1; \r\n');  %dwell
201 fprintf(fileID,'M29; \r\n');  % flood coolant #1 and #2 off
202 fprintf(fileID,'G04 X1; \r\n');  %dwell
203 fprintf(fileID,'\r\n');
204
205 %% Circumference measurements
206
207 for j = 1:rad_dist  % Number of circumferential traces
208
209 fprintf(fileID,'X%4.6f Z%4.6f C%4.4f; ...
       \r\n',Xmachn(1+371*(j-1)),Zmachn(1+371*(j-1)),... ...
       Cmachn(1+371*(j-1)));  % positioning
210 fprintf(fileID,'\r\n');
211
212 fprintf(fileID,'G04 X1; \r\n');  %dwell
213 fprintf(fileID,'M26; \r\n');  % flood coolant #1 on
214 fprintf(fileID,'G04 X1; \r\n');  %dwell
215 fprintf(fileID,'\r\n');
216
217 for i = 2:371 % number of points in each circumferential trace
```

```
218     fprintf(fileID,'X%4.6f Z%4.6f C%4.4f; ...
            \r\n',Xmachn(i+371*(j-1)),Zmachn(i+371*(j-1)),... ...
            Cmachn(i+371*(j-1)));  % positioning
219     fprintf(fileID,'\r\n');
220 end
221
222 fprintf(fileID,'G04 X1; \r\n');  %dwell
223 fprintf(fileID,'M29; \r\n');  % flood coolant #1 and #2 off
224 fprintf(fileID,'G04 X1; \r\n');  %dwell
225 fprintf(fileID,'\r\n');
226
227 end
228
229 %% X plus side of optic
230
231 for j = 1:rad_dist  % Number of circumferential traces
232
233 fprintf(fileID,'X%4.6f Z%4.6f C%4.4f; ...
       \r\n',Xmachp(1+371*(j-1)),Zmachp(1+371*(j-1)),... ...
       Cmachp(1+371*(j-1)));  % positioning
234 fprintf(fileID,'\r\n');
235
236 fprintf(fileID,'G04 X1; \r\n');  %dwell
237 fprintf(fileID,'M26; \r\n');  % flood coolant #1 on
238 fprintf(fileID,'G04 X1; \r\n');  %dwell
239 fprintf(fileID,'\r\n');
240
241 for i = 2:371 % number of points in each circumferential trace
242     fprintf(fileID,'X%4.6f Z%4.6f C%4.4f; ...
            \r\n',Xmachp(i+371*(j-1)),Zmachp(i+371*(j-1)),... ...
            Cmachp(i+371*(j-1)));  % positioning
243     fprintf(fileID,'\r\n');
244 end
```

```
245
246 fprintf(fileID,'G04 X1; \r\n');  %dwell
247 fprintf(fileID,'M29; \r\n');  % flood coolant #1 and #2 off
248 fprintf(fileID,'G04 X1; \r\n');  %dwell
249 fprintf(fileID,'\r\n');
250
251 end
252
253
254 %% Diameter traces
255 %% at Zero degrees
256 % fprintf(fileID,'X%4.6f Z%4.6f C%4.4f; ...
       \r\n',Xmach_trace(1),Zmach_trace(1),Cmach_trace(1));  % ...
       positioning
257 fprintf(fileID,'X%4.6f Z%4.6f C%4.4f; ...
       \r\n',Xmach_trace(1),Zmach_trace(1),0);  % hard coding the C ...
       carriage position
258 fprintf(fileID,'\r\n');
259
260 fprintf(fileID,'G04 X1; \r\n');  %dwell
261 fprintf(fileID,'M26; \r\n');  % flood coolant #1 on
262 fprintf(fileID,'G04 X1; \r\n');  %dwell
263 fprintf(fileID,'\r\n');
264
265 % at zero degrees
266 for h = 2:e/2
267
268 % fprintf(fileID,'X%4.6f Z%4.6f C%4.4f; ...
       \r\n',Xmach_trace(h),Zmach_trace(h),Cmach_trace(h));  % ...
       positioning
269 fprintf(fileID,'X%4.6f Z%4.6f C%4.4f; ...
       \r\n',Xmach_trace(h),Zmach_trace(h),0);  % hard coding the C ...
       carriage position
```

```
270 fprintf(fileID,'\r\n');
271
272 end
273
274 fprintf(fileID,'G04 X1; \r\n');  %dwell
275 fprintf(fileID,'M29; \r\n');  % flood coolant #1 and #2 off
276 fprintf(fileID,'G04 X1; \r\n');  %dwell
277 fprintf(fileID,'\r\n');
278
279 %% at 90 degrees
280 % fprintf(fileID,'X%4.6f Z%4.6f C%4.4f; ...
       \r\n',Xmach_trace(e/2+1),Zmach_trace(e/2+1),... ...
       Cmach_trace(e/2+1));  % positioning start at (e/2+1)
281 fprintf(fileID,'X%4.6f Z%4.6f C%4.4f; ...
       \r\n',Xmach_trace(e/2+1),Zmach_trace(e/2+1),90);  % ...
       positioning start at (e/2+1)% hard coding the C carriage position
282 fprintf(fileID,'\r\n');
283
284 fprintf(fileID,'G04 X1; \r\n');  %dwell
285 fprintf(fileID,'M26; \r\n');  % flood coolant #1 on
286 fprintf(fileID,'G04 X1; \r\n');  %dwell
287 fprintf(fileID,'\r\n');
288
289 % at ninety degrees
290 for hh = e/2+2:e
291
292 % fprintf(fileID,'X%4.6f Z%4.6f C%4.4f; ...
       \r\n',Xmach_trace(hh),Zmach_trace(hh),Cmach_trace(hh));  % ...
       positioning
293 fprintf(fileID,'X%4.6f Z%4.6f C%4.4f; ...
       \r\n',Xmach_trace(hh),Zmach_trace(hh),90);  % positioning % ...
       hard coding the C carriage position
294 fprintf(fileID,'\r\n');
```

```
295
296 end
297
298 fprintf(fileID,'G04 X1; \r\n');  %dwell
299 fprintf(fileID,'M29; \r\n');  % flood coolant #1 and #2 off
300 fprintf(fileID,'G04 X1; \r\n');  %dwell
301 fprintf(fileID,'\r\n');
302
303 %% at 180 degrees
304
305 % fprintf(fileID,'X%4.6f Z%4.6f C%4.4f; ...
      \r\n',Xmach_trace(1),Zmach_trace(1),Cmach_trace(1));  % ...
      positioning
306 fprintf(fileID,'X%4.6f Z%4.6f C%4.4f; ...
      \r\n',-Xmach_trace(1),Zmach_trace(1),180);  % hard coding the ...
      C carriage position % switch the X direction of travel for ...
      data age
307 fprintf(fileID,'\r\n');
308
309 fprintf(fileID,'G04 X1; \r\n');  %dwell
310 fprintf(fileID,'M26; \r\n');  % flood coolant #1 on
311 fprintf(fileID,'G04 X1; \r\n');  %dwell
312 fprintf(fileID,'\r\n');
313
314 % at zero degrees
315 for h = 2:e/2
316
317 % fprintf(fileID,'X%4.6f Z%4.6f C%4.4f; ...
      \r\n',Xmach_trace(h),Zmach_trace(h),Cmach_trace(h));  % ...
      positioning
318 fprintf(fileID,'X%4.6f Z%4.6f C%4.4f; ...
      \r\n',-Xmach_trace(h),Zmach_trace(h),180);  % positioning % ...
      hard coding the C carriage position % switch the X direction ...
```

```
      of travel for data age
fprintf(fileID,'\r\n');

end

fprintf(fileID,'G04 X1; \r\n');  %dwell
fprintf(fileID,'M29; \r\n');  % flood coolant #1 and #2 off
fprintf(fileID,'G04 X1; \r\n');  %dwell
fprintf(fileID,'\r\n');

%% at 270 degrees
% fprintf(fileID,'X%4.6f Z%4.6f C%4.4f; ...
      \r\n',Xmach_trace(e/2+1),Zmach_trace(e/2+1),... ...
      Cmach_trace(e/2+1));  % positioning start at (e/2+1)
fprintf(fileID,'X%4.6f Z%4.6f C%4.4f; ...
      \r\n',-Xmach_trace(e/2+1),Zmach_trace(e/2+1),270);  % ...
      positioning start at (e/2+1) % hard coding the C carriage ...
      position % switch the X direction of travel for data age
fprintf(fileID,'\r\n');

fprintf(fileID,'G04 X1; \r\n');  %dwell
fprintf(fileID,'M26; \r\n');  % flood coolant #1 on
fprintf(fileID,'G04 X1; \r\n');  %dwell
fprintf(fileID,'\r\n');

% at ninety degrees
for hh = e/2+2:e

% fprintf(fileID,'X%4.6f Z%4.6f C%4.4f; ...
      \r\n',Xmach_trace(hh),Zmach_trace(hh),Cmach_trace(hh));  % ...
      positioning
fprintf(fileID,'X%4.6f Z%4.6f C%4.4f; ...
      \r\n',-Xmach_trace(hh),Zmach_trace(hh),270);  % positioning % ...
```

```
      hard coding the C carriage position % switch the X direction ...
      of travel for data age
fprintf(fileID,'\r\n');

end

fprintf(fileID,'G04 X1; \r\n');  %dwell
fprintf(fileID,'M29; \r\n');  % flood coolant #1 and #2 off
fprintf(fileID,'G04 X1; \r\n');  %dwell
fprintf(fileID,'\r\n');


%% Z carriage and probe calibration
% move 0.5 um over 10 um centered on

fprintf(fileID,'\r\n');
fprintf(fileID,'X%4.4f Z%4.4f B%4.4f C%4.4f; \n',0,-0.0075,Bm,0);
fprintf(fileID,'\r\n');

fprintf(fileID,'G04 X5; \r\n');  %dwell
fprintf(fileID,'M26; \r\n');  % flood coolant #1 on
fprintf(fileID,'G04 X5; \r\n');  %dwell
fprintf(fileID,'M29; \r\n');  % flood coolant #1 and #2 off
fprintf(fileID,'G04 X1; \r\n');  %dwell
fprintf(fileID,'\r\n');


fprintf(fileID,'\r\n');
fprintf(fileID,'X%4.4f Z%4.4f B%4.4f C%4.4f; \n',0,-0.007,Bm,0);
fprintf(fileID,'\r\n');

fprintf(fileID,'G04 X5; \r\n');  %dwell
fprintf(fileID,'M26; \r\n');  % flood coolant #1 on
```

```
374 fprintf(fileID,'G04 X5; \r\n');  %dwell
375 fprintf(fileID,'M29; \r\n');  % flood coolant #1 and #2 off
376 fprintf(fileID,'G04 X1; \r\n');  %dwell
377 fprintf(fileID,'\r\n');
378
379
380
381
382 fprintf(fileID,'\r\n');
383 fprintf(fileID,'X%4.4f Z%4.4f B%4.4f C%4.4f; \n',0,-0.0065,Bm,0);
384 fprintf(fileID,'\r\n');
385
386 fprintf(fileID,'G04 X5; \r\n');  %dwell
387 fprintf(fileID,'M26; \r\n');  % flood coolant #1 on
388 fprintf(fileID,'G04 X5; \r\n');  %dwell
389 fprintf(fileID,'M29; \r\n');  % flood coolant #1 and #2 off
390 fprintf(fileID,'G04 X1; \r\n');  %dwell
391 fprintf(fileID,'\r\n');
392
393
394
395
396 fprintf(fileID,'\r\n');
397 fprintf(fileID,'X%4.4f Z%4.4f B%4.4f C%4.4f; \n',0,-0.006,Bm,0);
398 fprintf(fileID,'\r\n');
399
400 fprintf(fileID,'G04 X5; \r\n');  %dwell
401 fprintf(fileID,'M26; \r\n');  % flood coolant #1 on
402 fprintf(fileID,'G04 X5; \r\n');  %dwell
403 fprintf(fileID,'M29; \r\n');  % flood coolant #1 and #2 off
404 fprintf(fileID,'G04 X1; \r\n');  %dwell
405 fprintf(fileID,'\r\n');
406
```

```
407
408 fprintf(fileID,'\r\n');
409 fprintf(fileID,'X%4.4f Z%4.4f B%4.4f C%4.4f; \n',0,-0.0055,Bm,0);
410 fprintf(fileID,'\r\n');
411
412 fprintf(fileID,'G04 X5; \r\n');  %dwell
413 fprintf(fileID,'M26; \r\n');  % flood coolant #1 on
414 fprintf(fileID,'G04 X5; \r\n');  %dwell
415 fprintf(fileID,'M29; \r\n');  % flood coolant #1 and #2 off
416 fprintf(fileID,'G04 X1; \r\n');  %dwell
417 fprintf(fileID,'\r\n');
418
419
420
421 fprintf(fileID,'\r\n');
422 fprintf(fileID,'X%4.4f Z%4.4f B%4.4f C%4.4f; \n',0,-0.005,Bm,0);
423 fprintf(fileID,'\r\n');
424
425 fprintf(fileID,'G04 X5; \r\n');  %dwell
426 fprintf(fileID,'M26; \r\n');  % flood coolant #1 on
427 fprintf(fileID,'G04 X5; \r\n');  %dwell
428 fprintf(fileID,'M29; \r\n');  % flood coolant #1 and #2 off
429 fprintf(fileID,'G04 X1; \r\n');  %dwell
430 fprintf(fileID,'\r\n');
431
432
433 fprintf(fileID,'\r\n');
434 fprintf(fileID,'X%4.4f Z%4.4f B%4.4f C%4.4f; \n',0,-0.0045,Bm,0);
435 fprintf(fileID,'\r\n');
436
437 fprintf(fileID,'G04 X5; \r\n');  %dwell
438 fprintf(fileID,'M26; \r\n');  % flood coolant #1 on
439 fprintf(fileID,'G04 X5; \r\n');  %dwell
```

```
440 fprintf(fileID,'M29; \r\n');  % flood coolant #1 and #2 off
441 fprintf(fileID,'G04 X1; \r\n');  %dwell
442 fprintf(fileID,'\r\n');
443
444
445 fprintf(fileID,'\r\n');
446 fprintf(fileID,'X%4.4f Z%4.4f B%4.4f C%4.4f; \n',0,-0.004,Bm,0);
447 fprintf(fileID,'\r\n');
448
449 fprintf(fileID,'G04 X5; \r\n');  %dwell
450 fprintf(fileID,'M26; \r\n');  % flood coolant #1 on
451 fprintf(fileID,'G04 X5; \r\n');  %dwell
452 fprintf(fileID,'M29; \r\n');  % flood coolant #1 and #2 off
453 fprintf(fileID,'G04 X1; \r\n');  %dwell
454 fprintf(fileID,'\r\n');
455
456
457 fprintf(fileID,'\r\n');
458 fprintf(fileID,'X%4.4f Z%4.4f B%4.4f C%4.4f; \n',0,-0.0035,Bm,0);
459 fprintf(fileID,'\r\n');
460
461 fprintf(fileID,'G04 X5; \r\n');  %dwell
462 fprintf(fileID,'M26; \r\n');  % flood coolant #1 on
463 fprintf(fileID,'G04 X5; \r\n');  %dwell
464 fprintf(fileID,'M29; \r\n');  % flood coolant #1 and #2 off
465 fprintf(fileID,'G04 X1; \r\n');  %dwell
466 fprintf(fileID,'\r\n');
467
468
469 fprintf(fileID,'\r\n');
470 fprintf(fileID,'X%4.4f Z%4.4f B%4.4f C%4.4f; \n',0,-0.003,Bm,0);
471 fprintf(fileID,'\r\n');
472
```

```
473 fprintf(fileID,'G04 X5; \r\n');  %dwell
474 fprintf(fileID,'M26; \r\n');  % flood coolant #1 on
475 fprintf(fileID,'G04 X5; \r\n');  %dwell
476 fprintf(fileID,'M29; \r\n');  % flood coolant #1 and #2 off
477 fprintf(fileID,'G04 X1; \r\n');  %dwell
478 fprintf(fileID,'\r\n');
479
480
481 fprintf(fileID,'\r\n');
482 fprintf(fileID,'X%4.4f Z%4.4f B%4.4f C%4.4f; \n',0,-0.0025,Bm,0);
483 fprintf(fileID,'\r\n');
484
485 fprintf(fileID,'G04 X5; \r\n');  %dwell
486 fprintf(fileID,'M26; \r\n');  % flood coolant #1 on
487 fprintf(fileID,'G04 X5; \r\n');  %dwell
488 fprintf(fileID,'M29; \r\n');  % flood coolant #1 and #2 off
489 fprintf(fileID,'G04 X1; \r\n');  %dwell
490 fprintf(fileID,'\r\n');
491
492
493 fprintf(fileID,'\r\n');
494 fprintf(fileID,'X%4.4f Z%4.4f B%4.4f C%4.4f; \n',0,-0.002,Bm,0);
495 fprintf(fileID,'\r\n');
496
497 fprintf(fileID,'G04 X5; \r\n');  %dwell
498 fprintf(fileID,'M26; \r\n');  % flood coolant #1 on
499 fprintf(fileID,'G04 X5; \r\n');  %dwell
500 fprintf(fileID,'M29; \r\n');  % flood coolant #1 and #2 off
501 fprintf(fileID,'G04 X1; \r\n');  %dwell
502 fprintf(fileID,'\r\n');
503
504
505 fprintf(fileID,'\r\n');
```

```
506 fprintf(fileID,'X%4.4f Z%4.4f B%4.4f C%4.4f; \n',0,-0.0015,Bm,0);
507 fprintf(fileID,'\r\n');
508
509 fprintf(fileID,'G04 X5; \r\n');  %dwell
510 fprintf(fileID,'M26; \r\n');  % flood coolant #1 on
511 fprintf(fileID,'G04 X5; \r\n');  %dwell
512 fprintf(fileID,'M29; \r\n');  % flood coolant #1 and #2 off
513 fprintf(fileID,'G04 X1; \r\n');  %dwell
514 fprintf(fileID,'\r\n');
515
516
517 fprintf(fileID,'\r\n');
518 fprintf(fileID,'X%4.4f Z%4.4f B%4.4f C%4.4f; \n',0,-0.001,Bm,0);
519 fprintf(fileID,'\r\n');
520
521 fprintf(fileID,'G04 X5; \r\n');  %dwell
522 fprintf(fileID,'M26; \r\n');  % flood coolant #1 on
523 fprintf(fileID,'G04 X5; \r\n');  %dwell
524 fprintf(fileID,'M29; \r\n');  % flood coolant #1 and #2 off
525 fprintf(fileID,'G04 X1; \r\n');  %dwell
526 fprintf(fileID,'\r\n');
527
528
529 fprintf(fileID,'\r\n');
530 fprintf(fileID,'X%4.4f Z%4.4f B%4.4f C%4.4f; \n',0,-0.0005,Bm,0);
531 fprintf(fileID,'\r\n');
532
533 fprintf(fileID,'G04 X5; \r\n');  %dwell
534 fprintf(fileID,'M26; \r\n');  % flood coolant #1 on
535 fprintf(fileID,'G04 X5; \r\n');  %dwell
536 fprintf(fileID,'M29; \r\n');  % flood coolant #1 and #2 off
537 fprintf(fileID,'G04 X1; \r\n');  %dwell
538 fprintf(fileID,'\r\n');
```

```
539
540
541 fprintf(fileID,'\r\n');
542 fprintf(fileID,'X%4.4f Z%4.4f B%4.4f C%4.4f; \n',0,0.000,Bm,0);
543 fprintf(fileID,'\r\n');
544
545 fprintf(fileID,'G04 X5; \r\n');  %dwell
546 fprintf(fileID,'M26; \r\n');  % flood coolant #1 on
547 fprintf(fileID,'G04 X5; \r\n');  %dwell
548 fprintf(fileID,'M29; \r\n');  % flood coolant #1 and #2 off
549 fprintf(fileID,'G04 X1; \r\n');  %dwell
550 fprintf(fileID,'\r\n');
551
552
553 fprintf(fileID,'\r\n');
554 fprintf(fileID,'X%4.4f Z%4.4f B%4.4f C%4.4f; \n',0,0.0005,Bm,0);
555 fprintf(fileID,'\r\n');
556
557 fprintf(fileID,'G04 X5; \r\n');  %dwell
558 fprintf(fileID,'M26; \r\n');  % flood coolant #1 on
559 fprintf(fileID,'G04 X5; \r\n');  %dwell
560 fprintf(fileID,'M29; \r\n');  % flood coolant #1 and #2 off
561 fprintf(fileID,'G04 X1; \r\n');  %dwell
562 fprintf(fileID,'\r\n');
563
564
565 fprintf(fileID,'\r\n');
566 fprintf(fileID,'X%4.4f Z%4.4f B%4.4f C%4.4f; \n',0,0.001,Bm,0);
567 fprintf(fileID,'\r\n');
568
569 fprintf(fileID,'G04 X5; \r\n');  %dwell
570 fprintf(fileID,'M26; \r\n');  % flood coolant #1 on
571 fprintf(fileID,'G04 X5; \r\n');  %dwell
```

```
572 fprintf(fileID,'M29; \r\n');  % flood coolant #1 and #2 off
573 fprintf(fileID,'G04 X1; \r\n');  %dwell
574 fprintf(fileID,'\r\n');
575
576
577 fprintf(fileID,'\r\n');
578 fprintf(fileID,'X%4.4f Z%4.4f B%4.4f C%4.4f; \n',0,0.0015,Bm,0);
579 fprintf(fileID,'\r\n');
580
581 fprintf(fileID,'G04 X5; \r\n');  %dwell
582 fprintf(fileID,'M26; \r\n');  % flood coolant #1 on
583 fprintf(fileID,'G04 X5; \r\n');  %dwell
584 fprintf(fileID,'M29; \r\n');  % flood coolant #1 and #2 off
585 fprintf(fileID,'G04 X1; \r\n');  %dwell
586 fprintf(fileID,'\r\n');
587
588
589 fprintf(fileID,'\r\n');
590 fprintf(fileID,'X%4.4f Z%4.4f B%4.4f C%4.4f; \n',0,0.002,Bm,0);
591 fprintf(fileID,'\r\n');
592
593 fprintf(fileID,'G04 X5; \r\n');  %dwell
594 fprintf(fileID,'M26; \r\n');  % flood coolant #1 on
595 fprintf(fileID,'G04 X5; \r\n');  %dwell
596 fprintf(fileID,'M29; \r\n');  % flood coolant #1 and #2 off
597 fprintf(fileID,'G04 X1; \r\n');  %dwell
598 fprintf(fileID,'\r\n');
599
600
601 fprintf(fileID,'\r\n');
602 fprintf(fileID,'X%4.4f Z%4.4f B%4.4f C%4.4f; \n',0,0.0025,Bm,0);
603 fprintf(fileID,'\r\n');
604
```

```
605 fprintf(fileID,'G04 X5; \r\n');  %dwell
606 fprintf(fileID,'M26; \r\n');  % flood coolant #1 on
607 fprintf(fileID,'G04 X5; \r\n');  %dwell
608 fprintf(fileID,'M29; \r\n');  % flood coolant #1 and #2 off
609 fprintf(fileID,'G04 X1; \r\n');  %dwell
610 fprintf(fileID,'\r\n');
611
612
613 fprintf(fileID,'\r\n');
614 fprintf(fileID,'X%4.4f Z%4.4f B%4.4f C%4.4f; \n',0,0.003,Bm,0);
615 fprintf(fileID,'\r\n');
616
617 fprintf(fileID,'G04 X5; \r\n');  %dwell
618 fprintf(fileID,'M26; \r\n');  % flood coolant #1 on
619 fprintf(fileID,'G04 X5; \r\n');  %dwell
620 fprintf(fileID,'M29; \r\n');  % flood coolant #1 and #2 off
621 fprintf(fileID,'G04 X1; \r\n');  %dwell
622 fprintf(fileID,'\r\n');
623
624
625 fprintf(fileID,'\r\n');
626 fprintf(fileID,'X%4.4f Z%4.4f B%4.4f C%4.4f; \n',0,0.0035,Bm,0);
627 fprintf(fileID,'\r\n');
628
629 fprintf(fileID,'G04 X5; \r\n');  %dwell
630 fprintf(fileID,'M26; \r\n');  % flood coolant #1 on
631 fprintf(fileID,'G04 X5; \r\n');  %dwell
632 fprintf(fileID,'M29; \r\n');  % flood coolant #1 and #2 off
633 fprintf(fileID,'G04 X1; \r\n');  %dwell
634 fprintf(fileID,'\r\n');
635
636
637 fprintf(fileID,'\r\n');
```

```
638 fprintf(fileID,'X%4.4f Z%4.4f B%4.4f C%4.4f; \n',0,0.004,Bm,0);
639 fprintf(fileID,'\r\n');
640
641 fprintf(fileID,'G04 X5; \r\n');  %dwell
642 fprintf(fileID,'M26; \r\n');  % flood coolant #1 on
643 fprintf(fileID,'G04 X5; \r\n');  %dwell
644 fprintf(fileID,'M29; \r\n');  % flood coolant #1 and #2 off
645 fprintf(fileID,'G04 X1; \r\n');  %dwell
646 fprintf(fileID,'\r\n');
647
648
649 fprintf(fileID,'\r\n');
650 fprintf(fileID,'X%4.4f Z%4.4f B%4.4f C%4.4f; \n',0,0.0045,Bm,0);
651 fprintf(fileID,'\r\n');
652
653 fprintf(fileID,'G04 X5; \r\n');  %dwell
654 fprintf(fileID,'M26; \r\n');  % flood coolant #1 on
655 fprintf(fileID,'G04 X5; \r\n');  %dwell
656 fprintf(fileID,'M29; \r\n');  % flood coolant #1 and #2 off
657 fprintf(fileID,'G04 X1; \r\n');  %dwell
658 fprintf(fileID,'\r\n');
659
660
661 fprintf(fileID,'\r\n');
662 fprintf(fileID,'X%4.4f Z%4.4f B%4.4f C%4.4f; \n',0,0.005,Bm,0);
663 fprintf(fileID,'\r\n');
664
665 fprintf(fileID,'G04 X5; \r\n');  %dwell
666 fprintf(fileID,'M26; \r\n');  % flood coolant #1 on
667 fprintf(fileID,'G04 X5; \r\n');  %dwell
668 fprintf(fileID,'M29; \r\n');  % flood coolant #1 and #2 off
669 fprintf(fileID,'G04 X1; \r\n');  %dwell
670 fprintf(fileID,'\r\n');
```

```
671
672 fprintf(fileID,'\r\n');
673 fprintf(fileID,'X%4.4f Z%4.4f B%4.4f C%4.4f; \n',0,0.0055,Bm,0);
674 fprintf(fileID,'\r\n');
675
676 fprintf(fileID,'G04 X5; \r\n');  %dwell
677 fprintf(fileID,'M26; \r\n');  % flood coolant #1 on
678 fprintf(fileID,'G04 X5; \r\n');  %dwell
679 fprintf(fileID,'M29; \r\n');  % flood coolant #1 and #2 off
680 fprintf(fileID,'G04 X1; \r\n');  %dwell
681 fprintf(fileID,'\r\n');
682
683 fprintf(fileID,'\r\n');
684 fprintf(fileID,'X%4.4f Z%4.4f B%4.4f C%4.4f; \n',0,0.006,Bm,0);
685 fprintf(fileID,'\r\n');
686
687 fprintf(fileID,'G04 X5; \r\n');  %dwell
688 fprintf(fileID,'M26; \r\n');  % flood coolant #1 on
689 fprintf(fileID,'G04 X5; \r\n');  %dwell
690 fprintf(fileID,'M29; \r\n');  % flood coolant #1 and #2 off
691 fprintf(fileID,'G04 X1; \r\n');  %dwell
692 fprintf(fileID,'\r\n');
693
694 fprintf(fileID,'\r\n');
695 fprintf(fileID,'X%4.4f Z%4.4f B%4.4f C%4.4f; \n',0,0.0065,Bm,0);
696 fprintf(fileID,'\r\n');
697
698 fprintf(fileID,'G04 X5; \r\n');  %dwell
699 fprintf(fileID,'M26; \r\n');  % flood coolant #1 on
700 fprintf(fileID,'G04 X5; \r\n');  %dwell
701 fprintf(fileID,'M29; \r\n');  % flood coolant #1 and #2 off
702 fprintf(fileID,'G04 X1; \r\n');  %dwell
703 fprintf(fileID,'\r\n');
```

```
704
705 fprintf(fileID,'\r\n');
706 fprintf(fileID,'X%4.4f Z%4.4f B%4.4f C%4.4f; \n',0,0.007,Bm,0);
707 fprintf(fileID,'\r\n');
708
709 fprintf(fileID,'G04 X5; \r\n');  %dwell
710 fprintf(fileID,'M26; \r\n');  % flood coolant #1 on
711 fprintf(fileID,'G04 X5; \r\n');  %dwell
712 fprintf(fileID,'M29; \r\n');  % flood coolant #1 and #2 off
713 fprintf(fileID,'G04 X1; \r\n');  %dwell
714 fprintf(fileID,'\r\n');
715
716 fprintf(fileID,'\r\n');
717 fprintf(fileID,'X%4.4f Z%4.4f B%4.4f C%4.4f; \n',0,0.0075,Bm,0);
718 fprintf(fileID,'\r\n');
719
720 fprintf(fileID,'G04 X5; \r\n');  %dwell
721 fprintf(fileID,'M26; \r\n');  % flood coolant #1 on
722 fprintf(fileID,'G04 X5; \r\n');  %dwell
723 fprintf(fileID,'M29; \r\n');  % flood coolant #1 and #2 off
724 fprintf(fileID,'G04 X1; \r\n');  %dwell
725 fprintf(fileID,'\r\n');
726
727
728 %% Ending code
729 fprintf(fileID,'\r\n');
730
731 fprintf(fileID,'X%4.4f Z%4.4f B%4.4f C%4.4f; \n',0,10,Bm,0);  % ...
       set Bm, moves part away when finished (Z=10)
732
733 % Close the .NC file
734 fclose(fileID);
735 fclose('all');
```

E.7 Remove Fundamental

Fitting and removing the fundamental is used in Estler's Face Motion Reversal.

```
function [C_uniq, yhat] = remove_fundamental(C,Probe)

% remove duplicate C values
[C_uniq, ia, ¬] = unique(C,'stable');
Probe_uniq = Probe(ia);

C_uniq = C_uniq';
Probe_uniq = Probe_uniq';

% Not all of this is necessary since it has a period of 360 deg.
[n,¬] =  size(C_uniq);
X = ones(n,3); % three columns of 1s
X(:,2) = cos((2*pi)/360*C_uniq); % cosine with period of 360
X(:,3) = sin((2*pi)/360*C_uniq); % sine with period of 360

beta = X\Probe_uniq;

yhat = beta(1)+beta(2)*cos((2*pi)/360*C_uniq)+ ...
    (3)*sin((2*pi)/360*C_uniq); % plotting resulting fit

figure
plot(C,Probe)
hold on
plot(C_uniq, yhat)
ylabel '(\mum)'
xlabel '(deg)'
xlim([0 370])
```

```
27 set(gcf, 'Units', 'Normalized', 'OuterPosition', [0.2, 0.1, 0.6, ...
       0.8]);
28 set(gca, 'fontsize', 18,'fontweight','bold')
29 title 'Fit sine wave'
30 end
```